Synthetic Aperture Radar Using Non-Uniform Sampling

by

JONATHAN ANDREW LEGG

Thesis submitted for the degree of

Doctor of Philosophy

Department of Electrical and Electronic Engineering
Faculty of Engineering
The University of Adelaide
Adelaide, South Australia

August 1997

Contents

Abstract

Synthetic aperture radar is a well established technique for imaging the ground to one side of an airborne platform.

Moving target detection is a very useful capability for a long range sensor.

The combination of synthetic aperture radar and moving target detection has the potential to produce high resolution ground imagery with superimposed moving target information. Unfortunately, using conventional imaging data for detecting moving targets leads to ambiguities in the targets' positions and velocities.

By utilising a non-uniform pulse repetition interval, the proposed ground imaging / moving target detection radar overcomes this limitation and allows the azimuthal data to be focussed at any velocity of interest, whilst collecting data at the same average rate as a conventional synthetic aperture radar. This approach permits the flexible use of a multimode radar, relaxes the specifications of data acquisition systems, affords a degree of protection against electronic countermeasures and retains a large unambiguous range swath, but with the added complexity of processing the non-uniform samples. This thesis investigates the technique in detail, incorporating optimal target detection strategies and azimuthal beam patterns, and demonstrates it using simulations of non-uniform transmissions with real data.

Declaration

This work contains no material which has been accepted for the award of any other degree or diploma in any university or other tertiary institution and, to the best of my knowledge and belief, contains no material previously published or written by another person, except where due reference has been made in the text.

I give consent to this copy of my thesis, when deposited in the University Library, being available for loan and photocopying.

Date 8th August, 1997

Acknowledgments

I wish to thank a number of people and organisations, without whom this thesis would not exist.

Dr Alan Bolton is a colleague and friend who provided the original inspiration for this work and gave continual support and encouragement throughout its duration.

Prof. Douglas Gray, my Ph.D. supervisor, changed my attitude from one of 'try it and see' to one of careful and thorough analysis. His expertise in sonar beamforming provided me with useful insights regarding the treatment of synthetic aperture radar as a phased array.

Dr Don Sinnott, as Chief of Microwave Radar Division, approved my sponsorship through the Defence Science and Technology Organisation, Salisbury. My MRD supervisor, Marian Viola, kindly decided he could do without me during the period of my candidature and eagerly awaited its completion.

The Cooperative Research Centre for Sensor Signal and Information Processing provided excellent facilities and great people to work with. I will never forget the superlative morning teas.

My family, and particularly my darling Jan, provided encouragement regarding the furthering of my career. Jan was quite happy for me to work hard during the weekends!

List of Figures

List of Tables

Glossary

Abbreviations

AF	ambiguity function
CNR	clutter to noise ratio
CRLB	Cramér-Rao lower bound
MTD	moving target detection
MTI	moving target indication
PDF	probability density function
PRF	pulse repetition frequency
PRI	pulse repetition interval
ROC	receiver operating characteristic
SAR	synthetic aperture radar
SDR	signal to disturbance ratio
SNR	signal to noise ratio

Symbols

$\Re\{\cdot\}$	returns the real part
$\Im\{\cdot\}$	returns the imaginary part
$\mathcal{N}\left(\mu, \sigma^2\right)$	the Gaussian probability density function with mean μ and variance σ^2
$\mathcal{CN}_N(\mathbf{0}, \boldsymbol{R})$	the joint complex, circular Gaussian probability density function for a random process with N variables, having mean $\mathbf{0}$ and covariance $\boldsymbol{R}$.
$\boldsymbol{v}^T$	transpose of vector $\boldsymbol{v}$
$\boldsymbol{v}^H$	conjugate transpose of vector $\boldsymbol{v}$
$\boldsymbol{v} \odot \boldsymbol{w}$	Hadamard (element-wise) product
$\boldsymbol{R}^{-1}$	inverse of matrix $\boldsymbol{R}$
j	$j^2 = -1$
c	velocity of radiation propagation, m/s
f_c	centre frequency of the radar's transmitted waveform, Hz
λ	wavelength of the radar's transmitted radiation, m
v_p	velocity of the radar platform, m/s
$a(t; R)$	weighting due to the two-way antenna pattern
θ_{ra}	horizontal 3 dB beamwidth of the real antenna beam, rad
T_1	duration of the transmitted pulse, s
$T = T(R)$	time required to travel the length of the synthetic aperture, s
$\chi(\cdot)$	symmetrical ambiguity function
$\chi'(\cdot)$	asymmetrical ambiguity function
τ	time delay, s
$\tilde{\rho}$	target complex reflectivity
ρ	target amplitude
ϕ	target normalised phase or ambiguity function frequency, Hz
R	range, m
$\dot{R}$	range velocity, m/s
$\ddot{R}$	range acceleration, m/s^2
y	azimuthal position, m
$\dot{y}$	azimuthal velocity, m/s
$\ddot{y}$	azimuthal acceleration, m/s^2
N	number of samples in a processed block
t	time, s

$\{t_n\}, \boldsymbol{t}$	collection of discrete sample/radar transmission times, s
t_s	nominal pulse repetition interval, s
t_{frame}	duration of a block of intervals, s
$\boldsymbol{v}, v(t) = v(t; R)$	known form of the target's signal, including a constant phase
$\boldsymbol{v}_0$	known form of the target's signal, excluding a constant phase
$\hat{\boldsymbol{v}}$	target's signal weighted by the two-way antenna pattern
$x(t), \boldsymbol{x}$	measurement received by the radar
$y(t), \boldsymbol{y}$	azimuthal (range compressed) measurement
$\boldsymbol{z}$	filtered azimuthal signal
B_d	clutter Doppler bandwidth, Hz
*	complex conjugate

Boldface lower case variables are column vectors.

Boldface upper case variables are matrices.

Definitions

These are the definitions of some terms used in this thesis:

Conventional SAR This is a synthetic aperture radar (SAR) which operates in stripmap mode with its single antenna directed towards a scene of interest at broadside. It travels in a straight line at a constant velocity and transmits chirp pulses at a fixed pulse repetition frequency which is slightly greater than the 3 dB Doppler bandwidth. The returns are processed using phase corrections (which compensate for the transmitted waveform and changing radar-target geometry) to form a focussed image of the scene.

Imaging Graphically representing the estimated reflectivities of the scene at a set of discrete positions results in a two dimensional image of the ground. (If the position of a known scatterer were to be estimated, the process would be known as 'parameter estimation'.) Moving targets may be defocussed since their precise motions are not fully compensated for. (With inverse SAR, the motion compensated imaging of a moving target which undergoes a significant aspect change during the observation period produces a picture of the target itself. This is useful for identification.)

Ground clutter The distributed, stationary scatterers in a radar scene are known as ground clutter.

Moving target indication, MTI This is the process of determining the existence of a moving target using a radar which transmits at a pulse repetition frequency (PRF) high enough to oversample the spectrum of the ground clutter. The clutter is filtered out using a high pass filter, revealing the presence or otherwise of a moving target (which has a Doppler shifted spectrum). With a PRF low enough to avoid range ambiguities, this scheme has inherent blind speeds which result from the moving target's signal being subsampled and so made to overlap the ground clutter in the sampled spectrum: it is inadvertently removed by the filtering process. This problem is normally overcome by combining results from multiple PRFs.

Since target spectra may lie within the clutter spectrum, and targets may not have a purely radial velocity, MTI is a less sensitive moving target detector than MTD.

Moving target detection, MTD This refers to both determining the existence of, and estimating the velocity of, moving targets. A bank of narrowband filters is applied to the radar

data to detect targets moving with certain parameters corresponding to the parameters of the filters. This sensitive procedure may therefore combine detection and parameter estimation.

Parameter estimation The process of establishing the position and/or motion parameters of a moving target which is known to be present.

Radar cross section, RCS A moving target is detected when the magnitude of its (coherently integrated) radar return sufficiently exceeds that of the clutter. The amplitude of a single return depends upon the target's effective area, as seen by the radar; this is known as the radar cross section. More formally, it is the equivalent capture area of an isotropic radiator which causes the same field strength to appear at the radar receiver as the actual target, assuming antenna far field effects (Skolnik 1990).

Publications

This work has resulted in the following publications:

- Jonathan A. Legg, Alan G. Bolton and Douglas A. Gray, 'Moving Target Detection with SAR via Waveform Modifications', submitted to the IEEE Transactions on Aerospace and Electronic Systems, December 1995.
- Jonathan A. Legg, Alan G. Bolton and Douglas A. Gray, 'SAR Moving Target Detection using a Nonuniform PRI', Proceedings of EUSAR'96, VDE-VERLAG GMBH, pages 423–426, Königswinter, Germany, March 1996.
- Jonathan A. Legg, Douglas A. Gray and Alan G. Bolton, 'A SAR Moving Target Ambiguity Function', Proceedings of ISSPA'96, pages 841–844, Gold Coast, August 1996.
- Jonathan A. Legg and Douglas A. Gray, 'Polynomial Phase Parameter Estimation with Non-uniform and Random Sampling Schemes'; IEEE Transactions on Signal Processing; submission pending.

CHAPTER 1

Introduction

1.1 Motivation

Radar has been in continuous use since its invention early this century. Its ability to detect, locate and determine the velocity of objects at ranges beyond human vision, especially in situations of poor visibility, has made it a necessity of modern life. It has applications from air traffic control to surveillance and target identification. Radars have been used for years in civilian aircraft for weather avoidance, and in fighter aircraft for airborne target acquisition and tracking, fire control and many other tasks (Stimson 1983, Skolnik 1990).

Coherent radars have the ability to combine returns over a period of time: incorporating phase information from slight differences in the relative radar-target position permits the fine resolution of individual scatterers comprising an object (Wehner 1995). Applying this principle to a moving, side looking radar results in a *synthesised antenna* which can distinguish reflectivities from patches of ground, separated by a few metres, at ranges of tens or hundreds of kilometres. This is analogous to a very long phased array of antenna elements. Such a synthetic aperture radar, or SAR, is a relatively modern invention; its photograph-like results have applications in ground mapping, remote sensing and wide area surveillance (Cutrona 1990, Curlander and McDonough 1991, Wehner 1995).

Early in the history of radar it was noticed that moving targets may be detected by exploiting the Doppler effect on the radar return. This had important military consequences. It was said that movement was the Achilles heel of ground forces since it made them detectable beyond visible range by moving target indication (MTI) radar (Fowler 1996). The US Army investigated MTI radars which could be temporarily deployed to detect the enemy without giving away its own presence. It researched launching devices including mortars and flying

discs. Airborne MTI radars are now commonplace (Shrader and Gregers-Hansen 1990).

The more useful process of both finding the moving targets and determining their velocities is known as moving target detection (MTD).

There is great potential for a radar which can simultaneously image the ground at high resolution and indicate the positions and velocities of any moving targets, *i.e.*, SAR MTD. Such radars exist; the Joint Stars radar, which was demonstrated during the Gulf War, is one such example. Another is the AN/APG-76 (Tobin 1996). Civilian applications of this technology include traffic monitoring and search and rescue. SAR MTD can also be used to detect a moving target and prime the activation of an inverse SAR target recognition system by predicting when the vehicle will reach a turn in the road (Fowler 1996). (If the target undergoes an aspect change of several degrees, it may be imaged at high resolution with so-called *inverse* SAR (Wehner 1995).)

There is even more potential for a SA/MTD radar which uses a minimum number of transmissions: a modern multimode radar has many tasks, only one of which may be ground imaging/MTD. If this only requires few, irregular transmissions, the radar may be able to perform other tasks, such as searching for, tracking and identifying airborne targets by transmitting between the ground imaging pulses. In addition, there is the concern of sensitivity to electronic warfare (Farina 1990): radars are far more difficult to classify and/or mislead if their behaviour is unpredictable. Long unambiguous range swaths are also possible with a low average pulse repetition frequency (Wehner 1995).

This thesis addresses the problem of a minimum transmission SAR MTD system by investigating moving target detection and imaging using a chirp compression radar with non-uniform pulse repetition intervals (PRIs).

1.2 Thesis Outline and Contributions

The main contribution of this thesis is an analysis of the novel application of a non-uniform pulse repetition interval to a synthetic aperture radar for both moving target detection and ground imaging.

This thesis investigates a non-uniform PRI SAR MTD system by presenting background information, including the principles of SAR and existing SAR MTD techniques, and deriving a moving target ambiguity function which is used to explore its properties. Optimal detection and parameter estimation theory is applied, the imaging performance is investigated and the

idea is demonstrated by resampling uniformly sampled real data.

This research required the fusion of several areas of work:

- SAR and other high resolution radars,
- the narrowband range-Doppler ambiguity function,
- classical radar moving target indication and detection,
- non-uniform sampling theory, and
- optimal methods: detection and estimation theory. (Classical radar moving target indication and detection are a subset of this.)

This thesis is comprised as follows:

- Chapter 2 discusses the literature, covering the preliminary theory of synthetic aperture radar and the effects of moving targets. Existing SAR moving target detection techniques are covered in detail. Radar waveforms and non-uniform sampling issues, including spectral estimation and filtering, are also discussed.

  Contribution: A non-uniform PRI is proposed for SAR MTD and justified heuristically.

- The moving target ambiguity function of a stripmapping SAR is discussed in Chapter 3. This describes the degree to which a moving target is focussed when the ground is focussed, and vice versa. It is important that this function approximate a 'thumbtack', maximising the radar's ability to distinguish moving from stationary targets. This chapter serves as an introduction to later chapters; it formulates both range and azimuthal compression and considers moving target detection, parameter estimation and ground imaging using simplifying assumptions which are not made in later chapters.

  Contributions: The SAR moving target ambiguity function is derived and its properties are discussed. The effects of a non-uniform PRI are discussed with respect to the discrimination between moving and stationary targets. The case of two staggered PRIs is discussed in detail. The expected ambiguity function for a random PRI is derived and its performance is formulated for several sampling schemes.

- Optimal moving target detection theory is applied to a SAR with a non-uniform PRI in Chapter 4.

  Contributions: This chapter draws together many references to derive optimal conventional and non-uniform PRI SAR target detection filters, figures of merit and receiver operating characteristics. A new clutter cancellation technique is presented.

- Chapter 5 investigates the estimation of the parameters of moving targets.

  Contribution: The first part of this chapter applies maximum likelihood techniques to estimate the amplitude, position and polynomial phase coefficients of a signal in coloured noise, with arbitrary sample times. The issue of bias is considered.

- The lower variance bounds on the estimates of moving target motion and position parameters are also derived in Chapter 5 by considering the SAR moving target estimation problem in its most general form as one of estimating the parameters of a polynomial phase signal model.

  Contributions: The bounds on the estimation of the polynomial phase parameters are derived for non-white noise and arbitrary sample times. They are of particular interest when the probability density functions of the transmission times are incorporated into the formulation. It is shown that, in the limiting case, non-uniform sampling results in estimates which are as accurate as the estimates from uniformly sampled data, despite them not suffering from aliasing effects. The analytical results are supported by simulation.

- Chapter 6 discusses imaging issues.

  Contributions: The contributions of this chapter are maximum likelihood SAR imaging with a non-uniform PRI and the application of various sidelobe reduction techniques, including maximising the integrated sidelobe ratio (which also specifies optimal transmission times). The probability density functions of the transmission times are also incorporated, leading to the expected beam patterns for several sampling schemes.

- A non-uniform PRI SAR is simulated by resampling real data in Chapter 7.

  Contribution: Non-uniform SAR MTD is demonstrated by resampling and filtering uniformly sampled real data to simulate non-uniform transmission times. The parameters of a moving target are estimated, and it is shown that the target can successfully be distinguished from the ground in circumstances where a conventional SAR would confuse the two. A comparison between the conventional and non-uniform PRI SAR ground-focussed images shows no appreciable difference in image quality, which is emphasised by a demonstration of the clutter cancellation technique proposed in Chapter 4.

- The research is summarised and conclusions are drawn in Chapter 8. This chapter includes a list of future research topics.

- There are five appendices.

  - Appendix A lists properties of a generalised form of the Woodward ambiguity function,
  - Appendix B discusses SAR clutter modelling,
  - Appendix C derives the lower variance bounds for biased estimators,
  - Appendix D derives the complex Gaussian Fisher information matrix, and
  - Appendix E discusses optimal radar transmission times.

CHAPTER 2

Background Information

This chapter covers some of the theory this thesis is based upon. It discusses the principles of synthetic aperture radar (SAR), moving target detection (MTD) and non-uniform sampling and reviews the literature regarding existing SAR MTD techniques. It also proposes an alternative SAR MTD method.

After discussing the fundamental theory of SAR in Section 2.1 and radar moving target indication and detection in Section 2.2, the effects of moving targets are covered in Section 2.3. This is followed by a brief explanation of radar waveforms and the Woodward ambiguity function in Section 2.4. Section 2.5 categorises and discusses existing SAR MTD techniques. The proposed SAR MTD technique is introduced in Section 2.6. Non-uniform sampling theory is discussed in Section 2.7, both generally and in the context of SAR, and SAR performance measures are presented in Section 2.8.

2.1 Synthetic Aperture Radar Fundamentals

SAR is a method of obtaining real time, high resolution images of the ground to one side of a moving platform (Cutrona 1990, Curlander and McDonough 1991, Wehner 1995). Achieving one metre resolution from a range of tens of kilometres requires an antenna hundreds of metres long. It is impractical to carry a physical antenna of these dimensions aboard an air- or spaceborne platform; however, such an antenna may be synthesised by combining radar returns from a single target using a realisable antenna as the platform travels. This is analogous to phased array processing, but with one time shared array element rather than many operating simultaneously. See Figure 2.1 for a representation of this.

Applications for SAR are many and varied due to its day/night and all-weather capability;

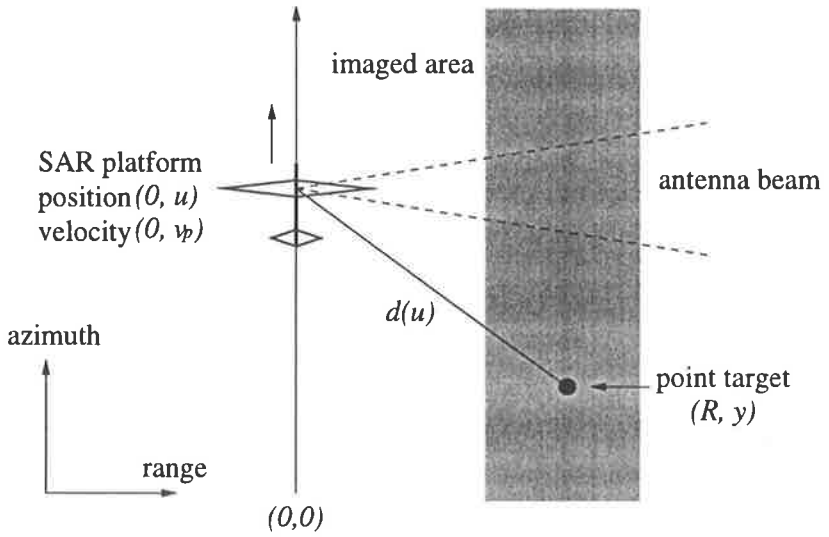

Figure 2.1: Simplified stripmapping SAR geometry in the plane of the radiation. One antenna element is moved along the length of the aperture being synthesised. The platform's altitude has not been shown.

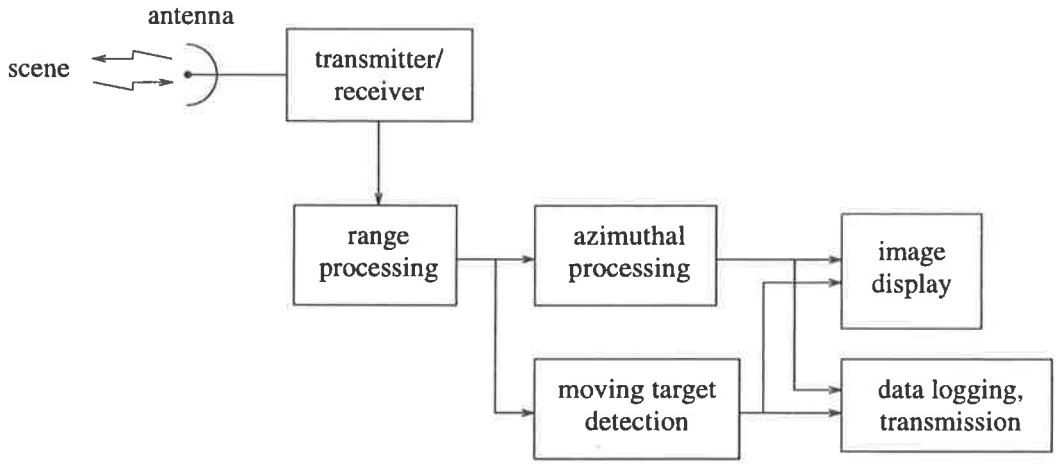

Figure 2.2: An overview of SAR processing.

they include ground mapping, remote sensing, search and rescue, ground target identification and the detection of moving targets, in both the defence and civilian areas.

To form an image, a SAR has to resolve radar scatterers in both the *slant range* (or just *range*) and *azimuthal* dimensions. The former is done by controlling the transmitted pulse's waveform, the latter by combining the returns from an ensemble of such pulses. See Figure 2.2 for an overview of SAR processing.

SARs may operate in a number of different modes, depending upon the imaging geometry. Forming an image continuously with the antenna pointed normally to the direction of travel is known as *broadside stripmap* mode. Having the antenna pointing at a fixed, arbitrary angle is *squint* mode, whereas continuously aiming the antenna at a specific target, thereby seeing

it undergo a large aspect change, is known as *spotlight* mode. If the motion of the target itself allows imaging, we have *inverse synthetic aperture radar,* which is excellent for target identification. Although any movable platform may theoretically carry a SAR, an aircraft will be assumed here.

The main reference for the following theory, describing SAR fundamentals, is (Wehner 1995).

2.1.1 Range Information

The first objective is to achieve high resolution in range.

A transmitted pulse with a duration such that the radiation travels a distance of only twice the desired resolution is difficult to generate: the amplitude required to provide an adequate detection performance is very large. However, matched filtering can be used to both maximise the receiver output signal to noise ratio for a given transmitted energy and allow independent control of the length of the transmitted pulse and the range resolution (Curlander and McDonough 1991, page 132). With such a filter, a long pulse with a wide bandwidth and achievable average power can satisfy both detection and resolution criteria. This technique is commonly used in a wide variety of high resolution radars. The signal used most often in SAR systems is the linear-FM, or *chirp* pulse.

The chirp waveform, representing the linear frequency ramp $f = f_c + Kt$, is given by

$$s(t) \;=\; \mathrm{rect}\Big(\frac{t}{T_1}\Big)\cos\Big(2\pi[f_c t + Kt^2/2]\Big)\,,$$

where t is time, f_c is the centre (carrier) frequency, T_1 is the uncompressed pulsewidth, K is the chirp rate (in Hz/s) and

$$\mathrm{rect}(t) \;=\; \begin{cases} 1, & \text{if } |t| < \frac{1}{2}, \\ 0, & \text{otherwise.} \end{cases}$$

Typically for SAR, $s(t)$ is considered to be a *narrowband* signal since the large absolute bandwidth (tens of megahertz) is still small when compared with its centre frequency (say X-band, or ten gigahertz). This bandwidth, B, is approximately KT_1. It can be shown that this provides slant range resolution

$$\Delta r_s \;\approx\; \frac{c}{2B},$$

where c is the speed of propagation.

A stationary point target with complex reflectivity $\tilde{\rho}$ at range delay $\tau(u)$, where u is the

position of the SAR (Figure 2.1), has the response

$$s'(t,u) \;=\; |\tilde{\rho}|\,\mathrm{rect}\left(\frac{t-\tau(u)}{T_1}\right)\cos\left(2\pi\left\{f_c\left[t-\tau(u)\right]+K\left[t-\tau(u)\right]^2/2\right\}\right)$$

(neglecting the amplitude of the transmitted signal, the propagation attenuation loss and system noise). The baseband response (after mixing with a reference signal at frequency f_c and quadrature demodulating) is therefore

$$s'(t,u) \;=\; \tilde{\rho}\,\mathrm{rect}\left(\frac{t-\tau(u)}{T_1}\right)e^{-j2\pi\left\{f_c\tau(u)-K\frac{[t-\tau(u)]^2}{2}\right\}}. \tag{2.1}$$

The fundamental azimuthal resolution limits of real and synthesised antennas will now be discussed.

2.1.2 *From Real to Synthetic Aperture*

Assuming a uniform taper, a physical phased array comprised of N elements separated by distance d has the beam pattern

$$f(\theta) \;=\; \frac{\sin\left(\pi\frac{Nd}{\lambda}\sin(\theta)\right)}{\sin\left(\pi\frac{d}{\lambda}\sin(\theta)\right)}, \tag{2.2}$$

where θ is the angle relative to broadside and λ is wavelength and the array has weights chosen to steer the main beam at broadside (Johnson and Dudgeon 1993, Stimson 1983, Cashman 1997). Since the same antenna is used for reception, the two-way pattern for large N and small θ is

$$f_2(\theta) \;\approx\; N^2\left[\frac{\sin\left(\pi\frac{D}{\lambda}\theta\right)}{\pi\frac{D}{\lambda}\theta}\right]^2, \tag{2.3}$$

where $D=(N-1)d$ is the length of the antenna. Thus the 3 dB beamwidth is

$$\theta_{ra} \;\approx\; 0.64\,\lambda/D$$

and the null-null beamwidth

$$\theta_{ra,n} \;=\; 2\lambda/D.$$

The first sidelobe is at -26.8 dB relative to the main lobe.

The antenna's spatial resolution at range R is given by

$$\begin{aligned} \rho_{ra} &= R\,\theta_{ra} \\ &= \frac{R\lambda}{D}, \end{aligned}$$

which is very poor at long range when D is small.

Alternatively, the antenna could be mounted on a moving platform and directed normally to its motion, as shown in Figure 2.1, with the radar storing complex returns as the platform travels. Combining them forms a synthetic array.

Simply summing the returns over the length of this array results in an *unfocussed SAR*. The best resolution which can then be achieved is $\rho_{su} \approx 0.5\sqrt{R\lambda}$ (Curlander and McDonough 1991, page 22).

An aperture may be synthesised by travelling a distance

$$L(R) = R\,\theta_{ra} \tag{2.4}$$

(the width of the real antenna beam at range R).

This synthesised array has an element to element phase shift which is twice that of the real array, due to the two-way travel of the radiation, and has no one way pattern. For omnidirectional elements, its unweighted pattern is

$$f_{2s}(\theta) \approx N \frac{\sin\left(\pi \frac{2L}{\lambda}\theta\right)}{\pi \frac{2L}{\lambda}\theta},$$

so that its 3 dB beamwidth is

$$\theta_{sa} \approx 0.44\,\lambda/L$$

(compared with $0.64\lambda/D$ for the real case) and the null-null beamwidth

$$\theta_{sa,n} = \lambda/L$$

(which is half the real case). The first sidelobe is at -13.4 dB.

Using the latter beamwidth result (without qualification), it is commonly stated that a synthetic antenna therefore has half the resolution of a real antenna of the same length (*e.g.*, (Stimson 1983)). This is doubly misleading: not only is it the null-null beamwidth rather than the 3 dB beamwidth, but sidelobes are not considered (Cashman 1997): the SAR's sidelobes

are worse than those of the real array. If the SAR's response were weighted using a triangular shading function, its modified response would be *identical* to that of the real array.

The best possible (Rayleigh) spatial resolution of the synthetic array is given by

$$\begin{aligned} \rho_{sa} &= R\theta_{sa} \\ &= \frac{R\lambda}{2L(R)} \\ &= \frac{1}{2}\frac{\lambda}{\theta_{ra}} \\ &= D/2, \end{aligned} \tag{2.5}$$

which is half that of the horizontal dimension of the real antenna aperture used as synthetic array elements, and is *independent of range*.

To achieve this, the data have to be focussed by correcting the phase variation which results from the distance to the target changing as the SAR platform travels. The position of the platform therefore has to be measured to a fraction of the wavelength (which is 3 cm at X-band).

2.1.3 Azimuthal Information

Referring to the SAR geometry in Figure 2.1, the position-dependent range delay between the radar and a stationary target at (R, y) is given by

$$\begin{aligned} \tau(u) &= 2d(u)/c \\ &= \frac{2}{c}\sqrt{R^2 + (u-y)^2}. \end{aligned}$$

The radar return, $s'(t,u)$, Equation (2.1), is valid only while the target is in the antenna beam. The width of this beam, $L(R)$, is given by Equation (2.4).

It is the form of the phase response which is of interest. If we assume that the beam illuminates the target uniformly, and neglect the amplitude of the transmitted signal, the propagation attenuation loss and system noise, the baseband response to a point target is given by

$$s'(t,u) = \tilde{\rho}\ \mathrm{rect}\left(\frac{t-\tau(u)}{T_1}\right)\mathrm{rect}\left(\frac{u-y}{L(R)}\right)e^{-j2\pi\left\{\frac{2\sqrt{R^2+(u-y)^2}}{\lambda} - K\frac{[t-\tau(u)]^2}{2}\right\}}. \tag{2.6}$$

An exponential argument in Equation (2.6) can be simplified by a Maclaurin series expansion

to be in the form

$$\sqrt{R^2 + a^2} \approx R + \frac{a^2}{2R}, \tag{2.7}$$

where $R^3 \gg a^4$ (Wehner 1995). $s'(t,u)$ can therefore be written

$$\begin{aligned} s'(t,u) &= \tilde{\rho}\,\mathrm{rect}\left(\frac{t-\tau(u)}{T_1}\right)\mathrm{rect}\left(\frac{u-y}{L(R)}\right)e^{-j2\pi\left\{\frac{2R}{\lambda}+\frac{(u-y)^2}{\lambda R}-K\frac{[t-\tau(u)]^2}{2}\right\}} \\ &= \tilde{\rho}\,s''(t,u). \end{aligned}$$

The overall phase response to a point target therefore appears as the sum of a constant offset and two quadratic functions. The constant phase offset is related to the wavelength and minimum target range. The quadratics represent the slowly varying azimuthal response and the rapidly varying range compression pulse response respectively. Since the azimuthal phase response is quadratic, it is commonly referred to as an "azimuthal chirp". (It is often said to be a result of Doppler effects, despite the fact that the SAR and target may be stationary during the radar transmissions.)

In order to approach the ideal $D/2$ azimuthal resolution (Equation (2.5)), the focussed SAR needs to correct for these phase variations. This can be achieved by applying the filter $g(t,u)$, which is matched to the form of the target's return: $g(t,u) = s''(-t,-u)$. Note that this filter is a function of range.

2.1.4 PRF Selection

Lower PRF Limit

To avoid aliasing ambiguities, the radar's uniform pulse repetition frequency (PRF), f_s, must exceed the frequency which ensures that a stationary target's two-way distance never changes by more than half a wavelength between samples. *i.e.*

$$\begin{aligned} f_s &\geq 2\max\left(\frac{\partial d(u)}{\partial t}\right)/\frac{\lambda}{2} \\ &= 2\left(\frac{2v_p\sin(\theta_{ra}/2)}{\lambda}\right) \\ &\approx 2\left(\frac{2v_p\theta_{ra}/2}{\lambda}\right); \end{aligned}$$

therefore,

$$f_s > \frac{2v_p\theta_{ra}}{\lambda}, \tag{2.8}$$

where v_p is the platform's speed in the azimuth direction relative to the stationary target. $\pm v_p\theta_{ra}/\lambda$ is the frequency extent of a signal returned by a scatterer from the ground. (f_s only needs to be larger than this, and not larger than twice this, since the samples are complex.) This frequency extent is known as the "3 dB Doppler bandwidth", B_d, and is *independent of range.* Under these conditions, the maximum resolution (Equation (2.5)) may be obtained. For example, if $v_p = 70\,\text{m/s}$, $\theta_{ra} = 1.5°$ and $\lambda = 3.2\,\text{cm}$, $B_d = 115\,\text{Hz}$. In practice, to avoid azimuthal ambiguity a safety margin is used to allow for beam pointing errors and a beamwidth greater than the 3 dB θ_{ra}. Azimuthal ambiguity is manifested as a target appearing in more than one azimuthal position in an image.

Upper PRF Limit

To avoid range aliasing effects, which result from simultaneous returns from two pulses in flight, the unambiguous range interval must be sufficiently large that returns from the ground at ranges other than the one of interest do not degrade the signal to noise ratio. (In the worst case, this ambiguity prevents the absolute determination of a target's range with a conventional radar (Stimson 1983). In SAR, however, the Doppler rates of the targets will differ, allowing them to be distinguished by azimuthal focussing (Tomiyasu 1993). However, this phenomenon is generally ignored by the literature, and SAR upper PRFs are chosen according to the same criteria as used for one dimensional radars (*e.g.*, (Wehner 1995)).) This imposes an upper limit on the range extent being imaged, known as the range swath, R_s. Thus there is the restriction that

$$f_s \leq c/2R_s. \tag{2.9}$$

The distance to the horizon is

$$R_h \approx \sqrt{2rh}$$

(*e.g.* (Hovanessian 1984, pages 179–180)) where $r \approx 6350\,\text{km}$ is the radius of the Earth and h is the altitude of the radar above the surface of the Earth. For example, if $h = 10000\,\text{m}$, $R_h = 370\,\text{km}$; if this represented the upper limit of an airborne radar's range swath, its lowest upper PRF limit would be

$$f_s \leq 405\,\text{Hz}.$$

Alternatively, for $R_s = 50\,\text{km}$, $f_s \leq 3\,\text{kHz}$. Therefore, range ambiguity is usually only a problem for spaceborne, rather than airborne, SARs due to their higher range swaths and ground speeds; under these conditions, the PRF needs to be high to satisfy the minimum

sampling rate requirement, Equation (2.8).

Additional PRF Considerations

f_s may also be chosen so that nulls is the synthetic antenna beam are placed on sidelobes of the real antenna beam.

Also, the data logging, processing or digital transmission capability of the SAR may ultimately impose restrictions on the selection of the PRF.

2.2 Radar Moving Target Detection

Moving targets are detected with radars using their Doppler frequency which differs from that corresponding to the ground.

The Doppler frequency is the difference between the frequency of the radar's transmitted signal and the received signal. This frequency shift phenomenon may be explained in two ways. Firstly, it is analogous to the familiar change in the pitch of a sound; an object transmits wavefronts which propagate at a uniform velocity, so they become more closely spaced as the target moves towards the observer, resulting in a higher frequency. This viewpoint involves actual *motion* between the source and the receiver. Alternatively, there is a geometrical viewpoint: a target moving a distance of half a wavelength towards the radar will cause the radar to see a phase change of 360°; therefore, moving at half a wavelength per second towards the radar results in a Doppler shift of 1 Hz. (This interpretation is appropriate when discussing synthetic aperture radar, since it is a physical aperture being synthesised and no motion is required *per se*.)

Radar moving target indication (MTI) is the process of determining the existence of a moving target in a particular region without necessarily finding its velocity. This is achieved using a high PRF and filtering out the clutter from the resulting Doppler spectrum. (Clutter is the unwanted signal due to returns from stationary targets on the ground.) For the indication of ground targets in strong clutter, incoherent cancellation techniques may work well; in addition, high frequencies should be used so that targets with slow speeds can be detected (Staudaher 1990).

Alternatively, the data may be passed through a bank of filters tuned to different moving target velocities. A filter output larger than a threshold indicates the presence of a moving target; the parameters of the corresponding filter are an estimate of the parameters of the target.

This process is known as moving target *detection,* MTD.

Classical optimal filtering theory, which assumes a particular model for the environment, may be applied to the MTI/MTD problem. This is done is Chapter 4. However, real-world complications, such as non-stationary rain clutter, may be better addressed using *ad hoc* techniques (D'Addio and Galati 1985).

2.3 The Effects of Moving Targets on SAR

This section discusses well known SAR moving target phenomena (*e.g.*, (Raney 1971)). A more detailed discussion may be found in Chapter 3.

Since the Doppler shifts associated with slowly moving targets are very much smaller than the bandwidth of the range compression chirp (kilohertz compared with tens of megahertz), only their azimuthal phase responses are of interest (Freeman 1984). Furthermore, moving targets will be accurately focussed in range even when treated as if stationary.

The azimuthal chirp, derived in Section 2.1.3, can be approximately specified by two parameters apart from the target's azimuthal position, neglecting range migration effects: frequency shift ("Doppler centroid") F_{dc} and frequency rate ("Doppler frequency rate") F_{dr}, *viz:*

$$v(t) = e^{j2\pi\psi(t)} = e^{j2\pi(F_{dc}t+F_{dr}t^2/2)}, \tag{2.10}$$

ignoring a constant phase term. (The Doppler centroid is "the Doppler frequency caused by the relative motion between the sensor and a target in the azimuth beam centre line" (Runge and Bamler 1989).) These terms are controlled by the velocity components of a moving target: using the instantaneous frequency-phase relation

$$f_i = \frac{1}{2\pi}\frac{d\psi(t)}{dt},$$

it can be shown that, for a target moving with velocity $(\dot{R}, \dot{y})$ at slant range R, these are

$$F_{dc} = -\frac{2\dot{R}}{\lambda} \tag{2.11}$$

and

$$F_{dr} = -\frac{2(v_p - \dot{y})^2}{\lambda R} \tag{2.12}$$

for a narrow antenna beamwidth, where the radar has velocity v_p and operates at wavelength λ.

In practice, the Doppler centroid may be nonzero for a stationary target since the SAR platform may have some lateral motion. Of course, if $\dot{R} = \dot{y} = 0$, the formulations would correspond to the scenario described in Section 2.1.3.

The automatic estimation of the Doppler centroid and frequency rate are known as "clutterlock" and "autofocus" respectively (Li, Held, Curlander and Wu 1985). (Clutterlocking is of vital importance to spaceborne SAR systems since the instantaneous ground Doppler is unknown due to errors in the antenna's pointing direction and the spacecraft's velocity and position (Elachi 1988, page 143).) Due to their similarity, clutterlocking and autofocussing techniques may provide insight for SAR MTD.

It was shown in Section 2.1.4 that if $v_p = 70\,\text{m/s}$, the antenna's azimuthal 3 dB beamwidth $\theta_{ra} = 1.5°$ and $\lambda = 3.2\,\text{cm}$, the Doppler bandwidth is 115 Hz. If this is the radar's PRF, sufficient to image the ground, we see that, with zero azimuthal motion, *any* range motion will cause part of the azimuthal chirp to become aliased, and targets moving faster than $\pm 3.3\,\text{kph}$ will have their Doppler centroids aliased. If $\dot{R} = \pm 100\,\text{kph}$, $F_{dc} = 3480\,\text{Hz}$ — *30 times larger* than the Doppler bandwidth. (If the radar were to use this as its PRF to see these targets, its unambiguous range swath would be under 50 km!) It is therefore desirable to image moving targets unambiguously with a lower PRF[1].

The bandwidth of the azimuthal chirp is dependent upon azimuthal velocity; it is given by

$$B_d = \frac{2\theta_{ra}}{\lambda}|v_p - \dot{y}|. \tag{2.13}$$

If $\dot{y} = 0$, this is equivalent to the 3 dB Doppler bandwidth, or minimum PRF (Equation (2.8)).

A ground-focussing matched filter gives a peak response when $v(t)$ crosses 0 Hz. This time is dependent upon a cross coupling between the chirp's centroid and position, hence y and $\dot{R}$, leading to an azimuth/Doppler ambiguity. The apparent azimuthal shift of a target is

$$\Delta Y \approx \left(\frac{R\dot{R}}{v_p} + \frac{R\theta_{ra}}{2}\right) \bmod (R\theta_{ra}) - \frac{R\theta_{ra}}{2} \tag{2.14}$$

(Raney 1971), which is valid if $\dot{R}t \ll R$ and $\dot{y} \ll v_p$. As an example, if $R = 30\,\text{km}$, $\dot{R} = 1\,\text{m/s}$ and $v_p = 70\,\text{m/s}$, $\Delta Y \approx 430\,\text{m}$!

Figure 2.3 shows the first order effects of moving targets on a ground-focussed image. In

[1] If the data processing is performed over a long interval, a lower PRF may be used since the azimuthal chirp is no longer linear, leading to a lower crosscorrelation with a return from the ground. However, this would negate some advantages of the technique.

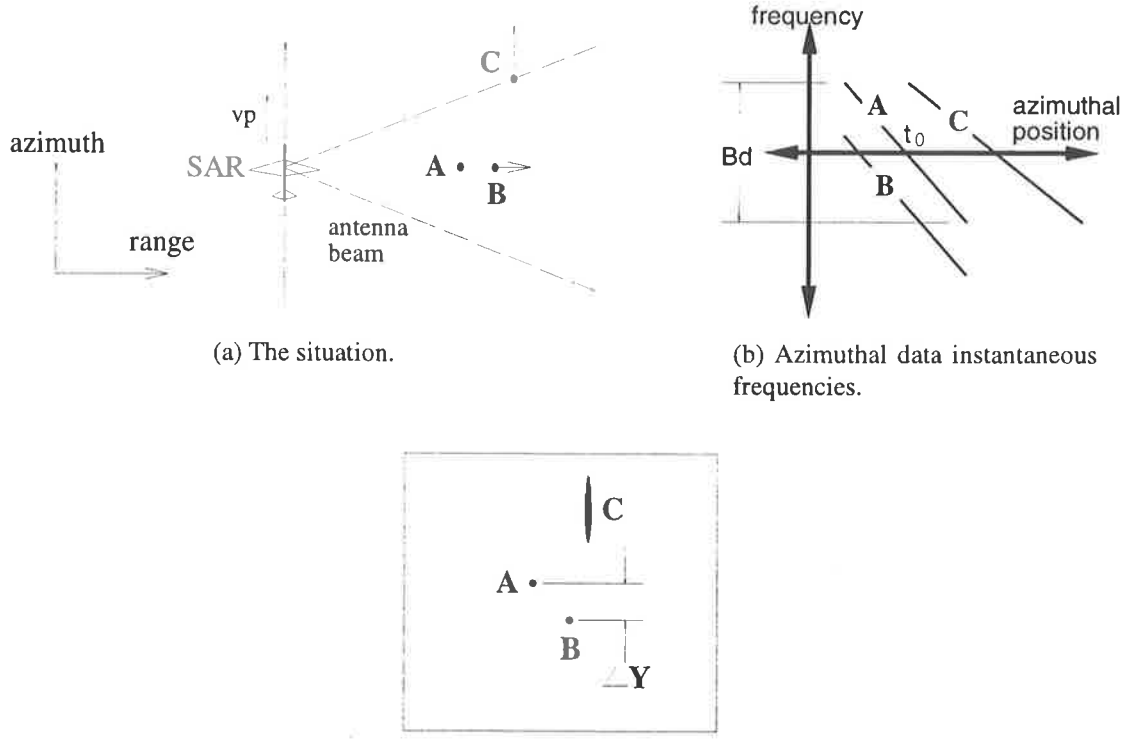

(a) The situation.

(b) Azimuthal data instantaneous frequencies.

(c) Resulting ground-focussed image.

Figure 2.3: The first order effects of moving targets on a SAR image.

Figure 2.3(a) the SAR platform and targets are shown at time t_0, with A stationary, B moving in range and C moving in azimuth. Figure 2.3(b) shows the corresponding azimuthal frequencies at all ranges. A's linear chirp is centred on 0 Hz, B's is similar but offset and C's has a different slope. (The PRF is assumed to be $\gtrsim 2B_d$ so as to unambiguously sample target B.) Figure 2.3(c) shows the resulting ground-focussed image, with A focussed, B displaced and C partially focussed (neglecting range migration effects).

Figure 2.4 shows the general moving target imaging case, including smearing due to range migration. This figure is similar to (Raney 1971, Figure 3(B)). (Since the radar may have a range resolution in the order of a few metres, it is possible that the target will traverse several range cells during the measurement period.)

As an aside, the Doppler rate is very sensitive to target range acceleration; it becomes

$$F_{dr} = -\frac{2\left[(v_p - \dot{y})^2 + R\ddot{R}\right]}{\lambda R}.$$

This has implications for imaging moving targets, which requires coherent integration over a period of time. The normal assumption of linear motion may not be valid, resulting in a

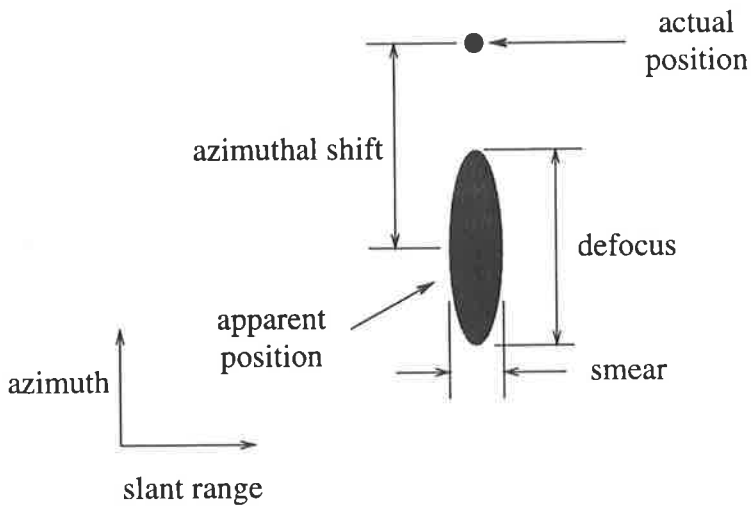

Figure 2.4: The general appearance of a moving target's return after being processed as if the target were stationary. It appears as a displaced, defocussed, stationary scatterer.

mismatch between the target's signal and the filter. This produces a defocussed image which makes velocity and position estimation difficult, and reduces the radar's ability to detect moving targets in areas of strong clutter. The result may be an image which is no better focussed than the object shown in Figure 2.4.

(If the assumption of linear motion is not made, so that the motion has to be estimated, better results may be obtained. This technique, inverse SAR, may allow the imaging of the target itself, but is inapplicable to target detection.)

2.4 Radar Waveforms

Conventionally, a radar signal's ambiguity function (AF) is the crosscorrelation of that signal with a time delayed, frequency shifted version of itself. This describes the radar receiver's response when it passes the signal returned from a distant, moving point target through a filter matched to the original signal. This asymmetrical, narrowband AF is written

$$\chi'_{s(t)}(\tau,\phi) = \int_{-\infty}^{\infty} s(t)\, s^*(t-\tau)\, e^{-j2\pi\phi t}\, dt \tag{2.15}$$

(Blahut 1991), where $s(t)$ is the radar's transmitted signal, τ is the delay between the signal's transmission and reception and ϕ is the Doppler frequency shift caused by the radar-target relative motion. This is known as the Woodward ambiguity function. (The properties of Equation (2.15) are a subset of those discussed in Appendix A.)

The corresponding cross AF is

$$\chi'_{s(t),r(t)}(\tau,\phi) = \int_{-\infty}^{\infty} s(t)\, r^*(t-\tau)\, e^{-j2\pi\phi t}\, dt. \tag{2.16}$$

This is used when the receiver's filter is different from the transmitted signal.

The magnitude of Equation (2.15) is commonly used to characterise the signal $s(t)$, or, conversely, the desired AF may determine the signal to be used by a particular radar. The difficult problem of designing signals from AFs is discussed by Vakman (1968) and Wong, Luo and Jin (1993). The desired envelope of Equation (2.15) depends, for example, upon the required range and Doppler resolutions. A ground-based radar searching for the presence of aircraft requires an ambiguity function which has a large magnitude for the entire range of possible ϕ. Alternatively, a radar wishing to accurately estimate both targets' velocities and positions requires a 'thumbtack' AF, whose magnitude is large at the origin and small elsewhere. Under these circumstances it is possible to tune the receiver's filter to achieve the largest output, thereby estimating the target's range and Doppler parameters.

In practice the AF may have spurious peaks or a periodic repetition, making it difficult to estimate the parameters of the target. The objective of special radar waveforms is to help the ambiguity function more closely resemble the ideal thumbtack by removing the periodicity in the signal. This may be possible by using irregular frequency, phase or timing variations (Blahut 1991, p. 23), reducing the signal's autocorrelation away from the origin: there are no general ways of working backwards from a desired AF to the required signal. To give some examples:

- rather than broadcasting periodic pulses for atmospheric sounding, Sulzer (1986) describes a long, phase switched pulse radar waveform to make full use of a klystron power stage. This stage would otherwise be inefficient, since the klystron is powered whether or not signals are being transmitted.

- Golestani, Chandrasekar and Keeler (1995) discuss a staggered PRI scheme with dual polarisations for weather radars.

- Martin, Jain and Bolton (1994) doubled the range resolution in a SAR system without collecting any more data by randomly switching between two range compression chirp signals with adjacent spectra. This resulted in an increased detection performance with the penalty of increased imaging sidelobes.

- In planetary SAR imaging with an Earth-based radar (using, for example, the antenna at Arecibo), there is a *two* way positioning ambiguity: both in range and azimuth. This 'overspread' problem may be overcome using a random radar waveform, as discussed in detail by Hagfors and Kofman (1991) and with regard to the imaging of Mercury by Harmon and Slade (1992).

The moving target ambiguity function for a SAR is derived in Chapter 3, and it is shown that the ambiguities inherent in a conventional SAR may be overcome using irregularities in the timing of the radar's transmissions. (Interestingly, the waveform $s(t)$ cannot be directly controlled by the radar in the SAR case since it is dependent upon the azimuthal geometry. The transmission timing is the only degree of freedom available (Section 3.2.5).)

2.5 Existing SAR MTD Techniques

This section summarises existing SAR moving target detection (MTD) techniques. They have been classified in Table 2.1. The proposed technique, discussed in Section 2.6, has been included in the table for comparison.

The functions listed in the table are

Indication The technique indicates the existence of moving targets without necessarily finding their parameters.

Estimation The technique estimates targets' velocities and positions.

Imaging The technique focusses the target in two dimensions (possibly to estimate its parameters).

The data required by the techniques have been classified thus:

Conventional The technique uses data from a conventional SAR.

Oversampled The technique requires a higher PRF than a conventional SAR (to avoid aliasing problems), or the collection of more data.

Radar modifications have also been classified:

Hardware modification The radar is different in some fundamental way from a conventional SAR (*e.g.*, it has several antennas).

Technique	Moving target function			Data		Radar mod.	
	Indication	Estimation	Imaging	Conv.	Oversamp.	Hard.	Wav.
Change detection	★		★		★§		
Standard MTI	★	★†			★		
'True' Doppler	★	★†		★			
Freq. detection	★	★	★		★		
Shadow detection	★			★			
Prefiltering	★				★		
DPCA	★	★				★	
Phase detection	★	★					★
1D hopped freq.		★	★				★
Clutterlock		§§	★		★		
Autofocus		§§	★	★			
Doppler rate		★	★	★			
Coord. transform		★	★	★			
Phase asymmetry		★	★		★		
Range walk		★	★	★			
Clutter cancel.		★		★			
STAP, *etc.*	★	★	★		★‡	★	
Wigner-Ville, *etc.*		★	★	★§†	★§†		
ISAR		★	★	★			
Proposed	★††	★	★				★

§: The site of interest must be revisited by the radar.
§§: This function is possible using some implementations of the technique.
§†: This type of data may be required by some implementations of the technique.
†: Range rate is estimated.
‡: The PRF may be low; however, there are many receiving channels.
††: Moving target indication may be performed using clutter cancellation techniques.

Table 2.1: SAR MTD summary. See the text for the meanings of the column headings.

Waveform modification The transmitted waveform differs from that of a conventional SAR.

There are many techniques which operate using oversampled data to unambiguously determine the target's Doppler, reflecting the greater ease with which MTD may then be performed.

The techniques are:

Change detection The concept is to detect movement over a long time frame (hours or days) by finding the differences between two SAR images of the same scene. There are two main problems, discussed by White (1991) in detail:

Geometric correction The images have to be adjusted so they can be correctly registered. This is to take account of unknown aircraft motion, turbulence, *etc.*, as well as any differences in the fields of view, which may not be perfectly aligned.

Image interpretation Speckle will cause differences between the images which need to be accounted for, with no prior information as to the area being imaged.

A third problem is the long delay between the sensor seeing the target on the first pass and the decision that a target was present, which is made only after the second pass. It is far more useful to detect a moving target with only one visit to an area.

An alternative approach is to find the difference between low resolution multilook images (Ouchi 1985). This is discussed under 'Range walk detection'.

Standard MTI Moving target indication (MTI) involves transmitting at a high PRF and observing the spectrum of the returns, using the principle that moving targets are separated in frequency, or 'Doppler shifted', from stationary ones ('ground clutter') (Shrader and Gregers-Hansen 1990). Using several PRFs avoids aliasing-related ambiguities (via the Chinese remainder theorem).

This technique gives range rate information, rather than two dimensional velocities, images or accurate positioning.

'True' Doppler See under 'Clutterlocking techniques'.

Frequency detection D'Addio, Di Bisceglie and Bottalico (1994) expand on Raney's suggestion of using a PRF which is sufficiently high to cover the necessary azimuthal frequency range (Raney 1971). It should be

$$f_s > 2|F_{dc,max} + B_{d,max}/2|,$$

where $F_{dc,max}$ and $B_{d,max}$ are given by Equations (2.11) and (2.13) respectively with their maximum velocity values substituted. Moving targets are found using a bank of Doppler filters.

Shadow detection Novak (1996) described a technique applicable to very high resolution millimetre-wave SARs. It relied on the moving target being displaced from its actual position in the ground-focussed image: since the vehicle is masking the road, there will be a dark patch on the road at the vehicle's position. (A 'shadow', as it were.)

Prefiltering To detect moving targets, Freeman (1984) suggests oversampling, high pass filtering (to remove ground clutter), and subsampling to the 3 dB Doppler bandwidth. This will alias moving target signals to frequencies below the Doppler bandwidth. The normal stationary target matched filter may then be used; any bright scatterers which appear represent moving targets. Problems include blind speeds (where targets are

aliased into the ground bandwidth) and its suboptimal detection of targets moving in azimuth — these have a similar Doppler centroid, but a different Doppler rate from that of the ground (Equation (2.12)).

Displaced phase centre antenna Stone and Ince (1980) describe a SAR system which has two identical, identically aligned antennas and forms an image with each. Since the trailing antenna receives when it is in the position occupied by the leading antenna when it received, the images formed should be identical if all targets are stationary. The difference between them indicates the existence of moving targets. This is a special case of along-track interferometry. Hammerle (1990), Smith and Clarkson (1992) and Coe and White (1995) also discuss DPCA techniques. The JSTARS radar, which received much publicity during the Gulf War, operates on similar principles.

Another existing radar is the AN/APG-76 multimode radar system (Tobin 1996), which may be fitted to existing aircraft. This has simultaneous ground mapping and moving target detection capability with Doppler beam sharpening and spotlight imaging modes. It uses a high PRF and many receiving apertures.

The main DPCA problems are with antenna differences and misalignment; space-time adaptive processing may be more robust for SARs with array antennas.

Phase detection Raney (1971) and (1992, pages 10-11–12) suggests transmitting pulses in pairs with small intervening delays, or receiving with two antennas. Subtraction of the returns results in a phase shift which has a characteristic indicative of moving targets. This is an approximation to the DPCA technique. Note that *subtraction is the optimum method if the clutter is highly correlated.*

Hopped frequencies Wehner (1995, pages 213-20) discusses the use of a radar waveform modification to obtain unambiguous range/velocity information in a one dimensional synthetic range profile with a stepped frequency radar. Instead of using a conventional monotonic frequency firing order, he randomises it, achieving an improved range/Doppler ambiguity.

Costas (1984) suggests a specific order which implements an almost ideal 'thumbtack' range/Doppler ambiguity function, making independent measurements realisable.

This technique could be applied directly to a SAR with synthetic range compression, since the PRF is high. (Stepped frequency SAR is covered by Wehner (1995, page 277–286).)

Its implications for chirp SAR, the radar of interest, are less apparent: fundamentally, the pulse is too short for the target to have moved significantly during the time it illuminates the target.

Clutterlocking techniques Since they both address the problem of estimating an unknown Doppler centroid, clutterlocking techniques may provide insight for SAR MTD. The difference is that clutterlocking is concerned with the scene as a whole, typically averaged to reduce the effects of data discontinuities, whereas MTD is concerned with isolated targets.

Ideally, one would estimate the unambiguous Doppler centroid, F_{dc}, in

$$F_{dc} = k f_s + \hat{F}_{dc} \tag{2.17}$$

(Chang and Curlander 1992, page 941) where k is an integer, f_s is the PRF and $\hat{F}_{dc}$ is the ambiguous Doppler centroid estimate. Most clutterlocking techniques find only $\hat{F}_{dc}$.

Antenna beam correlation Curlander and McDonough (1991, page 223) discuss basic clutterlocking techniques. The most fundamental exploit the fact that the power of the Doppler spectrum around its centroid should be the same as the two-way antenna characteristic: they crosscorrelate the two, before or after range or azimuth compression.

Range subaperture correlation Doppler centroid ambiguity may be resolved by cross-correlating multilook images (Curlander and McDonough 1991, page 240).

A slightly different approach is to carry out multilook processing and deduce the error in the assumed Doppler centroid iteratively by comparing image energies (Curlander and McDonough 1991, page 227).

Multiple PRFs Chang and Curlander (1992) describe the use of multiple PRFs to unambiguously determine F_{dc} in Equation (2.17). The technique involves transmitting at one PRF for a second, then another for a second, and staying on a third for the duration of the required measurement. The actual centroid is then determined using the Chinese remainder theorem, as per conventional MTI systems, but based on the three $\hat{F}_{dc}$s. This estimate is continuously updated during the entire measurement period using conventional techniques. The PRFs are retransmitted in reverse order at the conclusion of the measurement for checking purposes.

Apart from the data averaging issue and the use of multiple PRFs at only the start and finish, this concept could be applied to SAR MTD.

Multifrequency SAR Runge and Bamler (1989) suggest that a multifrequency SAR can unambiguously resolve the Doppler centroid. This is because the centroid is inversely proportional to wavelength (Equation (2.11)). In addition, the lower the operating frequency, the lower the required PRF: a Doppler centroid measurement at L-band may be used to correct an image taken with a higher PRF, simultaneously, at X-band.

'True' Doppler Moving targets cause a shift in the frequency of the received signal relative to the transmitted signal. (This is a true Doppler shift.) If it is measured, the target's velocity will be known. This is very difficult in conventional SAR since

- the target's Doppler shift will be a few hundred hertz compared with the pulse compression signal's bandwidth of tens of megahertz, and
- the ambiguity function of a typical pulse compression signal, a linear chirp, does not have a sharp peak. It is analogous to the moving target azimuthal compression problem with a conventional SAR.

When this technique is used for Doppler centroid estimation, many spectra have to be averaged to reduce speckle noise (Runge and Bamler 1989).

Autofocussing techniques Due to the similarity in effect between SAR platform velocity errors and targets moving in azimuth, autofocussing techniques provide insight for target velocity estimation.

Most SAR processors perform autofocussing, the estimation of azimuthal Doppler rate, in the same manner as clutterlocking: by exploiting the antenna beam pattern (Curlander and McDonough 1991, page 234). Alternatively, some use the fact that the image contrast decreases when the speed parameter is erroneous, and perform an iterative estimation. This is **Doppler rate filtering.** (Ping and Zongzhi (1996) use a wavelet transform.) The concept is applied to SAR MTD in (Barbarossa 1989, Peyregne 1996). Filters tuned to different Doppler rates may be able to distinguish moving from stationary targets, even though their spectra may overlap.

Another technique is to track the phase of the return from a bright scatterer. This may be used with moving targets provided that there is a sufficiently high signal to noise ratio.

Coordinate transformation Yang and Soumekh (1992) and (1993) show that a moving target can be imaged by processing its data as if it were a stationary squint mode target, with the focussing parameters dependent upon the target's velocity — to a first approximation, the two situations are analogous. (See Section 3.4.3.)

Correction of moving target phase asymmetry Chen and McGillem (1991) describe a scheme whereby the quadratic phase asymmetry of moving targets is removed prior to conventional SAR processing.

A threshold frequency is used to detect a moving target, *viz* conventional MTI. There is a higher sampling rate than that of a conventional SAR.

Range walk detection A moving target may traverse more range cells during the azimuthal integration period than a stationary target (Raney 1971). This can be detected using two dimensional filters matched to the responses of targets moving at the velocities of interest.

Runge and Bamler (1989) describe three techniques, the simplest of which is to crosscorrelate two outer looks after multilook processing. This technique is discussed in detail by Ouchi (1985); an apparently similar method is discussed by Yang and Soumekh (1992), although the processing is performed in another domain.

Clutter cancellation The cancellation of clutter using a predictive filter is discussed by Barbarossa (1989). The difference between the assumed homogeneous characteristics of clutter and those of a moving target permit the detection of targets moving within the clutter's bandwidth.

Space-time adaptive processing, *etc.* The STAP approach (*e.g.* (Klemm 1996b, Klemm 1996c, Klemm 1993, Klemm 1996a, Ender 1996)) uses a multichannel (array) antenna, treating SAR as a beamforming problem. This can give optimum performance (using any criterion of interest), allowing nulls to be positioned over jammers and ground clutter. It is the most powerful of the MTD techniques, and also the most signal processing intensive. It is currently receiving much interest, particularly in comparison with the DPCA technique, now that low cost, high performance signal processing devices are available. Ender (1996) discusses multichannel SAR MTI performance bounds, *etc.* An implementation is discussed by Jansen and Kirchner (1996).

Jingwen, Junxiang, Yinqing and Shizhang (1995) image moving targets with SAR at a low PRF by the careful, uniform positioning of the elements of an array antenna, using

the spatial separation to obtain the equivalent of a higher PRF.

Kent and Paker (1996) use the differential phase between two receive antennas to track non-uniform target motion.

Wigner-Ville, *etc.* Barbarossa and Farina (1990) and Barbarossa (1992a) used the Wigner-Ville distribution to estimate the parameters of moving targets. He later combined it with a Hough transform to reduce the cross terms (also (Yinfang, Guoan and Junfeng 1996)). Rieck (1996) reduced the effects of cross terms used an adaptively smoothed Wigner-Ville distribution.

To reduce the effects of range migration, the initial parameter estimation was performed on a version of the data with degraded range resolution. The results were later transferred to the high resolution data.

Barbarossa also discussed a technique using multilinear time-frequency distributions to estimate the parameters of a target where there are many scatterers in the same resolution cell and when the phase may not necessarily be second order (Barbarossa and Mascolo 1994).

Porchia, Barbarossa, Scaglione and Giannakis (1996) propose a SAR moving target detection and focussing method based on the multilag high order ambiguity function discussed in (Barbarossa, Porchia and Scaglione 1996). This function is also used for autofocussing stationary targets.

Wang, Wang, Jing and Liang (1996) use a chirp transform to focus the unambiguously sampled moving targets.

Ikram, Abed-Meraim and Hua (1996) describe an iterative technique which overcomes the problem in polynomial phase estimation of errors in a low order coefficient being increased by errors in the estimation of higher order coefficients.

(Moving target parameter estimation techniques are discussed in detail in Chapter 5.)

ISAR Unknown, arbitrary target motion over several seconds may prevent accurate imaging by a fixed filter. An alternative is inverse SAR (ISAR), where high resolution is obtained by exploiting the motion of the target itself, rather than the induced motion of the platform past it (Wehner 1995). Sophisticated processing techniques exist which contend with this arbitrary motion.

It is the best class of techniques for *imaging* moving targets over many seconds; its prime application is the long range identification of ships, although it has also been applied to ground vehicles, air- and spacecraft.

Radar imaging relies on the target undergoing an aspect change in order to obtain high resolution from the differential distance changes between the radar and each scatterer. In stripmapping SAR, the aspect change is restricted to the beamwidth of the antenna. In spotlight SAR, it can be chosen to suit the resolution requirements. In ISAR, it depends upon the target rotating while it is being viewed.

One ground target identification scenario is for a SAR MTD system to first image the ground and locate and determine the parameters of a moving target. By studying the road being used by the vehicle, the radar could predict when it will round a corner. A spotlight SAR/ISAR system could therefore be cued in anticipation of this aspect change (Fowler 1996).

2.6 Proposed SAR MTD Technique

A non-uniform PRI permits the unambiguous determination of the moving target's Doppler centroid without requiring any more data than collected by a conventional SAR. This technique will be discussed heuristically in the next section.

The main application for the proposed radar is that of wide area surveillance of terrain such as that found in outback Australia. Of primary importance is the detection of man made objects, both stationary and moving. Fundamentally, these are sparsely distributed and consist of discrete scatterers wi'h relatively large radar cross sections. Thus the accurate metrology of surface textures, for example, while appropriate for estimating foliage biomass, *etc.*, is of low priority. Thus it is reasonable to expect to obtain useful information about a scene from relatively few radar transmissions.

A non-uniform PRI for SAR is not new; such systems have been discussed previously for a variety of reasons (*e.g.*, Doppler centroid resolution (Chang and Curlander 1992), choosing the transmission times to suit a particular imaging geometry (harris 1984) and to improve SAR electronic warfare characteristics (Mobley 1995, Mobley and Maier 1996)). However, it has not previously been applied to the problem of moving target detection to the author's knowledge.

Note that several of the existing SAR MTD techniques discussed above, including Doppler

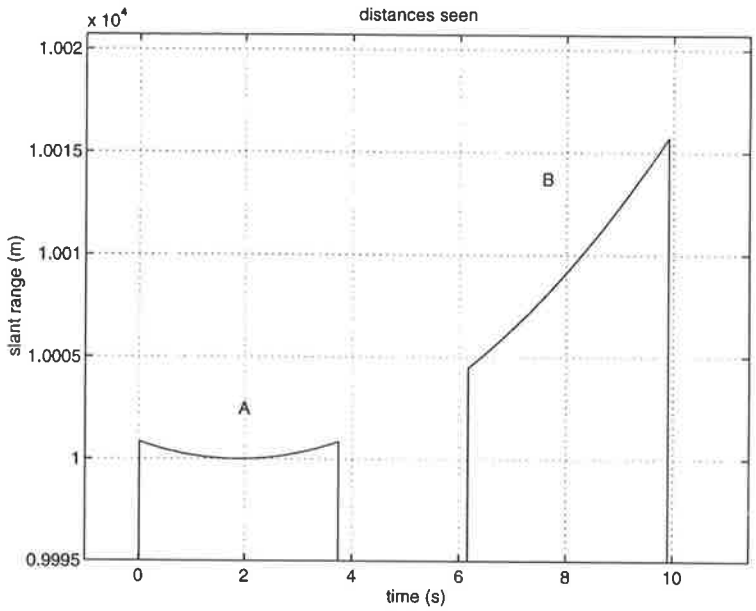

Figure 2.5: The distances to two targets seen by the radar.

rate filtering and clutter cancellation, may still be used with non-uniformly spaced data samples.

2.7 Non-Uniform Sampling

This section presents an intuitive explanation for the applicability of non-uniform sampling to SAR MTD, and discusses non-uniform sampling theory in general. The topic is discussed at length by Bilinskis and Mikelsons (1992). For the purposes of this thesis, the signal processing terms 'sampling times/sampling intervals/sampling frequency' may be taken as synonymous with the radar terms 'radar transmission times/pulse repetition intervals/pulse repetition frequency'.

It is assumed that the reader is familiar with uniform sampling concepts.

2.7.1 Heuristic Justification for Non-Uniform PRI SAR MTD

An intuitive way to understand the effectiveness of a non-uniform pulse repetition interval is to consider the unwrapped phase of a sampled azimuthal chirp. Phase unwrapping removes absolute discontinuities greater than π radians from a sequence of phase samples by offsetting samples by a multiple of 2π.

Figure 2.5 shows the distances between the radar and two targets: one stationary (A) and one moving in range at 3 m/s (B, illustrated in Figure 2.3(a)). These distances are shown at the times when the targets are inside the radar's antenna beam.

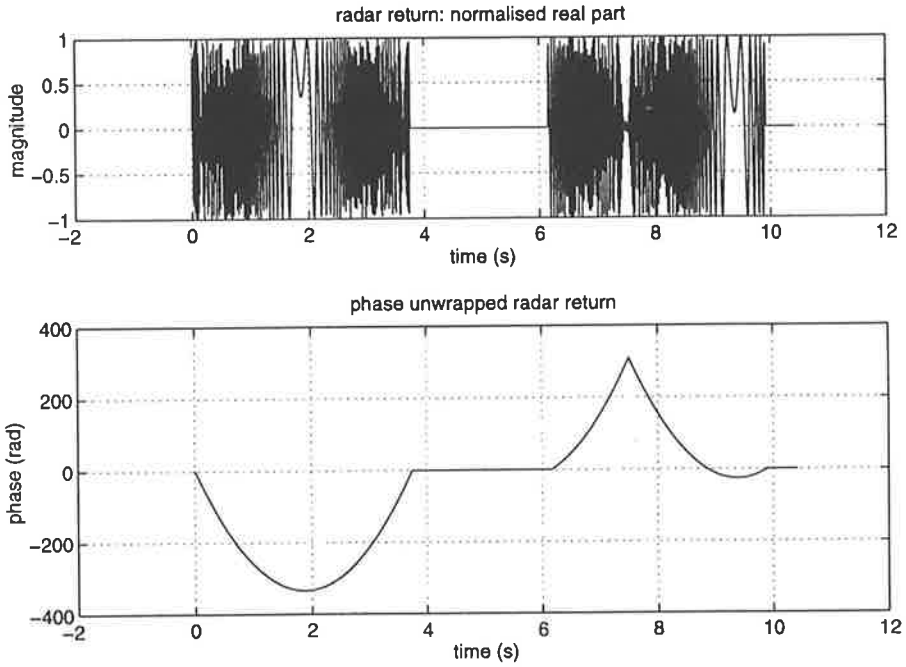

Figure 2.6: Radar azimuthal phase returns.

Figure 2.6 shows both the real part of the azimuthal return and the corresponding unwrapped phase response from these targets for a radar operating with a uniform PRI. Although the distances to the targets may be very different, the azimuthal data are very similar due to subsampling effects. A filter designed to focus the stationary target will clearly partially focus B.

A non-uniform PRI gives an azimuthal response like the one shown in Figure 2.7. Because the slope of the distance change is small for target A, a small change in timing will not have much effect on the radar returns, so the left hand side of Figure 2.7 is very like the left hand side of Figure 2.6. The same timing offsets have a profound effect on the return from the moving target, however, due to the increased slope of the distance plot. Intuitively, a filter used to focus A will now *not* accurately focus B. Conversely, a filter attempting to focus B will suppress the stationary target (*i.e.*, clutter) A. This will be discussed in detail in later chapters.

Non-uniform sampling theory will now be presented.

2.7.2 Introduction

Deliberate non-uniform sampling is an underrated branch of data acquisition and signal processing since, ideally, it permits an alias free, discrete representation of an analogue signal with a bandwidth far higher than the average sampling rate (Bilinskis and Mikelsons 1992).

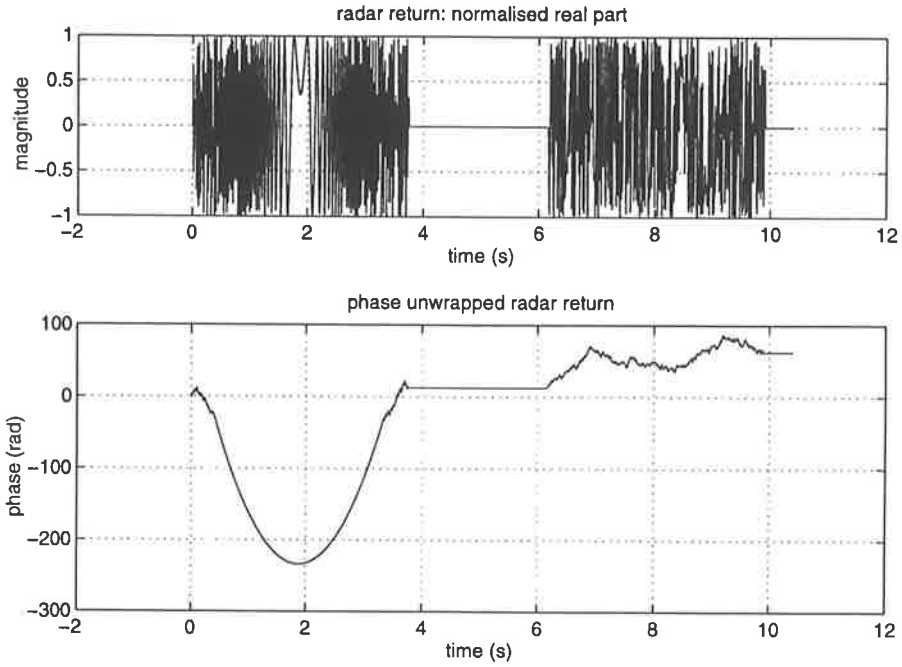

Figure 2.7: Radar azimuthal phase returns; non-uniform PRI.

Applications include spectral analysis where the bandwidths of interest are far higher than analogue to digital converters can sample directly, and where only the minimum amount of data is desired to characterise a given signal.

Non-uniform sampling and processing are well known in fields including astronomy, where measurements may be made at irregular intervals due to practical constraints, such as telescope availability and weather conditions (Lomb 1976, Scargle 1982). However, the data in this case are still oversampled: variable stars may have periods of months or years. The emphasis in this thesis is on undersampled data, where aliasing is an important issue.

Aliases are ambiguities which arise when more than one conceivable signal, usually from a model with differing parameters, can give rise to the set of measurements. It is then not known which represents the actual situation. It is important to realise that aliases are a result of *uniform* sampling, not sampling *per se*. Carefully chosen sampling times give very desirable characteristics, including alias suppression. It may be that the sampling times result from a random process. (The times are assumed to be accurately known, and are taken into account during processing; they are just specified randomly.) The *expected* performance of a signal processing operation with respect to the probability density function of the sampling times may therefore have to be calculated. In fact, it can be shown that the expected estimated spectrum produced from a signal sampled at times with a uniform probability density function $p_T(t)$ tends towards that of the original analogue signal (Bilinskis and Mikelsons 1992, page 38).

However, this is not achieved in practice since it requires an infinite number of samples with infinite precision.

Clearly, the performance of an estimator using randomly sampled data depends upon the degree of randomness in the sampling scheme. To reduce statistical error in this performance, there should be a minimal degree of randomness, such as a small deviation from uniform sampling times.

The amount of randomness required depends upon the number of samples processed: when filtering out aliases, for example, the greater the number of non-uniform samples processed, the smaller the deviation from uniform needs to be.

2.7.3 Minimum Sampling Requirements

The well known sampling theorem states that a real signal with bandwidth B may be reconstructed from samples collected at a rate equal to at least $1/(2B)$ hertz. This is known as the Nyquist rate (Roberts and Mullis 1987, 129). For complex signals, the complex sampling may be done at $\geq 1/B$ Hz.

The general bandpass sampling theorem is slightly more general (Martin 1997): the *average sampling rate* must be greater than the sum of the bandwidths of the components making up the signal, provided it is known which parts of the spectrum are occupied by the signal.

2.7.4 Pseudorandom Sampling

It is difficult in practice to generate samples at known, arbitrary times; the times themselves have to be known to high accuracy. An alternative is pseudorandom sampling (Bilinskis and Mikelsons 1992, page 55, 91–92), where a high frequency reference clock produces pulses at uniform intervals, and times are chosen from this set to satisfy a predetermined sampling scheme. The highest unaliased frequency of a sampled signal is given by half the frequency of the reference clock.

2.7.5 Signal Processing

Spectral Analysis

It is very useful to analyse the spectrum of sampled data. The power spectrum corresponding to the signal $q(t)$ sampled at the known times $\{t_n\}$, $n = 1, \ldots, N$, may be approximated by the squared discrete Fourier transform (DFT)

$$P_q(f) = \left| \int_{-\infty}^{\infty} \left[q(t) \sum_{n=1}^{N} \delta(t - t_n) \right] e^{-j2\pi ft}\, dt \right|^2 = \left| \sum_{n=1}^{N} q(t_n) e^{-j2\pi f t_n} \right|^2.$$

This results in slight errors which can be avoided using a more complex spectral estimator, such as least squares (Bilinskis and Mikelsons 1992, page 222–225), (Scargle 1982). (The DFT is the same as the least squares spectral estimator in the case of uniform samples.) This may require the (numerically intensive) inversion of a matrix, which may be precomputed if the sampling times are known beforehand. Alternatively, computationally efficient spectral estimators for non-uniform samples are discussed in (Lomb 1976) and (Bilinskis and Mikelsons 1992, pages 235–243).

Reconstruction of Spectra

An important issue is the effect that a random sampling scheme may have on the measured spectrum of a signal, and whether or not it is possible to uniquely reconstruct the signal (*i.e.*, whether or not the spectrum is alias free). This issue is important when considering a non-uniform PRI scheme for finding moving targets' Doppler centroids unambiguously. The main reference for the rest of this section is (Martin 1997).

It can be shown that the observed power spectrum

$$P_s(f) = P(f) * S(f),$$

where $P(f)$ is the true power spectrum. $S(f)$ is the spectrum of the sampling process, given by

$$S(f) = \begin{cases} \dfrac{1}{\mathrm{E}[p(t)]}, & f = 0, \\ \Re\left\{ \dfrac{1+\tilde{p}(f)}{1-\tilde{p}(f)} \right\}, & f \neq 0, \tilde{p}(f) \neq 1, \end{cases} \tag{2.18}$$

where $\tilde{p}(f)$ is the Fourier transform of $p(t)$, the probability density function of the intersample spacing.

The spectrum is alias free if it is possible to unambiguously reconstruct $P(f)$ from a knowledge of $P_s(f)$ and $S(f)$. It has been found that this is the case when the complex values of $\tilde{p}(f)$ are unique for all values of f. For example, the Poisson distribution

$$p(t) = ae^{-at} \rightarrow \tilde{p}(f) = \frac{a}{a + j2\pi f}$$

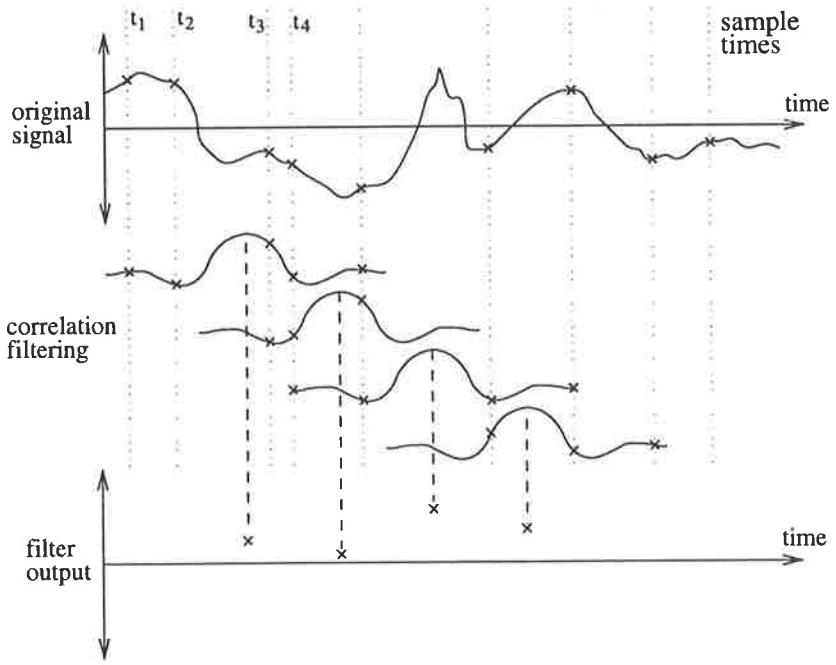

Figure 2.8: Correlation filtering of non-uniformly sampled data.

gives a flat spectrum (Marvasti 1987, page 96) which is alias free. On the other hand, regular sampling, with its repeated values, gives ambiguities.

It was conjectured that for a given distribution to be alias free, it must be nonzero near the origin. (However, although a scheme may exhibit aliases, they may be sufficiently low in amplitude not to cause difficulties.)

These results will be used when the ambiguity function is considered with a randomly switched stagger pattern Section 3.7.1, and when optimal random times are discussed Section E.2.3.

Filtering

Figure 2.8 shows the process of crosscorrelating a filter with data sampled at arbitrary times. (This figure is similar to Figure 11.1 in (Bilinskis and Mikelsons 1992, page 277).) The filter values are calculated at times corresponding to the data's sampling times. These are multiplied by the data samples for the duration of the filter, and the accumulated results are output. In this example, the filter is shifted along the time axis at uniform intervals.

Conventional digital filtering, by contrast, has uniform samples of the input data, and synchronous output samples. This means that the same filter values are used for each calculation, and the process can be described using a convolution operator.

General filtering cannot be performed with any acceptable level of performance using non-uniform samples (Bilinskis and Mikelsons 1992, pages 293–303). (This is because impulse responses which tend toward zero rapidly cannot be effectively represented with non-uniform samples.) However, it is possible to perform narrowband, selective filtering, even in parts of the spectrum outside what would normally be the unambiguous region.

This has an impact on non-uniform PRI SAR MTI with a low average pulse repetition frequency (PRF) (Section 4.4): since wideband clutter cannot be selectively filtered out from the signal, MTI cannot be performed.

The definitions of different sampling schemes will now be presented.

2.7.6 Timing Specifications

Sampling times $\{t_n\}, n = 1, \ldots, N$, will be specified in terms of their joint probability density function (PDF) $p_{\mathbf{T}}(\boldsymbol{t})$ thus:

Known If the sampling times are known,

$$p_{T_n}(t) \;=\; \delta(t - t_n) \;\; \forall n,$$

where $\delta(t)$ is the Dirac delta function.

Uniform If the sampling times have a uniform separation t_s and are centred on $t = 0$,

$$t_n \;=\; \left(n - 1 - \frac{N-1}{2}\right) t_s, \; n = 1, \ldots, N; \tag{2.19}$$

$$p_{T_n}(t) \;=\; \delta\left(t - \left[n - 1 - \frac{N-1}{2}\right] t_s\right) \;\; \forall n.$$

Figure 2.9 shows the estimated spectrum of a 2.2 Hz cisoid sampled uniformly at 1 Hz. Aliases make it impossible to determine which peak represents the true signal.

Random offsets The transmission times can also be specified relative to the uniform transmission times:

$$t_n \;=\; n\, t_s + \Delta\tau_{n \bmod M},$$

with M offsets $\{\Delta\tau_n\}, n = 0, \ldots, N-1; \Delta\tau_0 = 0$.

This scheme is also known as 'periodic sampling with jitter' (Bilinskis and Mikelsons 1992), 'independent jitter' (Berkovitz and Rusnak 1992) and the 'random deviation

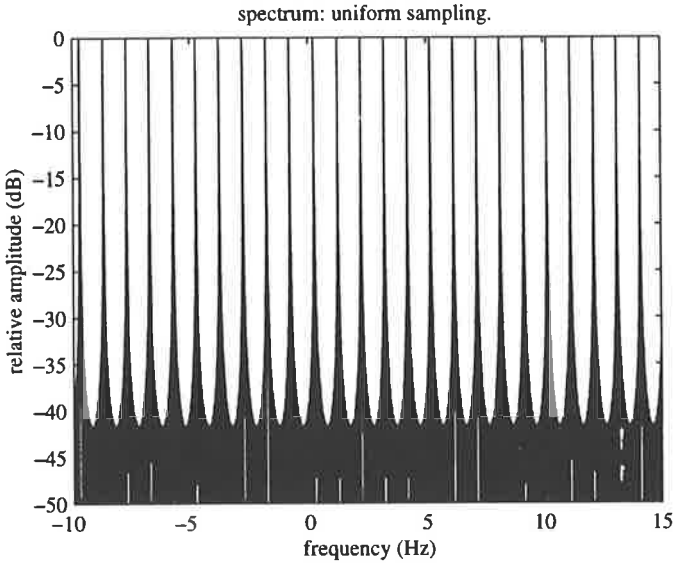

Figure 2.9: Estimated spectrum; uniform sampling.

method' (Vergara-Dominguez 1993).

It has poor properties since the corresponding sampling PDF in general drops to zero between the samples (Bilinskis and Mikelsons 1992, page 62): it is far better to have a finite probability over the entire sampling interval. The case when there are no nulls has $\Delta\tau = t_s/2$, which has two problems: a large random component (which means a large random error) and the fact that some intervals are going to be extremely small. The latter condition is unacceptable in a radar application due to range ambiguities.

Figure 2.10 shows the estimated spectrum of the 2.2 Hz cisoid sampled at 1 Hz on average with uniformly distributed random timing offsets of 20%. The least squares estimator was used. This spectrum clearly shows that the signal has been unambiguously identified. The first sidelobe is at ≈ -13 dB (not clearly shown).

Random intervals The times within a frame period correspond to the delays $\{\tau_n\}$: $t_{s,n} = t_{s,n-1} + \tau_{n-1}, n = 0, \ldots, N-1$ and $t_{frame} = \sum_{i=0}^{M-1} \tau_i$. $\tau_n > 0, n = 0, \ldots, M-1$.

This is also known as the 'additive random point process' (Bilinskis and Mikelsons 1992, page 35), 'accumulated jitter' (Berkovitz and Rusnak 1992) and 'random interval method' (Vergara-Dominguez 1993).

See Figure 2.11 for a representation of a non-uniform sampling scheme.

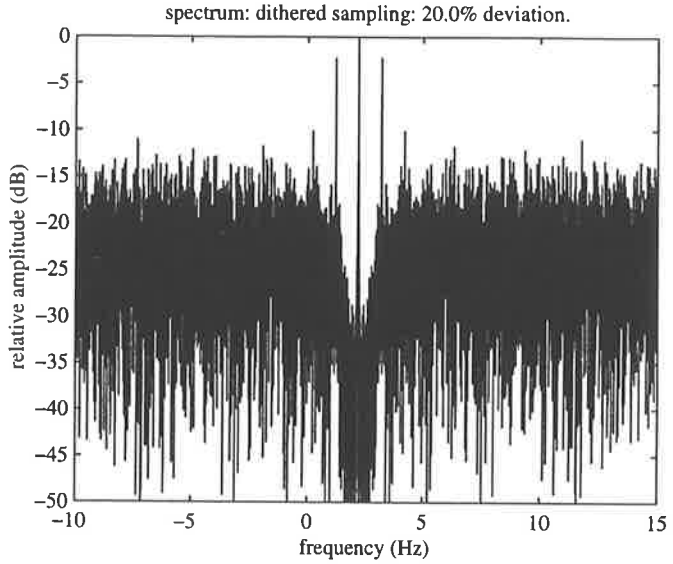

Figure 2.10: Estimated spectrum; random offsets.

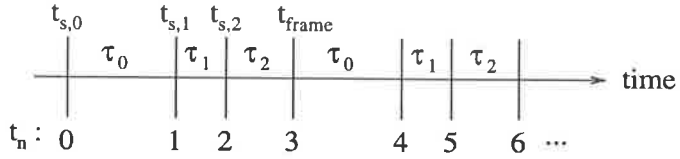

Figure 2.11: Non-uniform sampling with the specified notation for $M = 3$.

To obtain the desirable sampling properties, the actual distribution of τ is not important, since its effects are cumulative (Bilinskis and Mikelsons 1992, pages 35 and 66), eventually resulting in a flat probability density function by the central limit theorem. It is useful, though, to specify the ratio of standard deviation to the mean, σ/μ, and good results may be obtained for $0.01 \leq \sigma/\mu \leq 0.3$, depending upon the application.

Figure 2.12 shows the estimated spectrum of the 2.2 Hz cisoid sampled at 1 Hz on average with uniformly distributed random timing intervals of 20%. As with Figure 2.10, the signal has been identified, although the sidelobe structure has changed. Here there is a larger band around the signal without noise and the nearest aliases to the signal are smaller than in Figure 2.10, but the noise floor is higher. Again, the first sidelobe is at ≈ -13 dB.

Correlated intervals Further improvements may be realised by implementing the intervals τ as an autoregressive process with a positive correlation coefficient ρ (Bilinskis and Mikelsons 1992, page 66–69): a flat PDF is achieved with fewer samples. This results in a lower variance in the estimate of mean square value, for example (Bilinskis and Mikelsons 1992, page 130–131). It is lower than for jittered sampling.

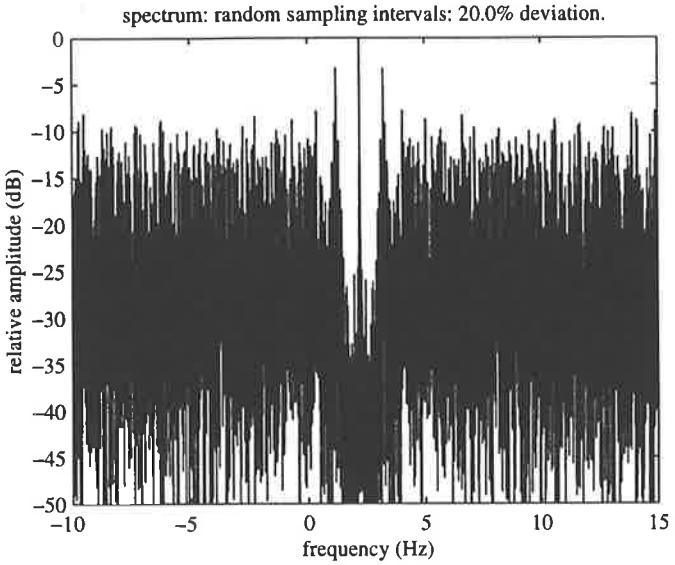

Figure 2.12: Estimated spectrum; random intervals.

However, a plot of the sampled spectrum using this scheme with $\rho = 0.5$ looks extremely similar to the spectrum obtained with random intervals using a Gaussian distribution (which is slightly different to Figure 2.12). This is because many samples were processed; differences would be more profound if only a few were considered.

Sampling periodic signals can be a problem if the signal's period is comparable to the average sampling interval: there is a tendency to sample the same part of the waveform. This tendency is alleviated using a positive correlation between intervals (Bilinskis and Mikelsons 1992, page 79–80).

Bilinskis and Mikelsons (1992, page 87–88) show the effects of the correlated additive random point sampling function on worst case alias suppression.

If the input signal is asynchronous with the sampling scheme, the sampling PDF may be flat initially, rather than just tend towards a constant value (Bilinskis and Mikelsons 1992, page 74).

2.7.7 SAR Specifics

This section discusses the specific application of non-uniform sampling to SAR.

From the minimum sampling rate requirement discussed in Section 2.7.3, it is reasonable to detect moving ground targets with a narrow range of predefined speeds with a SAR operating at the same average PRF as a ground imaging radar provided that the scene is not arbitrarily complex. (Although the moving target's signal is a chirp and occupies approximately the same

bandwidth as a stationary target, a low sampling rate may be used since the signals' chirp rate is approximately known and the signal's *dechirped* bandwidth is very small. It can be modelled as a *moving* scatterer, rather than an *extra* scatterer in the scene.) The technique can be applied to circumstances where there are few moving targets, such as detecting the presence of vehicles in remote areas. City traffic monitoring, on the other hand, requires a high average PRF due to the much greater information content of the radar return.

Some miscellaneous sampling issues follow:

- Having the number of sample time offsets $M = 1$ corresponds to a conventional SAR. The upper limit for M is the number of samples during the integration time (ultimately the number of transmissions over a synthetic aperture):

$$\begin{aligned} M_{max} &= L_{max}/\rho_{sa} \\ &= \frac{R_{max}\theta_{ra}}{\rho_{sa}}, \end{aligned}$$

  where R_{max} is the maximum slant range, θ_{ra} is the antenna's horizontal beamwidth and ρ_{sa} is the azimuthal resolution.

- The number of transmissions over the length of a synthetic aperture must be the same as the number used by a conventional SAR, a constraint imposed for this thesis.

- The lowest common denominator of the sampling intervals τ_{lcd} must be small enough to unambiguously detect the phase changes corresponding to a moving target, as well as that of the ground; *i.e.*

$$1/\tau_{lcd} > 2|F_{dc,max} + B_{d,max}/2|,$$

  where the maximum Doppler centroid $F_{dc,max}$ and maximum Doppler bandwidth $B_{d,max}$ are given by Equation (2.11) and Equation (2.13) respectively with the maximum target velocity values substituted (D'Addio et al. 1994). This is important when pseudorandom sampling is used.

- Let

$$\begin{aligned} \tau_{min} &= \text{the minimum transmission interval} \\ &= \min(\tau_n), \quad 0 \leq n < M. \end{aligned}$$

Then $f_{s,max}$ $(= 1/\tau_{min})$ must satisfy the conventional SAR upper PRF bound

$$f_{s,max} \leq c/2R_s$$

(Section 2.1.4), to avoid range ambiguities.

- The first target motion ambiguity must occur at a higher speed than the maximum target speed (Mao 1993, page 312).

2.7.8 Non-Uniform Arrays

There is a clear analogy between SAR and real array antennas: SAR is array processing with data collected from one time-shared antenna element. It follows that a non-uniform PRI is analogous to a non-uniform array.

Non-uniform arrays are used to achieve a higher resolution than uniform arrays with the same number of elements by permitting antennas to cover a larger area. If the elements of a uniform array have separations greater than half a wavelength, the antenna exhibits 'grating lobes', sidelobes analogous to the aliases associated with undersampling. (The SAR equivalent is termed 'azimuthal ambiguity'.)

Techniques exist which specify the optimal positions of non-uniform array elements. One technique, that of maximising the integrated sidelobe ratio (Boni, Richard and Barbarossa 1994), is applied to a non-uniform PRI SAR in this thesis (Section 6.4.3). Another, a minimum redundancy approach (Pearson, Pillai and Lee 1990) is used in Section E.3.

Throughout this thesis, sampling will be considered to be in the time domain without loss of generality.

2.7.9 Non-Uniform Sampling: Concluding Remarks

Non-uniform sampling is an appropriate technique for capturing a signal whose components occupy a small fraction of the spanned bandwidth using a small number of samples. It is well suited to synthetic aperture radar moving target detection.

Ideally, using the non-uniform sampling theory outlined above, for avoiding aliasing effects we would use an additive pseudorandom point process with small σ/μ (*e.g.*, 0.3) and a correlation of 0.3, precalculated for N samples, with a reference clock high enough to capture the entire range of frequencies of interest. Combined with asynchronous sampling, this scheme

Function	Property	Where
Ground imaging	3 dB resolution	Section 6.5.1
	unambiguous range	Section 2.1.4
	peak sidelobe	Table 6.2
	integrated sidelobe ratio	Table 6.2
MT indication	improvement factor	Section 4.4
	target velocity range	Section 4.6
MT detection	signal-to-disturbance ratio improvement	Section 4.3.3
	receiver operating characteristic (*i.e.*, detection prob. *vs.* false alarm prob. *vs.* signal to clutter ratio)	Section 4.3.4
MT parameter estimation	position error	Section 5.8
	velocity error	Section 5.8
Implementation	computational cost	Sections 4.6 and 5.7

Table 2.2: SAR imaging and moving target detection considerations.

approximates a uniform sampling PDF $p_T(t)$ of unity, which provides good alias suppression (Bilinskis and Mikelsons 1992, page 80-88). It is shown in this thesis (Chapter 5) that this also results in parameter estimation variances which approximate those of uniform sampling.

SAR performance requirements will now be presented.

2.8 Performance Requirements

The non-uniform sampling scheme to be adopted for simultaneous ground imaging and moving target detection should be considered with respect to the criteria listed in Table 2.2. Many schemes are discussed in Appendix E. Every scheme will be a compromise: ideal imaging/MTD/MTI cannot be performed with a minimum volume of data. These criteria will be referred to by later chapters.

2.9 Summary

This chapter discussed the fundamentals of synthetic aperture radar and the effects of moving targets. It covered radar waveforms in general, defining the Woodward ambiguity function and methods for reshaping it. Existing SAR moving target detection techniques were then discussed in detail, and the proposed technique, that of a non-uniform PRI for SAR, was introduced. This was followed by a discussion of non-uniform sampling theory in general, and the implications for SAR in particular. The criteria to be addressed by SAR MTD/imaging schemes were presented.

CHAPTER 3

Moving Target Ambiguity Function

This chapter derives the moving target ambiguity function (AF) of a chirp pulse compression synthetic aperture radar (SAR) with arbitrary and random transmission times. It is shown that such a radar is able to unambiguously determine ground targets' two dimensional positions and velocities whilst operating with the same average pulse repetition frequency (PRF) as a conventional ground mapping radar.

3.1 Introduction

A conventional SAR, with a PRF sufficient only to unambiguously sample the Doppler bandwidth of the ground, is incapable of determining the parameters of a moving target. As discussed in Section 2.3, the azimuthal signal returned from a stationary target is, ideally, a linear frequency ramp centred on 0 Hz. In contrast, a moving target's is a Doppler shifted, time scaled, possibly non-linear frequency ramp (Raney 1971). Since, in practice, the shift may be many times the PRF, there are ambiguities resulting from aliasing effects. A practical consequence of this is that moving targets are displaced from their actual positions, and are consequently not registered correctly in the image.

The AF is the response of the radar to a point target on the ground, allowing for mismatches between the parameters specifying the signal received from that target and those of the focussing filter. These parameters include the target's velocity and position, and it is important to investigate the effects on the AF on non-uniform sampling.

The contribution of this chapter is to derive the moving target AF of a ground mapping, airborne SAR and use it to investigate the effects of a non-uniform or random pulse repetition interval (PRI): it is shown that a non-uniform PRI gives this radar the dual capability of ground

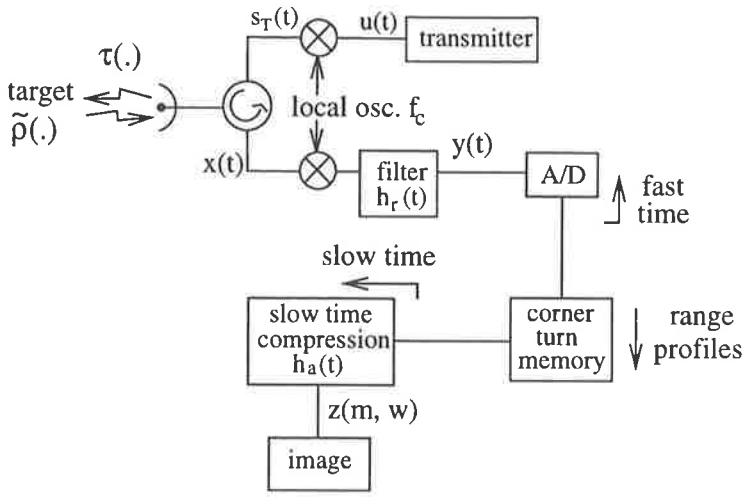

Figure 3.1: A block diagram of the radar model.

imaging and unambiguous, two dimensional moving target velocity and position determination. The AF is derived in Section 3.2, used for moving target focussing in Section 3.4 and applied to uniform and non-uniform PRI radars in Sections 3.5 and 3.6 respectively. The latter includes a detailed example with two alternating PRIs. Section 3.7 discusses the expected AF resulting from a random PRI when the sampling probability density function is known. Appendix A lists some properties of the extended AF, the form of the stripmapping SAR AF. This is a generalised version of the Woodward ambiguity function with a Doppler frequency rate term.

3.2 Ambiguity Function Derivation

In this section, the stripmapping SAR AF is derived, starting from a general pulsed radar scenario and becoming progressively more specific to stripmapping SAR. The initial derivation is based on Lush's analysis of a pulse Doppler radar (1990). Figure 3.1 shows a representation of the processes performed by a SAR.

3.2.1 Radar Scenario and Signals

The radar transmits the signal $s_T(t)$ which propagates towards the scene of interest, having the complex reflectivity $\tilde{\rho}(x, y, z)$, and is instantaneously retransmitted by it. In general, the scene is moving relative to the radar, resulting in a time- and position-dependent range delay $\tau(x, y, z, t)$ between the times of transmission and reception. The radar then coherently

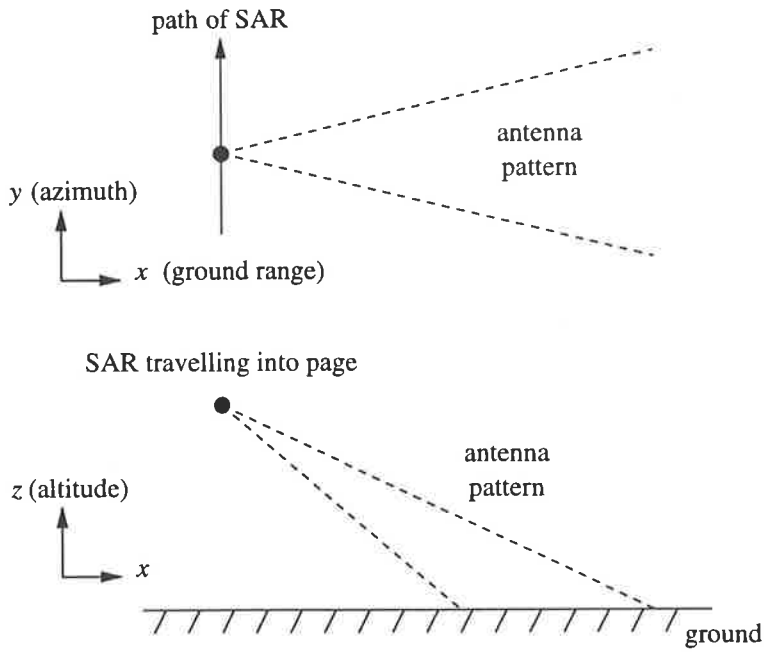

Figure 3.2: The SAR two-way antenna pattern, $\tilde{a}(x, y, z, t)$. (This is equivalent to $\breve{a}(x, t - y/v_p, z)$ since the radar is moving with velocity v_p in the azimuthal direction.)

receives the signal

$$\mathbf{x}(t) \approx \int_{\mathbf{Z}}\int_{\mathbf{Y}}\int_{\mathbf{X}} \tilde{\rho}(x, y, z)\, \tilde{a}(x, y, z, t)\, s_T(t - \tau(x, y, z, t))\, dx\, dy\, dz$$

(based on (Cutrona 1990)), neglecting attenuations due to range and radar hardware. The time- and position-dependent amplitude modulation term $\tilde{a}(x, y, z, t)$ permits great generality, allowing the modelling of the two-way antenna pattern for arbitrary imaging scenarios, and may incorporate effects such as antenna pointing errors. $\tilde{a}(x, y, z, t)$ is shown for SAR in Figure 3.2. The integration is over the entire scene.

We restrict attention to point scatterers moving relative to the radar, rather than the moving ensemble considered in inverse SAR. (Porter, Tough and Ward (1993) and Damini and Haslam (1996) unify inverse SAR and SAR ground imaging using such a model.) If it is assumed that the scatterers in the scene are isotropic over the observed aspect angles, their reflectivity $\tilde{\rho}(x, y, z) \approx \tilde{\rho}$, so the received signal from one scatterer becomes

$$\mathbf{x}(t) = s_R(t) + n(t),$$

where

$$s_R(t) = \tilde{\rho}\, a(t)\, s_T(t - \tau(t)). \tag{3.1}$$

$a(t)$ is the radar's two-way antenna pattern, centred on the transmission time of $t = 0$. $n(t)$ is an unknown disturbance (clutter and noise) and $\tau(t) = \tau(x, y, z, t)$. The time-dependent range delay

$$\tau(t) = 2d(t)/c, \tag{3.2}$$

where $d(t)$ is the one way distance to the target; it is reasonably assumed that the velocity of propagation c is much greater than the greatest radar-target speed. The effects of multiple scatterers may be found by superposition.

The form of the signals will now be discussed.

The transmitted signal may be represented by the real function

$$s_T(t) = \alpha(t)\cos(\beta(t)),$$

where $\alpha(t)$ and $\beta(t)$ are amplitude and phase modulation terms respectively. Without loss of generality, the analytic representation of this signal $s_t(t)$ will be used such that

$$s_T(t) = \Re\{s_t(t)\},$$

where $\Re\{\cdot\}$ returns the real part.

If we assume that the transmitted signal is narrowband, meaning that its bandwidth is small compared with its centre frequency, it can be represented by

$$s_t(t) = u(t)\, e^{j2\pi f_c t},$$

where $u(t)$ is a complex envelope modulating the carrier at frequency f_c. From Equation (3.1),

$$s_r(t) = \tilde{\rho}\, a(t)\, u(t - \tau(t))\, e^{j2\pi f_c[t-\tau(t)]}.$$

If the radar generates a train of N identical, coherent pulses $p_t(t)$, each centred at time t_n and of duration T_1, we have

$$u(t; \{t_n\}) = \sum_{n=0}^{N-1} p_t(t - t_n).$$

The $\{t_n\}$ are monotonically increasing. To avoid overlapping transmissions and range ambiguities, $T_1 + \max \tau(t) < \min(t_{n+1} - t_n)\ \forall n$. Then

$$s_r(t) \;=\; \tilde{\rho}\, a(t) \sum_n p_t(t - t_n - \tau(t))\, e^{j2\pi f_c[t-\tau(t)]}.$$

Since $p_t(\cdot)$ is nonzero only in the small range $\pm T_1/2$ about each t_n, and neither $a(t)$ nor $\tau(t)$ change significantly over $t_n \pm T_1/2$, $s_r(t)$ may be written

$$s_r(t) \;=\; \tilde{\rho} \sum_n a(t_n)\, p_t(t - t_n - \tau(t_n))\, e^{j2\pi f_c[t-\tau(t_n)]}.$$

Recall that $a(t_n)$ was centred on $t = 0$.

3.2.2 Range Compression

The transmitted pulse $p_t(t)$ is chosen to have the property that the convolution with a weighted matched filter with impulse response $p_r^*(-t)$

$$\int_{-\infty}^{\infty} p_t(\eta)\, p_r^*(\eta - t)\, d\eta \;=\; \bar{\delta}(t) \;\approx\; \delta(t),$$

where * is the conjugation operation and $\delta(t)$ is the Dirac delta function. (It is normal for SAR systems to incorporate weights for sidelobe suppression, such as those discussed by harris (1978).) A linear frequency ramp (chirp), where

$$p_t(t) \;=\; \begin{cases} e^{j\pi\alpha t^2}, & |t| < T_1/2, \\ 0, & \text{otherwise}, \end{cases}$$

is such a signal; its performance may be approximated by

$$\bar{\delta}(t) \;=\; \left\{ \begin{array}{ll} 1, & |t| < \Delta r/(2c), \\ 0, & \text{otherwise}, \end{array} \right\} \tag{3.3}$$

where $\Delta r \approx c/2B$ is the range resolution, $B \approx \alpha T_1$ being the chirp's bandwidth. In practice, T_1 is only a few tens of microseconds. The moving target does not move a significant fraction of a wavelength during such a short interval, so there can be no velocity discrimination between slow targets and the ground using the return from the range compression pulse.

The received signal is quadrature demodulated to baseband and passed through a linear,

time invariant filter with impulse response $h_r(t)$, giving

$$y(t) = \int_{-\infty}^{\infty} e^{-j2\pi f_c \eta} s_r(\eta) h_r(t-\eta) d\eta.$$

Let $h_r(t) = p^*(-t)$, neglecting the time delay required to make this filter realisable. The output due to the discrete scatterer is

$$y(t) = \tilde{\rho} \int_{-\infty}^{\infty} \sum_n a(t_n) p_t(\eta - t_n - \tau(t_n)) p_r^*(\eta - t) e^{-j2\pi f_c \tau(t_n)} d\eta \quad (3.4)$$

$$= \tilde{\rho} \sum_n a(t_n) e^{-j2\pi f_c \tau(t_n)} \bar{\delta}(t - t_n - \tau(t_n)). \quad (3.5)$$

$\bar{\delta}(t)$ was defined in Equation (3.3).

Equation (3.5) is an intuitive result: the output is zero unless $t = t_n + \tau(t_n)$, when there is a range delay-dependent phase term[1].

It is useful to perform SAR MTD on the range compressed data, therefore, because

- the slow speed of the moving target has a negligible effect on range compression, since its Doppler frequency is small compared with the bandwidth of the range compression signal,
- there is no stationary target/moving target discrimination with a short pulse,
- the volume of data to be processed when searching for a target is vastly reduced,
- range compression vastly reduces the amount of clutter with which the signal has to compete (Barbarossa 1992b, page 81), and
- after azimuthal compression it is difficult to distinguish moving from stationary scatterers (Barbarossa 1992b).

The range compressed signal $y(t)$ is then sampled at times $mT_r + t_n$, m: $0, \ldots, M_{rp} - 1$, where $1/T_r$ is larger than the bandwidth of $p_t(t)$. The sample rate then satisfies the Nyquist criterion. This produces a range profile of M_{rp} samples for each radar transmission. (Of course, the signal could have been digitised prior to range compression.)

---

[1] As an aside, for the case where $\tau(t) = \tau + \dot{\tau}t$, it can be shown that Equation (3.4) can be expressed in terms of the standard asymmetrical narrowband cross AF, Equation (2.16) (similarly to (Lush 1990)):

$$y(t) \approx \tilde{\rho} e^{-j2\pi f_c[\tau + \dot{\tau}t]} \sum_n a(t_n) \chi'_{p_r^*(t), p_t(t)}(\tau - [t - t_n], f_c\dot{\tau}).$$

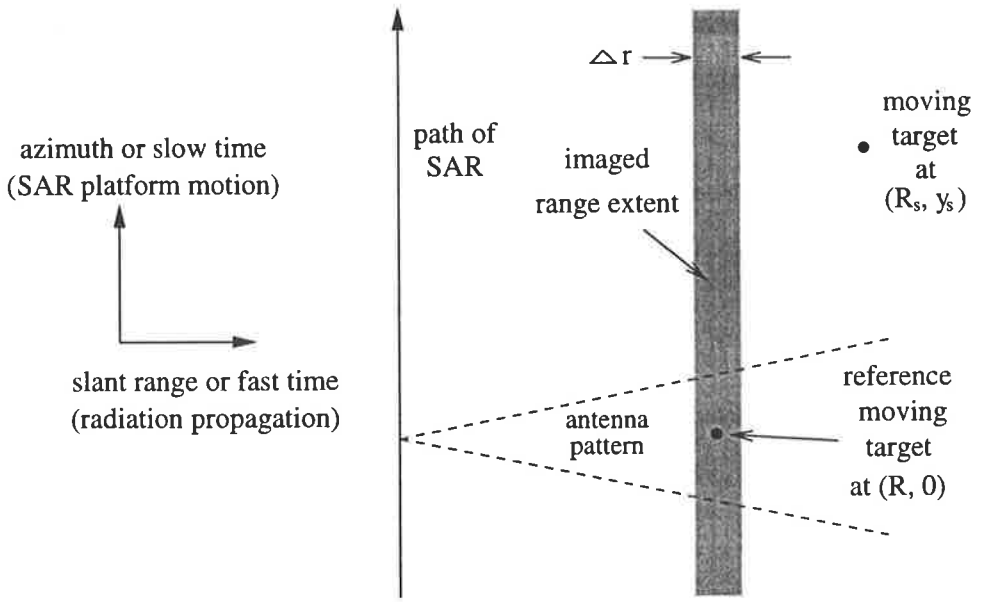

Figure 3.3: The SAR imaging scenario in the plane of the radiation.

3.2.3 *Slow Time Compression*

The radar collects compressed range profiles as it travels, storing them in a corner turn memory as illustrated in Figure 3.1. The data at each range, a function of time, may be processed in a variety of ways, including moving target indicator filtering (Lush 1990). Here, slow time compression will be performed by cross correlating the data with an appropriate filter. In SAR, slow time compression is imaging in the azimuthal dimension. See Figure 3.3 for a representation of this.

The response to a single scatterer is

$$z(m,w) \;=\; \sum_n y(mT_r + t_n)\, h_a(w - mT_r - t_n), \tag{3.6}$$

where m is the range index and w is a time delay. For matched filtering, $h_a(t)$ is a normalising $y^*(-t)$ (neglecting the delay required for causality)[2]; here, since the effects of mismatches due to target motion are of interest, let $h_a(t) = y_s^*(-t)$, where $y_s(t)$ is similar to $y(t)$ in Equation (3.5) but has range delay and amplitude terms $\tau_s(\cdot,t)$ and $a_s(t)$ which model a reference target.

$$y_s(t) \;=\; \sum_n a_s(t_n)\, e^{-j2\pi f_c \tau_s(\cdot,t_n)}\, \bar{\delta}(t - t_n - \tau_s(t_n)). \tag{3.7}$$

[2]For non-uniform $\{t_n\}$, this is strictly a *correlation,* rather than *matched,* filter since it changes depending upon the spanned sample times. See Section 2.7.5.

The reference target range delay $\tau_s(\cdot, t)$ incorporates *additional parameters* (represented by the dot) which are relevant to the situation of interest. In the stripmapping SAR case, for example, they could be the moving target's range and azimuthal velocities. (This is a more general approach than the ambiguity function theory discussed in Section 2.4.) $a_s(t)$ is a normalising version of $a(t)$; an optional amplitude weighting term is assumed to be unity. (Weights are considered for moving target detection in Section 4.3 and reducing imaging sidelobes in Section 6.4.2.) An additional amplitude masking term may be used to incorporate multilook processing (the effects of which are discussed in (Ouchi 1985)).

Using Equations (3.5), (3.6) and (3.7),

$$z(\cdot, m, w) = \tilde{\rho} \sum_n \sum_p b(t_p)\, \bar{\delta}(mT_r + t_n - t_p - \tau(t_p)) \sum_q b_s^*(t_q)\, \bar{\delta}(-w + mT_r + t_n - t_q - \tau_s(t_q)),$$

where $b(t_p) = a(t_p)\, e^{-j2\pi f_c \tau(t_p)}$ and $b_s(t_q) = a_s(t_q)\, e^{-j2\pi f_c \tau_s(\cdot, t_q)}$. $z(\cdot, m, w)$ will be zero unless the absolute values of the arguments of both $\bar{\delta}(\cdot)$ functions are less than $\Delta r/(2c)$ (Equation (3.3)).

Taking the argument of the first one, we have $|mT_r - \tau(t_p) + t_n - t_p| < \Delta r/(2c)$. We know that the difference between any two transmission times $t_n - t_p$ is much greater than both $mT_r - \tau(t_p)$ and $\Delta r/(2c)$, since range ambiguity has been avoided. Therefore, the expression can only be nonzero when $t_n = t_p$.

Therefore, $\bar{\delta}(mT_r + t_n - t_p - \tau(t_p))$ may be written in the form $\bar{\delta}(mT_r - \tau(t_p))\, \delta(t_n - t_p)$.

Hence, using

$$\sum_n \sum_p x(f(n), f(p))\ \delta(f(n) - f(p)) = \sum_n x(f(n), f(n)) \tag{3.8}$$

for $f(n) \neq f(p)$ when $n \neq p$,

$$z(\cdot, m, w) = \tilde{\rho} \sum_n \sum_q b(t_n)\, b_s^*(t_q)\, \bar{\delta}(mT_r - \tau(t_n))\, \bar{\delta}(mT_r - \tau_s(t_q) + t_n - t_q - w).$$

For this to be nonzero, $|mT_r - \tau_s(t_q) + t_n - t_q - w| < \Delta r/(2c)$. This happens when $t_q = mT_r - \tau_s(t_q) + t_n - w \pm \Delta r/(2c)$, allowing $z(\cdot, m, w)$ to be simplified according to Equation (3.8) again — $\bar{\delta}(\cdot) \approx \delta(\cdot)$. The fact that $b_s(t_q)$ (the slow time azimuthal chirp) changes slowly relative to $\tau_s(t_q)$ (the fast time range delay) implies that

$$b_s\left(mT_r - \tau_s(t_q) + t_n - w \pm \Delta r/(2c)\right) \approx a_s(t_n - w)\, e^{-j2\pi f_c \tau_s(\cdot, t_n - w)}.$$

Therefore, we have

$$z(\cdot, m, w) \;=\; \tilde{\rho}\, \chi'(\cdot, m, w),$$

where

$$\chi'(\cdot, m, w) \;=\; \sum_n a(t_n)\, a_s(t_n - w)\; e^{j2\pi f_c[\tau_s(\cdot, t_n - w) - \tau(t_n)]}\; \bar{\delta}(mT_r - \tau(t_n)).$$

$z(\cdot, m, w)$ has a peak magnitude of $|\tilde{\rho}|$ when the filter parameters match those of the target.

If $\bar{\delta}(t)$ is given by Equation (3.3), $\chi'(\cdot, m, w)$ is nonzero when $\tau(t_n)$ is within the range $mT_r c \pm \Delta r/2$. The expression therefore incorporates both range resolution and range migration effects, the latter of which is important when $\tau(t)$ varies markedly with time.

If it is assumed that the range resolution is sufficiently low that there is no moving target range migration during the integration time, we have the important ambiguity function

$$\boxed{\chi'(\cdot, w) \;=\; \sum_{n=0}^{N-1} a(t_n)\, a_s(t_n - w)\, e^{j2\pi f_c[\tau_s(\cdot, t_n - w) - \tau(t_n)]}.} \tag{3.9}$$

Any moving target parameters found from this data may be applied to the full resolution data set afterwards (Barbarossa 1992b, page 80).

This expression is more general for dealing with a time varying, arbitrary $\tau_s(\cdot, t)$ than that obtained by Lush and Hudson (1992), who analyse the AF by using a piecewise approximation to the range delay.

It is also more general than the chirp transform discussed by Wang et al. (1996) as it incorporates arbitrary amplitude variations, geometry and timing. In addition, Wang et al. (1996) implicitly assumes that the PRF is sufficiently high to sample the spectrum of the moving target unambiguously.

3.2.4 SAR Geometry

The radar is assumed to travel in a straight line at a constant altitude and constant, nonzero velocity v_p, directing its antenna towards a flat, stationary earth, as shown in Figures 3.2 and 3.3. (If this model is inaccurate, then the data will be assumed to have been compensated so the approximation can be made.) It is imaging the area at slant range[3] R. A reference target is at position (R_s, y_s) with velocity $(\dot{R}_s, \dot{y}_s)$ and acceleration $(\ddot{R}_s, \ddot{y}_s)$. It is assumed that the

[3]The range R is *slant range* in the plane of the radar-target line of sight, not *ground range* R_g, which is the distance between the target and the point on the ground directly below the radar. Note that they can easily be

reflectivity of the target does not vary during the imaging process, and that the target's motion is known. (Lush and Hudson (1992) discuss the effects of non-uniform target motion on the response of a radar with a large time-bandwidth product.)

Using Pythagoras's theorem, the distance to a modelled moving target at $(R, 0)$ is given by

$$d(t) = \left[(R + \dot{R}t + \ddot{R}t^2/2)^2 + (\dot{y}t + \ddot{y}t^2/2 - v_p t)^2\right]^{1/2} \tag{3.10}$$

(for example, (Raney 1971, Wehner 1995)).

Note that a time delay of w is equivalent to displacing the target a distance $y = v_p w$ in azimuth, so y is incorporated using $d(t - y/v_p)$.

Substituting Equation (3.10) and its equivalent for $d_s(t)$ into Equation (3.2) and Equation (3.9) along with an appropriate antenna pattern yields a very general SAR azimuthal moving target AF which can be applied to spotlight, squint and broadside stripmap imaging scenarios.

3.2.5 *Stripmapping SAR Ambiguity Function*

In the broadside stripmap case with a narrow antenna beam, Equation (3.10) may be simplified using a second order Maclaurin expansion (Equation (2.7)) to give

$$d(t) \approx R + \dot{R}t + \ddot{R}t^2/2 + \frac{(\dot{y}t + \ddot{y}t^2/2 - v_p t)^2}{2(R + \dot{R}t + \ddot{R}t^2/2)},$$

which simplifies to

$$d(t) \approx R + \dot{R}t + \frac{1}{2}\left[\ddot{R} + \frac{1}{R}(\dot{y} - v_p)^2\right] t^2. \tag{3.11}$$

(for example, (Wehner 1995)) since $\ddot{y}t$ is negligible when compared with v_p and $\dot{R}t + \ddot{R}t^2/2$ is negligible when compared with R. This gives rise to the well known Doppler centroid and rate expressions (Equations (2.11) and (2.12)).

The time varying amplitude of the received signal $a(t)$ is now given by the radar's two-way

---

expressed in terms of each other for the flat earth case using

$$R = \sqrt{h^2 + R_g^2},$$

where h is the altitude of the radar. Slant range is therefore used throughout this thesis without loss of generality.

antenna beam pattern, which can be approximated by

$$a(t;R) \;=\; \left\{ \begin{array}{ll} 1, & |t| \leq T/2, \\ 0, & \text{otherwise}, \end{array} \right\} \tag{3.12}$$

where $T = T(R) = R\theta_{ra}/v_p$ is the time taken for the SAR platform to travel the width of the real antenna beam, θ_{ra} is the small horizontal beamwidth of the real antenna. This assumes a wider main beam than Equation (2.3). ($a(\cdot)$ ignores the target's motion, making the assumption that $\dot{y}$, $\dot{R}$ and $\int \ddot{R}\,dt \ll v_p$, which is reasonable for ground based targets.) This approximation is invalid for SARs with large beamwidths, *e.g.* (Soumekh 1995).

If the modelled target is stationary, and the reference target is moving as previously described, we have from Equations (3.11), (3.2) and (3.9) the stripmapping SAR AF

$$\begin{aligned} &\chi'(R_s, \dot{R}_s, \ddot{R}_s, y_s, \dot{y}_s; R, \{t_n\}, v_p, \lambda) \;= \\ &\quad \sum_n a(t_n;R)\, a(t_n - y_s/v_p; R_s) \cdot \\ &\qquad \exp\!\left(j2\frac{2\pi}{\lambda} \left[R_s - R + \dot{R}_s \left(t_n - \frac{y_s}{v_p} \right) + \right.\right. \\ &\qquad\quad \left.\left. \frac{1}{2} \left(\ddot{R}_s + \frac{1}{R_s}(\dot{y}_s - v_p)^2 \right) \left(t_n - \frac{y_s}{v_p} \right)^2 - \frac{v_p^2}{2R} t_n^2 \right] \right). \end{aligned} \tag{3.13}$$

Interestingly, Equation (3.13) can be written in terms of a generalisation of the classical asymmetric cross AF (Equation (2.16)) with a Doppler rate term, known here as the 'extended ambiguity function',

$$\chi'_{s(t),r(t)}(\tau, \phi, \phi') \;=\; \int_{-\infty}^{\infty} s(t)\, r^*(t-\tau)\, e^{-j2\pi(\phi t + \phi' t^2)}\, dt, \tag{3.14}$$

as shown on the next page. (This result assumes that the target's return has been sampled by the radar at the correct times $(t_n + \tau)$.) In this formulation, the stationary target's slow time response $s(t;R)$ takes the place of the radar's transmitted signal in the conventional use of $\chi'(\cdot)$, and the moving target aspects are confined to the phase terms. This is known here as the 'extended cross-ambiguity function.' Note that if the range of the moving target is known, so $R = R_s$, then $s(t) = r(t)$, and the cross-ambiguity function becomes equivalent to the (auto-) ambiguity function.

If it is too difficult to work with the extended cross AF, the conventional Woodward equations, Equations (2.15) and (2.16), are still useful: ϕ' (Equation (3.18)) becomes zero for

$$\chi'_{az}(\psi,\tau,\phi,\phi';R,R_s,\{t_n\}) = e^{-j2\pi\psi}\,\chi'_{s(t;R),r(t;R_s)}(\tau,\phi,\phi'), \tag{3.15}$$

where

$$\begin{aligned}
\tau &= y_s/v_p,\\
s(t;R) &= \sum_n a(t;R)\exp\left(-j\frac{4\pi}{\lambda}\left[R+\frac{v_p^2}{2R}t^2\right]\right)\delta(t-t_n),\\
r(t;R_s) &= \sum_n a(t;R_s)\exp\left(-j\frac{4\pi}{\lambda}\left[R_s+\frac{v_p^2}{2R_s}t^2\right]\right)\delta(t-t_n),
\end{aligned} \tag{3.16}$$

$$\begin{aligned}
\psi &= \frac{2y_s}{\lambda v_p}\left\{\dot{R}_s-\frac{y_s}{2v_p}\left[\ddot{R}_s+\frac{\dot{y}_s}{R_s}(\dot{y}_s-2v_p)\right]\right\},\\
\phi &= \frac{2}{\lambda}\left\{\frac{y_s}{v_p}\left[\ddot{R}_s+\frac{\dot{y}_s}{R_s}(\dot{y}_s-2v_p)\right]-\dot{R}_s\right\}
\end{aligned} \tag{3.17}$$

and

$$\phi' = -\frac{1}{\lambda}\left[\ddot{R}_s+\frac{\dot{y}_s}{R_s}(\dot{y}_s-2v_p)\right]. \tag{3.18}$$

---

a range acceleration and azimuthal velocity of zero, so Equation (3.14) becomes equivalent to Equation (2.16). Range velocity may still be investigated since it influences the ϕ term (Equation (3.17)). The properties of Equation (3.14) with $r(t) = s(t)$ are listed in Appendix A.

It is important to notice that, although there is an apparent similarity between Equation (3.15) and the conventional radar ambiguity function, there is a profound difference in its meaning. In the conventional interpretation, the radar signal $s(t)$ is under the direct control of the radar designer, and may be changed to achieve a desired ambiguity function. Here, $s(t)$ is out of our control, being a function of the imaging geometry. The only degree of freedom we have is choosing the radar's transmission times.

3.3 Depth of Focus

The depth of focus considers the amount by which the azimuthal focussing parameters can be in error and still achieve a focussed image. It is commonly used to determine the range variation over which a given azimuthal filter may be used.

Using Equation (3.13) with the unwanted parameters set to zero,

$$\chi'(R_s,0,0,0,0;R,\{t_n\},v_p,\lambda) = \sum_n a(t_n;R)\,a(t_n;R_s)\cdot \exp\left(j2\frac{2\pi}{\lambda}\left[R_s-R+\frac{v_p^2}{2}\left(\frac{1}{R_s}-\frac{1}{R}\right)t_n^2\right]\right).$$

The phase error at the edge of the filter must be less than ϵ. Then

$$|\text{maximum phase}| - |\text{minimum phase}| \leq \epsilon.$$

We take time t_n to be its maximum value, which is $\frac{R\theta_{ra}}{2v_p}$ at the edge of the antenna beam. We have

$$2\pi\frac{v_p^2}{\lambda}\left(\frac{R-R_s}{R_sR}\right)\cdot\left(\frac{R\theta_{ra}}{2v_p}\right)^2 - 0 \leq \epsilon.$$

Since $R_s \approx R$, and letting $\delta R = R - R_s$,

$$\delta R \leq \frac{2\epsilon}{\pi}\frac{\lambda}{\theta_{ra}^2}.$$

Since the azimuthal resolution $\rho_{sa} = \frac{1}{2}\frac{\lambda}{\theta_{ra}}$, and letting $\epsilon = \pi/4$, an azimuthal compression filter may be used over the range extent

$$\delta R \leq \frac{2\rho_{sa}^2}{\lambda},$$

which is the standard result (*e.g.* (Curlander and McDonough 1991, page 173)), corresponding to a 0.3 dB power reduction.

3.4 Moving Target Focussing

Equation (3.13) results from the cross correlation between the azimuthal returns from stationary and moving targets. The more general ambiguity function for an arbitrarily positioned moving target requires a more general version of Equation (3.9) with both $\tau_s(\cdot)$ and $\tau(\cdot)$ having moving target parameters. Then Equation (3.9) takes the form shown in Equation (3.19), where $\boldsymbol{\theta}$ is a vector containing the reference target's parameters $[R, \dot{R}, \ddot{R}, y, \dot{y}]^T$. $\boldsymbol{\theta}_0$ is a vector containing the parameters of the modelled target, $[R_0, \dot{R}_0, \ddot{R}_0, y_0, \dot{y}_0]^T$.

$$\chi'_{az}(\boldsymbol{\theta};\boldsymbol{\theta}_0,\{t_n\},v_p,\lambda) = \sum_{n=-\infty}^{\infty} a(t_n - y_0/v_p; R_0)\, a(t_n - y/v_p; R) \cdot \exp\left\{ j2\frac{2\pi}{\lambda}\left[R - R_0 - \frac{y}{v_p}\left(\dot{R} - \frac{\ddot{R}y}{2v_p}\right) + \frac{y_0}{v_p}\left(\dot{R}_0 - \frac{\ddot{R}_0 y_0}{2v_p}\right) + \frac{y^2}{2R}\left(1 - \frac{\dot{y}}{v_p}\right)^2 - \frac{y_0^2}{2R_0}\left(1 - \frac{\dot{y}_0}{v_p}\right)^2 + \left[\dot{R} - \dot{R}_0 - \frac{\ddot{R}y}{v_p} + \frac{\ddot{R}_0 y_0}{v_p} + \frac{y}{R}\left(1 - \frac{\dot{y}}{v_p}\right)(\dot{y} - v_p) - \frac{y_0}{R_0}\left(1 - \frac{\dot{y}_0}{v_p}\right)(\dot{y}_0 - v_p)\right] t_n + \frac{1}{2}\left[\ddot{R} - \ddot{R}_0 + \frac{1}{R}(\dot{y} - v_p)^2 - \frac{1}{R_0}(\dot{y}_0 - v_p)^2\right] t_n^2 \right] \right\} \quad (3.19)$$

3.4.1 *Linearity*

It is important to know the extent to which Equation (3.19) can be approximated by Equation (3.13), so only the relative positions, velocities and accelerations of the moving target and the filter need to be considered. For example, is focussing a target with $\dot{R} = 6\,\text{m/s}$ using a filter adjusted for an $\dot{R}_0 = 5\,\text{m/s}$ the same as focussing a target with $\dot{R} = 1\,\text{m/s}$ using a ground-focussing filter? If so, it is only necessary to use Equation (3.13) when analysing range velocity effects. If not, it would be more difficult to investigate the effects of non-uniform sampling on the range velocity response, for example.

Linearity was investigated by testing to see if $\chi'_{az}(\boldsymbol{\theta} + \boldsymbol{\theta}_1; \boldsymbol{\theta}_0 + \boldsymbol{\theta}_1, \{t_n\}, v_p, \lambda) = \chi'_{az}(\boldsymbol{\theta}; \boldsymbol{\theta}_0, \{t_n\}, v_p, \lambda)$, where $\boldsymbol{\theta}$ is a vector containing the moving target's parameters.

There were non-linear effects with most of the parameters. The deviations from zero are summarised in Table 3.1. (Phase terms are unimportant since it is the magnitude of the AF which is of concern.) It appears that target range and azimuthal velocities, the main parameters of interest, may be considered to be linear for the purposes of this thesis. Therefore, the use of a stationary target as a reference is justified.

3.4.2 *Unique Identifiability*

An important consideration of an ambiguity function is whether or not an output peak corresponds to a unique set of parameters. (The term 'ambiguity' refers to the idea that it may not.) This will now be addressed in terms of the signals used to form the ambiguity function.

The modelled target has the five unknown parameters $R_0, \dot{R}_0, \ddot{R}_0, y_0$ and $\dot{y}_0$. (Azimuthal acceleration contributes only to a third order phase term, which was discounted from the ambiguity function.)

Parameter	t_n coefficient			Comment
	Phase	t_n	t_n^2	
R	—	—	—	Assumed to be matched by the range compression.
$\dot{R}$	$\frac{4\pi}{\lambda}\dot{R}_1(y_0 - y)$	0	0	*i.e.*, linear apart from phase.
$\ddot{R}$	$\frac{2\pi}{\lambda}\frac{\ddot{R}_1}{v_p^2}[y^2 - y_0^2 + 2y_1(y - y_0)]$	$\frac{4\pi}{\lambda}\frac{\ddot{R}}{v_p}(y_0 - y)$	0	
y	—	—	—	A time shift of $-y_1/v_p$ compensates for a shift in azimuthal position of y_1 for a stationary target and a uniform PRI. A non-uniform PRI implies a dependence upon position.
$\dot{y}$	≈ 0	≈ 0	≈ 0	Small errors only, provided that $\dot{y}, \dot{y}_0 \ll v_p$.

Table 3.1: Ambiguity function errors resulting from the non-linear effects of target motion.

However, the azimuthal chirp corresponding to a moving target has only four independent parameters: magnitude, initial phase, Doppler and Doppler rate. The phase is useless since it depends upon the exact range of the scatterer, which cannot be found to a fraction of a wavelength by range compression. In addition, it is extremely sensitive to minor variations in target motion, since a 360° phase change corresponds to a change in distance of only a few centimetres at X-band. There will therefore be inherent ambiguities unless some assumptions are made.

Due to range compression, the range R_0 is known to reasonable accuracy (several metres, say). This is sufficient to justify the assumption that $R = R_0$ when correlation processing.

The moving target's azimuthal position y_0 may be estimated using the magnitude information in the target's azimuthal response: the greatest correlation will occur when the moving target is broadside to the radar's antenna.

If the moving target's range acceleration is assumed to be zero, there are two remaining unknowns: range velocity and azimuthal velocity. It is possible to estimate these from the Doppler and Doppler rate measurements; indeed, they are independent to first order (Equations (2.11) and (2.12)). However, there is a coupling between the two; see Section 3.5.1.

If the range acceleration were assumed to be zero when in fact it wasn't, the range and azimuthal velocity estimates obtained by correlation processing would be biased. This correlation is modelled by the ambiguity function, Equation (3.19), which will peak when the coefficients of t_n and t_n^2 are made equal to zero, as stated by extended ambiguity function

property 6 in Appendix A. Instead of $\hat{\dot{y}} = \dot{y}_0$ and $\hat{\dot{R}} = \dot{R}_0$, the estimates would be

$$\hat{\dot{y}} = v_p - \sqrt{(v_p - \dot{y}_0)^2 + R_0\ddot{R}_0}$$

and

$$\begin{aligned}\hat{\dot{R}} &= \dot{R}_0 - \frac{\ddot{R}_0 y_0}{v_p} - \frac{y}{R_0}(1 - \dot{y}/v_p)(\dot{y} - v_p) + \frac{y_0}{R_0}(1 - \dot{y}_0/v_p)(\dot{y}_0 - v_p) \\ &= \dot{R}_0 + \frac{1}{R_0 v_p}[(y_0 + y)(v_p - \dot{y})^2 - 2y_0(v_p - \dot{y}_0)^2]\end{aligned}$$

(using the fact that $\dot{y} < v_p$). Note that $\hat{\dot{y}}$ is extremely sensitive to range acceleration, as it is multiplied by the range.

Parameters other than just $\dot{R}$ and $\dot{y}$ may be estimated if other measurements are obtained or other assumptions are made. For example, a target's direction may be known, since it may be known which road it is travelling along. In that case, its range acceleration may be estimated, or its azimuthal position may be estimated more accurately than would otherwise be possible. The position of the road itself may also be taken into consideration, assisting with the determination of y (see Chapter 5). However, it is assumed here that no information other than the azimuthal measurement is available.

3.4.3 *Squint Mode*

As an aside, the broadside moving target ambiguity function (Equation (3.19)) may be applied to the situation where the antenna is pointed away from broadside (*i.e.*, squint mode). This is because the response of a stationary squint mode target is approximately the same as that of a moving, broadside target when the antenna beamwidth is small (Yang and Soumekh 1992, Yang and Soumekh 1993).

The distance to a stationary, squint mode target with minimum range R_ϕ in the direction ϕ is given by:

$$d_\phi(t) = \sqrt{R_\phi^2 + v_p^2\left(t - \frac{R_\phi \phi}{v_p}\right)^2}.$$

A Taylor expansion of this about the beam's centre, $t = \frac{R_\phi \phi}{v_p}$, has been found as a polynomial in t. (The details have been omitted for brevity.)

A Legendre series expansion for the distance to a moving target, Equation (3.10), has also been found as a polynomial in t.

Equating the coefficients of these polynomials results in equivalents for the moving target parameters in the stationary, squint case:

$$\begin{aligned} R &= R_\phi \left(1 + \frac{\phi^2}{2} - \frac{\phi^4}{8}\right), \\ \dot{R} &= v_p \phi \left(\frac{\phi^2}{2} - 1\right) \\ \ddot{R} &= \frac{v_p^2}{R}\left(1 - \frac{3}{2}\phi^2\right) - \frac{v_p^2}{R\left(1 + \frac{\phi^2}{2} - \frac{\phi^4}{8}\right)}. \\ \dot{y} &= 0. \end{aligned}$$

Therefore, Equation (3.19) is capable of modelling more than just broadside scenarios.

Yang and Soumekh (1992), (1993) use this concept (but not this formulation) to focus moving targets as if they were stationary, squint mode targets.

3.5 Uniform PRI

This section discusses the effects of uniform sampling on the ambiguity function with respect to the target's parameters.

3.5.1 Azimuthal Position/Range Velocity

A pronounced SAR moving target effect is that of the azimuthal position/range velocity ambiguity (Raney 1971). This can be investigated by considering the magnitude of Equation (3.13) as a function of azimuth y_s and range velocity $\dot{R}_s$, with range acceleration $\ddot{R}_s$ and azimuthal velocity $\dot{y}_s$ set to zero, and the range terms matched ($R = R_s$). Setting the range, SAR platform velocity v_p and wavelength λ to realistic values results in the ambiguity function shown in Figure 3.4 when a uniform PRI is used.

The function has a series of diagonal stripes whose amplitudes are shown in Figure 3.5. (The shapes of these curves are governed by the crosscorrelation of the two-way antenna pattern and the filter's weighting function.) This means that a target moving in range, whose other parameters are matched to those of the azimuthal filter, may appear displaced from its true position, and multiple targets whose Doppler frequencies are subsampled by the PRF may appear in the same place. In fact, targets generally appear in two places: once inside the azimuthal coverage of the antenna beam, and once outside. (This phenomenon—the appearance of a target when it wasn't illuminated by the radar—is due to a correlation

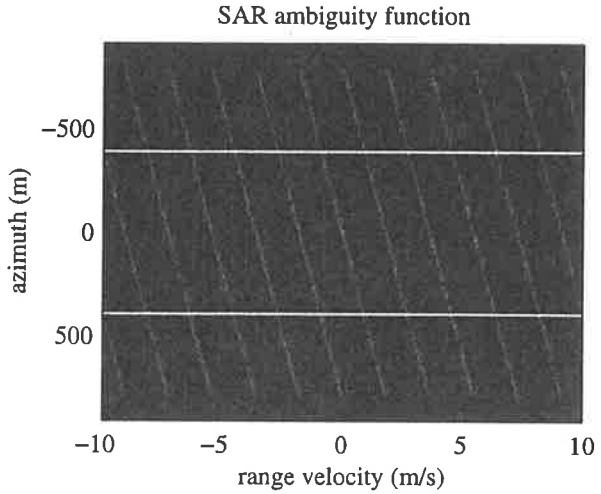

Figure 3.4: The log magnitude of the azimuthal ambiguity function of a broadside looking stripmapping SAR where the reference target's range velocity and azimuthal position are varied. The horizontal lines show the azimuthal extent of the antenna beam. Range is 30 km, antenna horizontal beamwidth 1.5°, wavelength 3.2 cm, platform velocity 70 m/s and PRF 114 Hz (the minimum); 11.3 s integration times. The dynamic range is 60 dB.

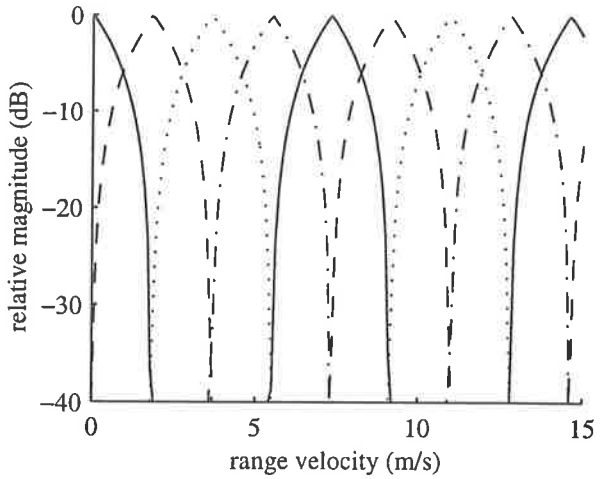

Figure 3.5: The magnitude of the ambiguity function evaluated along the diagonal lines shown in Figure 3.4. (These are described by Equation (3.21).)

between the target's return and the corresponding filter.)

Equation (3.13) reduces to

$$\chi'(R_s, \dot{R}_s, 0, y_s, 0; R_s, nt_s, v_p, \lambda) = \exp\left(j2\frac{2\pi}{\lambda}\left[\frac{y_s^2}{2R_s} - \frac{\dot{R}_s y_s}{v_p}\right]\right) \cdot \sum_n a(t_n; R_s)\, a(t_n - y_s/v_p; R_s) \exp\left(j2\frac{2\pi}{\lambda}\left[\dot{R}_s - \frac{y_s v_p}{R_s}\right] nt_s\right)$$

where t_s is the sampling interval. The summed exponential term has maxima when

$$\frac{2}{\lambda}\left(\dot{R}_s - \frac{y_s v_p}{R_s}\right) t_s = m,$$

where m is an integer. A target with velocity $\dot{R}_s$ therefore has the apparent positions

$$y_s = \frac{R_s}{v_p}\left(\dot{R}_s + m\frac{\lambda}{2t_s}\right), \tag{3.20}$$

reversing the sign of the arbitrary m.

Using the minimum PRF which satisfies the Nyquist sampling requirements of the Doppler frequency at the antenna's 3 dB points, $1/t_s = 2v_p\theta_{ra}/\lambda$ (Equation (2.8)), Equation (3.20) becomes

$$y_s = \left(\frac{R_s\dot{R}_s}{v_p} + \frac{R_s\theta_{ra}}{2}\right) \bmod (R_s\theta_{ra}) - \frac{R_s\theta_{ra}}{2}, \tag{3.21}$$

as stated by Raney (1971) and given in the introductory chapter (Equation (2.14)). This equation describes the lines shown in Figure 3.4.

The overall worst case range velocity response is therefore given by the magnitude of Equation (3.13) evaluated along the diagonal lines shown in Figure 3.4 and described by Equation (3.21). This is shown in Figure 3.5.

A higher PRF than the minimum has the effect of moving the diagonal lines further apart horizontally, so the moving target may not appear at all in a ground-focussed image when the PRF is greater than $2/t_s$.

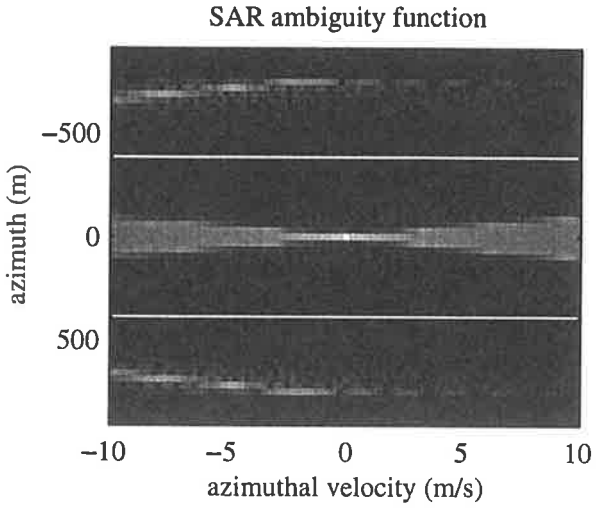

Figure 3.6: The log magnitude of the azimuthal ambiguity function where the reference target's azimuthal velocity and position are being varied.

3.5.2 *Azimuthal Position/Azimuthal Velocity*

As a function of just $\dot{y}$ and y, Equation (3.13) reduces to

$$\begin{aligned}
&\chi'(y, \dot{y}; R, \{t_n\}, v_p, \lambda) \\
&= \sum_n a(t_n; R)\, a(t_n - y/v_p; R)\, \exp\left(j2\frac{2\pi}{\lambda}\frac{1}{R}\left[(\dot{y} - v_p)^2(t_n - y/v_p)^2 - v_p^2 t_n^2\right]\right) \\
&= \sum_n a(nt_s; R)\, a(nt_s - y/v_p; R) \cdot \\
&\qquad \exp\left(j2\frac{2\pi}{\lambda}\frac{1}{R}\left[(\dot{y} - v_p)^2(nt_s - y/v_p)^2 - v_p^2 (nt_s)^2\right]\right)
\end{aligned} \tag{3.22}$$

for uniform sampling with interval t_s, assuming that $|\dot{y}| \ll v_p$ (and omitting the $_s$ subscripts for clarity). Range velocity and acceleration have been set to zero and $R = R_s$.

Figure 3.6 shows the magnitude of Equation (3.22) in two dimensions. Range, SAR platform velocity and wavelength parameters were set to the same values as for Figure 3.4. Figure 3.7 shows cross sections of Figure 3.6 along the azimuthal plane. The lines are separated by azimuthal velocity increments of 0.4 m/s. The defocussing of the scatterer as the azimuthal speed is increased is clearly visible.

3.6 Non-Uniform PRI

Figure 3.8 shows the magnitude of Equation (3.13) under similar conditions as the plot of Figure 3.4, except that the transmission intervals have been displaced from uniform by 20% using

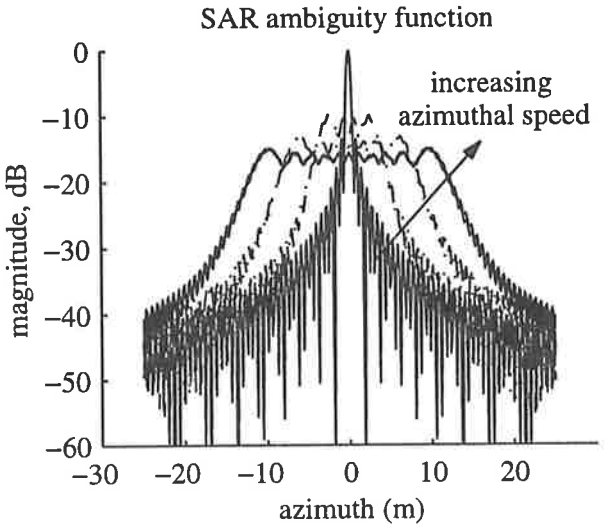

Figure 3.7: The log magnitude of the azimuthal ambiguity function where the reference target's azimuthal velocity and position are being varied. The curves differ by azimuthal velocity increments of 0.4 m/s.

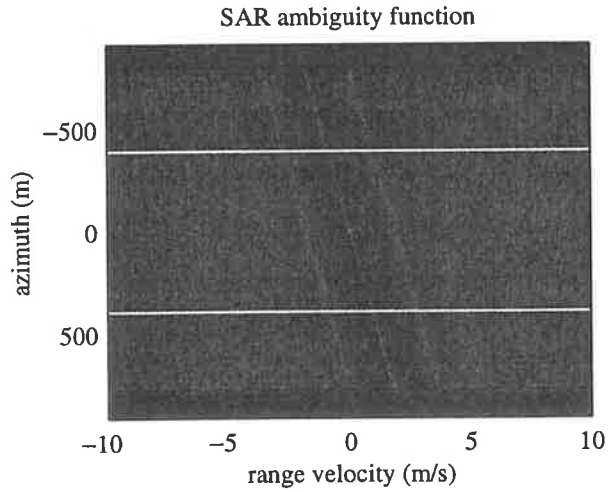

Figure 3.8: The log magnitude of the azimuthal ambiguity function with a non-uniform pulse repetition interval. Parameters are the same as for Figure 3.4.

a uniform distribution (Section 2.7.6). It can clearly be seen that the diagonal position/velocity ambiguity pattern evident in Figure 3.4 has been destroyed where $m \neq 0$ in Equation (3.20).

Figure 3.9 shows the magnitude of Equation (3.13) evaluated along the diagonal lines described by Equation (3.21) in a similar fashion to Figure 3.5. The non-uniform PRI has clearly made the AF more closely approximate the ideal thumbtack, permitting moving targets' parameters to be determined unambiguously. (Here, the main lobe occurs when the moving target parameters correspond to those of the reference stationary target, *i.e.* $\dot{R}_s = 0$ m/s.) The effect of the non-uniform PRI on the main lobe has been negligible.

The moving target/stationary target mismatch appears to be a stepwise function; this is

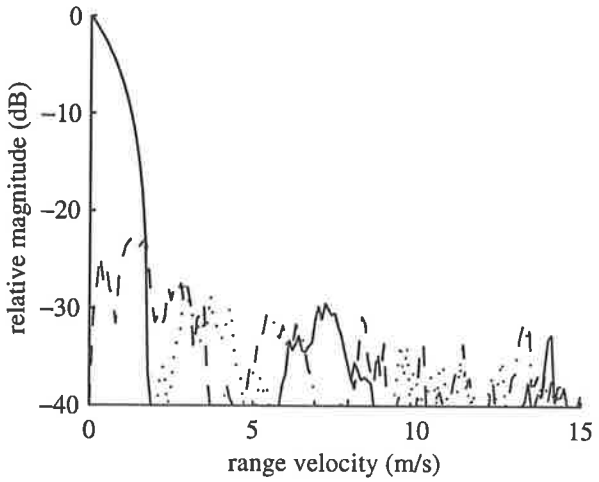

Figure 3.9: The magnitude of the non-uniform transmission time ambiguity function evaluated along the diagonal lines shown in Figure 3.4.

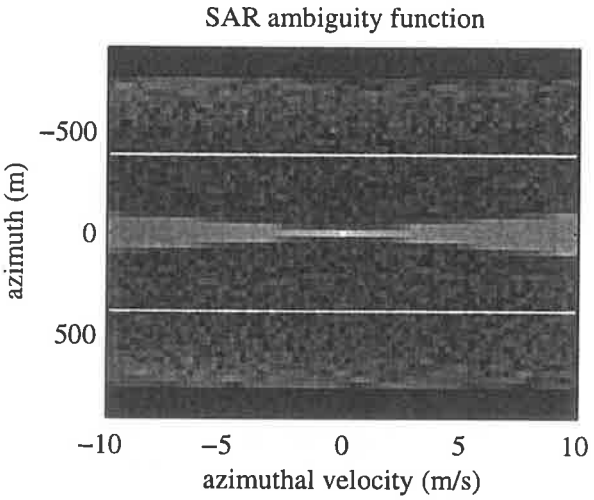

Figure 3.10: The log magnitude of the azimuthal ambiguity function with a non-uniform pulse repetition interval. Parameters are the same as for Figure 3.6.

similar to Bilinskis and Mikelsons's alias suppression plot (Bilinskis and Mikelsons 1992, page 86), which shows the level of aliases as a function of the ratio between the signal frequency and the sampling frequency.

Ideally, if the target's signal were completely defocussed, its energy would be divided equally among all of the azimuthal cells in a synthetic aperture, N. Compared with ideal focussing, where this energy is concentrated into one cell, this is an energy suppression S of $20\log_{10}(N)$ dB. For the figures used in this example, $N \approx 1300$, so $S \approx 62$ dB.

Figure 3.10 shows the magnitude of Equation (3.13) in a similar fashion to Figure 3.6, but with a non-uniform PRI. Figure 3.11 shows cross sections of Figure 3.10 in a similar fashion to Figure 3.7, but with a non-uniform PRI. Because these plots are so similar, it follows that

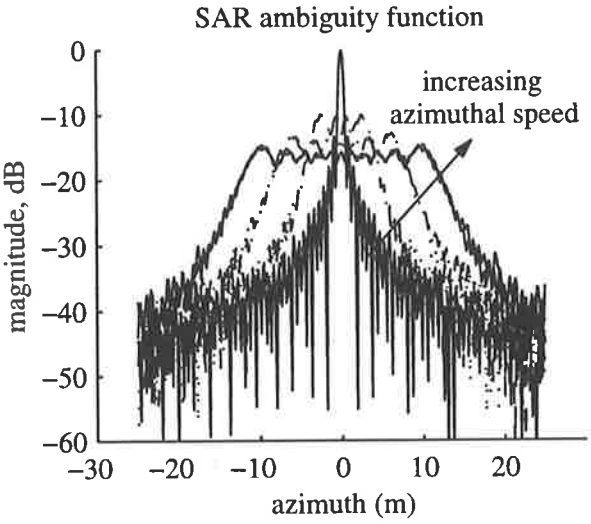

Figure 3.11: The log magnitude of the azimuthal ambiguity function with a non-uniform pulse repetition interval. Parameters are the same as for Figure 3.7.

the effects of the transmission times on the azimuthal velocity response is minimal. This is because the bandwidth occupied by the moving and stationary targets are similar.

3.6.1 The Effect of Two Staggered PRIs

It is instructive to compare the ambiguity function of a SAR with two sampling intervals with that of a conventional SAR.

For convenience, the AF in Equation (3.15) will be used with $s(t)$ (Equation (3.16)) written in the form

$$s(t) \;=\; \sum_n a(t)\, e^{-j2\pi(\psi' + \psi t^2)}\, \delta(t - t_n). \tag{3.23}$$

It is assumed that the moving target's range is approximately known, so that $r(t; R_s) \approx s(t; R)$.

Then, substituting Equation (3.23) and the equivalent $r(t)$ into Equation (3.14), we have

$$|\chi'_{az}(\psi, \tau, \phi, \phi'; \{t_n\})|^2 \;=\; |\chi'_{az}(\tau, \varepsilon, \phi'; \{t_n\})|^2 \;=\; \left|\sum_n a(t_n)a(t_n - \tau)e^{-j2\pi[\varepsilon t_n + \phi' t_n^2]}\right|^2 \tag{3.24}$$

where

$$\varepsilon \;=\; 2\psi\tau + \phi \tag{3.25}$$

can be thought of as a 'frequency' term, being the coefficient of t_n in the summed exponential. This term is of primary interest as it is the only one influenced by the range velocity.

For the purpose of this example, other parameters may take on assumed values:

- the antenna beam is assumed to be uniform, as specified by Equation (3.12).
- $\ddot{R}$ and $\dot{y}$ are assumed to be zero, so $\phi' = 0$ (Equation (3.18)).
- Only the amplitude of the main lobe of the synthetic antenna beam is considered here, so the AF is evaluated with $\tau = 0$.

Equation (3.24) may now be written

$$|\chi'_{az}(\varepsilon; \{t_n\})|^2 = \left| \sum_n e^{-j2\pi\varepsilon t_n} \right|^2.$$

One PRI For one PRI, $t_n = nt_s, n = 0, \ldots, N-1$ (Equation (2.19), neglecting the time centering on $t = 0$). N is chosen to be the number of transmissions which occur as the platform travels the width of the antenna beam's footprint on the ground. Then

$$\begin{aligned} |\chi'_1(\varepsilon)|^2 &= \left| \sum_{n=0}^{N-1} e^{-j2\pi\varepsilon n t_s} \right|^2 \\ &= \left| e^{-j\pi\varepsilon t_s(N-1)} \frac{\sin(\pi\varepsilon t_s N)}{\sin(\pi\varepsilon t_s)} \right|^2 \\ &= \left| \frac{\sin(\pi\varepsilon t_s N)}{\sin(\pi\varepsilon t_s)} \right|^2. \end{aligned} \tag{3.26}$$

For large N, this is $|\chi'_1(\varepsilon)|^2 \approx N^2\delta(\varepsilon - m/t_s)$.

Two PRIs Since the sampling order is arbitrary, the times with two intervals may be specified as two uniform sequences separated by the interval Δ, thus:

$$t_n = \begin{cases} 2nt_s, & n = 0, \ldots, N/2-1, \\ 2(n - N/2)t_s + \Delta & n = N/2, \ldots, N-1, \end{cases}$$

(assuming N is even), where $0 \leq \Delta < 2t_s$. Then, skipping some of the working,

$$\begin{aligned} |\chi'_2(\varepsilon; \Delta)|^2 &= \left| \sum_{n=0}^{N/2-1} e^{-j4\pi\varepsilon n t_s} + \sum_{n=N/2}^{N-1} e^{-j2\pi\varepsilon[2t_s(n-N/2)+\Delta]} \right|^2 \\ &= \left| e^{-j\pi\varepsilon t_s N} \left(e^{j2\pi\varepsilon t_s} + e^{j2\pi\varepsilon(t_s-\Delta)} \right) \frac{\sin(\pi\varepsilon t_s N)}{\sin(2\pi\varepsilon t_s)} \right|^2 \\ &= \left| 2e^{j\pi\varepsilon(2t_s - t_s N - \Delta)} \cos(\pi\varepsilon\Delta) \frac{\sin(\pi\varepsilon t_s N)}{\sin(2\pi\varepsilon t_s)} \right|^2 \end{aligned}$$

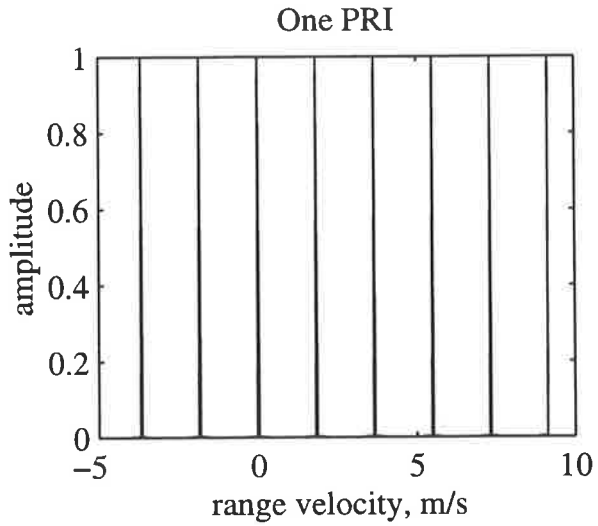

Figure 3.12: The normalised SAR azimuthal AF with one PRI plotted against range velocity.

$$\begin{aligned} &= 4\left|\cos(\pi\varepsilon\Delta)\,\frac{\sin(\pi\varepsilon t_s N)}{\sin(2\pi\varepsilon t_s)}\right|^2 \\ &\approx N^2\left|\cos(\pi\varepsilon\Delta)\right|^2\delta\left(\varepsilon-\frac{m}{2t_s}\right) \end{aligned} \tag{3.27}$$

for large N.

Of course, the single and two PRI formulations are equivalent if $\Delta = t_s$: applying the trigonometric identity

$$\sin(2\theta) \;=\; 2\,\sin(\theta)\,\cos(\theta),$$

to the denominator of Equation (3.27) allows the coefficient and cosine term to cancel, resulting in Equation (3.26).

Figure 3.12 shows the normalised *square root* of Equation (3.26) as a function of range velocity, using Equations (3.25) and (3.17) to convert between range velocity and ε. The range was 30 km, the radar velocity 70 m/s, the antenna beamwidth 1.15° and the wavelength 3.2 cm. The effects of aliasing are clearly present, with identical responses at velocities equal to half a wavelength per sample. This is the same as a horizontal cross section Figure 3.4 with an azimuth of zero.

Using Equation (3.27), normalised, with $\Delta = 0$ gives the response shown in Figure 3.13. The effective sampling rate is now half that of Figure 3.12, so that aliasing occurs at half the range velocity.

With $\Delta = 0.3t_s$, Figure 3.14, it is clear that the aliases shown in Figure 3.12 are being suppressed at the cost of allowing through some of those in Figure 3.13. The aliases clearly

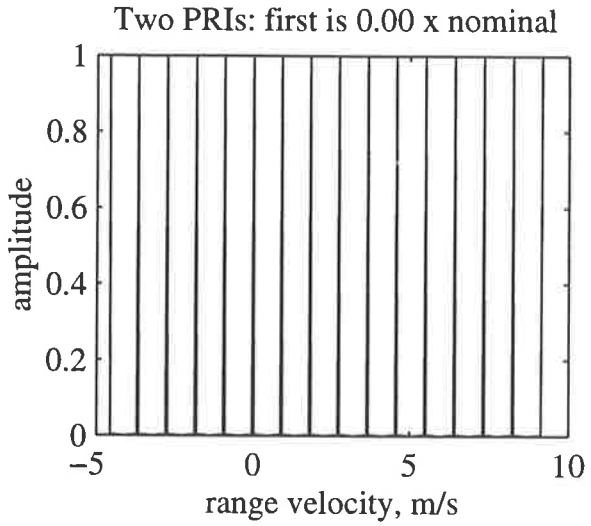

Figure 3.13: The normalised AF with superimposed sample times.

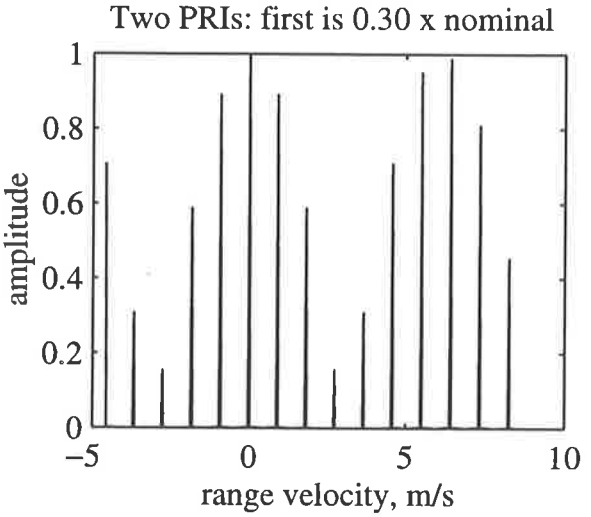

Figure 3.14: The normalised AF with two PRIs: the first is 0.3 $\times$ the nominal value.

have a cosinusoidal envelope, which is expected from Equation (3.27).

Having more PRIs permits these aliases to be suppressed to arbitrarily low levels, as discussed in Section 2.7.

Optimal Δ

The interval between the timing staggers, Δ, may be found to satisfy any criterion of interest. For example, if it were important to suppress the first alias at $\varepsilon = 1/t_s$, the relevant term inside Equation (3.27) is

$$\cos(\pi\Delta/t_s) \;=\; 0.$$

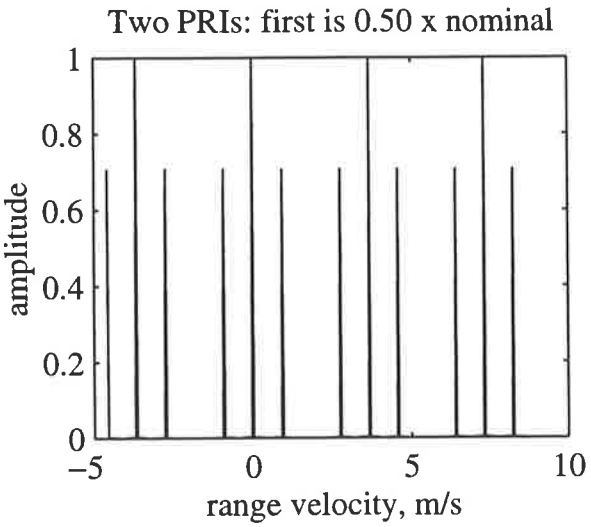

Figure 3.15: The normalised AF with two alternating PRIs: the first is 0.5 $\times$ the nominal value.

Then $\pi\Delta/t_s = \pi/2 + m\pi$, where m is an integer, so that

$$\Delta \;=\; t_s(m + 1/2).$$

Since $0 \leq \Delta < t_s$, the criterion is satisfied when $\Delta = t_s/2$. A normalised plot corresponding to this is shown in Figure 3.15. By comparing Figure 3.15 with Figure 3.12, it is clear that the odd aliases have been completely suppressed.

The AF with two PRIs, switched randomly, is discussed in Section 3.7.1.

3.7 The Ambiguity Function with Random Sampling

This section considers the *expected* ambiguity function given a distribution of sampling times, as opposed to the function obtained for a specific instance of a sampling scheme.

Using Equation (3.13), the expected AF is

$$\mathrm{E}_{\mathbf{T}}\left[\chi'(R_s, \dot{R}_s, \ddot{R}_s, y_s, \dot{y}_s; R, p_{\mathbf{T}}(\boldsymbol{t}), v_p, \lambda)\right] \;=$$
$$\exp\left(j2\frac{2\pi}{\lambda}\left[R_s - R - \dot{R}_s\frac{y_s}{v_p} + \frac{1}{2}\left(\ddot{R}_s + \frac{1}{R_s}(\dot{y}_s - v_p)^2\right)\frac{y_s^2}{v_p^2}\right]\right)\sum_{n=-\infty}^{\infty}\mathrm{E}_{\mathbf{T}}[x(t_n)], \quad (3.28)$$

where

$$\begin{aligned} x(t_n) &= a(t_n; R)\, a(t_n - y_s/v_p; R_s) \cdot \\ &\quad \exp\left(j2\frac{2\pi}{\lambda} \left[\left(\dot{R}_s - \frac{y_s}{v_p} \left(\ddot{R}_s + \frac{1}{R_s}(\dot{y}_s - v_p)^2 \right) \right) t_n + \right.\right. \\ &\quad \left.\left. \frac{1}{2} \left(\ddot{R}_s + \frac{1}{R_s}(\dot{y}_s - v_p)^2 - \frac{v_p^2}{R} \right) t_n^2 \right] \right), \end{aligned}$$

$p_{\mathbf{T}}(\boldsymbol{t})$ is the joint probability density function (PDF) of the sampling times which are stored in vector $\boldsymbol{t} = [t_1, t_2, \ldots, t_N]^T$, where N is the number of samples which occur during the time taken to travel the length of a synthetic aperture and the superscript ^{T} denotes the transpose operation.

We are normally interested in the *square* of the ambiguity function, rather than the function itself, to give a relative power: the phase is of no real interest. It is important to note that here we are finding the expected response, since it is the response which is exhibited by the radar.

So

$$\begin{aligned} \mathrm{E}_{\mathbf{T}}[\chi'(\cdot; p_{\mathbf{T}}(\boldsymbol{t}))] &= \exp(\cdot) \sum_{n=-\infty}^{\infty} \mathrm{E}_{\mathbf{T}}[x(t_n)] \\ &= \exp(\cdot) \sum_{n=-\infty}^{\infty} \int_{T_N} \cdots \int_{T_2} \int_{T_1} x(t_n)\, p_{T_1, T_2, \ldots, T_N}(t_1, t_2, \ldots, t_N) \\ &\qquad\qquad dt_1\, dt_2 \ldots dt_N, \\ &= \exp(\cdot) \sum_{n=-\infty}^{\infty} \int_{T_n} x(t)\, p_{T_n}(t)\, dt, \end{aligned} \tag{3.29}$$

if the sampling time PDFs are independent, and

$$\mathrm{E}_{\mathbf{T}}[\chi'(\cdot; p_T(t))] = N \exp(\cdot) \int_T x(t)\, p_T(t)\, dt, \tag{3.30}$$

if the PDFs are the same.

The expected AF for parameters of interest will now be considered with respect to several sampling PDFs. The imaging case may be found in Chapter 6.

3.7.1 Range Velocity/Azimuthal Position

Let $R = R_s$, $\ddot{R}_s = 0$ and $\dot{y}_s = 0$, so Equation (3.28) becomes a function of the target's range velocity and azimuthal position:

$$\begin{aligned}
&\mathrm{E}_{\mathbf{T}}\left[\chi'(\dot{R}, y; R, p_{\mathbf{T}}(\boldsymbol{t}), v_p, \lambda)\right] = \\
&\quad \exp\left(j2\frac{2\pi}{\lambda}\left[\frac{y^2}{2R} - \frac{\dot{R}y}{v_p}\right]\right) \cdot \\
&\quad \sum_n \mathrm{E}_{\mathbf{T}}\left[a(t_n)\, a(t_n - y/v_p)\, \exp\left(j2\frac{2\pi}{\lambda}\left[\dot{R} - \frac{yv_p}{R}\right] t_n\right)\right],
\end{aligned} \tag{3.31}$$

omitting the $_s$ subscripts for clarity.

Case 1: Uniformly Distributed Times

Suppose that the sampling PDFs are uniform:

$$p_{T_n}(t) = \begin{cases} 1/T, & -T/2 \le t \le T/2, \\ 0, & \text{otherwise}, \end{cases} \quad \forall n,$$

where $T = R\theta_{ra}/v_p$ is the time taken by the SAR platform to travel the length of the synthetic aperture, and that the antenna beam is uniform over the length of the aperture, as defined in Equation (3.12). Then, using Equation (3.30),

$$\begin{aligned}
&\mathrm{E}_T\left[\chi'(\dot{R}, y; R, p_T(t), v_p, \lambda)\right] \\
&= \begin{cases} \exp\left(j2\frac{2\pi}{\lambda}\left[\frac{y^2}{2R} - \frac{\dot{R}y}{v_p}\right]\right) \frac{N}{T} \int_{y/v_p - T/2}^{T/2} \exp\left(-j2\frac{2\pi}{\lambda}\left[\dot{R} - \frac{yv_p}{R}\right] t\right) dt, \\ \qquad\qquad 0 \le y \le R\theta_{ra}, \\ \exp\left(j2\frac{2\pi}{\lambda}\left[\frac{y^2}{2R} - \frac{\dot{R}y}{v_p}\right]\right) \frac{N}{T} \int_{-T/2}^{y/v_p + T/2} \exp\left(-j2\frac{2\pi}{\lambda}\left[\dot{R} - \frac{yv_p}{R}\right] t\right) dt, \\ \qquad\qquad -R\theta_{ra} \le y < 0, \\ 0, \qquad\qquad \text{otherwise}, \end{cases} \\
&= \begin{cases} \frac{N\lambda}{2\pi T\left(\dot{R} - \frac{yv_p}{R}\right)} \exp\left(-j\frac{2\pi}{\lambda}\frac{y\dot{R}}{v_p}\right) \sin\left(\frac{2\pi}{\lambda}\left[\dot{R} - \frac{yv_p}{R}\right]\left[T - \frac{y}{v_p}\right]\right), \\ \qquad\qquad -R\theta_{ra} \le y \le R\theta_{ra}, \\ 0, \qquad\qquad \text{otherwise}. \end{cases}
\end{aligned} \tag{3.32}$$

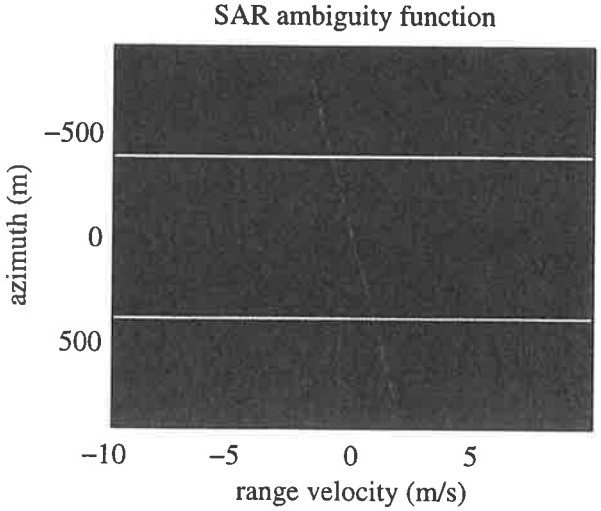

Figure 3.16: The log magnitude of the expected SAR AF; uniformly distributed sampling. Parameters are the same as for Figure 3.4.

(y's extent is twice that of the target's return to allow for overlap between the target response and the filter.)

Note that, as $\dot{R} \to yv_p/R$,

$$\mathrm{E}_T\left[\chi'(\dot{R}, y; R, p_T(t), v_p, \lambda)\right] \;\to\; \frac{N}{v_p T}\,(v_p T - y)\,\exp\!\left(-j\frac{2\pi}{\lambda}\frac{y^2}{R}\right),$$

providing a linear amplitude variation with y along the range velocity/azimuthal position ambiguity line described by Equation (3.20) with $m = 0$.

Figure 3.16 shows the normalised, squared magnitude of Equation (3.32) plotted as a function of azimuthal position and range velocity in a similar manner to Figure 3.4. All but the central diagonal line has been suppressed by the expectation operation.

Figure 3.17 shows the normalised, squared magnitude Equation (3.32) evaluated along the lines described by Equation (3.21), similarly to Figure 3.5 (although with a different vertical axis scale). These plots clearly demonstrate the dramatic alias suppression expected when uniformly distributed sampling times are used.

Case 2: Uniformly Distributed Offsets

This section considers using Equation (3.31) with a uniform beam pattern and uniformly distributed offsets (jitter) as discussed in the non-uniform sampling section (Section 2.7.6), so that

$$t_n \;=\; \left(n - 1 - \frac{N-1}{2}\right)t_s \;+\; \mathcal{U}(0, bt_s),\; n = 1, \ldots, N,$$

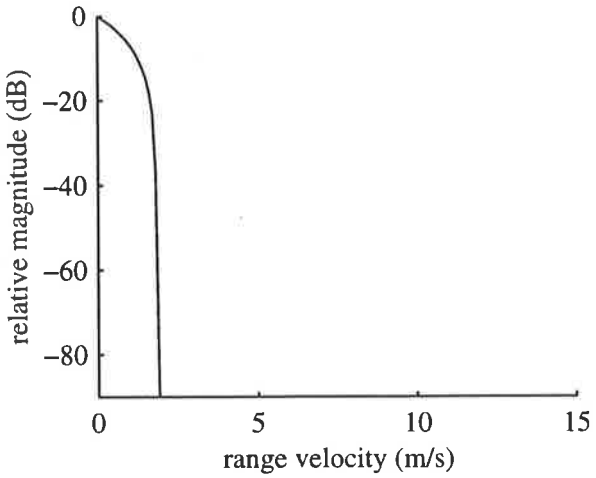

Figure 3.17: The magnitude of the expected ambiguity function for uniformly distributed sampling evaluated along the diagonal lines described by Equation (3.21).

where

$$\mathcal{U}_x(\mu, s) \triangleq \begin{cases} 1/(2s), & \mu - s \leq x \leq \mu + s, \\ 0, & \text{otherwise}, \end{cases}$$

for uniformly distributed offsets. Then

$$p_{T_n}(t) = \mathcal{U}([n - 1 - (N-1)/2]t_s, bt_s).$$

The measurement duration is then slightly greater than that with uniform sampling, since the PDFs of the extreme samples extend earlier and later than the respective nominal values. Their mean separation is the same, however.

Then, using Equation (3.29) we have

$$\begin{aligned} &\mathrm{E}_{\mathbf{T}}\left[\chi'(\dot{R}, y; R, p_{\mathbf{T}}(\boldsymbol{t}), v_p, \lambda)\right] \\ &= \exp\left(j2\frac{2\pi}{\lambda}\left[\frac{y^2}{2R} - \frac{\dot{R}y}{v_p}\right]\right)\frac{1}{2bt_s} \cdot \\ &\quad \sum_{n=1}^{N}\int_{(m-b)t_s}^{(m+b)t_s} a(t - y/v_p)\exp\left(j2\frac{2\pi}{\lambda}\left[\dot{R} - \frac{yv_p}{R}\right]t\right)dt, \end{aligned}$$

where $m = n - 1 - \frac{N-1}{2}$ and $a(t)$ has been assumed not to change over the interval $t_n \pm bt_s \; \forall n$.

The remaining antenna beam term may be incorporated by changing the summation:

$$\mathrm{E}_{\mathbf{T}}\left[\chi'(\dot{R}, y; R, p_{\mathbf{T}}(\boldsymbol{t}), v_p, \lambda)\right] = \begin{cases} \exp\left(j2\frac{2\pi}{\lambda}\left[\frac{y^2}{2R} - \frac{\dot{R}y}{v_p}\right]\right)\frac{1}{2bt_s}\sum_{m=m_1}^{m_2}\int_{(m-b)t_s}^{(m+b)t_s}\exp\left(j2\frac{2\pi}{\lambda}\left[\dot{R} - \frac{yv_p}{R}\right]t\right)dt, \\ \qquad\qquad -R\theta_{ra} \le y \le R\theta_{ra}, \\ 0, \qquad\qquad \text{otherwise,} \end{cases}$$

where $m_1 = (y/v_p - T/2)/t_s$ and $m_2 = T/(2t_s)$ for $0 \le y \le R\theta_{ra}$ and $m_1 = -T/(2t_s)$ and $m_2 = (y/v_p + T/2)/t_s$ for $-R\theta_{ra} \le y \le 0$.

After some arithmetic, this simplifies to

$$\mathrm{E}_{\mathbf{T}}\left[\chi'(\dot{R}, y; R, p_{\mathbf{T}}(\boldsymbol{t}), v_p, \lambda)\right] = \begin{cases} \exp\left(-j\frac{2\pi}{\lambda}\frac{\dot{R}y}{v_p}\right)\mathrm{sinc}\left(2\frac{2\pi}{\lambda}\frac{bt_s}{R}(yv_p - \dot{R}R)\right)\cdot \\ \qquad \frac{\sin\left(\frac{2\pi}{\lambda R v_p}(yv_p - \dot{R}R)([T + t_s]v_p - y)\right)}{\sin\left(\frac{2\pi}{\lambda}\frac{t_s}{R}(yv_p - \dot{R}R)\right)}, \\ \qquad\qquad -R\theta_{ra} \le y \le R\theta_{ra}, \\ 0, \qquad\qquad \text{otherwise,} \end{cases} \tag{3.33}$$

where $\mathrm{sinc}(x) \triangleq \sin(x)/x$.

When $b = 0$, indicating that there is no randomness to the sampling, the $\mathrm{sinc}(\cdot)$ term becomes 1 and Equation (3.33) is identical to the uniform sampling case.

When $b = 0.5$, the largest it can sensibly be, Equation (3.33) is identical to the result for the uniformly distributed times, except for an antenna beamwidth of $v_p(T + t_s)$ rather than v_pT. This is due to the extra integration period obtained using the extra $t_s/2$ terms at the start and finish of the integration period. (The results are similar since a definite integral results in the difference between the terms given by the indefinite integral evaluated at the two limits. When such definite integrals are summed, and the upper limit is equal to the lower limit at the next stage in the summation, the results cancel, resulting in the equivalent of a single definite integral evaluated at the extremes of the summation.)

Figure 3.18 shows the normalised, squared magnitude of Equation (3.33) plotted as a function of azimuthal position and range velocity for $b = 0.2$. All but the central diagonal line have been partially suppressed. However, the plot clearly shows higher sidelobes than the example using an instance of random intervals, Figure 3.8.

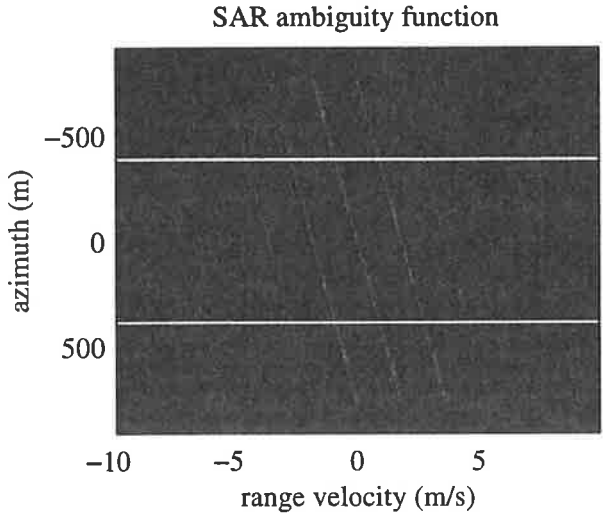

Figure 3.18: The log magnitude of the expected SAR AF; uniformly distributed offsets of $0.2t_s$. Parameters are the same as for Figure 3.4.

Randomly Switched Staggering

Rather than have arbitrarily valued random PRI, or have PRIs change regularly between two values as discussed in Section 3.6.1, it is also possible to randomly choose which of a set of values each interval will be.

If we let the probability density function of the transmission intervals be

$$p(t) = \frac{1}{2}\left[\delta(t - 0.5t_s) + \delta(t - 1.5t_s)\right],$$

having two possible intervals with a mean interval of t_s, and use Equation (2.18), we get the expected ambiguity function as a function of the range velocity (or the power spectrum of the sampling process) shown in Figure 3.19.

This maintains the zeroed first alias shown in Figure 3.15, but also reduces the amplitude of the sidelobes, the randomness in the sampling spreading them over a wide bandwidth. This is a desirable feature.

(Thus there are several ways in which randomness may enter the sampling process: by intervals which are random, and by randomly choosing between fixed intervals. With pseudo-random sampling, the distinction between the two is blurred.)

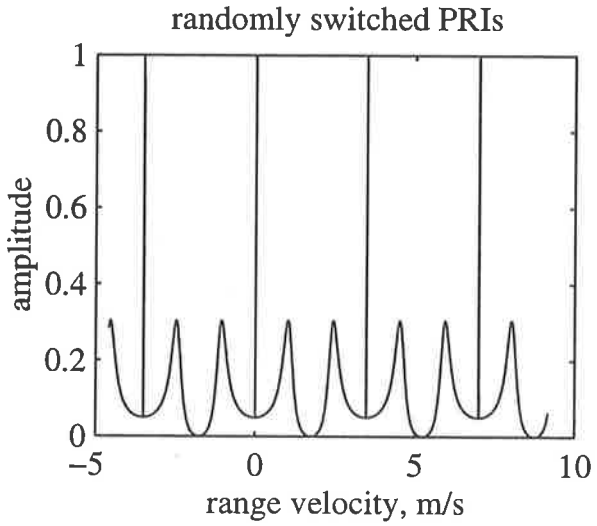

Figure 3.19: The normalised AF with randomly chosen PRIs.

3.7.2 *Azimuthal Velocity*

Let $R = R_s$, $\ddot{R}_s = 0$, $\dot{R}_s = 0$ and $y = 0$, so Equation (3.28) becomes a function of the target's azimuthal velocity:

$$\begin{aligned} &\mathrm{E}_{\mathbf{T}}[\chi'(\dot{y}; R, p_{\mathbf{T}}(\boldsymbol{t}), v_p, \lambda)] \;= \\ &\quad \sum_n \mathrm{E}_{\mathbf{T}}\left[a^2(t_n; R)\, \exp\left(j\frac{2\pi}{\lambda R}\left[\dot{y}^2 - 2\dot{y}v_p\right] t_n^2\right)\right], \end{aligned} \tag{3.34}$$

again omitting the $_s$ subscripts for clarity.

Case 1: Uniformly Distributed Times

Using the assumptions of uniform sampling PDFs and a uniform antenna beam, Equation (3.30) gives

$$\begin{aligned} \mathrm{E}_{\mathbf{T}}[\chi'(\dot{y}; R, p_T(t), v_p, \lambda)] &= \frac{N}{T}\int_{-T/2}^{T/2} \exp\left(j\frac{2\pi}{\lambda R}\left[\dot{y}^2 - 2\dot{y}v_p\right] t^2\right)\, dt, \\ &= \frac{N}{T}\sqrt{\pi}\,\frac{\mathrm{erf}\left(\frac{1}{2}\sqrt{-j\frac{2\pi}{\lambda R}\left[\dot{y}^2 - 2\dot{y}v_p\right]}T\right)}{\sqrt{-j\frac{2\pi}{\lambda R}\left[\dot{y}^2 - 2\dot{y}v_p\right]}} \end{aligned} \tag{3.35}$$

where the error function

$$\mathrm{erf}(x) \triangleq \frac{2}{\sqrt{\pi}}\int_0^x e^{-t^2}\, dt.$$

Now, as a function of just $\dot{y}$ (with $y = 0$), the ambiguity function with known times,

Equation (3.22), becomes

$$\begin{aligned}\chi'(\dot{y}; R, \{t_n\}, v_p, \lambda) &= \sum_n a^2(t_n; R) \exp\left(j\frac{2\pi}{\lambda R}\left[\dot{y}^2 - 2\dot{y}v_p\right] t_n^2\right) \\ &= \sum_{n=-T/(2t_s)}^{T/(2t_s)} \exp\left(j\frac{2\pi}{\lambda R}\left[\dot{y}^2 - 2\dot{y}v_p\right] n^2 t_s^2\right) \end{aligned} \tag{3.36}$$

for uniform transmissions and a uniform antenna beam. Since this function is being evaluated at fine intervals compared with the rate of change of the function, Equation (3.36) closely approximates Equation (3.35). Therefore, randomly distributed sampling gives approximately the same result as uniform, deterministic sampling. This will now be shown.

The discrete sum is equivalent to a numerical integration using the midpoint rule (Burden and Faires 1985). The error resulting from the integration of the function $f(t)$ between a and b using this rule with $m + 1$ evaluations is

$$I_{err} = \frac{(b-a)^3}{6(2m+2)^2}\frac{d^2 f(\mu)}{d\mu^2} \tag{3.37}$$

for some μ between a and b. $f(t)$ has a continuous second derivative over the interval $[a, b]$ and μ is chosen to maximise this second derivative (Burden and Faires 1985, page 166).

Here $a = -T/2, b = T/2$ and $m = T/t_s$, where t_s is the minimum pulse repetition interval. $f(t)$ is a real function, so the argument of the integral in Equation (3.35) is separated into real and imaginary parts, whose errors are calculated independently, *viz*:

$$f_r(t) = \cos\left(\frac{2\pi}{\lambda R}\left[\dot{y}^2 - 2\dot{y}v_p\right] t^2\right)$$

and

$$f_i(t) = \sin\left(\frac{2\pi}{\lambda R}\left[\dot{y}^2 - 2\dot{y}v_p\right] t^2\right).$$

Using Equation (3.37) with $T = 11.2\,\text{s}$, $\lambda = 0.032\,\text{m}$, $R = 30\,\text{km}$, $v_p = 70\,\text{m/s}$, $t_s = 1/115\,\text{s}$ and $\dot{y} = 5\,\text{m/s}$ gives relative errors of 0.14 and 0.15 for the real and imaginary parts, respectively. With $\dot{y} = 2\,\text{m/s}$, the errors are 0.014 and 0.017, respectively. (There is an error of zero when $\dot{y} = 0$.)

Had a significant degree of aliasing taken place, the errors would not have been so small. Non-uniform sampling only makes a significant difference when undersampling is involved. It is not necessary to consider Equation (3.34) evaluated for Case 2, as the results will be similar to this.

3.8 Conclusions

The response of a radar to a moving target is given by its ambiguity function, which incorporates the target's position and motion parameters. In SAR, moving target information is contained within the azimuthal signal, whose form is outside the radar designer's control, being a function of the imaging geometry. The only degree of freedom the designer has is that of choosing the radar's transmission times.

The original work in this chapter was to derive and investigate an expression for the slow time AF for a SAR. This was expressed in a form analogous to the Woodward ambiguity function; its properties are shown in Appendix A. Moving targets were focussed, with consideration given to unique identifiability, linearity and an equivalence with squint mode targets.

A uniform PRI was used with the function, showing an ambiguity between the range velocity and azimuthal position. This was suppressed with the use of non-uniform radar transmission times. The effects of two staggered PRIs were also discussed, as was the expected ambiguity function resulting from a random sampling scheme when the probability density functions of the transmission times were known. This was investigated for several different sampling schemes.

It was shown that non-uniform sampling causes the ambiguity function to more closely approximate the ideal 'thumbtack' shape, allowing moving targets' velocities and positions to be estimated unambiguously. They may be distinguished from stationary scatterers provided that their range velocity makes their Doppler centroid sufficiently large in comparison with the bandwidth of the stationary target, or if their azimuthal velocity causes a sufficient change in the Doppler rate.

CHAPTER 4

Moving Target Detection

This chapter formulates synthetic aperture radar (SAR) moving target detection (MTD) as an optimal detection problem, considering the decision of whether the measurement contains only the disturbance (clutter and noise), or a moving target signal in addition to the disturbance. The effects of a non-uniform pulse repetition interval are discussed in detail.

4.1 Introduction

MTD is a useful function for a long range sensor, assisting with the difficult problem of sifting those targets of interest from the clutter. In order to do it well it is necessary to accurately model the structures of the desired signal and the disturbance so it may be decided which of these best represents the measured data. Based on these models, theory exists which leads to an optimal decision.

The procedure used in this chapter is taken from the literature (*e.g.*, (McDonough and Whalen 1995, Galati and Crescimbeni 1993)); the contributions are to apply it to a SAR with a non-uniform pulse repetition interval (PRI), present some numerical examples and propose a clutter cancellation scheme for improving detection performance. A model representing the radar's received data is discussed in Section 4.2, Section 4.3 covers optimal detection theory, incorporating the signal-to-disturbance ratio improvement factor and receiver operating characteristic, and Section 4.4 briefly discusses moving target indication. Section 4.5 proposes the clutter cancellation method. Appendix B discusses SAR clutter modelling.

4.2 Data Model

This section establishes a model used to represent the data received by the radar.

It is assumed throughout this chapter that range compression has been performed prior to any moving target detection processing, so the azimuthal data are the sole concern. This reasonable assumption was discussed in Section 3.2.2.

4.2.1 Azimuthal Signal

From Section 2.3, the moving target's range-compressed azimuthal signal can be represented by

$$s(t) \;=\; a(t - y/v_p)\, e^{-j2\pi f_c \tau(t-y/v_p;R,\dot{R},\dot{y})} \tag{4.1}$$

where $a(t)$ is the radar's two-way antenna beam pattern, y is the target's position, v_p is the platform velocity, $f_c = c/\lambda$ is the carrier frequency, c is the velocity of propagation, λ is wavelength, R is range, $\dot{R}$ is the target's range velocity, $\dot{y}$ is the target's azimuthal velocity and

$$\tau(t;\dot{R},\dot{y}) \;=\; \frac{2}{c}\left(R + \dot{R}t + \frac{(\dot{y}-v_p)^2}{2R}t^2\right). \tag{4.2}$$

The target's acceleration is assumed to be zero.

The return from a scene incorporating a target and random disturbance may be approximated by the chirp model

$$y(t) \;=\; \rho\, a(t - y/v_p)\, e^{j2\pi[\phi + F_{dc}(t-y/v_p) + F_{dr}(t-y/v_p)^2]/2} + n(t), \tag{4.3}$$

where ρ is an unknown amplitude, ϕ is an unknown phase, F_{dc} is the Doppler centroid (Equation (2.11)), F_{dr} is the Doppler rate (Equation (2.12)) and $n(t)$ represents the disturbance, modelled as a known, zero mean, stationary, circular, Gaussian noise process (having real and imaginary parts which are independent and have the same variances). $y(t)$ is sampled at the times $\{t_i\}, i = 1, \ldots, N$.

4.2.2 Hypotheses

It is assumed that there is a particular position of interest, with a known range R and azimuth $y = 0$, in the scene visible to the radar. The detection problem is to decide whether or not a moving target of unknown amplitude and velocity is in that position. For convenience, time t

is taken to be 0 when the radar is adjacent to the position of interest. In order to detect a target *anywhere* in the scene, this procedure is repeated for every position which a target may occupy.

In order to determine the existence of a target, we wish to distinguish between alternative hypotheses where this vector is either composed purely of the disturbance, defined as the clutter (the signal received from innumerable scatterers in the scene) plus the noise (used to represent imperfections in the radar hardware, *etc.*), or the moving target plus the disturbance. If the target's amplitude and motion parameters are assumed to be unknown, the alternative hypotheses may be represented by

$$\left.\begin{array}{lll} H_0\colon & \boldsymbol{y} = \sigma_c \boldsymbol{v}_c + \sigma_n \boldsymbol{n} & \text{disturbance only} \\ H_1\colon & \boldsymbol{y} = \rho \boldsymbol{A} \boldsymbol{v}(\boldsymbol{\theta}, \phi) + \sigma_c \boldsymbol{v}_c + \sigma_n \boldsymbol{n} & \text{moving target and disturbance} \end{array}\right\} \tag{4.4}$$

where the range-compressed, sampled azimuthal signal for a particular range have been stored in the vector $\boldsymbol{y}$. σ_c is the amplitude of the normalised clutter vector $\boldsymbol{v}_c$ and σ_n is the amplitude of the noise vector $\boldsymbol{n}$. The signal's amplitude ρ scales the two-way antenna response $\boldsymbol{A}$ and the signal's structure $\boldsymbol{v}(\boldsymbol{\theta}, \phi)$. This is dependent upon the target's phase parameters $\boldsymbol{\theta} = [\theta_1, \theta_2, \ldots, \theta_K]^T$ and phase offset ϕ: $(\boldsymbol{v}(\boldsymbol{\theta}, \phi))_i = \exp(j2\pi(\phi + \theta_1 t_i + \theta_2 t_i^2))$. ^{T} denotes the transpose operation.

$$\boldsymbol{A} = \begin{bmatrix} a(t_1) & & & 0 \\ & a(t_2) & & \\ & & \ddots & \\ 0 & & & a(t_N) \end{bmatrix} \tag{4.5}$$

where $a(t)$ is the two-way antenna pattern as a function of time, centered on $t = 0$. $\{t_n\}, n = 1, \ldots, N$, are the radar's transmission times.

Assumptions will now be clarified.

4.2.3 Assumptions

1. There is only one moving target in the block of data being processed, as discussed in Section 2.7.7. (Identifying multiple targets is similar to finding the unknown position of a single target, except that the local peaks of threshold crossings may be used, instead of the overall maximum of the filtering operations.)

2. Moving target range migration was taken into account when the azimuthal data vector $\boldsymbol{y}$

was formed.

3. The signal vector $\boldsymbol{v}$ is scaled such that its energy $\|\boldsymbol{v}\|^2 = \boldsymbol{v}^H\boldsymbol{v} = N$, where the superscript ^{H} denotes the conjugate transpose and N is the number of samples processed.

4. The time series output due to the clutter is wide sense stationary.

5. The disturbance has an expected value of zero. This could be assumed, even if it weren't true, if the estimated expected value of the received signal were subtracted from it prior to MTD processing.

6. The disturbance has a Doppler centroid of zero. This could be assumed, even if it weren't true, if the received signal was frequency translated (after using standard clutterlocking techniques) prior to MTD processing.

7. $a(t), \sigma_c^2, \boldsymbol{v}_c, \sigma_n^2$ and $\boldsymbol{n}$ are known. (If not, there are techniques for estimating the parameters of the disturbance, for example (Barbarossa, Marsili and Mungari 1996)[1].)

Due to the prior range compression, the target's range is known to within the range resolution of the radar. This is not accurate to a fraction of a wavelength, being in the order of metres rather than centimetres, so the signal's constant phase offset is unknown; therefore, during the process of determining the optimal target detection filter and its performance, it is necessary to average the detection statistic over the range of possible phase angles (*i.e.*, 0–360°). This results in an incoherent detection.

4.2.4 *Disturbance Modelling*

The disturbance is assumed to consist of two terms: ground clutter and white noise. The covariances from each of these can be summed to form the disturbance covariance matrix.

The disturbance is also assumed to be stationary in the wide sense. The rejection of moving clutter is discussed by Mao (1993, page 358); in addition, Bühring (1980, page 191) presents a covariance modelling weather clutter.

The covariance of two complex random variables is defined to be

$$\mathrm{Cov}[X,Y] \;=\; \mathrm{E}[(X-\mathrm{E}[X])(Y-\mathrm{E}[Y])^*] \;=\; \mathrm{E}[XY^*] - \mathrm{E}[X]\mathrm{E}[Y^*]$$

[1]The emphasis of this work is to identify the theoretical difference in detection performance between uniform and non-uniform sampling.

where E[·] is the expectation operation and the superscript * denotes the conjugation operation.

The covariance of a random process $\boldsymbol{x} = [x_1, x_2, \ldots, x_N]^T$ may then be written in matrix notation as

$$\boldsymbol{R} = \mathrm{E}\Big[(\boldsymbol{x} - \mathrm{E}[\boldsymbol{x}])(\boldsymbol{x} - \mathrm{E}[\boldsymbol{x}])^H\Big].$$

(It is assumed here that $\mathrm{E}[\boldsymbol{x}] = \boldsymbol{0}$.) When $\boldsymbol{x}$ contains uniformly spaced samples of a stationary random process, the matrix has the form

$$\boldsymbol{R} = \begin{bmatrix} r(0) & r(1) & \cdots & r(N-1) \\ r(-1) & r(0) & r(1) & \cdots \\ \ddots & \ddots & \ddots & \ddots \\ r(-[N-1]) & \cdots & r(-1) & r(0) \end{bmatrix}$$

where $r(-\tau) = r^*(\tau)$.

Each disturbance term will now be considered in detail.

SAR ground clutter One approach to determining the covariance corresponding to the return from uniformly distributed, stationary ground clutter progresses from an expression for its power spectral density to the covariance matrix, making use of the Wiener-Khinchine relationship

$$(\boldsymbol{R}_c)_{k,l} = \frac{1}{2\pi}\int_{-\infty}^{\infty} G(f) e^{j2\pi(t_k - t_l)f}\, df,$$

(*e.g.*, (Cooper and McGillem 1986, page 253)) as done by Barbarossa (1992b). This is a Doppler viewpoint; it uses the motion of the radar.

The normalised two-way azimuthal radiation power pattern from a uniformly illuminated antenna is given by Equation (2.2) normalised and squared:

$$F(\theta) = \mathrm{sinc}^4\Big(\pi\frac{D}{\lambda}\sin(\theta)\Big), \tag{4.6}$$

where θ is the (assumed small) angle relative to the antenna broadside. ($\mathrm{sinc}(x) \triangleq \sin(x)/x$.)

With no SAR-clutter relative motion in the range direction, the Doppler shift of a stationary target at an angle θ is

$$f = \frac{2v_p}{\lambda}\sin\theta, \tag{4.7}$$

so, for small θ, $\theta = \lambda f/(2v_p)$. Substituting this into Equation (4.6), the spectrum of the

ground clutter is therefore

$$G(f) \;=\; \mathrm{sinc}^4\left(\pi \frac{D}{2v_p} f\right). \tag{4.8}$$

The inverse Fourier transform of this (in the time lag domain) is

$$r(\tau) = \begin{cases} B_d[\ \tfrac{1}{2}(B_d\tau)^3 - (B_d\tau)^2 + \tfrac{2}{3}], & 0 \leq |\tau| \leq \tfrac{1}{B_d}, \\ B_d[-\tfrac{1}{6}(B_d\tau)^3 + (B_d\tau)^2 - 2B_d\tau + \tfrac{4}{3}], & \tfrac{1}{B_d} < |\tau| \leq \tfrac{2}{B_d}, \\ 0, & \text{otherwise} \end{cases}$$

(which is what Barbarossa (1992b, page 82) intended). The clutter bandwidth $B_d = 2v_p/D = 2v_p\theta_{ra}/\lambda$, where v_p is the platform velocity, θ_{ra} is the beamwidth of the antenna and λ is the wavelength (Section 2.1.4).

This may be used to form the covariance matrix.

There are many other ways of modelling the clutter, as discussed in Appendix B. However, Equation (4.8) will be used throughout this thesis since it is a reasonable approximation to other, established models (see Appendix B). In addition, the emphasis here is comparing uniform and non-uniform PRI SAR: precise clutter modelling, a field in its own right (*e.g.*, (Skolnik 1990)), is a secondary consideration.

Simplified ground clutter There are many simplified models which can be used to represent clutter. These models may be implicitly assumed to be accurate by signal processors designed to be computationally efficient; assuming autoregressive clutter, for example, results in a far simpler optimal filter structure than does an accurate clutter model.

Gaussian antenna pattern Barbarossa and Farina (1994, page 356) discuss a more comprehensive clutter scenario using a Gaussian antenna radiation pattern. Brennan and Reed (1968, page 267), Hsiao (1974, page 623) and Mao (1993, page 290) use the Gaussian simplification also:

$$G(f) \;=\; \frac{1}{\sqrt{2\pi\sigma_c}} \exp\left(-\frac{f^2}{2\sigma_c^2}\right),$$

where σ_c is the bandwidth of the clutter. The clutter Doppler centroid is assumed to be zero. The corresponding covariance matrix entries are

$$(\boldsymbol{R}_c)_{i,j} \;=\; e^{-2\pi^2\sigma_c^2(t_i - t_j)^2}.$$

Autoregressive Another simplified clutter model is that of a first order autoregressive process (Barbarossa 1992b), where clutter samples are correlated:

$$v_c(nt_s) = \rho v_c([n-1]t_s) + \zeta_n,$$

where t_s is the sampling interval, $|\rho| < 1$ and ζ_n are samples of a white, Gaussian noise process: $\zeta \sim \mathcal{N}\left(0, \sigma^2\right)$. The significance of this model is the simple form of the inverse of its covariance matrix

$$\boldsymbol{R}_c^{-1} = \frac{1}{\sigma^2}\begin{bmatrix} 1 & -\rho & 0 & \cdots & \cdots & 0 \\ -\rho & 1+\rho^2 & -\rho & \ddots & & \vdots \\ 0 & -\rho & 1+\rho^2 & -\rho & \ddots & \vdots \\ \vdots & \ddots & \ddots & \ddots & \ddots & 0 \\ \vdots & & \ddots & -\rho & 1+\rho^2 & -\rho \\ 0 & \cdots & \cdots & 0 & -\rho & 1 \end{bmatrix}, \tag{4.9}$$

which translates into a simple, three tap, finite impulse response filter. When $\rho = 1$, this is a classical moving target indication filter (Shrader and Gregers-Hansen 1990, page 15.23).

White noise Other unwanted signals, such as thermal noise, analogue to digital converter quantising errors, *etc.*, are modelled as white Gaussian noise with zero mean and variance σ_n^2.

$$\boldsymbol{R}_n = \sigma_n^2 \boldsymbol{I}.$$

4.3 Optimal Detection

The objective of this section is to determine the optimal filters to best distinguish between the target present/target absent hypotheses, Equation (4.4).

The signal, stored in the vector $\boldsymbol{y}$, is passed through a filter bank $\boldsymbol{\Omega}$ to give the outputs

$$\boldsymbol{z} = \boldsymbol{\Omega y}.$$

We can specify which filter is to be designed using the vector $\boldsymbol{e}_i$, which has a 1 in its ith position and zeros elsewhere (McDonough and Whalen 1995, page 228). Then the output $\boldsymbol{z}_i = \boldsymbol{e}_i^T \boldsymbol{\Omega y}$.

We can let $\boldsymbol{e}_i^T \boldsymbol{\Omega} = \boldsymbol{\omega}$, so that

$$z = \boldsymbol{y}^H \boldsymbol{\omega}. \tag{4.10}$$

We now wish to determine the optimal filter $\boldsymbol{\omega}$.

The most appropriate detection criterion is the Neyman-Pearson criterion, which minimises the probability of a missed detection given a false alarm constraint. It makes no assumptions about the prior probability of the presence of a moving target. This optimal detection scheme is given by the likelihood ratio

$$L(\boldsymbol{y}|\rho, \boldsymbol{\theta}, \phi) = \frac{p(\boldsymbol{y}; \rho, \phi, \boldsymbol{\theta})}{p(\boldsymbol{y}; 0, \phi, \boldsymbol{\theta})} \underset{H_0}{\overset{H_1}{\gtrless}} \eta \tag{4.11}$$

where $p(\boldsymbol{y}; \rho, \phi, \boldsymbol{\theta})$ is the probability density function (PDF) of the measurement $\boldsymbol{y}$ parameterised by ρ, ϕ and $\boldsymbol{\theta}$. The corresponding threshold used by the detector, η, will be discussed in Section 4.3.4.

It is assumed that the disturbance is coloured and circular Gaussian (having real and imaginary parts which are independent and have the same variances), with the PDF

$$p(\boldsymbol{x}) = \frac{1}{\pi^N} |\boldsymbol{K}_x|^{-1} \exp\Big(-(\boldsymbol{x} - \mathrm{E}[\boldsymbol{x}])^H \boldsymbol{K}_x{}^{-1} (\boldsymbol{x} - \mathrm{E}[\boldsymbol{x}])\Big), \tag{4.12}$$

where $\boldsymbol{K}_x$ is a covariance matrix and $\boldsymbol{x}$ is a vector with length N (McDonough and Whalen 1995, page 459). (The covariance matrices discussed in Section 4.2.4 thus completely characterise the distribution.) This is representative of many types of clutter, and can arise from a homogeneous scene where each resolution cell contains a *large* number of independent scatterers (by the central limit theorem). This model could obviously be improved to represent more realistic situations; the presence of dominant scatterers may justify the use of the K-distribution, for example.

It is assumed that the mean of the disturbance is zero, as stated earlier; *i.e.*, $\mathrm{E}[\sigma_c \boldsymbol{v}_c + \sigma_n \boldsymbol{n}] = 0$.

The conditional PDF of the received data, given that a moving target is present, is then

$$p(\boldsymbol{y}; \rho, \phi, \boldsymbol{\theta}) = \frac{1}{\pi^N} \left|\boldsymbol{R}^{-1}\right| \exp\Big(-[\boldsymbol{y} - \rho \hat{\boldsymbol{v}}(\boldsymbol{\theta}, \phi)]^H \boldsymbol{R}^{-1} [\boldsymbol{y} - \rho \hat{\boldsymbol{v}}(\boldsymbol{\theta}, \phi)]\Big),$$

where

$$\boldsymbol{R} = \mathrm{E}\left[\boldsymbol{y}\boldsymbol{y}^H\right] - \mathrm{E}[\boldsymbol{y}]\mathrm{E}\left[\boldsymbol{y}^H\right]$$

and $\hat{\boldsymbol{v}}(\boldsymbol{\theta}, \phi)$ is the signal weighted by the two-way antenna pattern: $\hat{\boldsymbol{v}}(\boldsymbol{\theta}, \phi) = \hat{\boldsymbol{v}} = \boldsymbol{A}\boldsymbol{v}(\boldsymbol{\theta}, \phi)$. Since $\boldsymbol{y} = \rho\,\hat{\boldsymbol{v}} + \sigma_c \boldsymbol{v}_c + \sigma_n \boldsymbol{n}$,

$$\begin{aligned}
\boldsymbol{R} &= \rho^2\,\hat{\boldsymbol{v}}\,\hat{\boldsymbol{v}}^H + \sigma_c^2 \mathrm{E}\left[\boldsymbol{v}_c \boldsymbol{v}_c^H\right] + \sigma_n^2 \mathrm{E}\left[\boldsymbol{n}\boldsymbol{n}^H\right] - \rho^2\,\hat{\boldsymbol{v}}\,\hat{\boldsymbol{v}}^H, \text{ since } \hat{\boldsymbol{v}}, \boldsymbol{v}_c \text{ and } \boldsymbol{n} \text{ are uncorrelated,} \\
&= \sigma_c^2 \mathrm{E}\left[\boldsymbol{v}_c \boldsymbol{v}_c^H\right] + \sigma_n^2 \boldsymbol{I}, \text{ where } \boldsymbol{I} \text{ is the identity matrix,} \\
&= \boldsymbol{R}_c + \boldsymbol{R}_n \\
&= \sigma_d^2 \boldsymbol{R}_d
\end{aligned}$$

is the covariance of the disturbance. This is known, since σ_d^2, $\boldsymbol{v}_c$, σ_n^2 and $\boldsymbol{n}$ were assumed to be known. $\boldsymbol{R}_d$ is normalised to have unity down the diagonal, which is justified since the diagonal has the largest value (Hsiao 1974, page 623). The white noise component therefore has the effect of reducing the off-diagonal elements.

The logarithm of the likelihood ratio (Equation (4.11)) can be rearranged to give

$$-[\boldsymbol{y} - \rho\,\hat{\boldsymbol{v}}(\boldsymbol{\theta}, \phi)]^H \boldsymbol{R}^{-1} [\boldsymbol{y} - \rho\,\hat{\boldsymbol{v}}(\boldsymbol{\theta}, \phi)] + \boldsymbol{y}^H \boldsymbol{R}^{-1} \boldsymbol{y} \underset{H_0}{\overset{H_1}{\gtrless}} \ln \eta,$$

or

$$\rho\,\hat{\boldsymbol{v}}^H \boldsymbol{R}^{-1} \boldsymbol{y} + \rho \boldsymbol{y}^H \boldsymbol{R}^{-1}\,\hat{\boldsymbol{v}} - \rho^2\,\hat{\boldsymbol{v}}^H \boldsymbol{R}^{-1}\,\hat{\boldsymbol{v}} \underset{H_0}{\overset{H_1}{\gtrless}} \ln \eta.$$

Since $\boldsymbol{R}$ is Hermitian (it is its own conjugate transpose), $\boldsymbol{y}^H \boldsymbol{R}^{-1}\,\hat{\boldsymbol{v}} = (\hat{\boldsymbol{v}}^H \boldsymbol{R}^{-1} \boldsymbol{y})^*$, so

$$2\rho\,\Re\left\{\boldsymbol{y}^H \boldsymbol{R}^{-1}\,\hat{\boldsymbol{v}}\right\} - \rho^2\,\hat{\boldsymbol{v}}^H \boldsymbol{R}^{-1}\,\hat{\boldsymbol{v}} \underset{H_0}{\overset{H_1}{\gtrless}} \ln \eta, \tag{4.13}$$

where $\Re\{\cdot\}$ returns the real part of the argument. Therefore, the optimal hypothesis test for coherent detection can be written

$$\Re\left\{\boldsymbol{y}^H \boldsymbol{R}^{-1}\,\hat{\boldsymbol{v}}\right\} \underset{H_0}{\overset{H_1}{\gtrless}} \frac{1}{2\rho} \ln \eta + \frac{\rho}{2}\,\hat{\boldsymbol{v}}^H \boldsymbol{R}^{-1}\,\hat{\boldsymbol{v}}. \tag{4.14}$$

Since the phase of the target (*i.e.*, its minimum range to a fraction of a half-wavelength) is unknown, the likelihood ratio has to be altered. $\hat{\boldsymbol{v}}(\boldsymbol{\theta}, \phi)$ can be written as $\hat{\boldsymbol{v}}_0(\boldsymbol{\theta})e^{j2\pi\phi}$ (Galati and Crescimbeni 1993, page 41). Then, from Equation (4.13),

$$2\rho\Re\left\{\boldsymbol{y}^H\boldsymbol{R}^{-1}\,\hat{\boldsymbol{v}}_0 e^{j2\pi\phi}\right\} - \rho^2\,\hat{\boldsymbol{v}}_0^H\boldsymbol{R}^{-1}\,\hat{\boldsymbol{v}}_0 \underset{H_0}{\overset{H_1}{\gtrless}} \ln\eta.$$

Since $\boldsymbol{y}^H\boldsymbol{R}^{-1}\,\hat{\boldsymbol{v}}_0 = \left|\boldsymbol{y}^H\boldsymbol{R}^{-1}\,\hat{\boldsymbol{v}}_0\right|e^{j\alpha}$, $\Re\left\{\boldsymbol{y}^H\boldsymbol{R}^{-1}\,\hat{\boldsymbol{v}}_0 e^{j2\pi\phi}\right\} = \left|\boldsymbol{y}^H\boldsymbol{R}^{-1}\,\hat{\boldsymbol{v}}_0\right|\cos(\alpha + 2\pi\phi)$. The likelihood ratio can then be averaged over the unknown ϕ to give the optimal Bayes test (Galati and Crescimbeni 1993, page 41)

$$\begin{aligned} L(\boldsymbol{y}|\rho,\boldsymbol{\theta}) &= \mathrm{E}_\phi[L(\boldsymbol{y}|\rho,\boldsymbol{\theta},\phi)] \\ &= e^{-\rho^2\,\hat{\boldsymbol{v}}_0^H\boldsymbol{R}^{-1}\,\hat{\boldsymbol{v}}_0}\int_0^1 \exp\left(j2\rho\left|\boldsymbol{y}^H\boldsymbol{R}^{-1}\,\hat{\boldsymbol{v}}_0\right|\cos(\alpha+2\pi\phi)\right)\,d\phi \\ &= e^{-\rho^2\,\hat{\boldsymbol{v}}_0^H\boldsymbol{R}^{-1}\,\hat{\boldsymbol{v}}_0}\,\mathrm{I}_0\left(2\rho\left|\boldsymbol{y}^H\boldsymbol{R}^{-1}\,\hat{\boldsymbol{v}}_0\right|\right), \end{aligned}$$

where

$$\mathrm{I}_0(x) = \frac{1}{2\pi}\int_0^{2\pi}\exp(x\cos(\beta))\,d\beta$$

is the modified Bessel function of the first kind and order zero.

The hypothesis test (Equation (4.11)) therefore reduces to

$$\left|\boldsymbol{y}^H\boldsymbol{R}^{-1}\,\hat{\boldsymbol{v}}(\boldsymbol{\theta})\right| = |z(\boldsymbol{\theta})| \underset{H_0}{\overset{H_1}{\gtrless}} \gamma, \tag{4.15}$$

(writing $\hat{\boldsymbol{v}}$ instead of $\hat{\boldsymbol{v}}_0$ without loss of generality). The left hand side of this equation is the sufficient statistic.

This is an incoherent envelope detector; it requires about 0.5 dB greater signal to disturbance ratio for equivalent detection and false alarm probabilities to the coherent detector, Equation (4.14) (Mao 1993, page 43).

Recognising that Equation (4.15) is in the form of Equation (4.10), the optimal filter weights are therefore

$$\boldsymbol{\omega}(\boldsymbol{\theta}) = \boldsymbol{R}^{-1}\,\hat{\boldsymbol{v}}(\boldsymbol{\theta}). \tag{4.16}$$

This is the Wiener-Hopf equation (*e.g.*, (Kay 1993)).

Equation (4.15) may be evaluated for all plausible combinations of the parameters $\boldsymbol{\theta}$, each time comparing the result with the threshold. If the threshold is exceeded, indicating the presence of a moving target, the corresponding filter parameters provide an estimate of the parameters of the moving target. It will be shown in the numerical examples below that a target in a given position may give rise to thresholds being exceeded for widely varying parameters, reflecting the ambiguity resulting from subsampling effects. In addition, it was shown in Section 3.5.1 that SAR targets exhibit range velocity/azimuthal position ambiguities, so that multiple detections at different speeds in adjacent azimuthal cells may be caused by the same target.

When searching the parameter space $\boldsymbol{\theta}$ it is practical to perform a coarse resolution estimate, and then a fine resolution estimate, as discussed by Barbarossa (1992b). Practical considerations for both moving target detection and parameter estimation are made in Section 5.7.

The matrix multiplication in Equation (4.15) may be computationally expensive; Bühring describes a simplification which results in vast computational savings by decomposing the clutter covariance matrix into smaller, triangular matrices (Bühring 1980, page 190).

If the clutter were modelled as white noise, so that $\boldsymbol{R} = \sigma_d^2 \boldsymbol{I}$, Equation (4.15) would be a classical matched filtering operation, corresponding to the ambiguity function derived in Chapter 3. In the uniform sampling case, this operation could be performed efficiently using fast Fourier transforms.

Examples of optimal filters for a uniform PRI with differing values of clutter-to-noise ratio (CNR), σ_c^2/σ_n^2, are given in (Barbarossa 1992b, page 83).

4.3.1 Numerical Examples

Table 4.1 shows the parameters used for the following examples. The moving target was modelled using

$$(\hat{\boldsymbol{v}}_0)_i = e^{j2\pi(F_{dc}t_i + F_{dr}t_i^2/2)} \tag{4.17}$$

(see Equation (4.3)). The frequency domain clutter model, Equation (4.8), was a very good approximation to the time domain model discussed in Appendix B, Equation (B.2), since only 64 samples were processed (compared with more than 1000 for a full aperture) — the variation in t_d was very small.

Figure 4.1 shows the normalised spectra corresponding to the disturbance (dash-dotted), a moving target's signal (dashed) and the optimal moving target detection filter (solid) as

Parameter	Value(s)	Comments
range	30000 m	
platform velocity	70 m/s (140 kt)	
wavelength	3.2 cm (X-band)	
antenna beamwidth	1.5°	
Doppler bandwidth	115 Hz	(derived)
mean PRF	8×115 Hz or 115 Hz	
target amplitude	assumed constant	since only a small aperture
clutter model	coloured Gaussian	as per Equation (4.8)
antenna beam pattern	assumed constant	
clutter to noise ratio	40 dB	
number of samples processed	64	
sampling scheme	uniform, or random intervals	
moving target velocity	$\dot{R} = -3.67$ m/s (230 Hz), $\dot{y} = 0$ m/s	Range velocity is of interest.

Table 4.1: Parameters used for the moving target detection examples. These are similar to those used for the parameter estimation examples (Table 5.1) and the imaging examples (Table 6.1).

determined by Equation (4.16). The pulse repetition frequency (PRF) was eight times that of the 115 Hz Doppler bandwidth. The moving target's range velocity of -3.67 m/s corresponds to a Doppler centroid of twice the Doppler bandwidth. The optimal filter's spectrum peaks when there are nulls in the disturbance spectrum and vice versa, while being weighted by the spectrum of the moving target's signal. (Note that the spectrum of a matched filter is identical to that of the moving target, ignoring the spectral characteristics of the noise.)

The effects of aliasing are clear: the single target gives rise to identical responses at frequencies other than the target's true Doppler frequency. As discussed in previous chapters, these may be attenuated with a non-uniform PRI. Figure 4.2 shows the same situation as Figure 4.1, but uses an instance of transmission intervals which have been varied from uniform by up to 20% according to a uniform distribution (Section 2.7.6). (The least squares spectral estimator was used for generating the plot (Section 2.7.5).) The alias has clearly been suppressed, leading to an enhanced ability to distinguish the target from the disturbance.

Figure 4.3 shows a similar situation to Figure 4.1 but with a PRF which is equal to the Doppler bandwidth. Due to the clutter spectrum aliasing, the disturbance approximates white noise (within several decibels) and so has less effect on the optimal filter's spectrum, which therefore more closely resembles the moving target's spectrum.

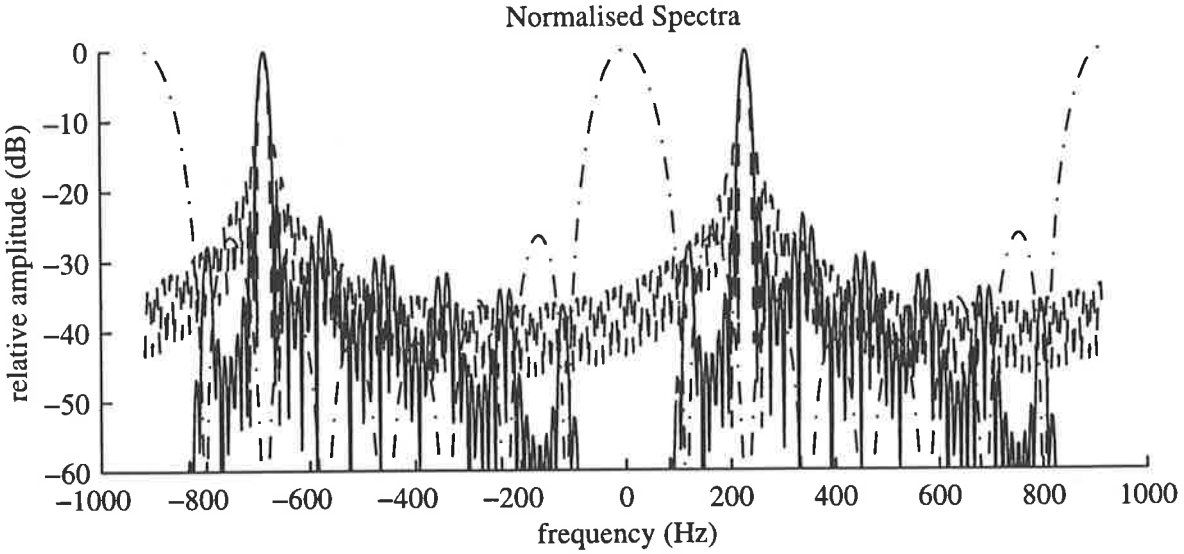

Figure 4.1: Unwindowed spectra of the disturbance (dash-dotted), moving target (dashed) and the corresponding optimal filter (solid) with a PRF of eight times the Doppler bandwidth. The nulls in the signal's spectrum have been suppressed for clarity.

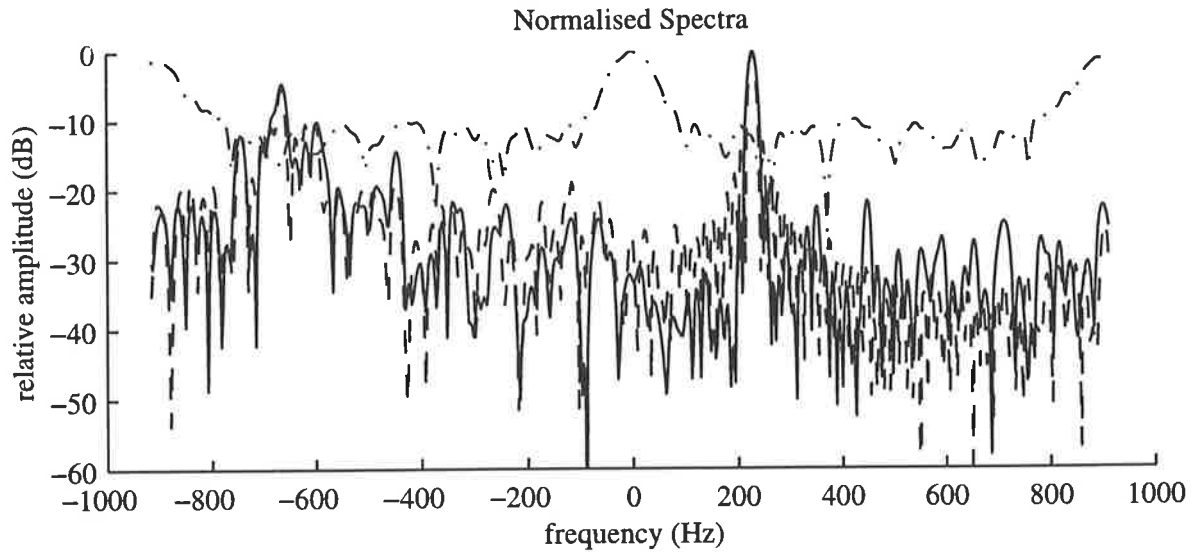

Figure 4.2: Unwindowed spectra of the disturbance (dash-dotted), moving target (dashed) and the corresponding optimal filter (solid) with non-uniform sampling intervals; the PRF averages eight times the Doppler bandwidth.

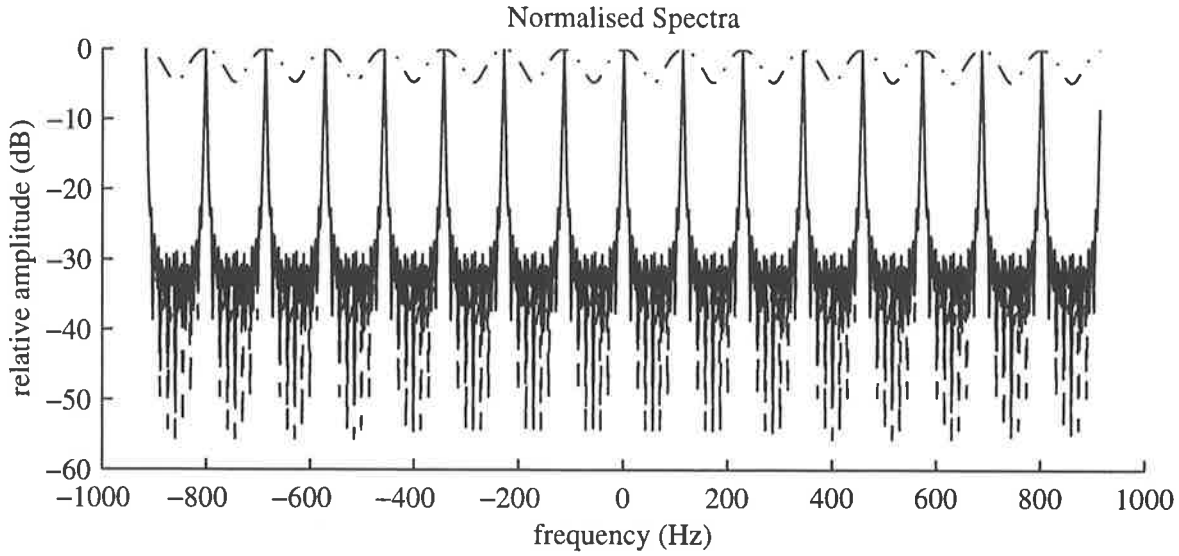

Figure 4.3: Unwindowed spectra of the disturbance (dash-dotted), moving target (dashed) and the corresponding optimal filter (solid) with a PRF equal to the Doppler bandwidth.

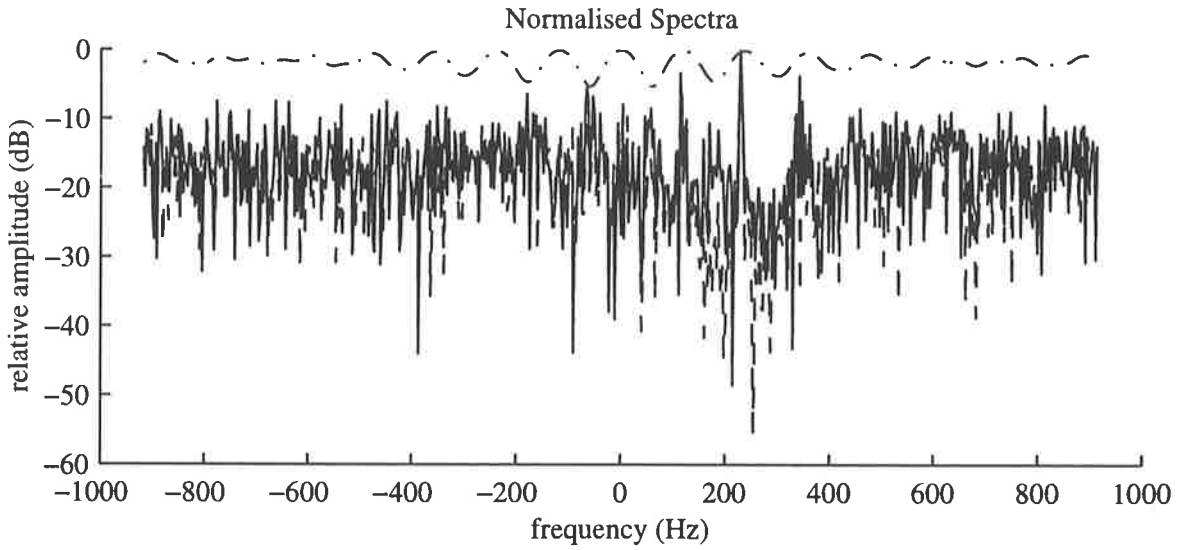

Figure 4.4: Unwindowed spectra of the disturbance (dash-dotted), moving target (dashed) and the corresponding optimal filter (solid) with non-uniform sampling intervals; the PRF averages the Doppler bandwidth.

Figure 4.4 shows a similar situation to Figure 4.3 but with a non-uniform PRI. Aliases have clearly been suppressed, albeit by only a few decibels at frequencies near the true value. (A transmission deviation of more than 20% from uniform results in greater suppression.) This result has been achieved at the cost of the raised noise floor, which will reduce the detection performance, particularly in situations of low signal to disturbance ratio. (See Section 4.3.4.)

4.3.2 Alternative Optimality Criterion

As an alternative to the Neyman-Pearson detection criterion, we can consider maximising the ratio of the signal power to the disturbance power at the output of the moving target detection filter.

For a target with parameters $\boldsymbol{\theta}$ and no disturbance, the output (signal) power is

$$\begin{aligned} P_s(\boldsymbol{\theta}) &= \mathrm{E}\left[z(\boldsymbol{\theta})^2\right] \\ &= \rho^2 \left| \widehat{\boldsymbol{v}}^H(\boldsymbol{\theta})\boldsymbol{\omega} \right|^2, \end{aligned} \tag{4.18}$$

using Equations (4.10) and (4.4).

When there is a disturbance and no target, the output (disturbance) power is

$$P_d(\boldsymbol{\theta}) = \boldsymbol{\omega}^H \boldsymbol{R} \boldsymbol{\omega}$$

(Brennan and Reed 1968).

Maximising the output signal to disturbance ratio is equivalent to minimising the output disturbance power for a given output signal power. We can form the sum $P_d(\boldsymbol{\theta}) + \lambda P_s(\boldsymbol{\theta})$, where λ is a Lagrange multiplier, and differentiate with respect to each weight ω_k (McDonough and Whalen 1995, page 228). As with the Neyman-Pearson criterion, this procedure gives Equation (4.16) as the optimal weights.

4.3.3 Signal-to-Disturbance Ratio Improvement

The signal-to-disturbance ratio improvement, a useful figure of merit for a moving target detection filter, is the signal-to-disturbance power ratio (SDR) at the output of the MTD filter divided by the signal-to-disturbance ratio at the input to the filter. It allows for both clutter attenuation and signal gain. This is

$$\begin{aligned} I_{sdr}(\boldsymbol{\theta}) &= \frac{\rho^2}{\sigma_d^2} \frac{\left| \widehat{\boldsymbol{v}}^H(\boldsymbol{\theta})\boldsymbol{\omega} \right|^2}{\boldsymbol{\omega}^H \boldsymbol{R}_d \boldsymbol{\omega}} \cdot \left(\frac{\rho^2}{\sigma_d^2} \right)^{-1} \\ &= \frac{\left| \widehat{\boldsymbol{v}}^H(\boldsymbol{\theta})\boldsymbol{\omega} \right|^2}{\boldsymbol{\omega}^H \boldsymbol{R}_d \boldsymbol{\omega}} \end{aligned} \tag{4.19}$$

(Shrader and Gregers-Hansen 1990, page 15.20), (Staudaher 1990), (Brennan and Reed 1968). It is analogous to array gain, a beamforming figure of merit given by the ratio of the phased

array's signal-to-noise ratio and the signal-to-noise ratio of an individual sensor (Johnson and Dudgeon 1993, page 138).

For an optimal filter, $\omega(\theta) = \boldsymbol{R}^{-1}\hat{v}(\theta)$, so that

$$I_{sdr}(\theta) = \hat{v}^H(\theta)\boldsymbol{R}_d^{-1}\hat{v}(\theta). \tag{4.20}$$

For a matched filter (which ignores the disturbance covariance, implicitly assuming the clutter is white), $\omega(\theta) = \hat{v}(\theta)$. Then

$$\begin{aligned} I_{sdr}(\theta) &= \frac{\left|\hat{v}^H(\theta)\hat{v}(\theta)\right|^2}{\hat{v}^H(\theta)\boldsymbol{R}\hat{v}(\theta)} \\ &= N^2\left(\hat{v}^H(\theta)\boldsymbol{R}\hat{v}(\theta)\right)^{-1}. \end{aligned} \tag{4.21}$$

I_{sdr} may also be interpreted as the gain in signal-to-disturbance power ratio obtained by filtering, and is given by

$$\begin{aligned} I_{sdr} &= \frac{[P_s/(P_c+P_n)]_{out}}{[P_s/(P_c+P_n)]_{in}} \\ &= \frac{P_{s\,out}}{P_{s\,in}}\frac{(P_c+P_n)_{in}}{(P_c+P_n)_{out}} \\ &= \text{signal gain} \times \text{clutter attenuation}, \end{aligned}$$

taking into account the statistical independence between noise and clutter (Barbarossa 1992b, page 84). P_s is the signal power, P_c is the clutter power and P_n is the thermal noise power.

The maximum signal gain is given by the coherent integration of N samples, $10\log_{10}(N)$ dB. The maximum clutter attenuation is the input CNR (which is shown in (Barbarossa and Farina 1994, page 348), and commonly expressed in decibels). Adding these gives the best I_{sdr} (Barbarossa 1992b).

Numerical Examples

Figure 4.5 shows the signal-to-disturbance ratio improvement for the example in Figure 4.1. (The parameters are shown in Table 4.1.) Figure 4.5(a) shows the case where the optimal filter for a Doppler centroid of 230 Hz is used and the actual target Doppler changes over the range indicated on the horizontal axis. (The Doppler centroid, F_{dc}, was used in the model shown in Equation (4.17).) Clearly there is a sharp peak when the target's Doppler is the same as that of the filter, or has offsets at multiples of the sample rate. This peak is almost the ideal 40 dB,

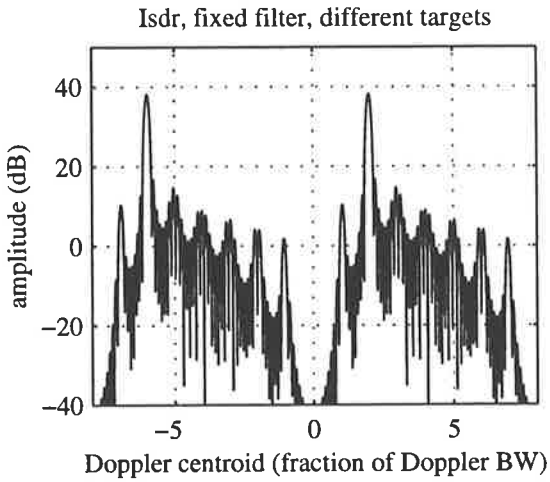

(a) Ambiguity function: I_{sdr} for a fixed, optimal filter and changing target Doppler.

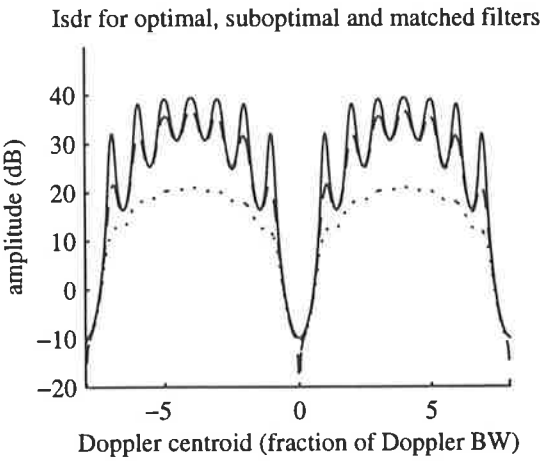

(b) I_{sdr} for changing filter and target. Solid: optimal filter; dashed: suboptimal; dotted: matched.

Figure 4.5: The signal to disturbance ratio improvement for a SAR with a PRF eight times the Doppler bandwidth.

the CNR, indicating that the filter is suppressing the clutter extremely well.

This plot is actually the ambiguity function, and would give the same results as the expression derived in Chapter 3 (Figure 3.13) if the CNR were small.

Figure 4.5(b) shows the I_{sdr} as the signal and filter are changed together, for three different types of filter. (The parameters of the signal and filter are matched, including their Doppler centroid.) The solid line shows the optimal filter, described by Equation (4.20). The dotted line shows the output resulting from a matched filter, *i.e.* Equation (4.21), which has a significantly worse performance due to the non-white nature of the disturbance. Between these is a dashed line corresponding to a suboptimal filter which uses the inverse covariance of an autoregressive process, Equation (4.9). Clearly this simple three tap filter structure, as used by classical moving target indication filters, achieves a performance within a few decibels of the optimal filter when the actual noise is coloured and Gaussian.

The common local minimum at a Doppler centroid of ± 8 times the Doppler bandwidth indicates that the filters cannot distinguish the signal from the clutter at this frequency. This is a result of aliasing.

Figure 4.6 shows similar results to Figure 4.5, but for non-uniform sampling. This corresponds to the situation of Figure 4.2. The ambiguity function now shows some ability to suppress the alias, and the I_{sdr} is vastly improved where the Doppler centroid is 8 times the Doppler bandwidth, showing the ability to successfully distinguish the aliased signal from the

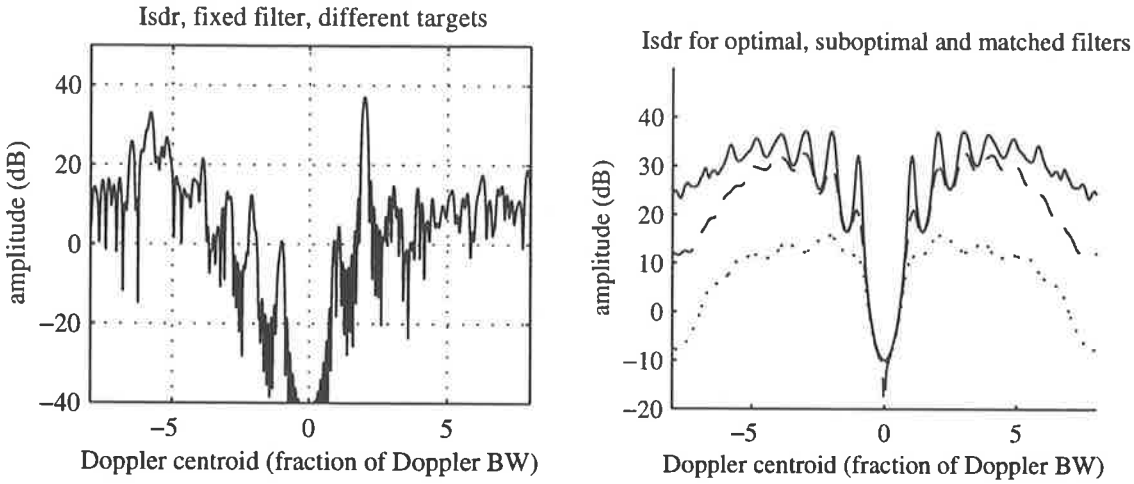

(a) Ambiguity function.

(b) I_{sdr} for changing filter and target.

Figure 4.6: The signal to disturbance ratio improvement for a SAR with a non-uniform PRI; the PRF averages eight times the Doppler bandwidth.

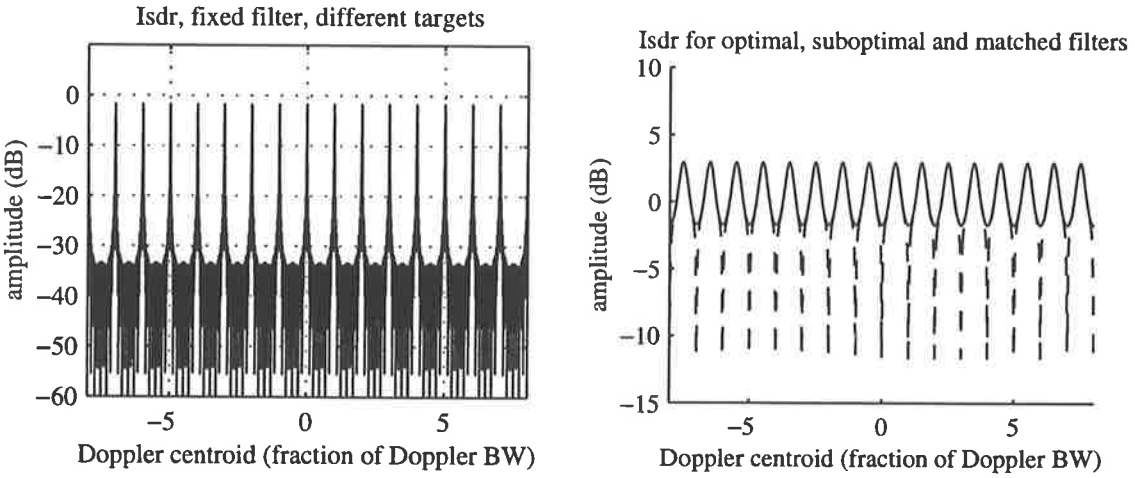

(a) Ambiguity function.

(b) I_{sdr} for changing filter and target.

Figure 4.7: The signal to disturbance ratio improvement for a SAR with a PRF equal to the Doppler bandwidth.

disturbance.

Figure 4.7 is similar again, and corresponds to Figure 4.3. Aliasing is the major problem with such a low, uniform PRF. The similarity between the plots in Figure 4.7(b) show that there is a negligible difference in performance between the filters, a result of the disturbance spectrum being smoothed by aliasing effects.

The I_{sdr} for a non-uniform PRI and low average PRF, corresponding to Figure 4.4, is shown in Figure 4.8. The aliasing phenomena have been overcome. Again, the small difference

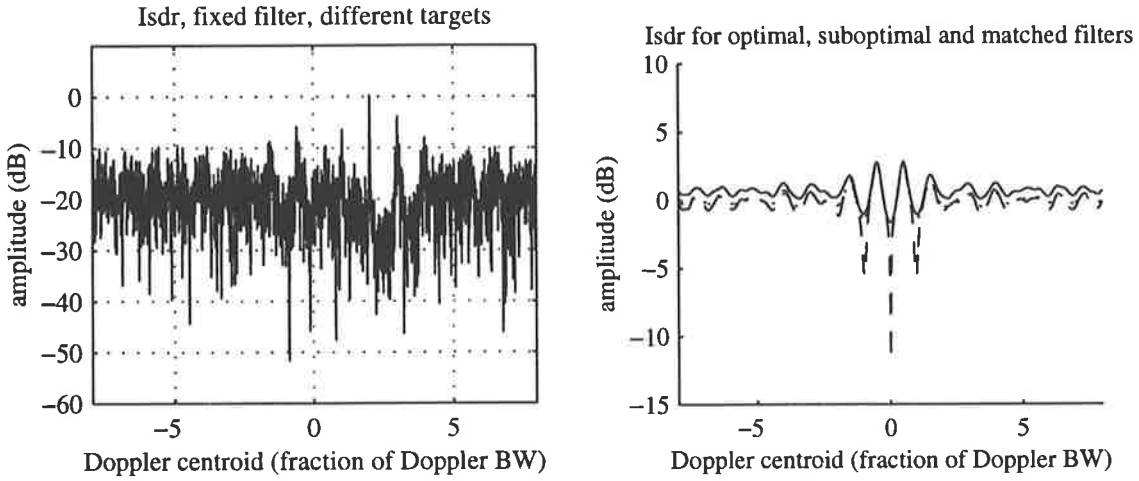

(a) Ambiguity function.

(b) I_{sdr} for changing filter and target.

Figure 4.8: The signal to disturbance ratio improvement for a SAR with a non-uniform PRI; the PRF averages the Doppler bandwidth.

between the performance of the filters justifies the use of the matched filter, as explicitly modelled by the ambiguity function in Chapter 3 (Equation (3.13)).

4.3.4 *Receiver Operating Characteristic*

The receiver operating characteristic is the relationship between the probability of detection of a moving target, the signal to disturbance ratio (SDR) and the probability of a false alarm, P_F. It requires the specification of the detection threshold γ, which is chosen to satisfy a false alarm constraint, as discussed previously.

Since we are also interested in the effects of the sample times $\{t_i\}$ and the moving target parameters $\boldsymbol{\theta}$, we wish to find the characteristic as a function of these parameters also:

$$P_D \;=\; \mathrm{ROC}(\mathrm{SDR}, P_F, \{t_i\}, \boldsymbol{\theta}). \tag{4.22}$$

This is found using the probability density function of the sufficient statistic, Equation (4.15), which is $\zeta = |z(\boldsymbol{\theta})|$ maximised by the use of an appropriate $\boldsymbol{\theta}$.

Since $z = \boldsymbol{y}^H \boldsymbol{\omega}$ has the complex Gaussian PDF

$$z \;\sim\; \mathcal{CN}_N\left(\mu_z, \sigma_z^2\right) \;=\; \mathcal{CN}_N\left(\mathrm{E}\left[\boldsymbol{y}^H\right]\boldsymbol{\omega}, \boldsymbol{\omega}^H \boldsymbol{R}\boldsymbol{\omega}\right), \tag{4.23}$$

ζ's PDF is Rayleigh (or chi with two degrees of freedom) with no target and Rician (or

non-central chi) when a target is present[2]:

$$p_{\zeta|H_0}(\zeta) = \frac{\zeta}{\sigma_z^2}\exp\left(-\frac{1}{2}\frac{\zeta^2}{\sigma_z^2}\right) \qquad \text{Rayleigh;}$$

$$p_{\zeta|H_1}(\zeta) = \frac{\zeta}{\sigma_z^2}\exp\left(-\frac{1}{2}\frac{\zeta^2+\mu_z^2}{\sigma_z^2}\right) I_0\left(\frac{\zeta\mu_z}{\sigma_z^2}\right) \qquad \text{Rician.}$$

In order to determine the threshold γ to distinguish between the hypotheses using Equation (4.15), we need to specify a false alarm probability P_F. This can be done since the sufficient statistic (Equation (4.15)) does not depend upon the unknown signal magnitude ρ. P_F, being the probability that the processed signal's amplitude lies above γ when no target is present, is given by

$$\begin{aligned} P_F &= \int_\gamma^\infty p_{\zeta|H_0}(\zeta)\,d\zeta \\ &= 1 - \int_0^\gamma p_{\zeta|H_0}(\zeta)\,d\zeta \\ &= \exp\left(-\frac{\gamma^2}{2\sigma_z^2}\right). \end{aligned}$$

Therefore, the threshold is given by

$$\begin{aligned} \gamma &= \sqrt{-2\sigma_z^2\ln(P_F)} \\ &= \sqrt{-2\boldsymbol{\omega}^H\boldsymbol{R}\boldsymbol{\omega}\ln(P_F)}. \end{aligned} \tag{4.24}$$

Similarly, the detection probability is the probability that the processed signal's amplitude lies above the threshold when a target is known to be present:

$$P_D = \int_\gamma^\infty p_{\zeta|H_1}(\zeta)\,d\zeta.$$

---

[2]For two independent Gaussian random variables $X : \mathcal{N}(p,\sigma^2)$ and $Y : \mathcal{N}(0,\sigma^2)$, the PDF of $Z = \sqrt{X^2+Y^2}$ is Rician:

$$f_Z(z) = \frac{z}{\sigma^2}\exp\left(-\frac{1}{2}\frac{p^2+z^2}{\sigma^2}\right) I_0\left(\frac{zp}{\sigma^2}\right)\cdot u(z),$$

where the step function $u(z)$ guarantees that the expression is zero for $z < 0$ (Stark and Woods 1986, pages 94–95). In the application of interest, X and Y are to represent the real and imaginary parts of the complex value z whose magnitude is to be found.

This may be written in a form approaching that of Equation (4.22):

$$\begin{aligned} P_D &= \mathcal{Q}(\mu_z/\sigma_z, \gamma/\sigma_z), \\ &= \mathcal{Q}\left(\sqrt{\frac{\rho^2}{\sigma_d^2}\frac{(\hat{\boldsymbol{v}}^H\boldsymbol{\omega})^2}{\boldsymbol{\omega}^H\boldsymbol{R}_d\boldsymbol{\omega}}}, \sqrt{-2\ln(P_F)}\right) \text{ since } \mu_z|H_1 = \rho\hat{\boldsymbol{v}} \\ &= \mathcal{Q}\left(\sqrt{\frac{\rho^2}{\sigma_d^2}I_{sdr}}, \sqrt{-2\ln(P_F)}\right), \end{aligned}$$

using Equation (4.19). ρ^2/σ_d^2 is the signal to disturbance ratio and $\mathcal{Q}(\cdot)$ is the Marcum-Q function

$$\mathcal{Q}(\alpha,\beta) \triangleq \int_\beta^\infty v\exp\left(-\frac{1}{2}[v^2+\alpha^2]\right) I_0(\alpha v)\,dv,$$

which is 1 minus the distribution function of a Rician distributed variable.

The greatest probability of detection P_D is achieved with the largest SDR, which requires the coherent processing of as many samples as possible (or as large a signal as possible). While the use of the whole synthetic aperture may attempt to do this, it is important to realise that the target may not be coherent (*i.e.*, moving in a predictable fashion to a fraction of a wavelength), resulting in a poorer performance than anticipated.

Optimal Processing

With optimal processing, $\boldsymbol{\omega}_{opt}(\boldsymbol{\theta}) = \boldsymbol{R}^{-1}\hat{\boldsymbol{v}}(\boldsymbol{\theta})$ so $\sigma_{zopt}^2 = \hat{\boldsymbol{v}}^H(\boldsymbol{\theta})\boldsymbol{R}^{-1}\hat{\boldsymbol{v}}(\boldsymbol{\theta})$ and the decision threshold

$$\gamma_{opt} = \sqrt{-2\hat{\boldsymbol{v}}^H(\boldsymbol{\theta})\boldsymbol{R}^{-1}\hat{\boldsymbol{v}}(\boldsymbol{\theta})\ln(P_{F\,opt})}.$$

Note that this is dependent upon the local covariance as well as the parameters being searched for.

Matched Filtering

Using matched filter processing, the clutter covariance is ignored, giving $\boldsymbol{\omega}(\boldsymbol{\theta}) = \hat{\boldsymbol{v}}(\boldsymbol{\theta})$. Then $\sigma_{zmf}^2 = \hat{\boldsymbol{v}}^H(\boldsymbol{\theta})\boldsymbol{R}\hat{\boldsymbol{v}}(\boldsymbol{\theta})$ and the decision threshold

$$\gamma_{mf} = \sqrt{-2\hat{\boldsymbol{v}}^H(\boldsymbol{\theta})\boldsymbol{R}\hat{\boldsymbol{v}}(\boldsymbol{\theta})\ln(P_{F\,opt})}.$$

Variable	Parameter of interest	Approx. value per square kilometre
# range cells	signal bandwidth	300
# azimuthal cells	integration time	300
# possible target $\dot{R}$	Doppler centroid	20
# possible target $\dot{y}$	Doppler rate	20

Table 4.2: The number of values which may be assumed by the various parameters for a square kilometre.

False Alarm Probability

It is necessary to determine a reasonable value for the false alarm probability, P_F, so an appropriate detection threshold may be determined using Equation (4.24).

Suppose we allow one false alarm per square kilometre. Table 4.2 shows the number of values each parameter of interest may assume. Since they are independent, their product gives the total number of filtering operations required: about 3.6×10^7. This gives a P_F of roughly 3×10^{-8} per filtering operation.

Numerical Examples

Figure 4.9 shows the receiver operating characteristic of a SAR with the parameters listed in Table 4.1, the PRF being eight times the Doppler bandwidth. An optimal filter was used. Both uniform and non-uniform sampling cases are shown, the latter with random intervals deviated 20% from the nominal PRI. The uniform case outperforms the non-uniform by about 1 dB.

Figure 4.10 is similar, but for a mean PRF which is equal to the Doppler bandwidth. The performance is far worse than in Figure 4.9, which results from the spectral density of the disturbance: a high average PRF is able to utilise the fact that the signal and disturbance spectra do not overlap.

Due to this overlapping with a low mean PRF, a result of subsampling, the discrimination offered by non-uniform sampling gives it a superior detection performance to that of uniform sampling.

Using a matched filter rather than an optimal filter gives results shown in Figure 4.11. The performance of the uniformly sampled system is almost indistinguishable from that using an optimal filter; the non-uniform case is worse by about 0.6 dB.

Having such a low average PRF for moving target detection clearly comes at a high price. The difference in SDR to achieve a comparable detection performance to a scheme with eight times the PRF is approximately 40 dB. This is a result of the clutter being coloured: the target and clutter spectra do not overlap in the high PRF case, allowing the filter to better distinguish

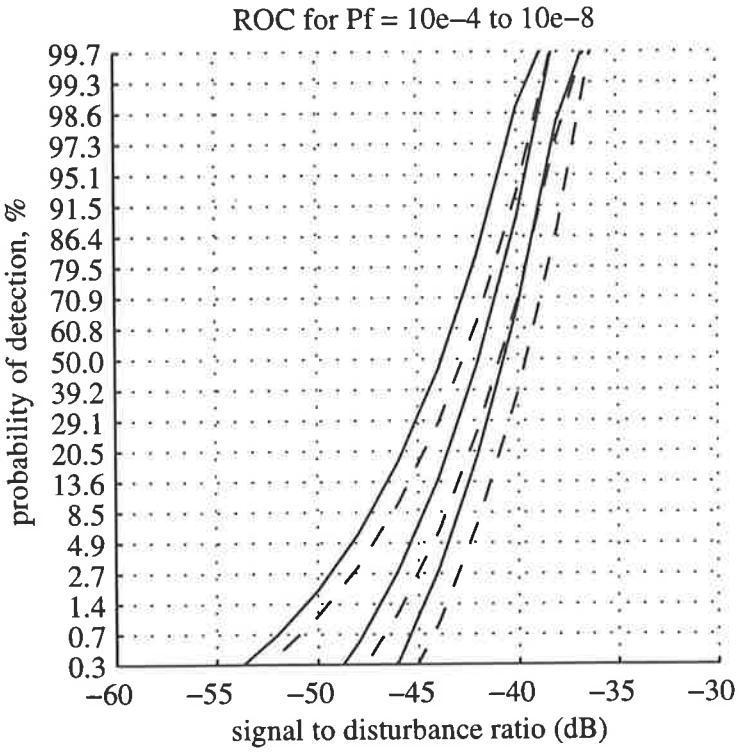

Figure 4.9: Receiver operating characteristics for the optimal filter detecting a target with a Doppler frequency of −230 Hz, using a mean PRF of eight times the Doppler bandwidth. Solid line, uniform transmissions; dashed, non-uniform.

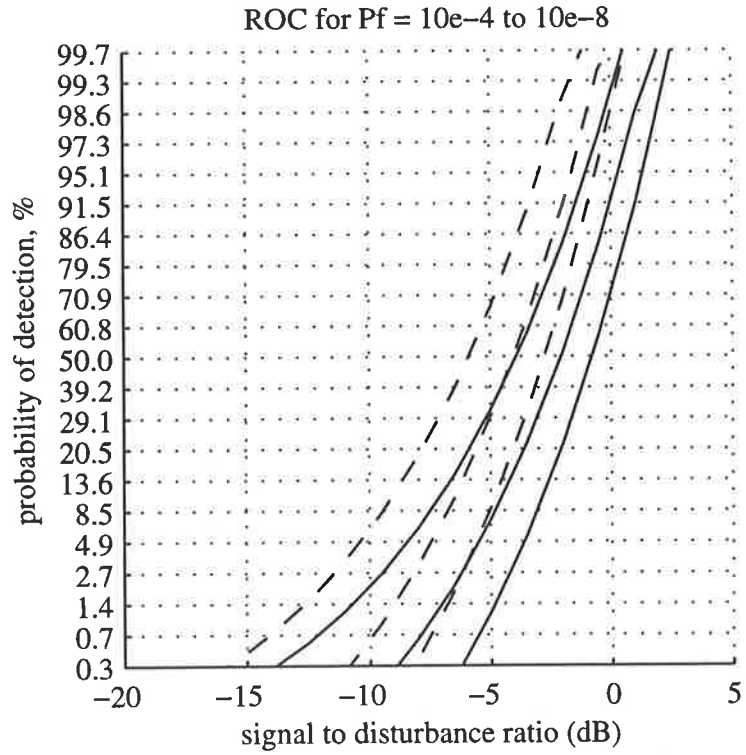

Figure 4.10: Receiver operating characteristics for the optimal filter detecting a target with a Doppler frequency of −230 Hz, using a mean PRF equal to the Doppler bandwidth. Solid line, uniform transmissions; dashed, non-uniform.

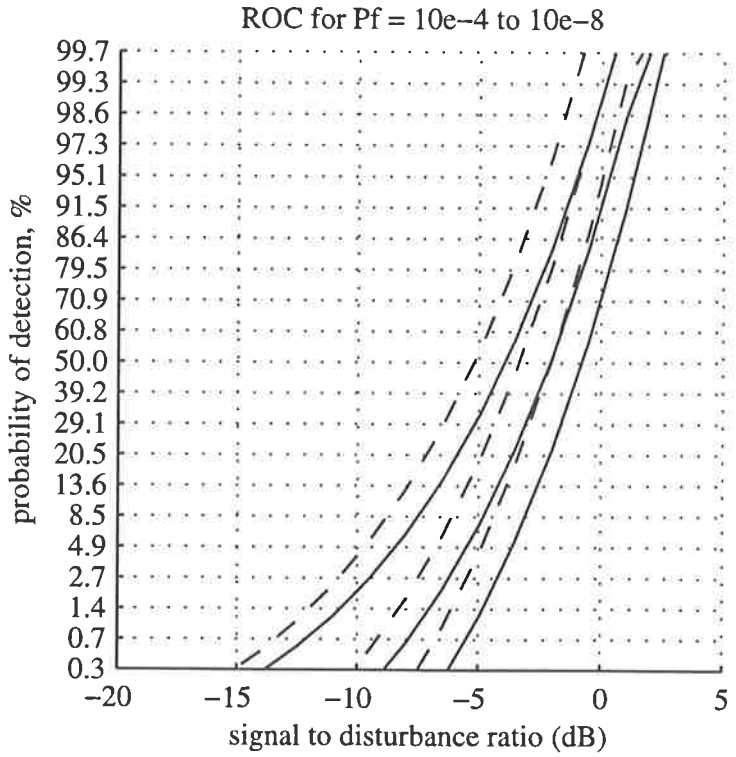

Figure 4.11: Receiver operating characteristic curve of a matched filter detecting a target with a Doppler frequency of −230 Hz, using a mean PRF equal to the Doppler bandwidth. Solid line, uniform transmissions; dashed, non-uniform.

the two.

If a low PRF is to be used, however, it is clear that a non-uniform scheme is preferable to uniform transmissions since it resolves ambiguities and has a *superior* detection performance, even when the processor assumes that the coloured clutter is white.

4.4 Moving Target Indication

The objective of moving target indication (MTI) is to determine the existence of a moving target with a single filter rather than use a bank of filters, as required by optimal moving target detection. Since the signal and clutter spectra overlap, there will be a corresponding loss in sensitivity.

A useful criterion to measure the performance of an MTI system is the average SDR improvement $\bar{I}_{sdr}$, given by I_{sdr} averaged over the parameters of interest (based on (Mao 1993, page 348)).

The preferable test variable for finding the optimal weights, an average of the likelihood ratio over the *a priori* distributions of the unknown parameters $\boldsymbol{\theta}$, appears to be intractable with

non-uniform samples (Brennan and Reed 1968). However, there is an alternative (Brennan and Reed 1968, page 267):

Averaging Equation (4.18) over the uniform *a priori* distribution of parameters θ, where for example the target Doppler centroid is assumed to be between α_1 and α_2, where[3]

$$(\alpha_2 - \alpha_1)(t_{n+1} - t_n) \ll 1 \ \forall n \tag{4.25}$$

gives

$$\bar{P}_s = \omega^H \omega.$$

Using a Lagrange multiplier, the output disturbance power is minimised for a given $\bar{P}_s$ when

$$P_d - \lambda \bar{P}_s = \omega^H (\boldsymbol{R} - \lambda \boldsymbol{I}) \omega,$$

where $\boldsymbol{I}$ is the identity matrix. Setting the derivatives of this to zero with respect to the elements of ω gives (Johnson and Dudgeon 1993, page 501), (D'Assumpcao and Gray 1995, page 17)

$$(\boldsymbol{R} - \lambda \boldsymbol{I}) \omega = \boldsymbol{O} \tag{4.26}$$

i.e., $|\boldsymbol{R} - \lambda \boldsymbol{I}| = 0$. The average MTI gain is then

$$\begin{aligned} \bar{G} &= \frac{\bar{P}_s}{P_d} \\ &= \frac{\omega^H \omega}{\omega^H \boldsymbol{R} \omega} = \frac{\omega^H \omega}{\omega^H \lambda \omega} \\ &= \frac{1}{\lambda}. \end{aligned}$$

The smallest eigenvalue gives the largest MTI gain; the corresponding weights are given by Equation (4.26).

Hsiao (1974) shows that for reasonable clutter rejection with a single filter, the PRF must be much greater than the clutter bandwidth, even when using non-uniform PRIs. This agrees with Bilinskis and Mikelsons (1992, pages 293–303) and is implied by the assumption of Equation (4.25). (See Section 2.7.5.) This means that a SAR with an average PRF equal to the clutter bandwidth cannot perform MTI, unless there is a short burst at a high PRF: Hsiao (1974, Figure 3) shows that even a 10 pulse MTI filter is capable of useful clutter suppression.

[3]This inequality was inverted in the publication.

4.5 Clutter Cancellation

In order to improve moving target detection performance, it is desirable to subtract the disturbance from the measured data prior to MTD processing. This requires an estimate of the disturbance which has not been corrupted by the moving target signal.

Freedman, Bose and Steinberg (1996) and Kesteven (1997) discuss an appropriate technique for spurious sidelobe reduction called CLEAN. This involves thresholding the ground image to estimate the positions and intensities of bright scatterers. The measurement required to generate these images is then calculated (since it may be accurately predicted) and subtracted from the data. This lowers the noise floor, permitting other scatterers to be cancelled. The iterative procedure is stopped when a criterion is met. The resulting data may then be used to find moving targets. The technique assumes a sparse distribution of bright scatterers, which is in accordance with the assumptions in this thesis.

Another method is now proposed.

If the available average PRF were *twice* that of the minimum, staggered PRI data could be collected at the same time as conventional SAR data by interleaving the transmissions as appropriate, maintaining a minimum PRI. This allows two independent ground images to be formed: one from each set of data. Incoherent subtraction of the two reveals the moving targets, which appear only in the conventional image, and whose positions and velocities may be found by processing the staggered PRI data. Since azimuthal motion causes defocussing, it may be necessary to perform this process with a range of Doppler rates. This technique could be applied to superior ground map generation: the higher quality conventional image (see Chapter 6) may have the defocussed moving targets removed.

Since the technique requires twice the volume of data as a conventional radar, it is reasonable to compare it with two antenna MTD techniques, such as a displaced phase centre antenna (Section 2.5). This is able to detect slowly moving targets, with spectra overlapping that of the ground clutter, although at the expense of a greater volume of hardware (requiring two, well aligned antennas and an additional receiver).

An example of the proposed clutter cancellation technique is shown in Section 7.4.

4.6 Practical Considerations

Theoretically, for a target with arbitrary velocity parameters occurring anywhere in the scene, Equation (4.15) needs to be evaluated at all combinations of parameters in order to achieve optimal detection performance. This is impractical, so coarse estimates need to be made, at least as a first approximation.

When moving target velocities and positions are being found coarsely, the spacing of filtering evaluations is given by the variations of θ which produce a reduction in the response of the MTD filter's main lobe by several decibels. An example of such a filter is shown in Figure 4.5.

If the spacing between the parameters used for the evaluations are sufficiently small, no finer estimates need to be found and the coarse spacing then gives the resolution of the estimate.

This was discussed by Barbarossa (1992b): when considering the frequency and frequency rate parameters, the frequency resolution $\delta\alpha$ is inversely proportional to the integration time $T(R)$ and the rate $\delta\beta$ is inversely proportional to $T(R)^2$. If the expected possible ranges of α and β are $\Delta\alpha$ and $\Delta\beta$ respectively, the total number of filters is given by

$$\frac{\Delta\alpha}{\delta\alpha}\frac{\Delta\beta}{\delta\beta},$$

where $\delta\alpha = 0.88/T$ and $\delta\beta = 1.8/T^2$ for a 3 dB resolution.

Note that the smallest interval between the parameter values specifying a stationary target and those for the closest coarse evaluation specify the smallest velocity at which a moving target can travel and still be detected. This point is well illustrated by the main lobes of Figures 3.9 and 3.10 representing a stationary target.

There is no obvious limit on the maximum speed with which a target may travel and still be detected or have its parameters estimated (provided it has a sufficiently large radar cross section and is seen by the radar several times). It is necessary, though, for the processor to perform the required assembling of data according to the expected range migration.

The maximum *unambiguous* target speed depends upon the resolution of the sample time generator: if samples are pseudorandom (Section 2.7.4), the maximum unambiguous Doppler corresponds to half the frequency of the reference clock. With arbitrarily positioned random times, however, all detectable targets may have unambiguous parameter estimates.

In practice, there is a significant difference (low correlation) between the return from a stationary target and the return from a target with a large Doppler. This is because the linear

azimuthal chirp approximation becomes invalid. Therefore, it may only be necessary for the pseudorandom sampling to exhibit unambiguous spectra out to (say) ten times the Doppler bandwidth of the ground.

The practical considerations mentioned in this section also apply to the parameter estimation problem (Chapter 5).

4.7 Conclusions

This chapter applied optimal detection theory to investigate the effects of a non-uniform PRI on the moving target detection performance of a ground imaging SAR. It derived the optimal filter for an unknown phase using both Neyman-Pearson and maximum signal to disturbance power ratio criteria. The chapter also derived the signal to disturbance ratio improvement and the receiver operating characteristic. It was shown that a non-uniform PRI has a superior performance to a uniform PRI SAR with the same average pulse repetition frequency. It was also shown that a higher average PRF gives much better results, which may be attributed to the optimal detector utilising the non-white structure of the clutter. Some consideration was given to moving target indication. The proposed clutter cancellation method improves detection performance at the price of a higher average PRF.

CHAPTER 5

Moving Target Parameter Estimation

This chapter investigates the estimation of the parameters of a moving target using azimuthal synthetic aperture radar (SAR) data sampled at arbitrary times. It discusses the literature, both optimal and practical estimation techniques, estimator bias and the Cramér-Rao lower variance bounds. These bounds are derived for both deterministic and random sampling times and are verified by simulation.

5.1 Introduction

Once a moving target is known to be present in the radar scene, its position and velocity can be estimated. The moving target's signal may be modelled as a sampled exponential with a slowly varying amplitude and complex, polynomial phase (Section 2.3). The contributions of this chapter are to investigate the problem of estimating the target's unknown parameters for arbitrary, but fixed, radar transmission times by taking an optimal (maximum likelihood) approach and finding the theoretical lower bounds on the variance of the estimates. The variance bounds are also found for a variety of random transmission schemes, and it is shown that the attainable polynomial phase coefficient estimation accuracy with a random pulse repetition interval approaches that of a uniform interval as the number of processed samples is increased, even though the former overcomes the range velocity ambiguities inherent in the latter.

Whilst many other authors have found the Cramér-Rao lower bounds for various circumstances, I know of none who model a polynomial phase signal in coloured noise with non-uniform sampling times, and none who consider different probability density functions for various sampling schemes. I also know of none who relate the results to the actual unknown

parameters in a SAR moving target scenario (Section 5.8).

Section 5.3 discusses polynomial phase estimation methods covered in the literature, Section 5.2 defines the model of the radar's data and Section 5.4 derives the maximum likelihood (ML) estimator for the unknown parameters, including its bias and lower variance bounds for arbitrary transmission times. Section 5.5 discusses the variance bounds for random samples with known distributions. Several examples are given. Simulations verify the analytical results in Section 5.6 and practical considerations are given in Section 5.7. Section 5.8 relates the parameter estimation model to the actual SAR parameters and shows several numerical examples. Section 5.9 concludes. Appendices C and D derive lower variance bounds for a biased estimator and the Fisher information matrix for a complex Gaussian scenario respectively.

5.2 Signal Model

The model to be used to represent the signal in this chapter is similar to that used for moving target detection in Chapter 4. The moving target's range compressed azimuthal signal can be represented by Equations (4.1) and (4.2). The return from a scene incorporating a target and random disturbance may be approximated by

$$y(t) \;=\; \rho\, a(t-w)\, e^{j2\pi[\phi+\theta_1(t-w)+\theta_2(t-w)^2+\ldots+\theta_K(t-w)^K]} + n(t),$$

where ρ is an unknown amplitude, $a(t)$ is the radar's two-way antenna beam pattern, w is the time the target is centred in the antenna beam, ϕ and $\{\theta_k\}, k = 1, \ldots, K$, are unknown polynomial phase coefficients and $n(t)$ represents the disturbance, modelled as a known, zero mean, stationary, circular, Gaussian noise process (having real and imaginary parts which are independent and have the same variances). Note that the unknown signal model parameters are non-random, and that there is a relationship between $a(t)$ and $n(t)$ (Section 4.2.4). $y(t)$ is sampled at the times $\{t_i\}, i = 1, \ldots, N$. The use of the polynomial phase makes this formulation more general than that used in Chapter 4.

The target's slant range is assumed to be known to within the range resolution of the radar due to the prior range compression. A justification for using range compressed data when estimating the parameters of moving targets was given in Section 3.2.2.

Figure 5.1 shows a representation of the parameters to be estimated. For narrow antenna beam, it is reasonable to restrict $K = 2$, so that the instantaneous frequency is a straight line (indicated by the dashed line). It is then clear that the estimation accuracy of the unknown

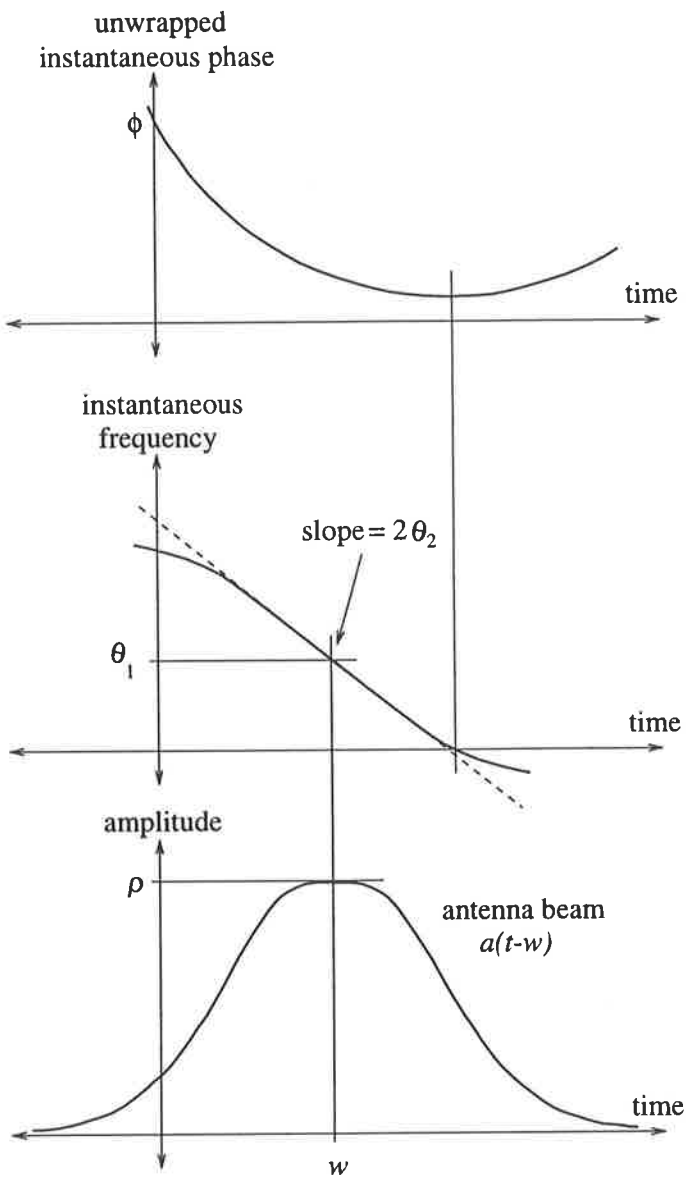

Figure 5.1: A representation of the model and its unknown parameters.

time w depends primarily upon the shape of the antenna beam pattern. Since $a(t)$ is a slowly varying function, it follows that w cannot be found very accurately; consequently, the Doppler centroid θ_1 and hence range velocity $\dot{R}$ of the moving target (via Equation (2.11)) cannot be found accurately either.

Alternatively, if $a(t)$ had a narrow peak, w could be found accurately; however, that would mean that the signal to noise ratio away from time w would be poor, degrading the quality of the phase parameter estimations. This is the classical time-frequency estimation problem: accuracy in one dimension is at the expense of degraded accuracy in the other.

In SAR ground imaging, it is normal to assume that $a(t)$ is uniform. Although there is insufficient information to determine the w corresponding to a specific target under these

circumstances, it is quite practical to find the amplitude of a target with an assumed w, corresponding to a scatterer's azimuthal position.

It is possible in the moving target problem to assume that w is known to be zero (say), which is often done for analytical convenience, reducing the problem to one of polynomial phase parameter estimation, *e.g.*, (Ikram et al. 1996). This corresponds to a scenario where a target is assumed to be travelling on a road which is located accurately in the azimuthal dimension. With w known, the target's range velocity may be found very accurately (Section 5.8.1). (It may be thought that the $w = 0$ assumption is valid in any case, since the target's parameters are estimated following its detection, and w was estimated *then*. However, that process was not performed without error, so the argument is invalid.) The target's azimuthal position is assumed to be unknown at this stage, although it will be assumed to be known later in this chapter.

The sampled signal can be represented by

$$\boldsymbol{y}(\boldsymbol{t}) \;=\; \rho\, e^{j2\pi\phi}\, \boldsymbol{A}(\boldsymbol{t} - w\mathbf{1})\, \boldsymbol{v}_0(\boldsymbol{\theta}, \boldsymbol{t} - w\mathbf{1}) + \boldsymbol{n}.$$

(Boldface indicates vectors or matrices.)

$$\boldsymbol{A}(\boldsymbol{t}) \;=\; \begin{bmatrix} a(t_1) & & & 0 \\ & a(t_2) & & \\ & & \ddots & \\ 0 & & & a(t_N) \end{bmatrix}$$

(as defined in Equation (4.5)), $\boldsymbol{t} = [t_1, t_2, \ldots, t_N]^T$ and $\mathbf{1} = [1, 1, \ldots, 1]^T$ where the superscript ^{T} denotes the transpose operation. The signal

$$(\boldsymbol{v}_0(\boldsymbol{\theta}, \boldsymbol{t}))_i \;=\; e^{j2\pi(\theta_1 t_i + \theta_2 t_i^2 + \ldots + \theta_K t_i^K)}$$

with $\boldsymbol{\theta} = [\theta_1, \theta_2, \ldots, \theta_K]^T$. The disturbance vector

$$\begin{aligned} \boldsymbol{n} \;&\sim\; \mathcal{CN}_N(\mathbf{0}, \boldsymbol{R}) \\ &=\; \frac{1}{\pi^N} \left|\boldsymbol{R}^{-1}\right| \exp\!\left(-[\boldsymbol{x} - \mathrm{E}[\boldsymbol{x}]]^H \boldsymbol{R}^{-1} [\boldsymbol{x} - \mathrm{E}[\boldsymbol{x}]]\right). \end{aligned}$$

$\boldsymbol{R} = \mathrm{E}\left[\boldsymbol{n}\boldsymbol{n}^H\right]$ is the noise covariance matrix, the superscript ^{H} denoting the Hermitian conjugate-transpose operator. $\mathrm{E}[\cdot]$ denotes the expectation operator.

For convenience, the unknowns are stored in the vector $\boldsymbol{u} = [\rho, w, \phi, \boldsymbol{\theta}^T]^T$. It is assumed that the number of measurements N exceeds the number of unknowns.

5.3 Existing Work

This complex signal parameter estimation problem is well known; some practical techniques are:

Discrete polynomial transform Peleg and Porat (1991b) introduced the continuous and discrete polynomial transforms, which are powerful, computationally efficient tools for estimating the parameters of signals with polynomial phases, including the order. Estimation accuracy is considered in (Peleg and Porat 1991a). Later papers extend the algorithm to allow for a time varying amplitude and multiple component signals (Friedlander and Francos 1995). O'Shea (1996) extended the algorithm to allow for low signal to noise ratios.

Interpolation Dowski, Whitmore and Avery (1988) estimate the parameters of real sinusoids sampled at arbitrary times by first interpolating to find the values which would have been obtained using uniform sampling times (using singular value decomposition). Principle component autoregressive modelling is applied to identify the line spectra and then the amplitudes and phases are found using a linear least squares approach. The variance of the method is shown to compare favourably with the Cramér-Rao lower bound.

Minimum variance Kitchen (1992) performed a polyphase signal estimation using a minimum variance estimator.

Kay's estimator Kay (1988) described an estimator which was based on measurement phase differences (but did not use phase unwrapping).

Pisarenko's estimator has been extended for coloured noise (Sakai 1986).

Some authors have applied techniques to the SAR moving target problem specifically:

Iterative Barbarossa (1992b) discusses an iterative scheme which estimates the Doppler centroid and rate simultaneously. This is done in coarse and then fine resolution stages; the former provides an initial guess for the latter. This is a simple, practical technique.

High order multilag ambiguity function The multilag high order ambiguity function was introduced by Peleg and Porat in 1991 as a parameter estimator for multicomponent polynomial phase signals in white noise. (It is not a ML estimator.) It has been applied to SAR recently (Barbarossa, Porchia and Scaglione 1996, Porchia et al. 1996).

Wigner-Ville The Wigner-Ville (WV) distribution has been used a great deal for instantaneous frequency estimation; it is appropriate for SAR since the azimuthal chirps appear as straight lines, which may be detected through the use of a Hough transform following the WV processing. Integrating along the possible lines in the 2D time-frequency space overcomes the cross-term problem with the WV distribution: since the cross terms alternate in sign along their length, they will cancel. This technique has been applied to SAR data in (Barbarossa and Farina 1990) and (Barbarossa 1992a).

Phase unwrapping A curve may be fitted to the unwrapped phase of the signal, for example (Slocumb and Kitchen 1994).

Multilinear time-frequency representation Barbarossa and Mascolo (1994) use another non-linear estimation technique to focus SAR moving target signals in the presence of strong clutter and for imaging geometries which depart from the usual quadratic assumption.

ISAR Inverse SAR accommodates arbitrary target motion and uses it to resolve scatterers on the target itself (Wehner 1995). This was discussed in Section 2.5.

Note that an optimal technique, the **exact maximum likelihood** (given that there is a uniform prior), involves an exhaustive search over the parameter space. Although this is impractical, it is of interest as it is theoretically optimal.

Soumekh (1996) argues that most SAR super-resolution techniques in the literature (including, by implication, maximum likelihood) will not meet the claimed performance in practice due to inaccurate modelling of the target's complex amplitude characteristic, which is typically assumed to be uniform. In reality, the target's amplitude may vary dramatically, and may not even peak at the shortest range (when the target is centred in the antenna beam).

However, meaningful theoretical results may still be found while using the uniform amplitude assumption, since the SAR of interest here has a narrow beamwidth (in the order of a degree). It is unlikely that the target's amplitude will vary to the extent shown by Soumekh over such a small aspect change. (A more important assumption is that of linear target motion.)

In summary, the differences between the problem of interest and that of the well known polynomial phase parameter estimation problem are

- coloured Gaussian noise,
- the amplitude term with an unknown delay,
- the parameters of interest are derived from the polynomial coefficients rather than being the coefficients themselves, and in particular
- the sampling is at arbitrary times, rather than at fixed intervals. For the case of random sampling, the estimator's performance should incorporate the sampling probability density function.

5.4 Maximum Likelihood Estimation

The maximum likelihood (ML) estimator for these parameters is found by applying classical theory, for example (Rife and Boorsteyn 1974, Peleg and Porat 1991a). It is of interest since it returns the most likely value of the parameters, given an equal prior probability, with variances achieving the Cramér-Rao lower bound asymptotically. The ML estimate corresponds to the parameters which maximise the probability density function (PDF) of the observations $p(\boldsymbol{y};\boldsymbol{t},\boldsymbol{u})$ (termed the likelihood function). This PDF is parameterised by the sampling times and the vector of unknowns $\boldsymbol{u}$. Then

$$\begin{aligned}
\hat{\boldsymbol{u}} &= \arg\max_{\boldsymbol{u}} \; p(\boldsymbol{y};\boldsymbol{t},\boldsymbol{u}) \\
&= \arg\max_{\boldsymbol{u}} \; \frac{1}{\pi^N}\left|\boldsymbol{R}^{-1}\right| \exp\left(-[\boldsymbol{y}-\rho e^{j2\pi\phi}\boldsymbol{A}\boldsymbol{v}_0]^H \boldsymbol{R}^{-1}[\boldsymbol{y}-\rho e^{j2\pi\phi}\boldsymbol{A}\boldsymbol{v}_0]\right) \\
&= \arg\min_{\boldsymbol{u}} \; (\boldsymbol{y}-\rho e^{j2\pi\phi}\,\hat{\boldsymbol{v}}_0)^H \boldsymbol{R}^{-1}(\boldsymbol{y}-\rho e^{j2\pi\phi}\,\hat{\boldsymbol{v}}_0).
\end{aligned}$$

where $\hat{\boldsymbol{v}}_0 = \boldsymbol{A}\boldsymbol{v}_0$, the weighted polynomial phase signal. For any w and $\boldsymbol{\theta}$, the ML estimator of the amplitude and initial phase

$$\{\hat{\rho},\hat{\phi}\} = \arg\min_{\rho,\,\phi} \; (\boldsymbol{y}-\rho e^{j2\pi\phi}\,\hat{\boldsymbol{v}}_0)^H \boldsymbol{R}^{-1}(\boldsymbol{y}-\rho e^{j2\pi\phi}\,\hat{\boldsymbol{v}}_0). \tag{5.1}$$

If we consider the amplitude and initial phase to comprise a complex amplitude with real and imaginary components $\rho_r + j\rho_i = \rho e^{j2\pi\phi}$, we can differentiate the right hand side of Equation (5.1) with respect to these components and set the results to zero. This gives

$$\begin{aligned}\hat{\rho}_r &= \frac{\Re\left\{\hat{\boldsymbol{v}}_0{}^H \boldsymbol{R}^{-1}\boldsymbol{y}\right\}}{\hat{\boldsymbol{v}}_0{}^H \boldsymbol{R}^{-1}\hat{\boldsymbol{v}}_0} \text{ and} \\ \hat{\rho}_i &= \frac{\Im\left\{\hat{\boldsymbol{v}}_0{}^H \boldsymbol{R}^{-1}\boldsymbol{y}\right\}}{\hat{\boldsymbol{v}}_0{}^H \boldsymbol{R}^{-1}\hat{\boldsymbol{v}}_0},\end{aligned}$$

where $\Re\{\cdot\}$ and $\Im\{\cdot\}$ return the real and imaginary parts, respectively. Since $\boldsymbol{R}$ is positive definite, $\boldsymbol{R}^{-1}$ is positive definite, which means that $\hat{\boldsymbol{v}}_0{}^H \boldsymbol{R}^{-1}\hat{\boldsymbol{v}}_0$ is real. Therefore,

$$\hat{\rho}e^{j2\pi\hat{\phi}} = \frac{\hat{\boldsymbol{v}}_0{}^H \boldsymbol{R}^{-1}\boldsymbol{y}}{\hat{\boldsymbol{v}}_0{}^H \boldsymbol{R}^{-1}\hat{\boldsymbol{v}}_0}, \tag{5.2}$$

which is the least squares amplitude estimator. If the noise were white with variance σ^2 (so $\boldsymbol{R} = \sigma^2\boldsymbol{I}$ where $\boldsymbol{I}$ is the identity matrix), the antenna beam were uniform (so $\boldsymbol{A} = \boldsymbol{I}$) and $w = 0$, this would reduce to the matched filter: $\hat{\rho}e^{j2\pi\hat{\phi}} = \boldsymbol{v}_0{}^H\boldsymbol{y}$. If $\boldsymbol{\theta} = [\theta_1]$, this would be equivalent to evaluating the discrete time Fourier transform (DTFT) of the sampled signal at the frequency of interest.

The estimator for the delay and polynomial phase coefficients

$$\begin{aligned}\hat{w}, \hat{\boldsymbol{\theta}} &= \underset{w,\boldsymbol{\theta}}{\arg\min}\ (\boldsymbol{y} - \hat{\rho}e^{j2\pi\hat{\phi}}\hat{\boldsymbol{v}}_0)^H \boldsymbol{R}^{-1}(\boldsymbol{y} - \hat{\rho}e^{j2\pi\hat{\phi}}\hat{\boldsymbol{v}}_0) \\ &= \underset{w,\boldsymbol{\theta}}{\arg\max}\ \frac{\left|\boldsymbol{y}^H \boldsymbol{R}^{-1}\hat{\boldsymbol{v}}_0\right|^2}{\hat{\boldsymbol{v}}_0{}^H \boldsymbol{R}^{-1}\hat{\boldsymbol{v}}_0},\end{aligned} \tag{5.3}$$

using Equation (5.2). Thus $\boldsymbol{\theta}$ can be estimated without knowledge of the amplitude or initial phase[1]. Again, in the case of white noise, uniform antenna beam, $w = 0$ and $\boldsymbol{\theta} = [\theta_1]$, this is the frequency which maximises the squared magnitude of the DTFT. (In practice, a coarse frequency estimation may be performed by finding the maximum squared value of the discrete

[1] As an aside, if the amplitude and initial phase were known *a priori*, the maximum likelihood estimator of $\boldsymbol{\theta}$ would be

$$\hat{\boldsymbol{\theta}} = \underset{\boldsymbol{\theta}}{\arg\max}\ \rho\,\Re\{e^{j2\pi\phi}\boldsymbol{y}^H \boldsymbol{R}^{-1}\hat{\boldsymbol{v}}_0\} - \rho^2\,\hat{\boldsymbol{v}}_0{}^H \boldsymbol{R}^{-1}\hat{\boldsymbol{v}}_0.$$

The known phase compensates for the fixed phase shift of the measurement, thereby allowing the estimator to be coherent. (Equation (5.3), by contrast, squares the $\boldsymbol{y}^H \boldsymbol{R}^{-1}\hat{\boldsymbol{v}}_0$ term, destroying the requirement for a knowledge of the phase information.)

Fourier transform evaluated at a finite number of frequency bins. As the signal to noise ratio is reduced, it suddenly becomes more likely that a noise spike will be larger than the value in the frequency bin nearest the signal, leading to a gross error. This is known as the 'threshold effect' (Rife and Boorsteyn 1974).)

With $w = 0$ it is possible to prewhiten the measurement using

$$\boldsymbol{y}' = (\boldsymbol{R}^{-1}\boldsymbol{A})^{1/2}\boldsymbol{y},$$

but this approach will not be considered due to possible systematic errors.

The performance of the ML estimator will now be considered.

5.4.1 Bias

Firstly, the expected value of the complex amplitude estimate

$$\mathrm{E}\left[\hat{\rho}e^{j2\pi\hat{\phi}}\right] = \frac{\hat{\boldsymbol{v}}_0{}^H\boldsymbol{R}^{-1}\mathrm{E}[\boldsymbol{y}]}{\hat{\boldsymbol{v}}_0{}^H\boldsymbol{R}^{-1}\hat{\boldsymbol{v}}_0} = \rho e^{j2\pi\phi},$$

so the estimator in Equation (5.2) is unbiased, irrespective of the sampling times.

Ambiguities result when more than one signal can give rise to the set of observations. This is well known with uniform sampling since a cisoid can be fitted to the data at the signal's frequency or at multiples of the sampling frequency away from this. These aliases may be interpreted as estimation *biases* since, with no prior knowledge, a practical estimation strategy which searches for cisoids from a predefined starting point will consistently take one of them as the true value. (Another possibility, that the estimator has a random frequency at which it starts its search for cisoids, is not worth considering. The errors in the estimates which result from choosing an alias would then depend upon the strategy adopted. For the evaluation of the variance below it is assumed that none of the aliases have been chosen.) These biases will now be considered in detail.

Suppose that w is known to be 0 and $\boldsymbol{A} = \boldsymbol{I}$. Then the expected value of the polynomial phase coefficient estimator (Equation (5.3))

$$\begin{aligned}
\mathrm{E}\left[\hat{\boldsymbol{\theta}}\right] &= \mathrm{E}\left[\arg\max_{\boldsymbol{\theta}} \frac{\left|\boldsymbol{y}^H \boldsymbol{R}^{-1} \boldsymbol{v}_0\right|^2}{\boldsymbol{v}_0{}^H \boldsymbol{R}^{-1} \boldsymbol{v}_0}\right] \\
&= \mathrm{E}\left[\arg\max_{\boldsymbol{\theta}} \frac{1}{\boldsymbol{v}_0{}^H \boldsymbol{R}^{-1} \boldsymbol{v}_0} \left|\sum_{k,l} \left[\rho' e^{-j2\pi(\phi' + \theta_1' t_k + \theta_2' t_k^2)} + \boldsymbol{n}_k\right] \boldsymbol{R}^{-1}{}_{k,l}\, \rho\, e^{j2\pi(\phi + \theta_1 t_l + \theta_2 t_l^2)}\right|^2\right],
\end{aligned}$$

where the parameters of the actual signal are primed $\boldsymbol{u}'$, and only a second order polynomial phase is being considered for brevity.

For white noise and a high signal to noise ratio this becomes

$$\mathrm{E}\left[\hat{\boldsymbol{\theta}}\right] = \mathrm{E}\left[\arg\max_{\boldsymbol{\theta}} \left|\sum_k e^{j2\pi[(\theta_1 - \theta_1')t_k + (\theta_2 - \theta_2')t_k^2]}\right|^2\right].$$

For uniform sampling, where $t_k = kt_s$, t_s being the sampling interval, the sum of the exponentials will reach a maximum when the exponential's arguments are multiples of $j2\pi$. This will happen when both

$$\left.\begin{aligned}
\theta_1 &= \theta_1' + x/t_s \\
\text{and}\quad \theta_2 &= \theta_2' + y/{t_s}^2
\end{aligned}\right\} \tag{5.4}$$

for arbitrary integers x and y. The estimated spectrum will reach the same value in each of these cases. Thus *the estimator is biased*[2].

In theory, any other sampling scheme will suppress these effects, since the phases will then not be aligned. However, it may be important to suppress aliases as much as possible. This is especially true when there are several signals, a case not considered here. Bilinskis and Mikelsons (1992, pages 80-88) discuss the degree of aliasing, defined as the squared sum of the Fourier coefficients at aliasing frequencies, for a variety of different random sampling schemes. They show that random intervals with a positive correlation perform better than with no correlation, or periodic sampling with jitter. These were discussed in Section 2.7.6. (In

[2]This is true in practice for the frequency term in the SAR moving target parameter estimation scenario. (This was discussed in relation to the range velocity in Section 3.5.1.) However, since the radar's speed is assumed to be much larger than the moving target's azimuthal speed, there are no aliasing problems for the frequency rate term.

general, sampling schemes which approximate a uniform probability of a sample occurring as a function of time have the best properties.) These schemes will be discussed later.

5.4.2 Variance

The variance of an estimator is a measure of its inaccuracy. It is useful to put a theoretical lower limit on this variance; this provides a convenient way of comparing the performance of estimators under different conditions. The lower variance bounds on the estimation errors of sinewave parameters were possibly first discussed in detail by Rife and Boorsteyn (1974), (1976).

This lower variance bound for an unbiased estimator, the Cramér-Rao bound, is given by

$$\mathrm{CRLB}\left\{\widehat{(\boldsymbol{u})_k}\right\} \;=\; (\boldsymbol{J}^{-1})_{k,k} \tag{5.5}$$

(*e.g.*, (Kay 1993)), where the Fisher information matrix

$$\boldsymbol{J} \;\triangleq\; \mathrm{E}\left[\left(\frac{\partial \ln p(\boldsymbol{y};\boldsymbol{t},\boldsymbol{u})}{\partial \boldsymbol{u}}\right)\left(\frac{\partial \ln p(\boldsymbol{y};\boldsymbol{t},\boldsymbol{u})}{\partial \boldsymbol{u}}\right)^T\right]$$

has the elements

$$(\boldsymbol{J})_{k,l} \;\triangleq\; \mathrm{E}\left[\frac{\partial \ln p(\boldsymbol{y};\boldsymbol{t},\boldsymbol{u})}{\partial(\boldsymbol{u})_k}\frac{\partial \ln p(\boldsymbol{y};\boldsymbol{t},\boldsymbol{u})}{\partial(\boldsymbol{u})_l}\right]. \tag{5.6}$$

Since the ML estimator has unbiased amplitude and phase estimates and only additive bias for the polynomial phase coefficient estimates (Equation (5.4)),

$$\mathrm{E}[\hat{\boldsymbol{u}}] \;=\; \boldsymbol{u} + \boldsymbol{b},$$

where $\boldsymbol{b}$ is a vector containing the offsets. It is shown in Appendix C that the lower variance bound for this biased estimator is still the Cramér-Rao bound, the result achieved by an unbiased estimator. This is expected, since variance is not affected by an additive offset.

It is shown in Appendix D that for $\boldsymbol{y} \sim \mathcal{CN}(\boldsymbol{m}(\boldsymbol{u}), \boldsymbol{R})$, Equation (5.6) simplifies to

$$\begin{aligned}(\boldsymbol{J})_{k,l} &= 2\Re\left\{\frac{\partial \boldsymbol{m}(\boldsymbol{u})^H}{\partial(\boldsymbol{u})_k}\boldsymbol{R}^{-1}\frac{\partial \boldsymbol{m}(\boldsymbol{u})}{\partial(\boldsymbol{u})_l}\right\} \\ &= 2\Re\left\{\frac{\partial(\rho e^{j2\pi\phi}\,\hat{\boldsymbol{v}}_0)^H}{\partial(\boldsymbol{u})_k}\boldsymbol{R}^{-1}\frac{\partial \rho e^{j2\pi\phi}\,\hat{\boldsymbol{v}}_0}{\partial(\boldsymbol{u})_l}\right\}\end{aligned}$$

for this problem, where $\hat{\boldsymbol{v}}_0 = \boldsymbol{A}\boldsymbol{v}_0$, $(\boldsymbol{v}_0)_i = e^{j2\pi(\theta_1 t_i + \theta_2 t_i^2 + \ldots + \theta_K t_i^K)}$ and $\boldsymbol{u} = [\rho, w, \phi, \boldsymbol{\theta}^T]^T$.

Here we have, using vector notation for brevity,

$$\begin{aligned}
\frac{\partial \rho e^{j2\pi\phi}\,\hat{\boldsymbol{v}}_0}{\partial \rho} &= e^{j2\pi\phi}\,\hat{\boldsymbol{v}}_0, \\
\frac{\partial \rho e^{j2\pi\phi}\,\hat{\boldsymbol{v}}_0}{\partial w} &= e^{j2\pi\phi}\left[\frac{\partial \boldsymbol{A}(\boldsymbol{t}-w\boldsymbol{1})}{\partial w} - j2\pi\boldsymbol{A}(\theta_1\boldsymbol{I} + 2\theta_2\boldsymbol{T} + 3\theta_3\boldsymbol{T}^2 + \ldots + K\theta_K\boldsymbol{T}^{K-1})\right]\boldsymbol{v}_0 \\
&= e^{j2\pi\phi}\boldsymbol{B}\boldsymbol{v}_0, \\
\frac{\partial \rho e^{j2\pi\phi}\,\hat{\boldsymbol{v}}_0}{\partial \phi} &= j2\pi\rho e^{j2\pi\phi}\,\hat{\boldsymbol{v}}_0, \text{ and} \\
\frac{\partial \rho e^{j2\pi\phi}\,\hat{\boldsymbol{v}}_0}{\partial \theta_n} &= j2\pi\rho e^{j2\pi\phi}\boldsymbol{T}^n\,\hat{\boldsymbol{v}}_0,
\end{aligned}$$

where $\boldsymbol{T}$ is a matrix containing the sampling times and unknown delay

$$\boldsymbol{T} = \begin{bmatrix} t_1 & & 0 \\ & t_2 & \\ & & \ddots \\ 0 & & t_N \end{bmatrix} - w\boldsymbol{I}.$$

$\boldsymbol{J}$ may then be written as shown in Equation (5.7). (Note that $\boldsymbol{A}^H = \boldsymbol{A}$.)

This expression is difficult to simplify, since $\boldsymbol{B}$ is dependent upon the form of $a(t)$. Therefore, we shall consider the case when w is known to be zero. Then the unknowns $\boldsymbol{u} = [\rho, \phi, \boldsymbol{\theta}^T]^T$, so

$$\left.\begin{aligned}
(\boldsymbol{J})_{1,1} &= 2\Re\left\{\hat{\boldsymbol{v}}_0{}^H\boldsymbol{R}^{-1}\hat{\boldsymbol{v}}_0\right\}, \\
(\boldsymbol{J})_{k,1} &= 4\pi\rho\Im\left\{\hat{\boldsymbol{v}}_0{}^H\boldsymbol{T}^{k-2}\boldsymbol{R}^{-1}\hat{\boldsymbol{v}}_0\right\}, & k \geq 2, \\
(\boldsymbol{J})_{1,l} &= -4\pi\rho\Im\left\{\hat{\boldsymbol{v}}_0{}^H\boldsymbol{R}^{-1}\boldsymbol{T}^{l-2}\hat{\boldsymbol{v}}_0\right\}, & l \geq 2, \\
(\boldsymbol{J})_{k,l} &= 8\pi^2\rho^2\Re\left\{\hat{\boldsymbol{v}}_0{}^H\boldsymbol{T}^{k-2}\boldsymbol{R}^{-1}\boldsymbol{T}^{l-2}\hat{\boldsymbol{v}}_0\right\}, & k,l \geq 2.
\end{aligned}\right\} \tag{5.8}$$

For white noise, this is

$$\begin{aligned}
(\boldsymbol{J})_{1,1} &= 2\textstyle\sum_{n=1}^{N} a^2(t_n), \\
(\boldsymbol{J})_{k,1} &= 0, & k \geq 2, \\
(\boldsymbol{J})_{1,l} &= 0, & l \geq 2, \\
(\boldsymbol{J})_{k,l} &= 8\pi^2\rho^2\textstyle\sum_{n=1}^{N} a^2(t_n)\,t_n^{k+l-4}, & k,l \geq 2.
\end{aligned}$$

$$
\boldsymbol{J} = \begin{bmatrix}
2\Re\left\{\boldsymbol{v}_0{}^H \boldsymbol{A}\boldsymbol{R}^{-1}\boldsymbol{A}\boldsymbol{v}_0\right\} & 2\rho\Re\left\{\boldsymbol{v}_0{}^H \boldsymbol{A}\boldsymbol{R}^{-1}\boldsymbol{B}\boldsymbol{v}_0\right\} \\
2\rho\Re\left\{\boldsymbol{v}_0{}^H \boldsymbol{B}^H\boldsymbol{R}^{-1}\boldsymbol{A}\boldsymbol{v}_0\right\} & 2\rho^2\Re\left\{\boldsymbol{v}_0{}^H \boldsymbol{B}^H\boldsymbol{R}^{-1}\boldsymbol{B}\boldsymbol{v}_0\right\} \\
4\pi\rho\Im\left\{\boldsymbol{v}_0{}^H \boldsymbol{A}\boldsymbol{R}^{-1}\boldsymbol{A}\boldsymbol{v}_0\right\} & 4\pi\rho^2\Im\left\{\boldsymbol{v}_0{}^H \boldsymbol{A}\boldsymbol{R}^{-1}\boldsymbol{B}\boldsymbol{v}_0\right\} \\
4\pi\rho\Im\left\{\boldsymbol{v}_0{}^H \boldsymbol{A}\boldsymbol{T}\boldsymbol{R}^{-1}\boldsymbol{A}\boldsymbol{v}_0\right\} & 4\pi\rho^2\Im\left\{\boldsymbol{v}_0{}^H \boldsymbol{A}\boldsymbol{T}\boldsymbol{R}^{-1}\boldsymbol{B}\boldsymbol{v}_0\right\} \\
4\pi\rho\Im\left\{\boldsymbol{v}_0{}^H \boldsymbol{A}\boldsymbol{T}^2\boldsymbol{R}^{-1}\boldsymbol{A}\boldsymbol{v}_0\right\} & 4\pi\rho^2\Im\left\{\boldsymbol{v}_0{}^H \boldsymbol{A}\boldsymbol{T}^2\boldsymbol{R}^{-1}\boldsymbol{B}\boldsymbol{v}_0\right\} \\
\vdots & \vdots
\end{bmatrix}
$$

$$
\begin{bmatrix}
-4\pi\rho\Im\left\{\boldsymbol{v}_0{}^H \boldsymbol{A}\boldsymbol{R}^{-1}\boldsymbol{A}\boldsymbol{v}_0\right\} & -4\pi\rho\Im\left\{\boldsymbol{v}_0{}^H \boldsymbol{A}\boldsymbol{R}^{-1}\boldsymbol{T}\boldsymbol{A}\boldsymbol{v}_0\right\} \\
-4\pi\rho^2\Im\left\{\boldsymbol{v}_0{}^H \boldsymbol{B}^H\boldsymbol{R}^{-1}\boldsymbol{A}\boldsymbol{v}_0\right\} & -4\pi\rho^2\Im\left\{\boldsymbol{v}_0{}^H \boldsymbol{B}^H\boldsymbol{R}^{-1}\boldsymbol{T}\boldsymbol{A}\boldsymbol{v}_0\right\} \\
8\pi^2\rho^2\Re\left\{\boldsymbol{v}_0{}^H \boldsymbol{A}\boldsymbol{R}^{-1}\boldsymbol{A}\boldsymbol{v}_0\right\} & 8\pi^2\rho^2\Re\left\{\boldsymbol{v}_0{}^H \boldsymbol{A}\boldsymbol{R}^{-1}\boldsymbol{T}\boldsymbol{A}\boldsymbol{v}_0\right\} \\
8\pi^2\rho^2\Re\left\{\boldsymbol{v}_0{}^H \boldsymbol{A}\boldsymbol{T}\boldsymbol{R}^{-1}\boldsymbol{A}\boldsymbol{v}_0\right\} & 8\pi^2\rho^2\Re\left\{\boldsymbol{v}_0{}^H \boldsymbol{A}\boldsymbol{T}\boldsymbol{R}^{-1}\boldsymbol{T}\boldsymbol{A}\boldsymbol{v}_0\right\} \\
8\pi^2\rho^2\Re\left\{\boldsymbol{v}_0{}^H \boldsymbol{A}\boldsymbol{T}^2\boldsymbol{R}^{-1}\boldsymbol{A}\boldsymbol{v}_0\right\} & 8\pi^2\rho^2\Re\left\{\boldsymbol{v}_0{}^H \boldsymbol{A}\boldsymbol{T}^2\boldsymbol{R}^{-1}\boldsymbol{T}\boldsymbol{A}\boldsymbol{v}_0\right\} \\
\vdots & \vdots
\end{bmatrix}
$$

$$
\begin{bmatrix}
-4\pi\rho\Im\left\{\boldsymbol{v}_0{}^H \boldsymbol{A}\boldsymbol{R}^{-1}\boldsymbol{T}^2\boldsymbol{A}\boldsymbol{v}_0\right\} & \cdots \\
-4\pi\rho^2\Im\left\{\boldsymbol{v}_0{}^H \boldsymbol{B}^H\boldsymbol{R}^{-1}\boldsymbol{T}^2\boldsymbol{A}\boldsymbol{v}_0\right\} & \cdots \\
8\pi^2\rho^2\Re\left\{\boldsymbol{v}_0{}^H \boldsymbol{A}\boldsymbol{R}^{-1}\boldsymbol{T}^2\boldsymbol{A}\boldsymbol{v}_0\right\} & \cdots \\
8\pi^2\rho^2\Re\left\{\boldsymbol{v}_0{}^H \boldsymbol{A}\boldsymbol{T}\boldsymbol{R}^{-1}\boldsymbol{T}^2\boldsymbol{A}\boldsymbol{v}_0\right\} & \cdots \\
8\pi^2\rho^2\Re\left\{\boldsymbol{v}_0{}^H \boldsymbol{A}\boldsymbol{T}^2\boldsymbol{R}^{-1}\boldsymbol{T}^2\boldsymbol{A}\boldsymbol{v}_0\right\} & \cdots \\
\vdots & \ddots
\end{bmatrix}. \tag{5.7}
$$

For white noise, $w = 0$, $\boldsymbol{A} = \boldsymbol{I}$ and $\boldsymbol{\theta} = [\theta_1, \theta_2]^T$, the matrix becomes

$$
\boldsymbol{J} = \frac{1}{\sigma^2}\begin{bmatrix}
2N & 0 & 0 & 0 \\
0 & 8\pi^2\rho^2 N & 8\pi^2\rho^2\textstyle\sum_k t_k & 8\pi^2\rho^2\textstyle\sum_k t_k^2 \\
0 & 8\pi^2\rho^2\textstyle\sum_k t_k & 8\pi^2\rho^2\textstyle\sum_k t_k^2 & 8\pi^2\rho^2\textstyle\sum_k t_k^3 \\
0 & 8\pi^2\rho^2\textstyle\sum_k t_k^2 & 8\pi^2\rho^2\textstyle\sum_k t_k^3 & 8\pi^2\rho^2\textstyle\sum_k t_k^4
\end{bmatrix}. \tag{5.9}
$$

This second order case is of interest since it equates to the simplified azimuthal response of the moving target in a SAR scene (Section 2.3).

Since absolute times $\{t_k\}$ are referred to, it is necessary to specify a reference, here denoted t_0, relative to the origin. For uniform sampling, let the times be centred on t_0:

$$
t_k = \left[(k-1) - \frac{N-1}{2}\right] t_s + t_0, \; k = 1, \ldots, N,
$$

where t_s is the sampling interval.

Using Equation (5.5), we get

$$\left.\begin{aligned}
\mathrm{CRLB}\{\hat{\rho}\} &= \sigma^2/(2N), \\
\mathrm{CRLB}\left\{\hat{\phi}\right\} &= \frac{3}{32}\frac{\sigma^2}{\rho^2}\frac{t_s{}^4[N^2(3N^2-10)+7]+24t_0^2[10t_0^2-t_s{}^2(N^2+1)]}{\pi^2 t_s{}^4 N(N^4-5N^2+4)}, \\
\mathrm{CRLB}\left\{\hat{\theta}_1\right\} &= \frac{3}{2\pi^2}\frac{\sigma^2}{\rho^2}\frac{[t_s{}^2(N^2-4)+60t_0^2]}{t_s{}^4 N(N^4-5N^2+4)}, \text{ and} \\
\mathrm{CRLB}\left\{\hat{\theta}_2\right\} &= \frac{45}{2\pi^2}\frac{\sigma^2}{\rho^2}\frac{1}{t_s{}^4 N(N^4-5N^2+4)}.
\end{aligned}\right\} \quad (5.10)$$

(Note that σ^2/ρ^2 is the signal to noise ratio.)

Some of the Cramér-Rao lower bounds therefore depend on t_0, which is not intuitive, although the effect was observed for the simpler problem of estimating both ϕ and θ_1 by Rife and Boorsteyn (1974, p. 592), who stated that the minimum Cramér-Rao lower bound on $\hat{\phi}$ was obtained by choosing $t_0 = -\left(\frac{N-1}{2}\right)t_s$. An explanation is that the parameters form part of the model of the continuous function $y(t)$, which is valid for all time. By finding the phase we are implicitly specifying the value of the function at $t = 0$. For the linear phase case it can intuitively be seen that choosing the centralised $t_0 = -\left(\frac{N-1}{2}\right)t_s$ minimises the variance of the y intercept.

However, it transpires that the lower variance bound for phase in Equation (5.10) reaches a minimum when the sample times are centred on $t_0 = \pm\sqrt{t_s{}^2(N^2+1)/20}$, a significant departure from 0. Whilst this is an interesting phenomenon, it will not be discussed further here.

The most appropriate t_0 to use may be found by arranging the cross terms in the Fisher information matrix Equation (5.9) to be 0. With the uniform sampling scheme described above, this happens when $t_0 = 0$: elements with sums of t to odd powers become zero, so the bounds become

$$\left.\begin{aligned}
\mathrm{CRLB}\{\hat{\rho}\} &= \sigma^2/(2N), \\
\mathrm{CRLB}\left\{\hat{\phi}\right\} &= \frac{3}{32\pi^2}\frac{\sigma^2}{\rho^2}\frac{3N^2-7}{N(N^2-4)}, \\
\mathrm{CRLB}\left\{\hat{\theta}_1\right\} &= \frac{3}{2\pi^2}\frac{\sigma^2}{\rho^2}\frac{1}{t_s{}^2 N(N^2-1)}, \text{ and} \\
\mathrm{CRLB}\left\{\hat{\theta}_2\right\} &= \frac{45}{2\pi^2}\frac{\sigma^2}{\rho^2}\frac{1}{t_s{}^4 N(N^4-5N^2+4)}.
\end{aligned}\right\} \quad (5.11)$$

For non-uniform samples, we have

$$t_k = \sum_{i=0}^{k-1} \tau_i, \; k = 1, \ldots, N,$$

where the $\{\tau_i\}$ is the interval between samples t_i and t_{i+1}, τ_0 being the offset of t_1 from $t_0 = t = 0$. For the sum of the times to be zero, we have

$$\tau_0 = \frac{1}{N} \sum_{i=0}^{N-1} (i - N)\tau_i, \tag{5.12}$$

so t_0 is intuitively positioned at the 'centre of gravity' of the times. For the sum of cubed times to be zero, we need to solve the cubic equation

$$\sum_{k=1}^{N} \left(\tau_0 + \sum_{i=1}^{k-1} \tau_i \right)^3 = 0.$$

Since this will give a different result to Equation (5.12) in general, the value of τ_0 to be used is not clear; the global minimum of the Cramér-Rao lower bounds may need to be found.

5.5 Random Sampling

Provided the sampling times are fixed, the Cramér-Rao lower bounds in the coloured Gaussian case can be found using Equations (5.7) and (5.5). However, of particular interest here are the effects of *random* sampling on the parameter estimation accuracy. If the times are specified in terms of distributions $p_{\mathbf{T}}(\boldsymbol{t})$ rather than specific instants, it is desirable to know the *expected* Cramér-Rao lower bounds. An additional complication is a variable time delay between the actual sample times and the times used for processing the data, which models the effects of an unknown radar position at the time of transmission. The situation is shown in Figure 5.2. The model of the data is now

$$\boldsymbol{y}(\boldsymbol{t}) = \rho e^{j2\pi\phi} \boldsymbol{v}_0(\boldsymbol{\theta}, \boldsymbol{t} + \boldsymbol{\delta}) + \boldsymbol{n},$$

where $\boldsymbol{\delta}$ is an $N \times 1$ vector containing the random timing errors, which are assumed to have the form $\boldsymbol{\delta} \sim \mathcal{N}_N\left(0, \sigma_\delta^2\right)$. (This aspect of the problem is similar to work of Swingler (1996), who approximated the Cramér-Rao lower bound for frequency estimates with sampling jitter.)

If the sampling times were not known at all, the vector of unknowns would be $\boldsymbol{u}'' =$

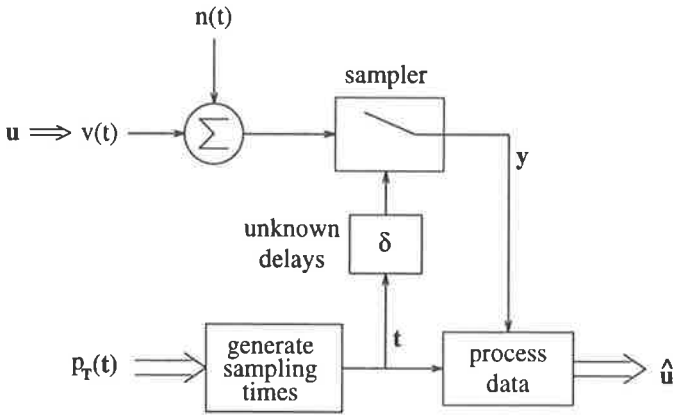

Figure 5.2: A representation of the random sampling estimation scenario. The sampling times are randomly distributed, but approximately known.

$[\boldsymbol{u}^T, \sigma_\delta^2, \boldsymbol{t}^T]^T$ and the Fisher information matrix would be

$$(\boldsymbol{J}'')_{k,l} = \mathrm{E}_{Y,U''}\left[\frac{\partial \ln p(\boldsymbol{y},\boldsymbol{u}'')}{\partial(\boldsymbol{u}'')_k}\frac{\partial \ln p(\boldsymbol{y},\boldsymbol{u}'')}{\partial(\boldsymbol{u}'')_l}\right]$$

(which is similar to (Van Trees 1968)), where $p(\boldsymbol{y},\boldsymbol{u}'')$ is the joint PDF of the measurements and unknowns. Note that the expectation is over the sample spaces of both the random measurements and the random unknowns. The unknowns' PDF $p_{U''}(\boldsymbol{u}'')$ implicitly appears as *a priori* information (via the conditional probability expression $p(\boldsymbol{y},\boldsymbol{u}'') = p(\boldsymbol{y}|\boldsymbol{u}'')\,p_{U''}(\boldsymbol{u}'')$). It is assumed here, however, that the nominal sampling times $\boldsymbol{t}$ are *known*, but differ from one realisation to the next. Therefore, let $\boldsymbol{u}' = [\boldsymbol{u}^T, \sigma_\delta^2]^T$ be the vector of unknowns. There are two clear approaches to finding the expected Cramér-Rao lower bounds:

1. Find the expectation of the bounds assuming constant transmission times with respect to the known timing distributions

$$\mathrm{E}_T[\mathrm{CRLB}\{(\boldsymbol{u}')_i\}] = \int_{\mathbf{T}} \mathrm{CRLB}\{(\boldsymbol{u}')_i;\boldsymbol{t}\}\,p_{\mathbf{T}}(\boldsymbol{t})\,d\boldsymbol{t}. \tag{5.13}$$

   This is an intuitive method; however, its true meaning is not clear.

2. Since the likelihood function now contains random (but known) times, $p_{\mathbf{T}}(\boldsymbol{t})$ should be incorporated into the Fisher information matrix (Equation (5.6)):

$$(\boldsymbol{J}')_{k,l} \triangleq \mathrm{E}_{Y,\Delta,T}\left[\frac{\partial \ln p(\boldsymbol{y},\boldsymbol{t};\boldsymbol{u}')}{\partial(\boldsymbol{u}')_k}\frac{\partial \ln p(\boldsymbol{y},\boldsymbol{t};\boldsymbol{u}')}{\partial(\boldsymbol{u}')_l}\right]. \tag{5.14}$$

$p(\boldsymbol{y}, \boldsymbol{t}; \boldsymbol{u}')$ is the joint probability density function of the sampled signal and the transmission times, parameterised by the unknowns. The expectation is now over the sample spaces of the random measurements, the unknown delays and the random measurement times.

This is the approach which has been adopted here.

Using a conditional probability expression,

$$p(\boldsymbol{y}, \boldsymbol{t}; \boldsymbol{u}') = p(\boldsymbol{y}|\boldsymbol{t}; \boldsymbol{u}')\, p_{\mathbf{T}}(\boldsymbol{t}; \boldsymbol{u}'),$$

and letting $p_{\mathbf{T}}(\boldsymbol{t}; \boldsymbol{u}') = p_{\mathbf{T}}(\boldsymbol{t})$, since the sampling times do not depend upon the parameters, from Equation (5.14)

$$\begin{aligned}
(\boldsymbol{J}')_{k,l} &= \mathrm{E}_{\mathbf{Y},\Delta,\mathbf{T}}\left[\frac{\partial \ln(p(\boldsymbol{y}|\boldsymbol{t}; \boldsymbol{u}')\, p_{\mathbf{T}}(\boldsymbol{t}))}{\partial(\boldsymbol{u}')_k} \frac{\partial \ln(p(\boldsymbol{y}|\boldsymbol{t}; \boldsymbol{u}')\, p_{\mathbf{T}}(\boldsymbol{t}))}{\partial(\boldsymbol{u}')_l}\right] \\
&= \mathrm{E}_{\mathbf{Y},\Delta,\mathbf{T}}\left[\frac{\partial\{\ln p(\boldsymbol{y}|\boldsymbol{t}; \boldsymbol{u}') + \ln p_{\mathbf{T}}(\boldsymbol{t})\}}{\partial(\boldsymbol{u}')_k} \frac{\partial\{\ln p(\boldsymbol{y}|\boldsymbol{t}; \boldsymbol{u}') + \ln p_{\mathbf{T}}(\boldsymbol{t})\}}{\partial(\boldsymbol{u}')_l}\right] \\
&= \mathrm{E}_{\mathbf{Y},\Delta,\mathbf{T}}\left[\frac{\partial \ln p(\boldsymbol{y}|\boldsymbol{t}; \boldsymbol{u}')}{\partial(\boldsymbol{u}')_k} \frac{\partial \ln p(\boldsymbol{y}|\boldsymbol{t}; \boldsymbol{u}')}{\partial(\boldsymbol{u}')_l}\right].
\end{aligned}$$

With σ_δ^2 assumed to be zero, our vector of unknowns is just $\boldsymbol{u}$ and we have

$$\begin{aligned}
(\boldsymbol{J}')_{k,l} &= \int_{\mathbf{T}} \int_{\mathbf{Y}} \frac{\partial \ln p(\boldsymbol{y}|\boldsymbol{t}; \boldsymbol{u})}{\partial(\boldsymbol{u})_k} \frac{\partial \ln p(\boldsymbol{y}|\boldsymbol{t}; \boldsymbol{u})}{\partial(\boldsymbol{u})_l} p(\boldsymbol{y}, \boldsymbol{t}; \boldsymbol{u})\, d\boldsymbol{y}\, d\boldsymbol{t}. \\
&= \int_{\mathbf{T}} \left[\int_{\mathbf{Y}} \frac{\partial \ln p(\boldsymbol{y}|\boldsymbol{t}; \boldsymbol{u})}{\partial(\boldsymbol{u})_k} \frac{\partial \ln p(\boldsymbol{y}|\boldsymbol{t}; \boldsymbol{u})}{\partial(\boldsymbol{u})_l} p(\boldsymbol{y}|\boldsymbol{t}; \boldsymbol{u})\, d\boldsymbol{y}\right] p_{\mathbf{T}}(\boldsymbol{t})\, d\boldsymbol{t} \\
&= \int_{\mathbf{T}} (\boldsymbol{J})_{k,l}\, p_{\mathbf{T}}(\boldsymbol{t})\, d\boldsymbol{t} \\
&= \mathrm{E}_{\mathbf{T}}[(\boldsymbol{J})_{k,l}],
\end{aligned}$$

where $\boldsymbol{J}$ was defined in Equation (5.6). The final result is similar in concept to Equation (5.13), except that the expectation is over the Fisher matrix elements rather than the Cramér-Rao lower bounds.

$\boldsymbol{J}$'s elements (Equation (5.7)) can be written in the form

$$(\boldsymbol{J})_{k,l} = \alpha(k,l)\, f\{\boldsymbol{w}^H(k)\boldsymbol{R}^{-1}\boldsymbol{x}(l)\},$$

where $f\{\cdot\}$ extracts the real or imaginary part, so

$$(\boldsymbol{J}')_{k,l} = \alpha(k,l)\, f\left\{\int_{\mathbf{T}} \boldsymbol{w}^H(k)\boldsymbol{R}^{-1}\boldsymbol{x}(l)\, p_{\mathbf{T}}(\boldsymbol{t})\, d\boldsymbol{t}\right\}. \tag{5.15}$$

$\boldsymbol{R}^{-1}$ cannot readily be simplified since the covariance matrix entries are in the form $(\boldsymbol{R})_{m,n} = r(t_m - t_n)$: they are a function of the variables being integrated over.

In the case of white noise, Equation (5.15) becomes

$$(\boldsymbol{J}')_{k,l} = \frac{\alpha(k,l)}{\sigma^2} f\left\{\int_{\mathbf{T}} \boldsymbol{w}^H(k)\boldsymbol{x}(l)\, p_{\mathbf{T}}(\boldsymbol{t})\, d\boldsymbol{t}\right\}.$$

For w known to be 0, this is

$$\begin{aligned}
(\boldsymbol{J}')_{k,l} &= \frac{\alpha'(k,l)}{\sigma^2} f\left\{\int_{\mathbf{T}} \hat{\boldsymbol{v}}_0{}^H \boldsymbol{T}^{g(k,l)}\, \hat{\boldsymbol{v}}_0\, p_{\mathbf{T}}(\boldsymbol{t})\, d\boldsymbol{t}\right\} \\
&= \frac{\alpha'(k,l)}{\sigma^2} f\left\{\sum_n \int_{\mathbf{T}} (\hat{\boldsymbol{v}}_0)_n^*\, a^2(t_n)\, t_n^{g(k,l)} (\hat{\boldsymbol{v}}_0)_n\, p_{\mathbf{T}}(\boldsymbol{t})\, d\boldsymbol{t}\right\}, \\
&= \frac{\alpha'(k,l)}{\sigma^2} f\left\{\sum_n \int_{\mathbf{T}} a^2(t_n)\, t_n^{g(k,l)}\, p_{\mathbf{T}}(\boldsymbol{t})\, d\boldsymbol{t}\right\},
\end{aligned}$$

since the phase terms cancel. The superscript * indicates the conjugation operation. Here

$$\alpha'(k,l) = \begin{cases} 2, & k = l = 1, \\ 4\pi\rho, & k > 1, l = 1, \\ -4\pi\rho, & k = 1, l > 1, \\ 8\pi^2\rho^2, & k, l > 1 \end{cases}$$

and $g(k,l)$ expresses the powers of t:

$$g(k,l) = \begin{cases} 0, & k = l = 1, \\ k + l - 4, & k, l \geq 2, \\ \text{undefined}, & \text{otherwise.} \end{cases}$$

If the PDFs are independent, we have

$$\begin{aligned}
(\boldsymbol{J}')_{k,l} &= \frac{\alpha'(k,l)}{\sigma^2} f\left\{\sum_n \int_{T_N} \cdots \int_{T_2}\int_{T_1} a^2(t_n)\, t_n^{g(k,l)} \prod_m p_{T_m}(t_m)\, dt_1\, dt_2 \cdots dt_N\right\} \\
&= \frac{\alpha'(k,l)}{\sigma^2} f\left\{\sum_n \int_{T_n} a^2(t_n)\, t_n^{g(k,l)}\, p_{T_n}(t)\, dt\right\},
\end{aligned}$$

and

$$(\boldsymbol{J}')_{k,l} = \frac{\alpha'(k,l)}{\sigma^2} N f\left\{\int_T a^2(t_n)\, t^{g(k,l)}\, p_T(t)\, dt\right\}$$

if the PDFs are the same. (Note that if $a(t) = 1\ \forall t$ the argument of f is the $g(k,l)^{\text{th}}$ moment of the PDF of t.)

5.5.1 Example Sampling Distributions

The timing specifications for several sampling schemes were discussed in Section 2.7.6.

Known times If the sampling times are known, so that

$$p_{T_n}(t) = \delta(t - t_n)\ \forall n,$$

where $\delta(t)$ is the Dirac delta function, it can easily be shown that $\boldsymbol{J}' = \boldsymbol{J}$.

Random offsets If there are random offsets from uniform samples centred on $t = 0$ (*i.e.*, jitter), we have

$$t_n = \left(n - 1 - \frac{N-1}{2}\right) t_s + \mathcal{U}(0, bt_s),\ n = 1, \ldots, N,$$

as discussed in Section 3.7.1, where

$$\mathcal{U}_x(\mu, s) \triangleq \begin{cases} 1/(2s), & \mu - s \leq x \leq \mu + s, \\ 0, & \text{otherwise,} \end{cases}$$

for uniformly distributed offsets. Then

$$p_{T_n}(t) = \mathcal{U}([n - 1 - (N-1)/2]t_s, bt_s).$$

The duration of the measurement is then slightly greater than with uniform sampling, as mentioned in Section 3.7.1, since the PDFs of the extreme samples extend earlier and later than the respective nominal values.

It can be shown that, for w known to be 0 and $\boldsymbol{A} = \boldsymbol{I}$,

$$\left.\begin{aligned}
(\boldsymbol{J}')_{1,1} &= 2N/\sigma^2, \\
(\boldsymbol{J}')_{k+2,1} &= 0, \\
(\boldsymbol{J}')_{1,k+2} &= 0, \text{ and} \\
(\boldsymbol{J}')_{k+2,l+2} &= \frac{8\pi^2\rho^2}{\sigma^2}\frac{1}{2b(k+l+1)}\sum_{n=1}^{N}\{[n-1-(N-1)/2]t_s+b\}^{k+l+1} \\
&\qquad -\{[n-1-(N-1)/2]t_s-b\}^{k+l+1}.
\end{aligned}\right\} \tag{5.16}$$

Of course, if $b \to 0$ these PDFs approaches delta functions: the Fisher matrix result is the same as for uniform sample times discussed above.

Uniformly distributed over whole interval In this case, for all n,

$$p_{T_n}(t) = \begin{cases} 1/(2b_w), & -b_w \le t \le b_w, \\ 0, & \text{otherwise.} \end{cases}$$

This distribution may be approximated in practice by using random intervals between samples; the distribution of the intervals is of no real importance when N is large. (Section 2.7.6 discussed this.)

It can be shown that, for w known to be 0 and $\boldsymbol{A} = \boldsymbol{I}$,

$$\begin{aligned}
(\boldsymbol{J}')_{1,1} &= 2N/\sigma^2, \\
(\boldsymbol{J}')_{k+2,1} &= 0, \\
(\boldsymbol{J}')_{1,k+2} &= 0, \text{ and} \\
(\boldsymbol{J}')_{k+2,l+2} &= \begin{cases} 8\pi^2\dfrac{\rho^2}{\sigma^2}\dfrac{Nb_w^{k+l}}{(k+l+1)}, & k+l \text{ even}, \\ 0, & \text{otherwise.} \end{cases}
\end{aligned}$$

This is the same as the result achieved with random offsets (Equation (5.16)) where the offsets are $\pm 0.5t_s$. However, it is preferable to use random intervals in practice: the intervals may be constrained to have a minimum sampling time separation, unlike with random offsets, and there need only be a small degree of randomness; a large amount, such as $\pm 0.5t_s$, leads to a degree of unpredictability in performance (Bilinskis and Mikelsons 1992). This was also discussed in Section 2.7.2.

If $b_w = (N-1)t_s/2$, making the time span the same as for a uniform sequence, and $\boldsymbol{\theta} = [\theta_1, \theta_2]^T$, the corresponding Cramér-Rao lower bounds are

$$\left.\begin{aligned} \mathrm{CRLB}\{\hat{\rho}\} &= \sigma^2/(2N), \\ \mathrm{CRLB}\left\{\hat{\phi}\right\} &= \frac{9}{32\pi^2}\frac{\sigma^2}{\rho^2}\frac{1}{N}, \\ \mathrm{CRLB}\left\{\hat{\theta}_1\right\} &= \frac{3}{2\pi^2}\frac{\sigma^2}{\rho^2}\frac{1}{{t_s}^2 N(N-1)^2}, \text{ and} \\ \mathrm{CRLB}\left\{\hat{\theta}_2\right\} &= \frac{45}{2\pi^2}\frac{\sigma^2}{\rho^2}\frac{1}{{t_s}^4 N(N-1)^4}. \end{aligned}\right\} \tag{5.17}$$

This is *equivalent to Equation (5.11) for large* N, but larger for small N, meaning that the parameter estimation accuracy is the same for uniform and non-uniform sampling times with an infinite number of samples. (Increasing the interval b_w will not make them the same for finite N: the effects are non-linear.)

This result is expected: for random intervals, which approximate uniformly distributed samples, the noise floor of the sample spectrum near a single signal is very low, as shown in Figure 2.12. Intuitively, this implies that, once the signal has been identified, estimating its parameters may be done accurately.

Figure 5.3 shows a comparison between the Cramér-Rao lower bounds corresponding to uniform sampling (Equation (5.11)) and uniformly distributed random sampling (Equation (5.17)) as a function of the number of samples N. The variance $\sigma^2 = 1$, the squared amplitude $\rho^2 = 1$, the time offset w is known to be 0, the weights $\boldsymbol{A} = \boldsymbol{I}$ and sampling interval $t_s = 1$. There is a difference of only about 1 dB between the two when $N > 15$.

Random intervals Here the PDF of each sample depends upon the previous one:

$$t_1 = -(N-1)T_s/2; \;\; t_{n+1} = t_n + \tau_n.$$

For Gaussian offsets, $\tau_n \sim \mathcal{N}\left(t_s, \sigma^2\right)$:

$$\begin{aligned} p_{T_1}(t) &= \delta(t - [N-1]t_s/2), \\ p_{T_2}(t) &= \mathcal{N}\left([1-(N-1)/2]t_s, \sigma^2\right), \\ &\vdots \\ p_{T_n}(t) &= \mathcal{N}\left([n-1-(N-1)/2]t_s, [n-1]\sigma^2\right). \end{aligned}$$

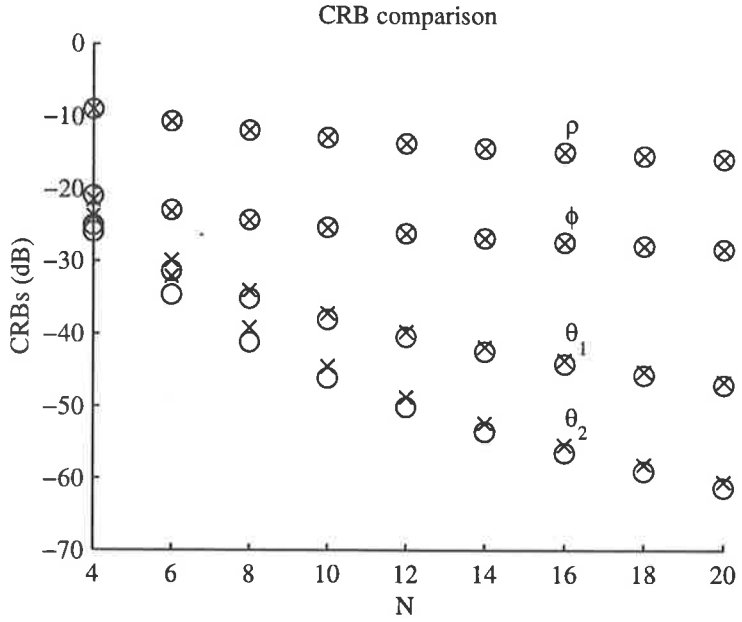

Figure 5.3: Cramér-Rao lower bounds for uniform sampling (o) and uniformly distributed random sampling (x) with normalised parameters and w known to be 0.

In this case,

$$(\boldsymbol{J}')_{k+2,l+2} = \frac{1}{\sqrt{2\pi\,(n-1)\nu^2}} \int_{-\infty}^{\infty} \exp\left(-\frac{[t-mt_s]^2}{2(n-1)\nu^2}\right) t^{k+l}\, dt,$$

where $m = (n - 1 - [N - 1]/2)t_s$. This is a difficult integral to evaluate for arbitrary $k + l$.

For large n and any non-trivial offset distribution, it is as if the offsets were Gaussian by the central limit theorem; in fact, $p_{T_n}(t)$ tend towards being uniformly distributed. This case was discussed above.

5.6 Simulations

Figure 5.4 shows the estimation errors obtained as a function of the noise variance when the four parameters ρ, ϕ, θ_1 and θ_2 were estimated with simulated data and uniform samples. The signal's magnitude ρ was 1, the number of samples N was 20, the sampling interval t_s was 2, the delay w was known to be 0, the amplitude term $a(t) = 1\ \forall t$, the phase parameter ϕ was 0.123, the frequency θ_1 was 0.106 and the frequency rate θ_2 0.01. 15 estimations were performed for each noise variance; the vertical bars in the figure show the corresponding 99% confidence intervals. The noise values were the same for each of the three simulations. The

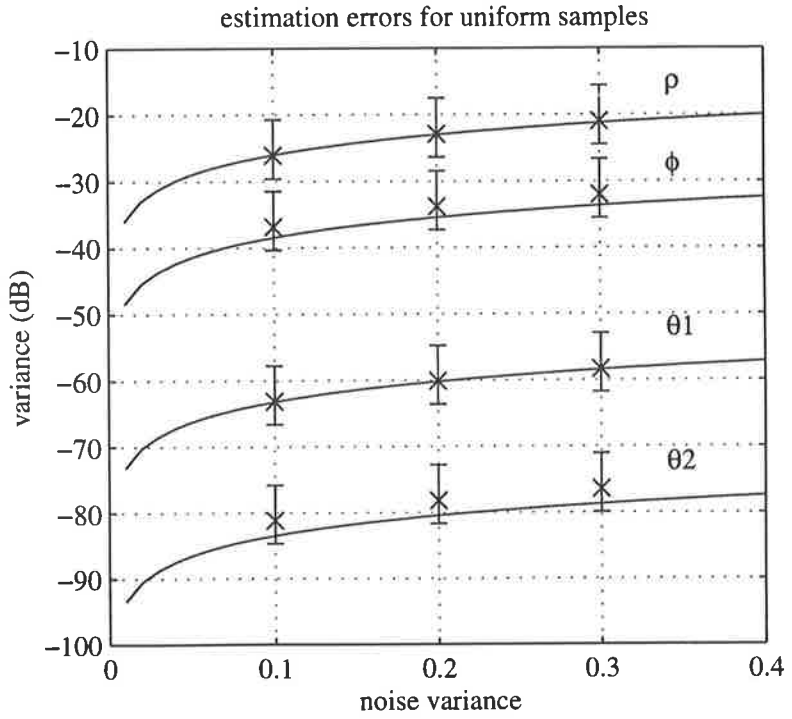

Figure 5.4: Estimation errors found by simulation with uniform sampling. The horizontal curves show the Cramér-Rao lower bounds.

antenna beam $a(t)$ was assumed to be unity as it only varies very slightly over 16 samples in the stripmapping SAR case.

Figure 5.5 shows the errors obtained during a similar simulation, but using uniformly distributed samples. The sample times were the same for each of the three noise variances. There is excellent agreement between the sample variances and the Cramér-Rao lower bounds in all cases.

5.7 Practical Considerations

Theoretically, the ML estimator demands that the parameters of the moving target be found by exhaustive search, since only then will the optimal estimates be obtained under conditions of arbitrarily poor signal to noise ratios. (This is also true for the detection problem, where the likelihood ratio needs to be evaluated with the exact target parameters in order to achieve the optimal detection performance.)

This is impractical, since there are too many combinations of parameters which have to be used in Equation (5.3). However, once an approximation to the result is known, the ML technique may be implemented using a variety of algorithms including gradient descent (*e.g.*, (Haykin 1991)) and expectation maximisation (*e.g.*, (Kay 1993)). In order for these algorithms

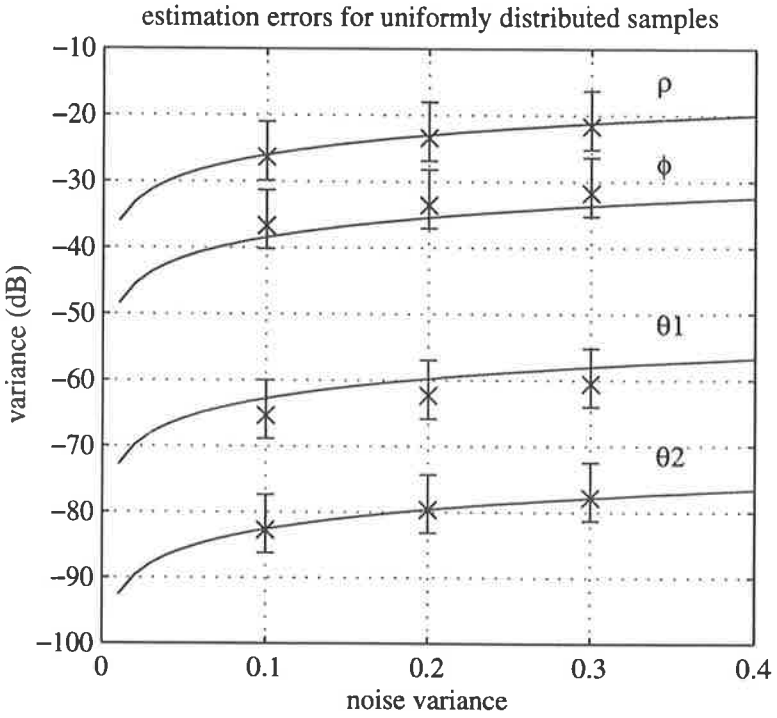

Figure 5.5: Estimation errors found using uniformly distributed samples.

to converge on the true parameters in an environment with a poor signal to noise ratio, they must be initialised with a good first approximation to the true parameters.

This gives rise to the idea of coarse parameter estimates which are used to initialise the ML algorithms. As mentioned previously, there is a 'threshold effect' which is a property of coarse evaluation methods when there is a low signal to noise ratio.

Section 4.6 discuss practical considerations relating to moving target detection with coarse parameter steps. These also apply to the problem of parameter estimation.

5.8 Actual Unknown Parameters

The derived Cramér-Rao lower bounds for the polynomial phase signal parameters can be related to the errors in estimating moving target azimuthal position and range and azimuthal velocities[3]. If the parameters of interest are stored in the $r \times 1$ vector $\boldsymbol{\alpha}$ and specified in terms of a continuous and differentiable r-dimensional function of the parameters $\boldsymbol{u}$, $\boldsymbol{\alpha} = \boldsymbol{g}(\boldsymbol{u})$, then the matrix

$$\boldsymbol{C} - \frac{\partial \boldsymbol{g}(\boldsymbol{u})}{\partial \boldsymbol{u}} \boldsymbol{J}^{-1} \frac{\partial \boldsymbol{g}(\boldsymbol{u})^T}{\partial \boldsymbol{u}} \geq \boldsymbol{0}$$

[3]The other moving target parameters are not of concern; see Section 3.4.2 for a discussion of the parameters which can be determined.

(meaning that the left hand side is non-negative definite) (Kay 1993, p. 45). The $r \times r$ matrix $\boldsymbol{C}$ contains the parameter covariance Cramér-Rao lower bound. This assumes that $\boldsymbol{\alpha}$ is real (which will almost certainly be true in practice).

Here, the parameters of interest are the azimuthal position y, range velocity $\dot{R}$ and azimuthal velocity $\dot{y}$: $\boldsymbol{\alpha} = [y, \dot{R}, \dot{y}]^T$. The unknowns in the model are $\boldsymbol{u} = [\rho, w, \phi, \theta_1, \theta_2]^T$. The model was $e^{j2\pi\phi}\boldsymbol{A}(\boldsymbol{t} - w\mathbf{1})\,\boldsymbol{v}_0(\boldsymbol{\theta}, \boldsymbol{t} - w\mathbf{1})$ where

$$(\boldsymbol{v}_0(\boldsymbol{\theta}, \boldsymbol{t}))_i \;=\; e^{j2\pi[\theta_1 t_i + \theta_2 t_i^2 + \ldots + \theta_K t_i^K]}.$$

Relating this to the structure of the azimuthal signal, Equations (4.1) and (4.2), gives

$$\boldsymbol{g} \;=\; \begin{bmatrix} v_p w \\ -\lambda\theta_1/2 \\ \sqrt{-\lambda R\theta_2} + v_p \end{bmatrix}.$$

(Note that θ_2 is half the Doppler frequency rate, F_{dr}.) Since

$$\frac{\partial \boldsymbol{g}(\boldsymbol{u})}{\partial \boldsymbol{u}} \;=\; \begin{bmatrix} 0 & v_p & 0 & 0 & 0 \\ 0 & 0 & 0 & -\lambda/2 & 0 \\ 0 & 0 & 0 & 0 & -\frac{1}{2}\lambda R(-\lambda R\theta_2)^{-1/2} \end{bmatrix},$$

$$\boldsymbol{C} \;\geq\; \begin{bmatrix} v_p^2\,\mathrm{CRLB}\{\hat{w}\} & -\frac{v_p\lambda}{2}\,\mathrm{Cov}\left[\hat{w}\hat{\theta}_1\right] & -\frac{v_p\lambda R}{2\sqrt{-\lambda R\theta_2}}\,\mathrm{Cov}\left[\hat{w}\hat{\theta}_2\right] \\ -\frac{v_p\lambda}{2}\,\mathrm{Cov}\left[\hat{\theta}_1\hat{w}\right] & \frac{\lambda^2}{4}\,\mathrm{CRLB}\left\{\hat{\theta}_1\right\} & \frac{\lambda^2 R}{4\sqrt{-\lambda R\theta_2}}\,\mathrm{Cov}\left[\hat{\theta}_1\hat{\theta}_2\right] \\ -\frac{v_p\lambda R}{2\sqrt{-\lambda R\theta_2}}\,\mathrm{Cov}\left[\hat{\theta}_2\hat{w}\right] & \frac{\lambda^2 R}{4\sqrt{-\lambda R\theta_2}}\,\mathrm{Cov}\left[\hat{\theta}_2\hat{\theta}_1\right] & -\frac{\lambda R}{4\theta_2}\,\mathrm{CRLB}\left\{\hat{\theta}_2\right\} \end{bmatrix}.$$

Therefore

$$\boxed{\begin{aligned} \mathrm{CRLB}\{\hat{y}\} \;&=\; (\boldsymbol{C})_{1,1} \;=\; v_p^2\,\mathrm{CRLB}\{\hat{w}\} \\ \mathrm{CRLB}\left\{\hat{\dot{R}}\right\} \;&=\; (\boldsymbol{C})_{2,2} \;=\; \left(\frac{\lambda}{2}\right)^2 \mathrm{CRLB}\left\{\hat{\theta}_1\right\}, \\ \mathrm{CRLB}\left\{\hat{\dot{y}}\right\} \;&=\; (\boldsymbol{C})_{3,3} \;=\; -\frac{\lambda R}{4\theta_2}\,\mathrm{CRLB}\left\{\hat{\theta}_2\right\}. \end{aligned}} \tag{5.18}$$

(Note that θ_2 will be negative, so $\mathrm{CRLB}\left\{\hat{\dot{y}}\right\}$ will be positive.)

For white noise, w known to be zero, a uniform antenna beam, uniform samples centred on

Parameter	Value(s)	Comments
range	29500 m	chosen to match the real data
platform velocity	70 m/s (140 kt)	
wavelength	3.2 cm (X-band)	
antenna beamwidth	1.5°	
Doppler bandwidth	115 Hz	(derived)
mean PRF	115 Hz	
target amplitude	assumed constant	since only a small aperture
target position	$y = 0$ m ($w = 0$ s)	unknown, except for Figure 5.11
clutter model	coloured Gaussian	as per Equation (4.8)
antenna beam pattern	$\text{sinc}^4(\cdot)$	as per Equation (B.4)
clutter to noise ratio	-80 dB	*i.e.*, white noise only
(CNR)	40 dB	clutter dominates
number of samples	64	to show the variation
processed	256	
signal to disturbance	0 dB	
ratio (SDR)	20 dB	
target Doppler centroid	$0 \rightarrow 5 \times$ Doppler	0 to about 25 kph towards
	bandwidth	the radar

Table 5.1: Parameters used for the parameter estimation examples. These are similar to those used for the moving target detection examples (Table 4.1) and the imaging examples (Table 6.1).

$t = 0$ and large N we have

$$\boxed{\begin{aligned} \text{CRLB}\left\{\hat{\dot{R}}\right\} &\approx \frac{3\lambda^2\sigma^2}{8\pi^2\rho^2T^2N^3}, \\ \text{CRLB}\left\{\hat{\dot{y}}\right\} &\approx \frac{-45\lambda R\sigma^2}{8\pi^2\theta_2\rho^2T^4N^5} \end{aligned}}$$

and $(C)_{1,2} = (C)_{2,1} = 0$.

5.8.1 *Numerical Examples*

The Cramér-Rao bounds for actual parameters were found using Equations (5.18) and (5.5) evaluated for the Fisher matrix given in Equations (5.7) and (5.8) for different combinations of parameters. Parameters common to the plots are shown in Table 5.1. The clutter is described by the power spectral density of Equation (4.8), and the antenna beam $a(t)$ is described by the corresponding pattern, Equation (B.4).

Figure 5.7	Uniform, high PRF (4 × Doppler BW).
Figure 5.8	An instance of random intervals (20% deviation from uniform); average PRF is 4 × Doppler BW.
Figure 5.9	Uniform, low PRF (equal to the Doppler BW).
Figure 5.10	An instance of random intervals (20% deviation from uniform); average PRF is the same as the Doppler BW.
Figure 5.11	Uniform, high PRF (4 × Doppler BW) with known position $y = 0$ (*i.e.*, $w = 0$). For white noise, the expected bounds for the non-uniform sampling case are the same as those for the uniform sampling case.

Table 5.2: A summary of the numerical example plots.

The plots are summarised in Table 5.2. The corresponding legend is shown in Figure 5.6.

The most important features of the plots are the variations with respect to the Doppler centroid, the clutter to noise ratio (CNR) and the sampling scheme. The numerical values are of less significance, since real world situations may deviate from the model. (For example, the target's motion may not be perfectly linear.)

In the white noise cases (with the low CNR), the Cramér-Rao lower bounds are uniform with respect to the target's Doppler centroid. This is expected since there is no frequency dependence.

In the coloured noise (high CNR) case in Figure 5.7, the bounds reflect the moving target aliasing phenomenon — at 4 times the Doppler bandwidth, the PRF, they are the same as for zero Hertz. This is clearly an undesirable situation.

The azimuthal velocity (Doppler rate) bound is interesting. It is clearly difficult to estimate this to any reasonable accuracy at low signal to disturbance ratio (SDR) with samples spanning a short duration, although it was found that spanning several seconds' worth of data has the potential to resolve fractions of metres per second.

The well known relationship between azimuthal position y and range velocity $\dot{R}$, Equation (2.14) (also derived in Chapter 3), implies that

$$y \propto \frac{R}{v_p}\dot{R}.$$

Therefore, it is expected that $\mathrm{CRLB}\{\hat{y}\} \propto \left(\frac{R}{v_p}\right)^2 \mathrm{CRLB}\left\{\hat{\dot{R}}\right\} = \left(\frac{29500}{70}\right)^2 \mathrm{CRLB}\left\{\hat{\dot{R}}\right\} \approx 178000\,\mathrm{CRLB}\left\{\hat{\dot{R}}\right\}$. This is true. For example, for the range velocity dot-dashed line in Figure 5.7, there is a bound of about $0.002\,\mathrm{m^2/s^2}$. 178000×0.002 is $300\,\mathrm{m^2}$, the azimuthal

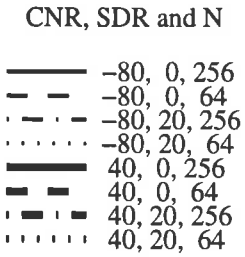

Figure 5.6: The legend for Figures 5.7–5.11.

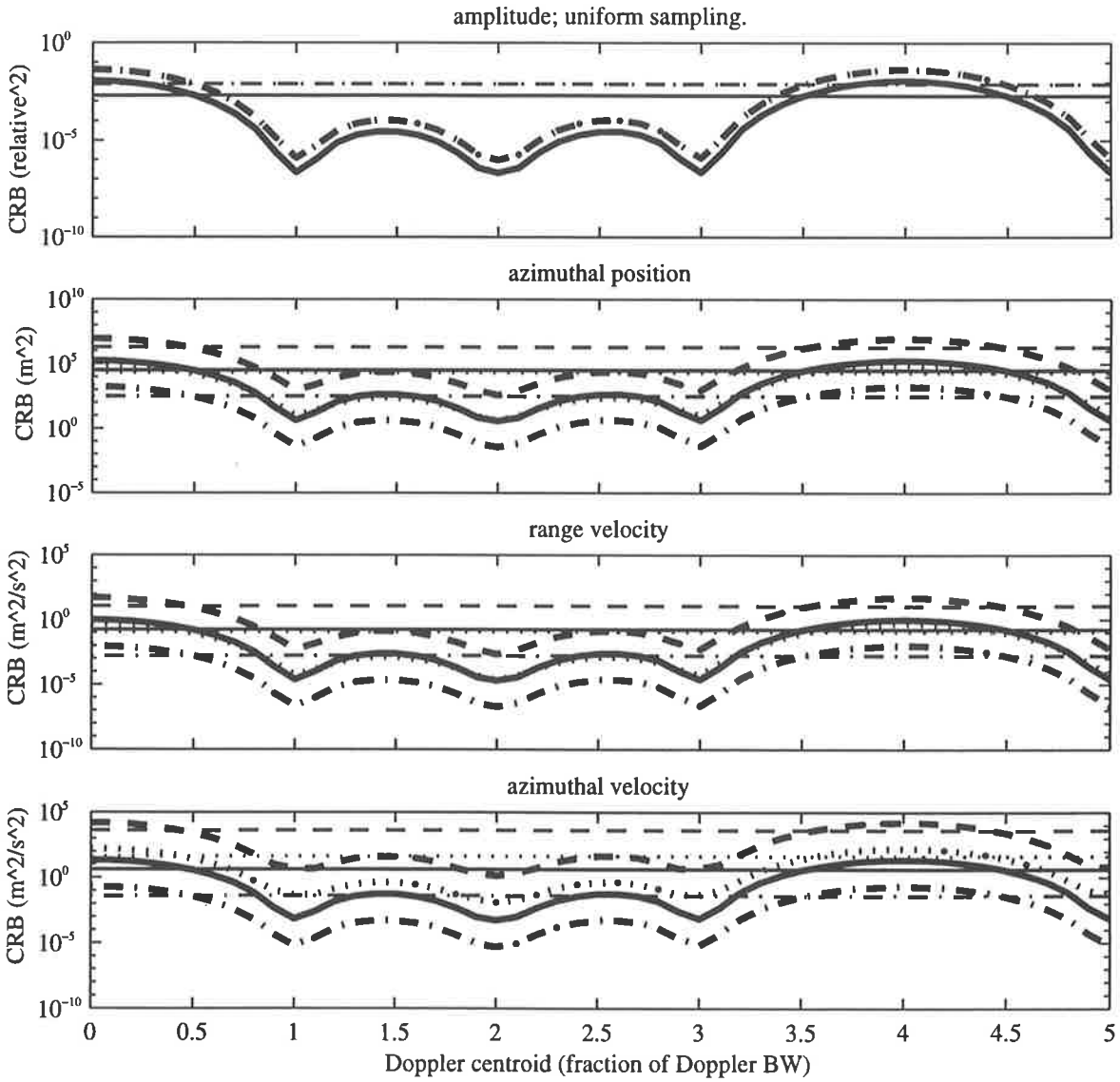

Figure 5.7: The amplitude, azimuthal position, range velocity and azimuthal velocity Cramér-Rao bounds as a function of Doppler centroid (expressed as a fraction of the Doppler bandwidth). The error in phase, CRLB$\left\{\hat{\phi}\right\}$, has not been shown as there is no value in estimating this parameter. The uniform PRF is four times the Doppler bandwidth.

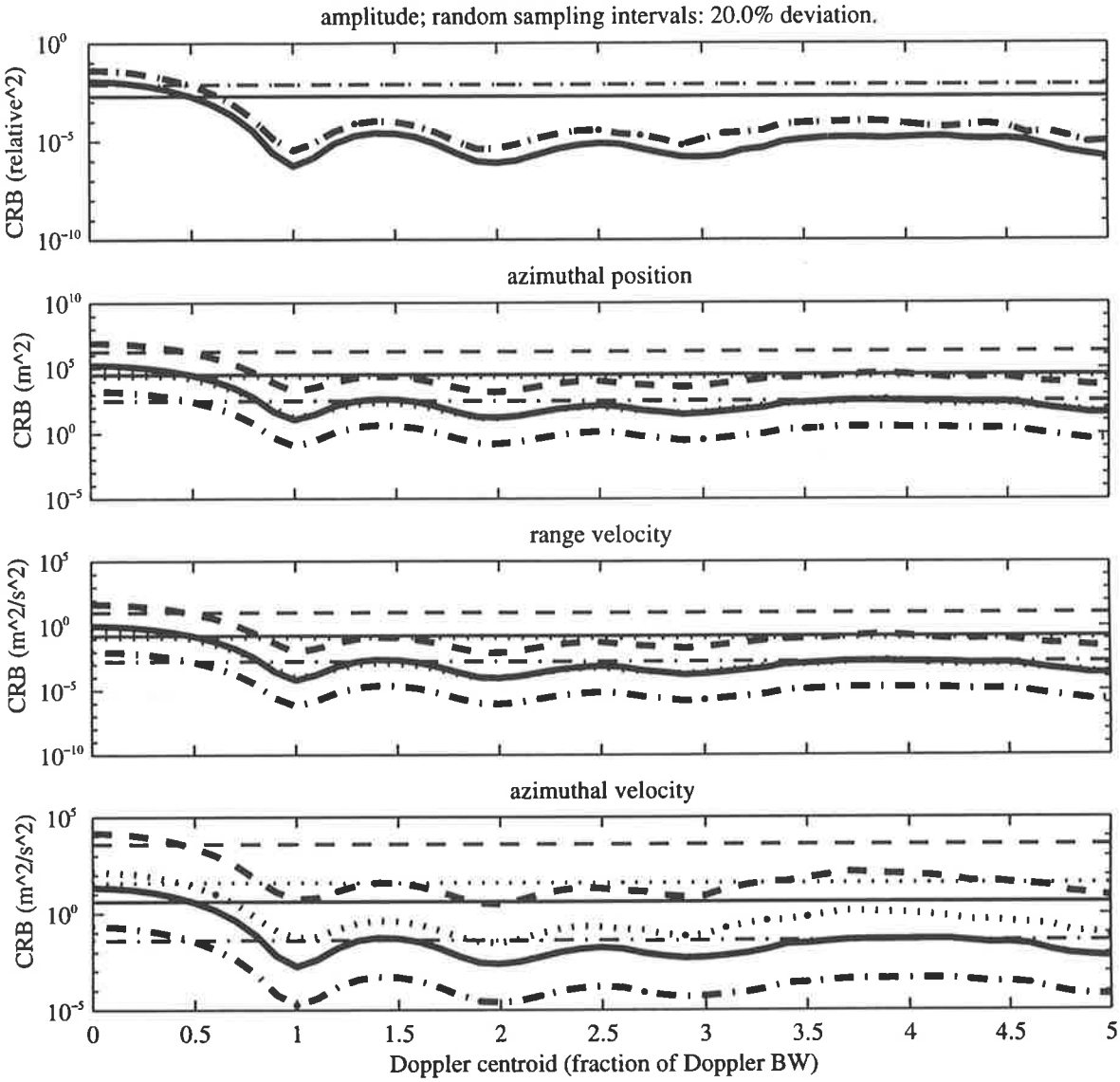

Figure 5.8: Cramér-Rao lower bounds: the non-uniform PRF averages four times the Doppler bandwidth.

position bound. y's inaccuracy may be explained by considering the number of samples processed, which is around a twentieth of the 3 dB antenna beamwidth for 256 points. (It was the irregular shape of the beam which determined w's accuracy.) From the bounds' variation with N it is apparent that a fourfold increase in the number of samples lowers the bounds by about 1.8 orders of magnitude. Therefore, assuming linearity, a factor of 20 should be equivalent to around 3.9 orders, giving a lower bound around 0.039 m^2 for a full aperture and 20 dB signal to disturbance ratio. The effects are believed to be non-linear, due to the increased slope of the antenna beam edges as more samples are used, reducing the bound below this. (It was found separately that there is an improvement of four magnitudes if the antenna beamwidth is reduced by a factor of ten, thereby making the shape of the antenna beam less linear.)

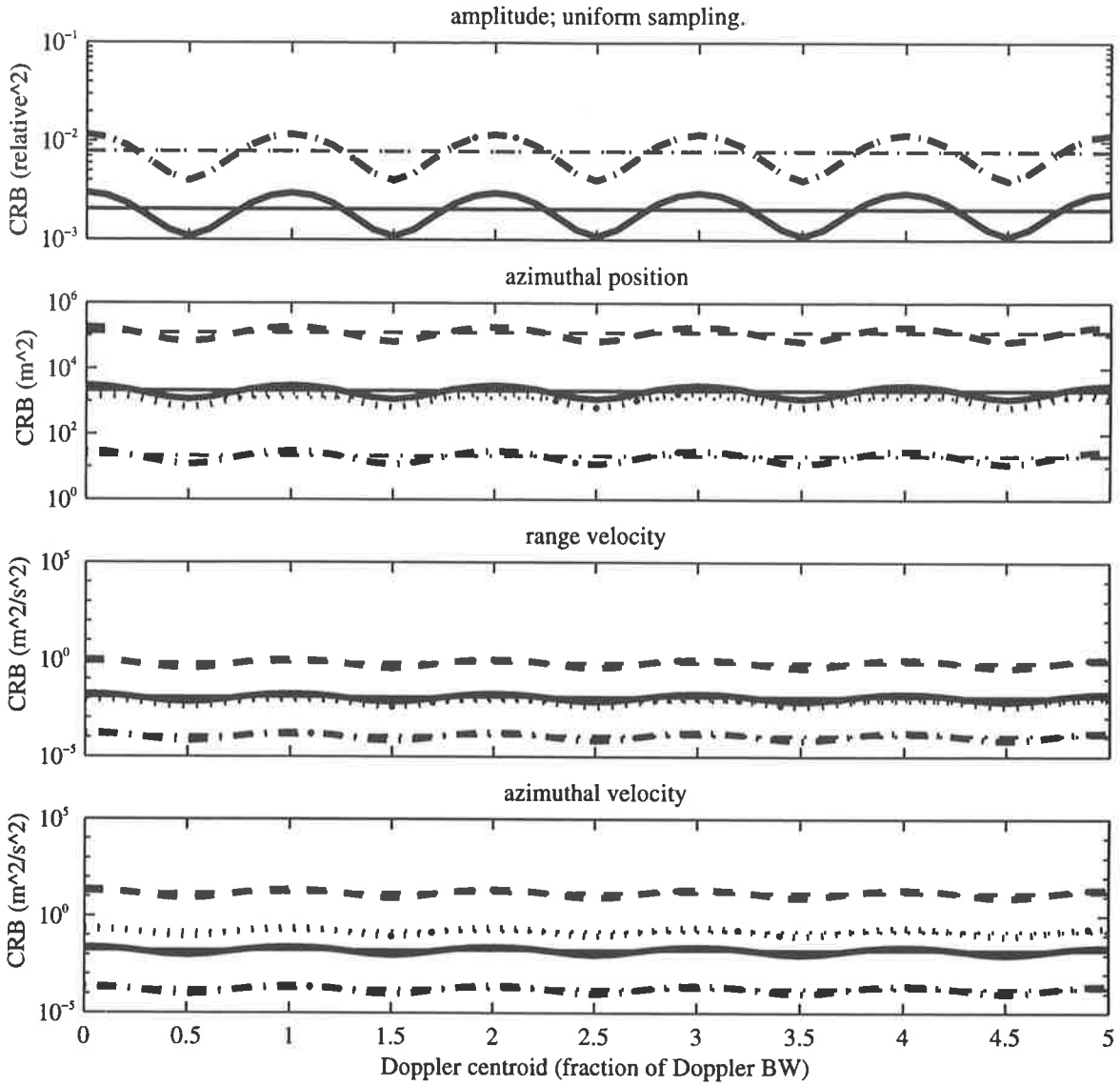

Figure 5.9: Cramér-Rao lower bounds: the uniform PRF averages the Doppler bandwidth.

It is clear from the model that the error in y could not be much greater than the width of the real antenna beam, which is of the order of many hundreds of metres (for a narrow antenna beam at a range of tens of kilometres). However, larger errors may occur if, for example, the target had a much larger radar cross section away from the radar's broadside than at that angle.

As expected, the SDR makes an important contribution to the quality of the estimates; it is clear that a variation of 20 dB changes most of the lower bounds by 20 dB (two orders of magnitude).

Figure 5.8 shows that non-uniform sampling has kept the bounds low at frequencies away from that of the ground clutter. The effects due to aliasing have been suppressed, showing a benefit of non-uniform sampling.

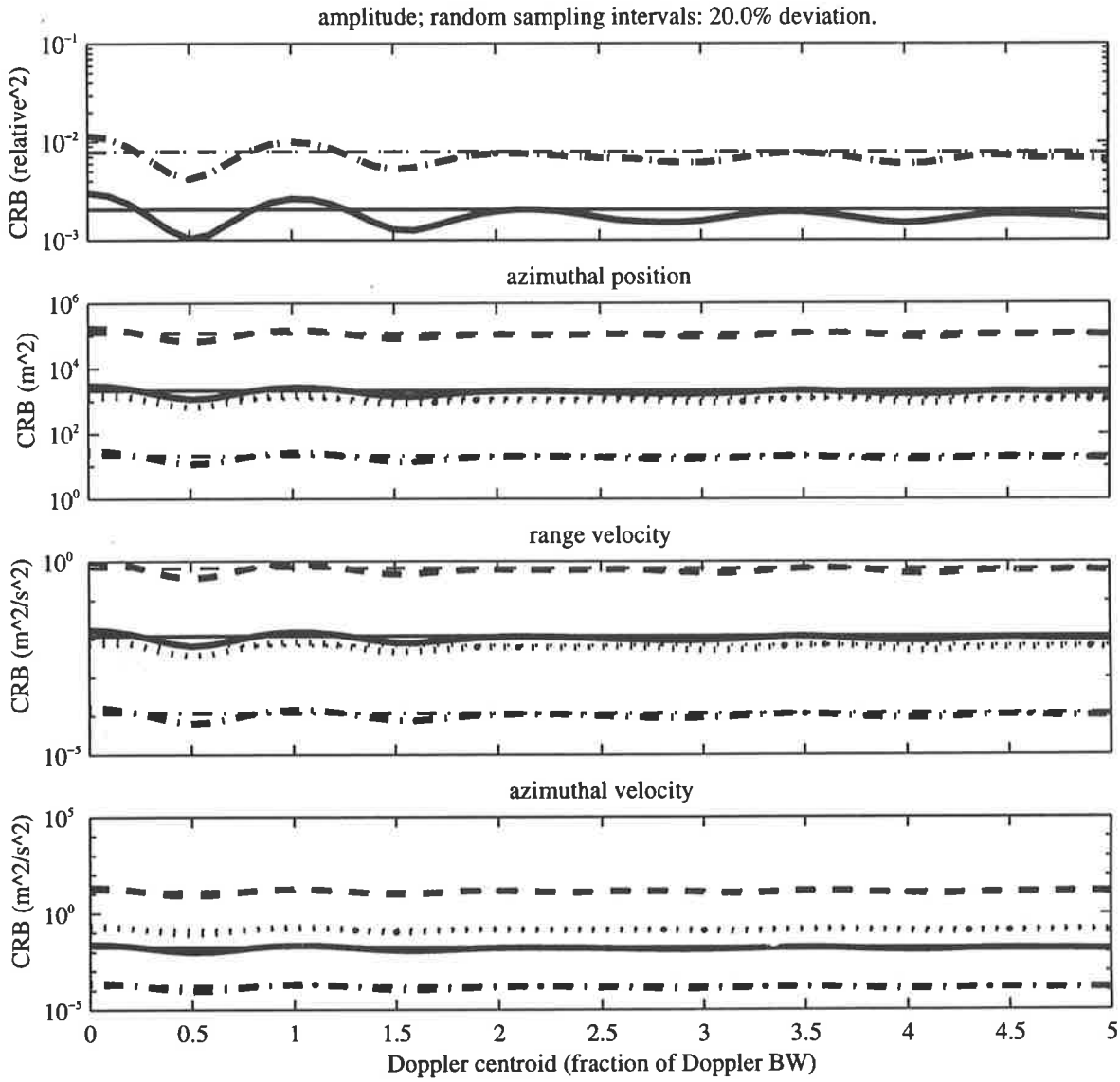

Figure 5.10: Cramér-Rao lower bounds: the non-uniform PRF averages the Doppler bandwidth.

At a constant, low PRF (Figure 5.9), the bounds apart from the one corresponding to amplitude are almost uniform, reflecting the approximation that the coloured noise occupies the entire unambiguous bandwidth and therefore almost appears white.

This plot needs to be interpreted carefully. It tells of the minimum *variance* of the estimate; it does not take bias into account. The estimation itself is ambiguous due to aliasing effects since the Doppler centroid may be beyond the sampling rate of the radar, so the plot gives an optimistic impression of the quality of the estimator.

In the non-uniform case (Figure 5.10) the curves are almost identical, except that the amplitude estimation accuracy never becomes as poor as for low velocities when targets have Doppler centroids below half the Doppler bandwidth. In addition, there is no bias error, as

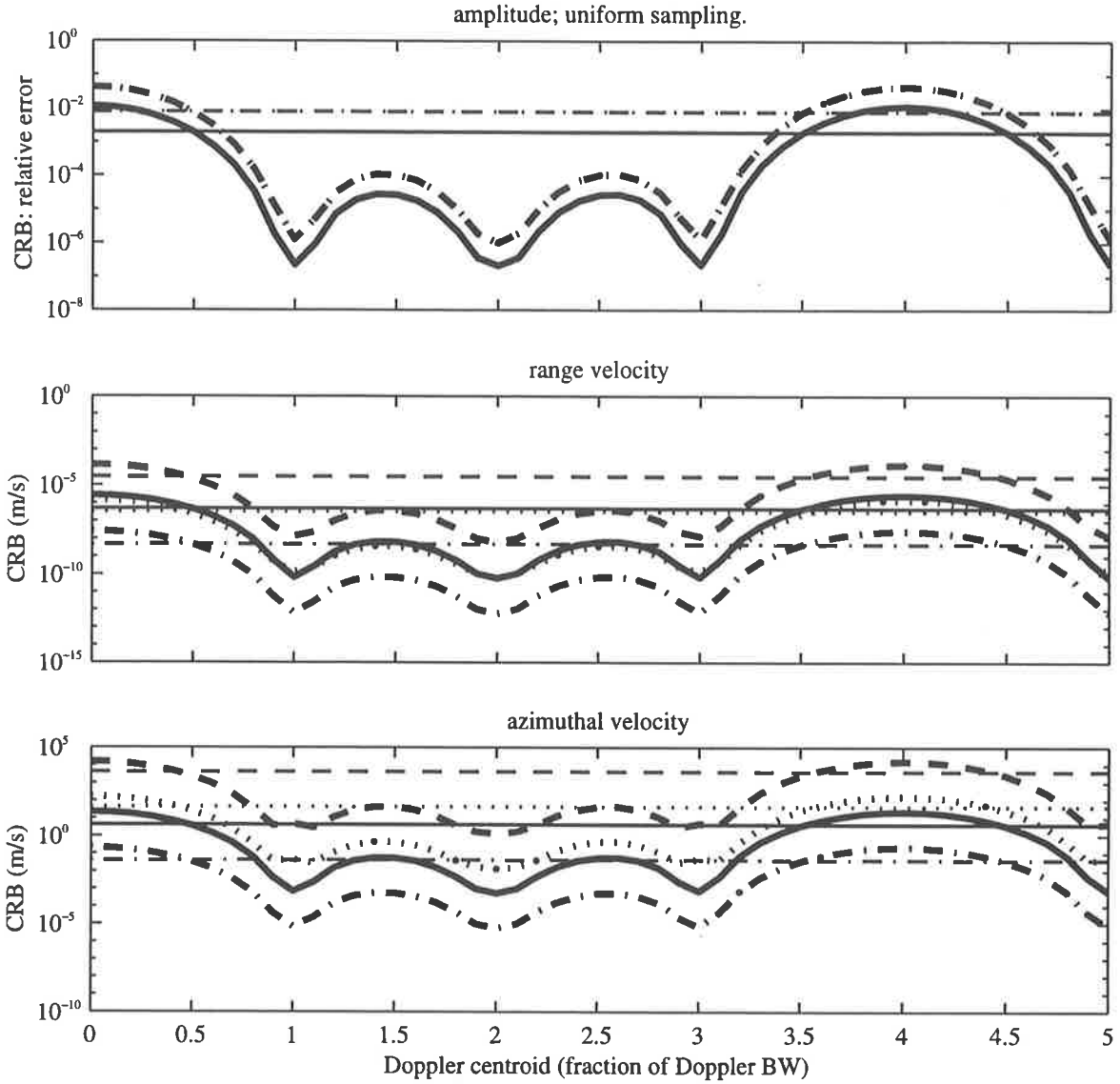

Figure 5.11: Cramér-Rao lower bounds: the uniform PRF averages four times the Doppler bandwidth. Azimuthal position is assumed to be known.

there would be for the situation of Figure 5.9.

It is to be noted that the bounds for the white noise, non-uniform sampling case are very similar to those of the uniform case, as predicted, despite the low number of samples.

Figure 5.11 is similar to Figure 5.7, but assumes that the azimuthal position is known. The amplitude lower bound is unchanged, the azimuthal velocity has changed marginally, while the range velocity bound is dramatically lowered (by about five orders of magnitude). These effects were expected from the consideration of Figure 5.1.

5.9 Conclusions

This chapter has many contributions.

- It derived the ML estimator for the parameters of moving targets in a SAR scene where non-uniform transmission times are used.
- It discussed the subsampling bias which results from uniform sampling.
- It found Fisher information matrices which incorporate non-uniform sampling: where the sampling times are explicitly specified, or their distribution is known.
- It has shown that, for white noise and large N, the Cramér-Rao lower bounds are the same if random samples are distributed uniformly over the entire time frame of interest, or if they are distributed uniformly within half a sampling interval of the nominal uniform positions.
- It has also shown that, under these conditions, the Cramér-Rao lower bounds are the same as those achieved in the uniform sampling case, even though the estimator does not exhibit the bias which results from uniform sampling aliasing effects. (This permits the accurate measurement of signal parameters well beyond the limits encountered with uniform sampling.) These results were demonstrated by simulation.
- The variance bounds for the parameters used in the model were translated into real world moving target parameters. These were plotted for a variety of conditions, showing the effects described.

CHAPTER 6

Imaging

This chapter considers the azimuthal focussing of stationary scatterers in a synthetic aperture radar (SAR) scene for the purpose of producing an image of the ground. (As such, the requirements are quite different from those of detecting moving targets.) It is shown that the beam pattern produced using a SAR with a non-uniform pulse repetition interval (PRI) compares favourably with that of a conventional SAR, allowing the accurate representation of the bright scatterers in a scene.

6.1 Introduction

Imaging is the representation of an arbitrary radar scene as a collection of discrete scatterers in two dimensions. Its requirements are therefore entirely different from those of moving target detection: instead of estimating the parameters of a single target which may or may not be present, the scene is divided into arbitrarily many cells whose reflectivities are estimated. The focussing filters must be capable of accurately performing the estimation in one cell while ignoring the effects of the signals in adjacent cells, which may be very large.

As discussed in Chapter 2, the intended application for a non-uniform PRI SAR is for the detection of sparsely distributed, man made objects in a background of relatively uniform terrain. Thus the existence of some imaging sidelobes is not a serious handicap. It is recognised from the outset that a non-uniform PRI SAR will not produce as good an image as a conventional SAR, nor will it have the same computational efficiency; however, it is felt that the increase in capability — simultaneous imaging and moving target detection using no more data — makes it worthy of consideration.

It is assumed that the radar has performed a range compression operation, as discussed in

Section 3.2.2, allowing us to consider only the azimuthal data. It is further assumed that the azimuthal cells have been aligned correctly, taking range migration effects into account. The focussing filter has only the measurements received by the radar to work with, which for SAR in the azimuthal dimension are dependent upon the changing geometry as the radar travels past the targets. These data may or may not lead to a unique reconstruction of the scene. For example, if the quadratic approximation is made, as discussed in Section 3.2.5, the signals may be treated as linear frequency ramps. In this case, there is a unique reconstruction with a uniform PRI in the same way that a discrete Fourier transform (DFT) has frequency bins which are independent. This is because the situations are the same, except for a fixed, quadratically varying exponential term. However, if the PRIs are non-uniform, there is no such set of basis functions, leading to worse sidelobe performance or azimuthal ambiguity (grating lobes) in the extreme case.

The original contribution of this chapter is coherent imaging with a non-uniform PRI SAR: the optimal imaging process, the use of several different sidelobe reduction strategies, a comparison of performance with that of a conventional SAR and the derivation of an *expected* beam pattern for random transmission times. Section 6.2 discusses existing work, Section 6.3 formulates the optimal imaging process for arbitrary transmission times in an environment containing an arbitrary number of scatterers and a background of stationary, Gaussian noise, Section 6.4 discusses several different processing and sidelobe reduction strategies and Section 6.5 considers non-uniform PRI effects.

6.2 Existing Work

Most texts on SAR (reasonably) treat imaging as its sole purpose. There are many levels of sophistication, however, from filtering the raw ground return through to geocoding (accurately determining which patch of the ground corresponds to the pixel in an image, compensating for the many sources of distortion). This chapter is concerned with the most fundamental level, that of filtering, since that is where the differences between uniform and non-uniform PRIs are found.

It is normal for SAR to incorporate weights for sidelobe reduction, such as those discussed by harris (1978) (which will be considered in Section 6.4.2).

Other techniques include:

CLEAN: thresholding the image, calculating the predicted sidelobes associated with the result and subtracting them from the image, allowing smaller targets to be detected (as discussed in Section 4.5) (Kesteven 1997, Freedman et al. 1996),

Constraints to specify the beam pattern's real and imaginary parts separately,

Data interpolation, as was done for computational efficiency with a non-uniform PRI by Mobley (1995) and Mobley and Maier (1996),

Minimax: minimising the maximum sidelobe level, and

Non-linear apodisation: lowering sidelobes while maintaining the full resolution achievable with an unwindowed response by choosing the minimum corresponding pixels in images produced using different windowing functions (Stankwitz, Dallaire and Fienup 1995).

Flynn (1992) gives an altered wavenumber-domain algorithm which allows for non-uniform aircraft motion, incorporating a non-uniform PRI.

Mobley (1995) and Mobley and Maier (1996) investigated the imaging performance of a SAR using different PRI schemes by interpolating the azimuthal data and comparing the results with those of uniform transmission times. For comparison purposes, the data were first processed using a standard DFT (which assumed uniform sampling times and was therefore naturally subject to error), and then with a DFT after interpolation. The advantage of this technique over exact phase corrections is computational; provided the general bandpass sampling theorem is satisfied, the interpolated reconstruction should be good.

6.3 Azimuthal Imaging Formulation

The objective of this section is to formulate the optimal imaging estimator with an assumed number of independent scatterers superimposed on a background of noise. (This is different from the ambiguity function formulation, which concentrated on focussing a single scatterer.)

The azimuthal signal returned from a scatterer at range R and azimuthal position $v_p\nu$ is given by

$$x(t;R,\nu) \;=\; a(t-\nu;R)\,v_0(t-\nu;R)\,\tilde{\rho}_{R,\nu},$$

where v_p is the velocity of the SAR platform, t is time, $\tilde{\rho}_{R,\nu}$ is the complex amplitude of the scatterer, $v_0(t;R)$ is its chirp-like response (which results from the geometry), ν is the time the

scatterer is adjacent to the radar and $a(t;R)$ is the two-way azimuthal antenna beam pattern. (This is the same as the expression used to model the disturbance in Appendix B.)

The signal seen by the radar is

$$y(t;R) \;=\; x(t;R,\nu) + n(t),$$

neglecting attenuation due to the radar and propagation losses, *etc.* $n(t)$ is a complex noise process which will be discussed later.

If the radar transmits at the discrete times $\{t_n\}$, $n = 1, \cdots, N$, the measurements can be written in matrix form as

$$\begin{aligned} \boldsymbol{y}(R,\nu) &= (\boldsymbol{w} \odot \boldsymbol{v}_0)\tilde{\rho} + \boldsymbol{n} \\ &= \hat{\boldsymbol{v}}_0 \tilde{\rho} + \boldsymbol{n}, \end{aligned} \tag{6.1}$$

where $(\boldsymbol{w})_n = a(t_n - \nu; R)$, $\odot$ is the Hadamard (element-wise) product and ^{T} is the transpose operation. (This formulation is equivalent to the one used in earlier chapters, where $\hat{\boldsymbol{v}}_0 = \boldsymbol{A}\boldsymbol{v}_0$, $\boldsymbol{A}$ having the two-way antenna pattern along its diagonal, $(\boldsymbol{A})_{n,n} = a(t_n - \nu; R)$, and zeros elsewhere: $(\boldsymbol{A})_{m,n} = 0, m \neq n$ (Equation (4.5)).)

The signal returned from M scatterers at time t is given by

$$\begin{aligned} y(t;R) &= \sum_{m=1}^{M} x(t;R,\nu_m) + n(t) \\ &= \sum_{m=1}^{M} a(t-\nu_m;R)\, v_0(t-\nu_m;R)\, \tilde{\rho}_{R,\nu_m} + n(t). \end{aligned}$$

This can be written in matrix form as

$$\begin{aligned} \bar{\boldsymbol{y}} &= (\boldsymbol{W} \odot \boldsymbol{V}_0)\, \tilde{\boldsymbol{\rho}} + \boldsymbol{n} \\ &= [\hat{\boldsymbol{v}}_{0,\nu_1}, \hat{\boldsymbol{v}}_{0,\nu_2}, \cdots, \hat{\boldsymbol{v}}_{0,\nu_M}]\, \tilde{\boldsymbol{\rho}} + \boldsymbol{n} \\ &= \bar{\boldsymbol{V}}(\boldsymbol{\theta})\tilde{\boldsymbol{\rho}} + \boldsymbol{n}. \end{aligned} \tag{6.2}$$

$\tilde{\boldsymbol{\rho}} = [\tilde{\rho}_1, \cdots, \tilde{\rho}_M]^T$. $\bar{\boldsymbol{V}}(\boldsymbol{\theta})$ is a known $N \times M$ matrix dependent upon the known parameters $\boldsymbol{\theta} = [\{t_n\}, \{\nu_m\}]^T$. Neither the $\{t_n\}$ nor the $\{\nu_m\}$ need to be uniformly spaced.

If the antenna beam is assumed to be an ideal broadside wedge shape as defined in Equation (3.12), *i.e.*

$$a(t;R) = \begin{cases} 1, & \text{if } |t| < T/2, \\ 0, & \text{otherwise,} \end{cases}$$

where $T = T(R) = R\theta_{ra}/v_p$ is the time taken for the SAR to travel the length of the antenna beam and θ_{ra} is the antenna beamwidth, $\boldsymbol{V}(\boldsymbol{\theta})$ can be written as shown in Equation (6.3). $t_{lim}^{(n)}$ and $t_{-lim}^{(n)}$ are the maximum and minimum values of $t_n - \nu$ less than $T/2$, respectively.

$$\bar{\boldsymbol{V}}(\boldsymbol{\theta}) = \begin{bmatrix} v_0(t_1-\nu_1) & v_0(t_1-\nu_2) & \cdots & v_0(t_{-lim}^{(1)}) & 0 & \cdots & 0 \\ v_0(t_2-\nu_1) & v_0(t_2-\nu_2) & v_0(t_2-\nu_3) & \cdots & v_0(t_{-lim}^{(2)}) & \ddots & \vdots \\ \cdots & v_0(t_3-\nu_2) & v_0(t_3-\nu_3) & \cdots & \cdots & \ddots & 0 \\ & & & \ddots & & & \ddots \\ 0 & \ddots & & & & & \\ \vdots & \ddots & v_0(t_{lim}^{(N-1)}) & \cdots & & & v_0(t_{N-1}-\nu_M) \\ 0 & \cdots & 0 & v_0(t_{lim}^{(N)}) & \cdots & & v_0(t_N-\nu_M) \end{bmatrix} \tag{6.3}$$

(More simply, for uniform sampling ($t_n = nt_s$) and a scatterer adjacent to the radar during each transmission ($M = N$), Equation (6.2) can be written as shown in Equation (6.4), where $t_{lim} = (nt_s)_{max} < T/2$.

$$\begin{bmatrix} y_1 \\ y_2 \\ y_3 \\ \vdots \\ y_N \end{bmatrix} = \begin{bmatrix} v_0(0) & v_0(-t_s) & \cdots & v_0(-t_{lim}) & 0 & \cdots & 0 \\ v_0(t_s) & v_0(0) & v_0(-t_s) & \cdots & v_0(-t_{lim}) & \ddots & \vdots \\ \cdots & v_0(t_s) & v_0(0) & v_0(-t_s) & \cdots & \ddots & 0 \\ & & & \ddots & & & \\ 0 & \ddots & \cdots & v_0(t_s) & v_0(0) & v_0(-t_s) & \cdots \\ \vdots & \ddots & v_0(t_{lim}) & \cdots & v_0(t_s) & v_0(0) & v_0(-t_s) \\ 0 & \cdots & 0 & v_0(t_{lim}) & \cdots & v_0(t_s) & v_0(0) \end{bmatrix} \begin{bmatrix} \tilde{\rho}_1 \\ \tilde{\rho}_2 \\ \tilde{\rho}_3 \\ \vdots \\ \tilde{\rho}_N \end{bmatrix} \tag{6.4}$$

The more general case will be assumed here, however.)

For an antenna with a narrow beamwidth directed at broadside, the signal from a stationary scatterer is assumed to be given by

$$v_0(t;R) = e^{j2\pi[F_{dc}t + F_{dr}(R)t^2/2]}, \tag{6.5}$$

as discussed in Section 2.3, where F_{dc} is the Doppler centroid, nominally zero, and the Doppler rate

$$F_{dr}(R) = -2\frac{v_p^2}{\lambda R}, \tag{6.6}$$

with λ being wavelength.

6.3.1 *Focussing*

If the noise $n(t)$ is assumed to result from a homogeneous scene with many independent scatterers in each resolution cell, its probability density function is stationary and Gaussian by the central limit theorem (Barbarossa 1992b). It is assumed at this stage that the noise is white (which is justified by the low average sampling rate in comparison with the clutter's spectral density (Section 4.2.4)).

Conventional SAR processing is done by the maximum SNR estimator, the matched filter, which is given by

$$\hat{\tilde{\rho}}_{mf} = \bar{\boldsymbol{V}}^H \bar{\boldsymbol{y}}. \tag{6.7}$$

The many processing algorithms, including wavenumber domain (Flynn 1992) and step transform (Curlander and McDonough 1991) are different implementations of this, with reduced computational requirements. These computational benefits may not be available when the radar's transmission times are arbitrary, however. (This topic is beyond the scope of this thesis.)

Note that the azimuthal ambiguity function, Equation (3.13), is equivalent to Equation (6.7) for the case of a single, stationary scatterer.

Normally, for each range cell, a unique scatterer is assumed to correspond to each resolution cell on the ground. Due to the broadside antenna pattern with stripmapping SAR, the cells are adjacent to the radar. If the minimum PRF is used, there will be one adjacent to the radar for each transmission.

Unfortunately, this makes Equation (6.2) an under-determined system ($N < M$): at the start and finish of the measurements, the antenna beam sees scatterers which are *never* adjacent to the radar[1].

Therefore, instead of Equation (6.7), we can use the maximum likelihood estimator for

[1] This isn't a problem with spotlight SAR, since the same patch of ground is viewed repeatedly.

additive Gaussian noise, the least squares estimator, which uses the Moore-Penrose pseudoinverse

$$\hat{\bar{\rho}}_{ls} = \bar{V}^{+}\bar{y}, \tag{6.8}$$

where

$$\bar{V}^{+} = (\bar{V}^{H}\bar{V})^{-1}\bar{V}^{H}$$

for $N > M$ (more measurements than scatterers), or

$$\bar{V}^{+} = \bar{V}^{H}(\bar{V}\bar{V}^{H})^{-1}$$

for $M > N$. (Recall that $\bar{V}$ is $N \times M$.)

It is well known that

$$\hat{\bar{\rho}}_{ls} = (\bar{V}^{H}\bar{V})^{-1}\hat{\bar{\rho}}_{mf}.$$

$\bar{V}^{H}\bar{V}$ is the synthetic aperture's beam response pattern, ideally the identity, I. (The columns of this matrix correspond to the ambiguity function of stationary targets as a function of y. This is discussed in Section 6.4.) The inverse of this is being used as a correction factor to the standard matched filter processor.

Equation (6.8) can be applied to the task of increasing the azimuthal resolution of a SAR system: since $M > N$, we can apply it to obtain the least squares solution.

The minimum variance estimator is useful if the additive noise, $\boldsymbol{n}$, is correlated or has a changing variance. It is given by

$$\hat{\bar{\rho}}_{mv} = (\bar{V}^{H}K^{-1}\bar{V})^{-1}\bar{V}^{H}K^{-1}\bar{y}, \tag{6.9}$$

where K is a weighting matrix. It is normal to make K be the covariance matrix of the noise (*i.e.*, $K = \mathrm{E}[nn^{H}]$).

More complex processors can be found in (D'Assumpcao 1980).

6.4 Processing Techniques

Several SAR target focussing techniques are of interest:

Exact phase corrections as was done with the ambiguity function. This assumes a rectangular window and makes a useful frame of reference.

Weighted using standard weighting functions, such as the Hann window, and exact phase corrections.

Maximum integrated sidelobe level based on work with real arrays by Boni et al. (1994).

These are discussed in detail below for a single scatterer with an arbitrary azimuthal position, in which case

$$(\boldsymbol{y})_n \;=\; \tilde{\rho}\, a(t_n - \nu; R)\, \exp\!\left(-j2\pi \frac{v_p^2}{\lambda R}(t_n - \nu)^2\right) + (\boldsymbol{n})_n,$$

using Equations (6.1), (6.5) and (6.6).

The corresponding filter, tuned to a target centred at $\nu = 0$, is given by

$$(\widehat{\boldsymbol{v}}_\nu)_n \;=\; a(t_n; R)\, \exp\!\left(-j2\pi \frac{v_p^2}{\lambda R} t_n^2\right).$$

Using Equation (6.7), by letting the azimuthal time offset be referenced by an equivalent position offset $y = v_p \nu$ and neglecting the amplitude $\tilde{\rho}$ and noise $n(t)$ terms gives

$$\chi'_{az}(y; R, \{t_n\}, v_p, \lambda) \;=\; \exp\!\left(j\frac{2\pi y^2}{\lambda R}\right) \sum_{n=-\infty}^{\infty} a(t_n; R)\, a(t_n - y/v_p; R)\, \exp\!\left(-j2\frac{2\pi}{\lambda}\frac{y v_p}{R} t_n\right). \tag{6.10}$$

This is the same as the SAR ambiguity function, Equation (3.13), with a matched target range and zeroed target motion parameters.

6.4.1 *Phase Corrections*

For the case of a uniform antenna beam, Equation (3.12), Equation (6.10) becomes

$$\chi'_{az}(y; R, t_s, v_p, \lambda) \;=\; \begin{cases} \exp\!\left(j\dfrac{2\pi y^2}{\lambda R}\right) \displaystyle\sum_{n=(y/v_p - T/2)/t_s}^{T/(2t_s)} \exp\!\left(-j2\frac{2\pi}{\lambda}\frac{y v_p}{R} n t_s\right), \\ \qquad\qquad\qquad\qquad\qquad\qquad -T \le y \le T, \\ 0, \qquad\qquad\qquad\qquad\qquad\qquad \text{otherwise}, \end{cases}$$

where T is the time taken to travel the length of a synthetic aperture and t_s is the mean PRI.

Using the result

$$\sum_{n=n_1}^{n_2} \alpha^{xn} \;=\; \frac{\alpha^{x(n_2+1)} - \alpha^{xn_1}}{\alpha^x - 1},$$

it follows that, for uniform sampling times and a uniform antenna beam,

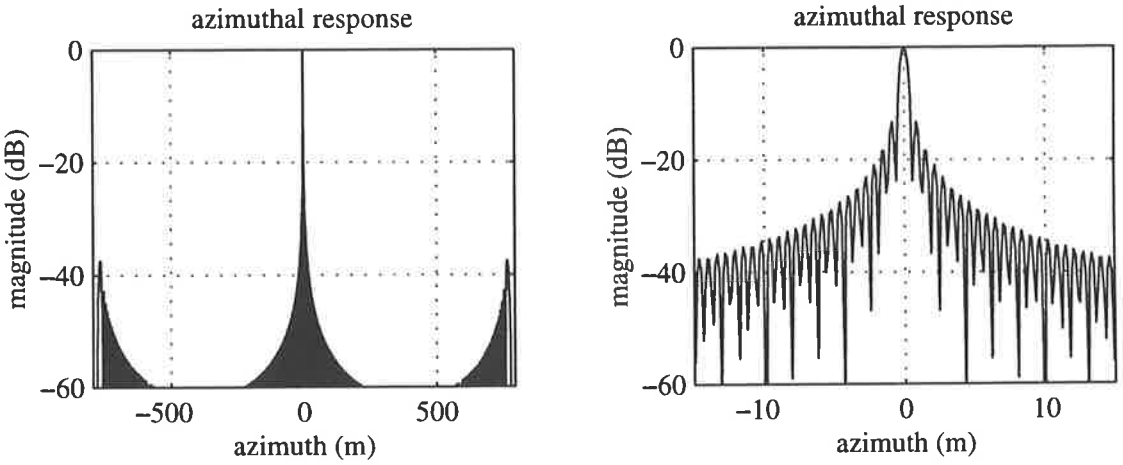

(a) Whole beam.

(b) Main lobe structure.

Figure 6.1: A magnitude squared SAR azimuthal response with uniform sampling.

Parameter	Value(s)	Comments
range	29500 m	
platform velocity	70 m/s (140 kt)	
wavelength	3.2 cm (X-band)	
antenna beamwidth	1.5°	
Doppler bandwidth	115 Hz	(derived)
mean PRF	115 Hz	
target amplitude	assumed constant	since only a small aperture
clutter model	white Gaussian, zero amplitude	due to low average sample rate

Table 6.1: Parameters used for the imaging examples. These are similar to those used for the moving target detection examples (Table 4.1) and the parameter estimation examples (Table 5.1).

$$\begin{aligned} \chi'_{az}(y; R, t_s, v_p, \lambda) &= \frac{\exp\left(-j\frac{2\pi}{\lambda R}y\,[Tv_p + 2t_s v_p - y]\right) - \exp\left(j\frac{2\pi}{\lambda R}y\,[Tv_p - y]\right)}{\exp\left(-j2\frac{2\pi}{\lambda R}v_p t_s y\right) - 1} \\ &= \frac{\sin\left(\frac{2\pi}{\lambda R}[v_p(T + t_s) - y]y\right)}{\sin\left(\frac{2\pi}{\lambda R}v_p t_s y\right)} \end{aligned} \tag{6.11}$$

Figure 6.1 shows Equation (6.11) evaluated for the parameters listed in Table 6.1. A uniform antenna beam between the beamwidth extremes gives a pessimistic sidelobe performance: real sidelobes would be lower than this.

The normalised, squared response has been plotted to show the relative power of the return from a specified direction.

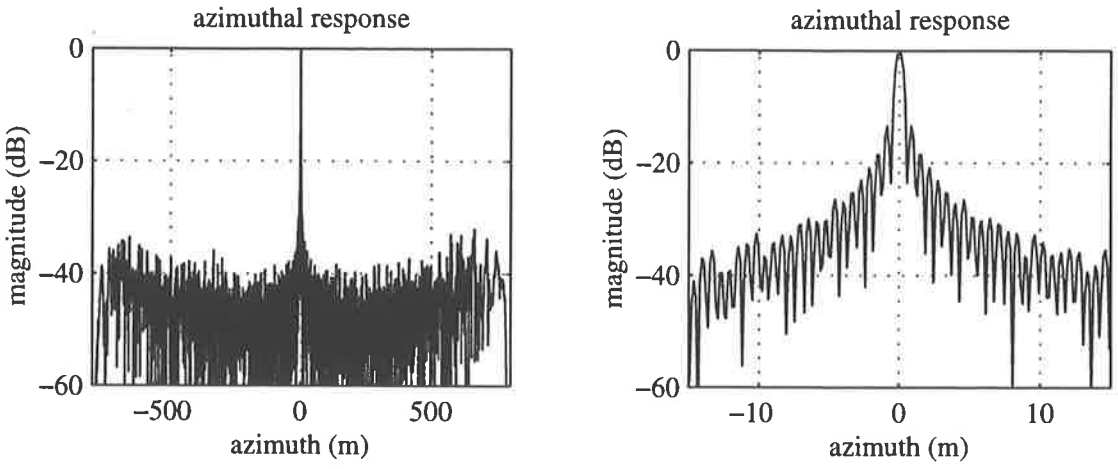

(a) Whole beam.

(b) Main lobe structure.

Figure 6.2: The magnitude squared azimuthal response with non-uniform sampling.

The skirt visible at the edges of Figure 6.1 is a result of the crosscorrelation of two rectangular chirp functions which are sampled at the Nyquist rate. Intuitively, when the functions start to overlap, there are samples which do not cancel, resulting in large values. As the overlap increases, averaging results in the expected low correlation. This skirt can be reduced by windowing (see below). (In practice, the skirt may not appear since the antenna beam may not be accurately modelled by a rectangular window function.)

It is interesting to note that the azimuthal response is twice as wide overall as the radar's antenna beam, extending to a distance of $\pm v_p T$ each side of the target, implying a non-causal system: there is a response from a target *before* (and *after*) it is visible to the radar. This real effect is due to the overlap between the filter and the target's response.

Figure 6.2 shows the azimuthal response with one instance of sampling with additive random intervals which are uniformly distributed with a 30% deviation. It is clear from Figure 6.2(a) that the noise floor is poorer than in Figure 6.1, being $-40\,\text{dB}$ rather than below $-60\,\text{dB}$, although there is very little difference between the plots' sidelobe structures in the vicinity of the main lobe, shown in Figure 6.2(b).

In the uniform sampling case, Figure 6.1, the convolution of the target's response — an impulse — and the rectangular window result in the distinctive beam pattern. In the non-uniformly sampled case, the target's response is no longer a impulse, due to the samples not being orthogonal. Convolving this with the rectangular window only suppresses sidelobes to a limited extent.

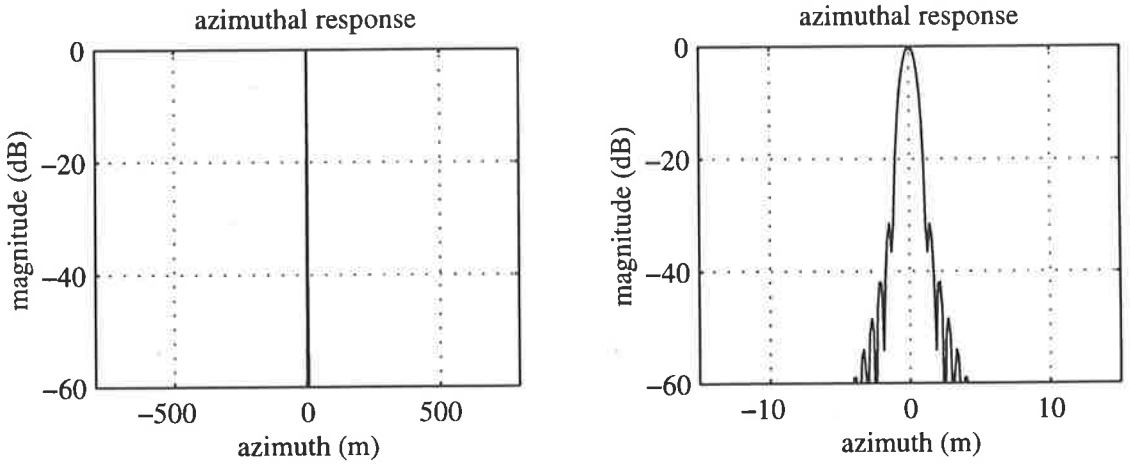

(a) Whole beam.

(b) Main lobe structure.

Figure 6.3: The magnitude squared azimuthal response with uniform sampling and a Hann window.

6.4.2 *Weighting*

Generalising Equation (6.10), the weighted azimuthal response to a single stationary target is

$$\chi'_{az}(y; R, \{t_n\}, v_p, \lambda) = \exp\left(j\frac{2\pi y^2}{\lambda R}\right) \sum_{n=-\infty}^{\infty} a(t_n; R)\, a(t_n - y/v_p; R)\, (\boldsymbol{d})_n \cdot \exp\left(-j2\frac{2\pi}{\lambda}\frac{y v_p}{R} t_n\right), \tag{6.12}$$

where $\boldsymbol{d}$ is a vector of weights.

Let $(\boldsymbol{d})_n = d(t_n)$, where $d(t)$ is a continuous weighting function and $\{t_n\}$ are the radar's transmission times.

Figure 6.3 shows $|\chi'_{az}(y; R, \{t_n\}, v_p, \lambda)|^2$ from Equation (6.12) evaluated for the parameters listed in Table 6.1 for uniform sampling times and a Hann window:

$$d(t) = \begin{cases} \frac{1}{2}[1 + \cos(2\pi t/T)], & |t| \leq T/2, \\ 0, & \text{otherwise.} \end{cases}$$

The magnitude has been normalised to the peak.

The skirt visible in Figure 6.1 has been suppressed in Figure 6.3, as expected. The shape is that expected, being similar to that of the Hann window's spectrum.

Figure 6.4 shows the azimuthal response for one instance of sampling with additive random intervals which are uniformly distributed with a 30% deviation. The main lobe is like that of Figure 6.3(b). The sidelobes, however, differ greatly for the reasons discussed in the last

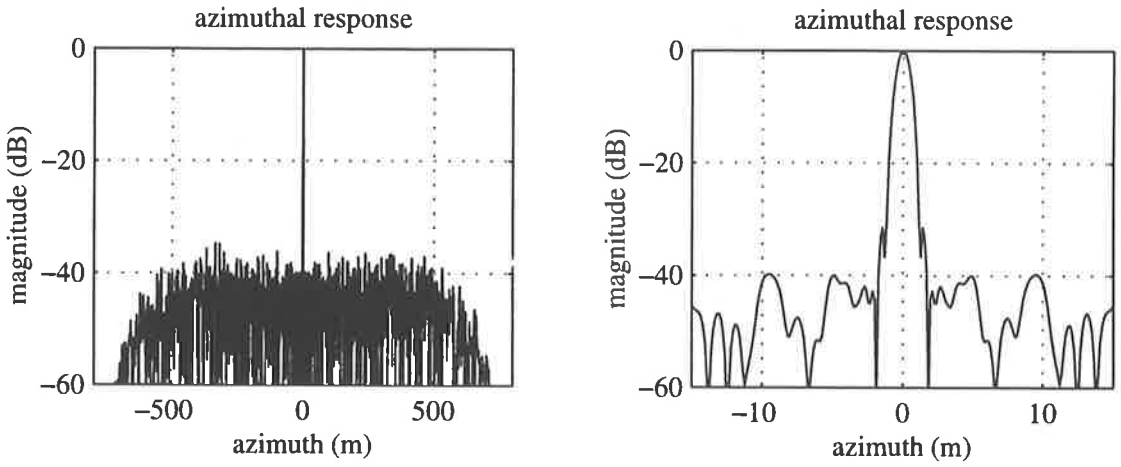

(a) Whole beam.

(b) Main lobe structure.

Figure 6.4: The magnitude squared azimuthal response with non-uniform sampling and a Hann window.

section: with an inherently noisy beam pattern, rather than an impulse, a Hann window does not completely solve the problem.

6.4.3 *Maximum ISLR*

The integrated sidelobe ratio (ISLR) is a useful criterion as it simultaneously takes into account both contrast and resolution.

Boni et al. (1994) optimises the weightings and the positioning of elements of a non-uniformly spaced, linear array. The ideas in this section were taken from that paper.

The ISLR is defined as the ratio of the mainlobe to sidelobe energies

$$\text{ISLR} = \frac{E_M}{E_T - E_M},$$

where E_M is the mainlobe energy and E_T is the total energy. Maximising the ISLR therefore suppresses sidelobes.

Note that the energies do not need to be normalised prior to finding the ISLR, since any scaling factor will cancel.

Using the weighted azimuthal response Equation (6.12), the energy over a specified az-

imuthal interval $-l \leq y \leq l$

$$\begin{aligned} E &= \int_{-l}^{l} |\chi'_{az}(y;\cdot)|^2 \, dy \\ &= \sum_n d_n \sum_m d_m^* \, a(t_n;R)\, a(t_m;R) \cdot \\ &\quad \int_{-l}^{l} a(t_n - y/v_p;R)\, a(t_m - y/v_p;R) \, \exp\left(j2\frac{2\pi}{\lambda}\frac{v_p}{R}[t_m - t_n]y \right) dy. \end{aligned} \tag{6.13}$$

This can be expressed as $\boldsymbol{d}^H \boldsymbol{A}_l \boldsymbol{d}$, where $\boldsymbol{d}$ is the vector of weights and $\boldsymbol{A}_l$ is a matrix with entries

$$\begin{aligned} (\boldsymbol{A}_l)_{m,n} &= a(t_n;R)a(t_m;R) \int_{-l}^{l} a(t_n - y/v_p;R)\, a(t_m - y/v_p;R) \cdot \\ &\qquad \exp\left(j2\frac{2\pi}{\lambda}\frac{v_p}{R}[t_m - t_n]y \right) dy. \end{aligned} \tag{6.14}$$

The energy in the main lobe is given by Equation (6.13) with $l = a$:

$$E_M = \int_{-a}^{a} |\chi'_{az}(y;\cdot)|^2 \, dy.$$

The width of the main lobe, $2a$, is the synthetic aperture resolution

$$2a = \rho_{sa} = \frac{R\lambda}{2L(R)} = \frac{R\lambda}{2v_p(t_{max} - t_{min})},$$

where the target is visible to the radar between the times t_{min} and t_{max}. Since $(-a, a)$ is small, equivalent to a very small fraction of a degree of beamwidth, the antenna beam pattern does not vary much from its maximum value, so $a(t - y/v_p;R) \approx 1$. E_M can then be expressed using a simplified version of Equation (6.14)

$$(\boldsymbol{A}_a)_{m,n} = 2a \, \mathrm{sinc}\left(\frac{4\pi a v_p}{R\lambda}(t_m - t_n) \right) \tag{6.15}$$

(where $\mathrm{sinc}\,(x) \triangleq \sin(x)/x$).

The total energy, given by Equation (6.13) with $l = b$

$$E_T = \int_{-b}^{b} |\chi'_{az}(y;\cdot)|^2 \, dy$$

may have to be solved numerically, since $b \leq R\theta_{ra}/2$ is large. This results in the matrix $\boldsymbol{A}_b$, which is defined similarly to $\boldsymbol{A}_l$ in Equation (6.14).

The optimal weights $\boldsymbol{d}$ are then given by the generalised eigenvector associated with the minimum generalised eigenvalue of the pencil matrix

$$\boldsymbol{A}_b\boldsymbol{d} = \lambda\boldsymbol{A}_a\boldsymbol{d}$$

(Boni et al. 1994).

Unfortunately, $\boldsymbol{d}$ has to be recalculated for focussing each pixel as the radar travels, since the transmission positions are in a different place relative to the main beam[2]. This fact, combined with the high computational load required, restricts the usefulness of this technique in practice.

Although this criterion could be applied to the problem of determining the optimal transmission times, it makes little sense to, since the radar is moving continuously, so that the optimal positions cannot be maintained relative to a given scatterer. In addition, The main objective of this thesis is the detection of moving targets, not ground imaging.

To demonstrate the beam pattern with optimal ISLR weights, a short range scenario was chosen (so there would be a computationally feasible number of sampling times): $R = 330\,\text{m}$. Under these circumstances, the main beam approximation Equation (6.15) was not valid, so $\boldsymbol{A}_a$ was determined using Equation (6.14). Figure 6.5 shows the short range azimuthal responses for uniform sampling with rectangular and optimal ISLR weights, respectively. The main beam was assumed to extend to $\pm 0.5\,\text{m}$ and the sidelobes were constrained out to $\pm 5\,\text{m}$ for illustration purposes. It can clearly be seen that the sidelobes are unconstrained outside $\pm 5\,\text{m}$! ISLRs: rectangular window, 9.22 dB; optimal, 14.88 dB.

Figure 6.6 shows the corresponding azimuthal beam patterns for an instance of sampling with additive random intervals which are uniformly distributed with a 30% deviation. ISLRs: rectangular window, 7.56 dB; optimal, 12.71 dB.

6.5 Effects of a Non-Uniform PRI

The performance of an instance of a non-uniform PRI is summarised by Table 6.2. The ISLRs are parameterised by the width of the main lobe, which is either the width where its response has dropped to $-3\,\text{dB}$ of the peak, the position of the first null or where the main lobe reaches the level of the peak sidelobe.

[2]It may be possible to generate the weights for a large number of samples by interpolating those found for a small number (private conversation with Dr Barbarossa, EUSAR'96).

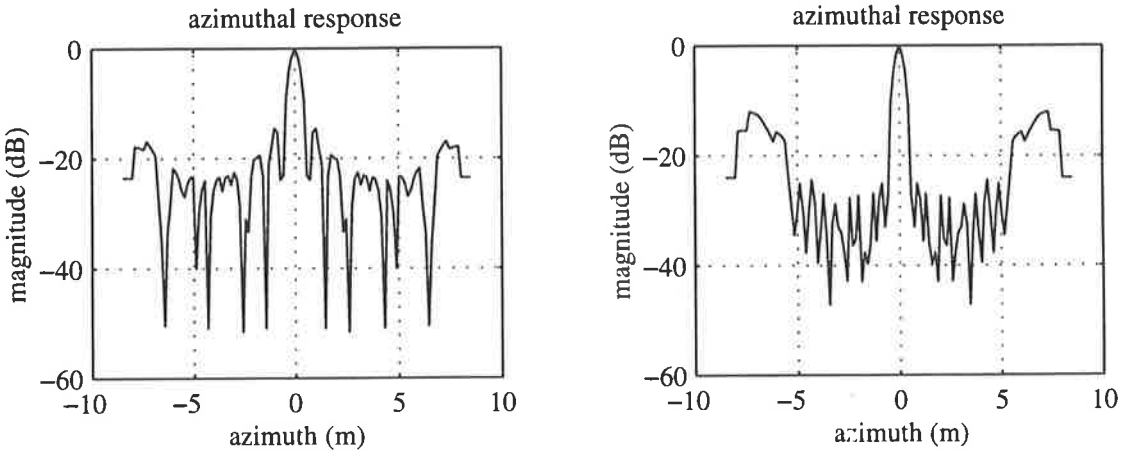

(a) Using a rectangular window.

(b) Using optimal ISLR weights.

Figure 6.5: The magnitude squared azimuthal response with a short range and uniform sampling.

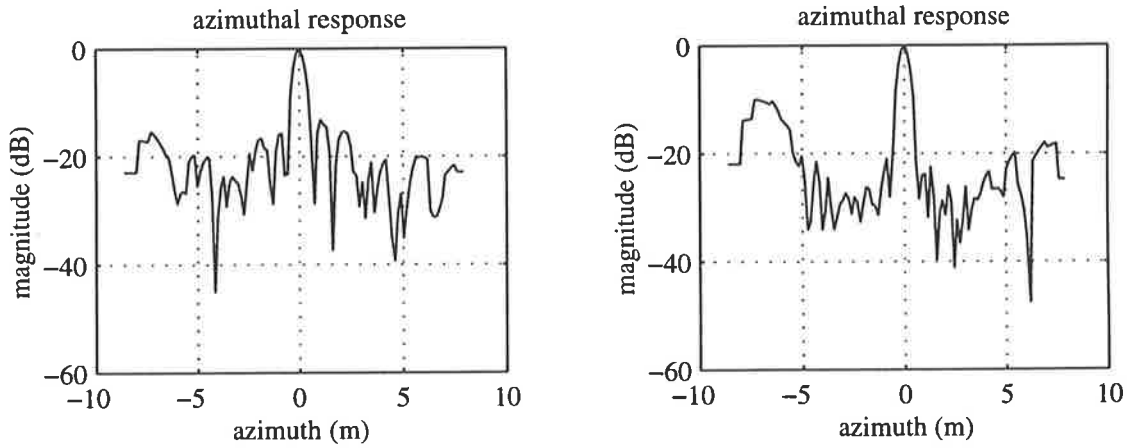

(a) Using a rectangular window.

(b) Using optimal ISLR weights.

Figure 6.6: The magnitude squared azimuthal response with a short range and non-uniform sampling.

Transmission times and weights	ISLR (dB)			PSL (dB)
	−3 dB width	first null	peak sidelobe	
Uniform, rectangular	4.00	9.30	9.05	−13.3
Uniform, Hann	5.49	29.86	29.6	−31.5
Non-uniform, rectangular	2.70	6.40	6.25	−13.1
Non-uniform, Hann	4.56	12.61	12.61	−29.79

Table 6.2: Imaging performance: integrated sidelobe ratios and peak sidelobe levels for various sampling schemes, weights and resolutions; 11.2 s integration period. The non-uniform sampling scheme uses random intervals with 30% deviations.

6.5.1 Resolution

The resolution of an imaging system depends upon the aperture — the distance between the ends of the antenna being used. The longer the aperture, the finer the resolution. In SAR, the aperture length equates to the integration period. The sample times during this period do not affect the resolving capability of the aperture, although they do affect the sidelobe performance. Therefore, for an arbitrary scene, the 3 dB resolution of a SAR is given by Equation (2.5) whether the transmission times are uniform or not.

However, using a model based approach, such as the one outlined in Section 6.3.1, has the potential to increase the resolution beyond this, provided that the model is valid.

6.6 The Azimuthal Response with Random Sampling

The objective of this section is to determine the expected azimuthal response given the distribution of sampling times, rather than to just use a particular azimuthal response resulting from an instance of a sampling scheme.

For the weighted response, the expected result is

$$\mathrm{E}_{\mathbf{T}}[\chi'_{az}(y; R, p_{\mathbf{T}}(\boldsymbol{t}), v_p, \lambda)] \;=\; \exp\left(j\frac{2\pi y^2}{\lambda R}\right) \sum_{n=-\infty}^{\infty} (\boldsymbol{d})_n \, \mathrm{E}_{\mathbf{T}}[x(t_n)],$$

where

$$x(t_n) \;=\; a(t_n; R)\, a(t_n - y/v_p; R) \exp\left(-j2\frac{2\pi}{\lambda}\frac{y v_p}{R} t_n\right),$$

based on Equation (6.12). (As previously noted, the expected response is of interest, rather than the expected squared response, since it is the response which is exhibited by the radar.) This is a special, weighted case of the expected ambiguity function, Equation (3.28), where all the parameters of the reference target are known except for its position.

So

$$\begin{aligned}\mathrm{E}_{\mathbf{T}}[\chi'_{az}(y; R, p_{\mathbf{T}}(\boldsymbol{t}), v_p, \lambda)] \;&=\; \exp(\cdot) \sum_{n=-\infty}^{\infty} (\boldsymbol{d})_n \int_{T_N} \cdots \int_{T_2}\int_{T_1} x(t_n)\, p_{T_1,T_2,\ldots,T_N}(t_1, t_2, \ldots, t_N) \\ &\qquad\qquad dt_1\, dt_2 \ldots dt_N, \\ &=\; \exp(\cdot) \sum_{n=-\infty}^{\infty} (\boldsymbol{d})_n \int_{T_n} x(t)\, p_{T_n}(t)\, dt, \qquad (6.16)\end{aligned}$$

if the PDFs are independent, or

$$\mathrm{E_T}[\chi'_{az}(y;R,p_T(t),v_p,\lambda)] \;=\; \exp(\cdot)\left[\sum_{n=-\infty}^{\infty}(\boldsymbol{d})_n\right]\int_T x(t)\,p_T(t)\,dt, \tag{6.17}$$

if the PDFs are the same. Note that in the latter case, the shape of the expected response doesn't depend upon the values of the weights, provided that their sum is nonzero and finite.

As an aside, note that when $a(t) = 1\ \forall t$, we have $\mathrm{E_T}\left[\exp\left(-j2\frac{2\pi}{\lambda}\frac{yv_p}{R}t_n\right)\right]$, which is the characteristic function of the random variable t_n (Cooper and McGillem 1986).

Several sampling PDFs will now be considered.

6.6.1 Case 1: Uniformly Distributed Times

Suppose that

- the sampling PDFs are uniform:

$$p_{T_n}(t) \;=\; \begin{cases} 1/T, & -T/2 \le t \le T/2, \\ 0, & \text{otherwise,} \end{cases} \quad \forall n,$$

  where $T = \frac{R\theta_{ra}}{v_p}$ is the time taken by the SAR platform to travel the length of the synthetic aperture,

- the $\{(\boldsymbol{d})_n\}$ sum to N, the number of samples in the synthetic aperture, and that

- the antenna beam is uniform over the length of the aperture, as described by Equation (3.12).

Then, using Equation (6.17),

$$\begin{aligned}
&\mathrm{E_T}[\chi'_{az}(y;R,p_T(t),v_p,\lambda)] \\
&= \begin{cases} \exp\left(j\dfrac{2\pi y^2}{\lambda R}\right)\dfrac{N}{T}\displaystyle\int_{y/v_p-T/2}^{T/2}\exp\left(-j2\tfrac{2\pi}{\lambda}\tfrac{yv_p}{R}t\right)dt, & 0 \le y \le T, \\ \exp\left(j\dfrac{2\pi y^2}{\lambda R}\right)\dfrac{N}{T}\displaystyle\int_{-T/2}^{y/v_p+T/2}\exp\left(-j2\tfrac{2\pi}{\lambda}\tfrac{yv_p}{R}t\right)dt, & -T \le y < 0, \\ 0, & \text{otherwise,} \end{cases} \\
&= \begin{cases} \dfrac{N\lambda R}{2\pi v_p T y}\sin\left(\dfrac{2\pi}{\lambda}\dfrac{y}{R}[y - Tv_p]\right), & -T \le y < T, \\ 0, & \text{otherwise.} \end{cases}
\end{aligned} \tag{6.18}$$

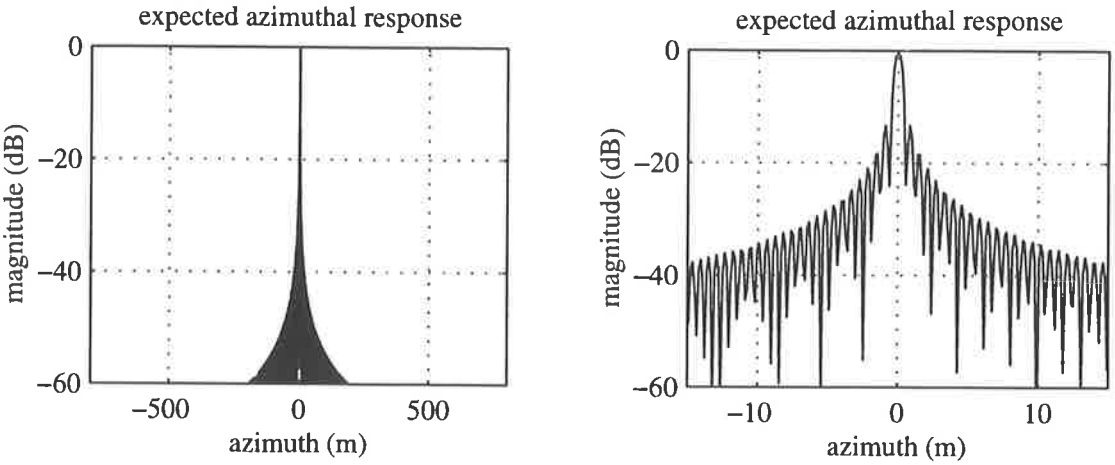

(a) Whole beam.

(b) Main lobe structure.

Figure 6.7: The magnitude squared expected azimuthal response with uniformly distributed random sampling.

This is a continuous version of the unweighted response (Equation (6.11)). Its square has been plotted in Figure 6.7 for the parameters shown in Table 6.1.

There is a strong resemblance to the uniform antenna beam, Figure 6.1, although the skirt does not appear in this plot.

6.6.2 *Case 2: Uniformly Distributed Offsets*

This case uses Equation (6.16), a uniform beam pattern and uniformly distributed offsets as discussed in the non-uniform sampling section (Section 2.7.6). Borrowing a result from Section 3.7.1,

$$\begin{aligned}&\mathrm{E_T}[\chi'_{az}(y;R,p_T(t),v_p,\lambda)]\\ &= \begin{cases} \exp\left(j\frac{2\pi}{\lambda}\frac{y^2}{R}\right)\frac{1}{2bt_s}\sum_{m=m_1}^{m_2}\int_{y/v_p-T/2}^{T/2}\exp\left(-j\frac{2\pi}{\lambda}\frac{yv_p}{R}t\right)dt, & -r\theta_{ra}\le y\le R\theta_{ra},\\ 0, & \text{otherwise.}\end{cases}\end{aligned}$$

where $m_1 = (y/v_p - T/2)/t_s$ and $m_2 = T/(2t_s)$.

From Equation (3.33),

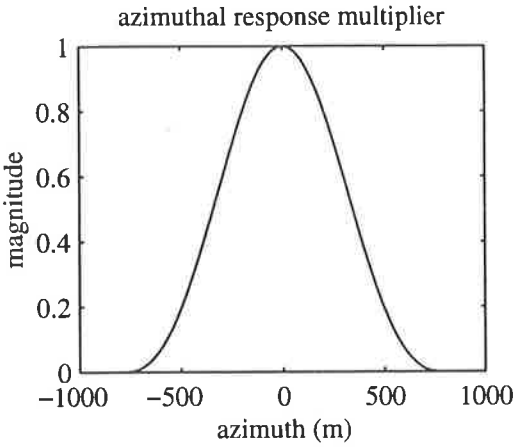

Figure 6.8: The $\text{sinc}^2(\cdot)$ scaling factor for the radar's expected beam power pattern when non-uniform sampling with uniformly random offsets are used.

$$\begin{aligned}
&\mathrm{E}_{\mathbf{T}}[\chi'_{az}(y; R, \{t_n\}, v_p, \lambda)] \\
&= \begin{cases} \operatorname{sinc}\left(2\dfrac{2\pi}{\lambda}\dfrac{yv_p}{R}t_s b\right) \dfrac{\sin\left(\frac{2\pi}{\lambda}\frac{y}{R}([T+t_s]v_p - y)\right)}{\sin\left(\frac{2\pi}{\lambda}\frac{yv_p t_s}{R}\right)}, & -R\theta_{ra} \leq y \leq R\theta_{ra}, \\ 0, & \text{otherwise.} \end{cases}
\end{aligned}$$

With $b = 0$, the result is the same as the uniform sampling case (Equation (6.11)). Otherwise, the response is multiplied by the $\text{sinc}(\cdot)$ function, which has little effect over the range $0 \leq b \leq 0.5$. (If it could get larger, to say 5, it would be able to usefully suppress sidelobes, which is an ironic application for non-uniform sampling.) Figure 6.8 shows this $\text{sinc}(\cdot)$ function squared, plotted for the parameters shown in Table 6.1 and $b = 0.5$, the largest it can sensibly be.

As was noted in Section 3.7.1, having $b = 0.5$ gives the same result as using uniformly random sampling times, Equation (6.18), except for the slightly different integration time.

6.7 Conclusion

The contribution of this chapter was to perform coherent imaging with a SAR with arbitrary transmission times, discuss several sidelobe reduction strategies and derive the expected azimuthal response when random transmission times are employed.

The use of a non-uniform PRI inevitably incurs an imaging performance penalty which may be at least partially suppressed by using fixed weights, such as Hann windows, or position-varying weights, such as those used to optimise the integrated sidelobe ratio. However, the primary consideration here is simultaneous imaging and moving target detection: computationally expensive, slightly degraded imaging may be worth the benefit.

CHAPTER 7

Application to Real Data

This chapter demonstrates the use of a synthetic aperture radar (SAR) with a non-uniform pulse repetition interval (PRI) to both image the ground and perform moving target detection. Non-uniform transmission times are simulated by the resampling of real, oversampled radar data, which are focussed on the ground and on the moving target.

7.1 Introduction

Data from the airborne SAR INGARA were obtained for moving target experimentation from the Microwave Radar Division of the Defence Science and Technology Organisation, Australia (Stacy and Burgess 1996)[1]. The data were uniformly spaced and oversampled the signal by a factor of 3.5: since they satisfied the general bandpass sampling criterion for capturing the signals from both the stationary and the moving targets, they could then be resampled according to any desired scheme, realistically simulating non-uniform transmission times.

The contribution of this chapter is to perform imaging and moving target detection using non-uniformly resampled real SAR data. Section 7.2 discusses the data, its resampling to simulate both a conventional and a non-uniform PRI SAR and the focussing of both the ground and a trials vehicle with a known velocity. The vehicle's parameters are estimated from the data in Section 7.3. Clutter cancellation is demonstrated in Section 7.4. Conclusions are presented in Section 7.5.

[1]The author expresses his thanks to Dr Nick Stacy for his kind assistance.

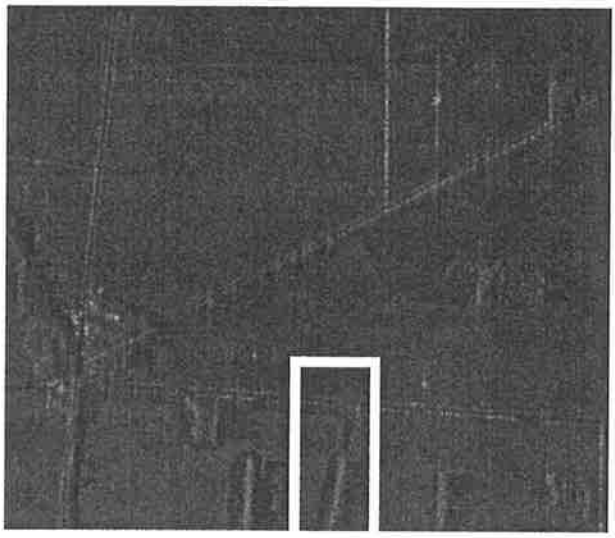

(a) SAR Image.

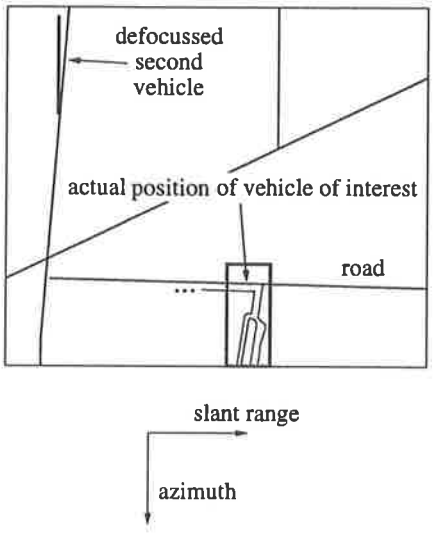

(b) Key.

Figure 7.1: An area containing moving targets. Slant range is left-right; azimuth is top-bottom. The vehicle of interest, not visible in the image, is travelling from left to right along the road in the box. A second vehicle appears immediately to the left of the vertical road in the upper left of the image; it is grossly defocussed, but still appears, due to its large azimuthal velocity and small range velocity.

7.2 Moving Target Imaging

Figure 7.1 shows an X-band SAR image of a scene in South Australia. The white outlined box highlights an area containing a trials vehicle carrying a corner reflector and travelling approximately in the range direction at 18 kph. Table 7.1 contains the radar parameters. The data were provided already range compressed and motion compensated, requiring only azimuthal compression.

Figure 7.2 shows the range compressed data. The moving vehicle and its mounted corner reflector are clearly visible as a diagonal line. Its brightest return is offset from its actual broadside position — just above the centre of the image — probably because the corner reflector was not directed normally to the aircraft's direction of travel. This causes a bias in the parameter estimation, discussed in Section 7.3.

The pulse repetition frequency (PRF) was 378 Hz, about 3.5 times the 3 dB Doppler bandwidth of the ground clutter, which was 115 Hz. It was intended that the trials vehicle indicated in Figure 7.1 be travelling at 1.4 m/s so the data would be unaliased — this PRF could accommodate an unambiguous range velocity variation of ± 3.02 m/s. Unfortunately, the target moved at approximately 4.9 m/s; its Doppler centroid was at about -310 Hz, so its response was subsampled. Fortuitously, this spectrum was mostly outside that of the ground clutter, so

Given	Platform velocity	69.768 m/s
	Real antenna beamwidth	1.5°
	Frequency	9.375 GHz (X-band)
	Sampling interval	0.184343 m
	A/D sample rate	50 MHz
	Range	29500 m
Misc.	Doppler centroid (nominal)	−0.100 cycles/azimuthal sample†
Derived	3 dB Doppler bandwidth, B_d	$\approx$ 115 Hz
	PRF	378.47 Hz ($\approx 3.5B_d$)
	Range resolution	2.998 m
	Ground integration time	11 s (2D filter)
		8.5 s (1D filter‡)

†The centroid was found to be −0.04 cycles/azimuthal sample in the areas of interest.
‡The integration time is reduced by range migration.

Table 7.1: Parameters corresponding to the real data.

Range	Intended	Actual velocity	
(m)	Speed (m/s)	Speed (m/s)	Direction† (deg)
29617	1.4	4.93	−5

†Relative to the platform's port broadside.

Table 7.2: Moving target information. The speed was estimated by 2D focussing of the image to place the vehicle on the road.

the data were still usable. The target's parameters are shown in Table 7.2; a representation of the spectrum of the data is shown in Figure 7.3.

To simulate a radar operating with a PRF approximately equal to the 3 dB Doppler bandwidth, the data were corrected for the Doppler centroid error, upsampled, the moving target was translated in frequency to its correct spectral position, and the result was subsampled. This process is illustrated in Figure 7.4. The parameters are shown in Table 7.3.

Given	Doppler centroid offset	−0.04 cycles/azimuth cell
	Range	29617 m
	Range resolution	2.998 m
	1D integration times	ground 8.5 s
		target 0.59 s
Chosen	PRF	108.1 Hz (378.47 ÷ 3.5)
	Integration time	4 s
	Target lower frequency	47.25 Hz (0.25 × Nyquist)
Derived	Azimuthal pixel spacing	0.65 m
	Azimuthal resolution	ground 1.7 m (2.6 cells)
		target 24 m (37 cells)

Table 7.3: Parameters used when imaging the moving target area.

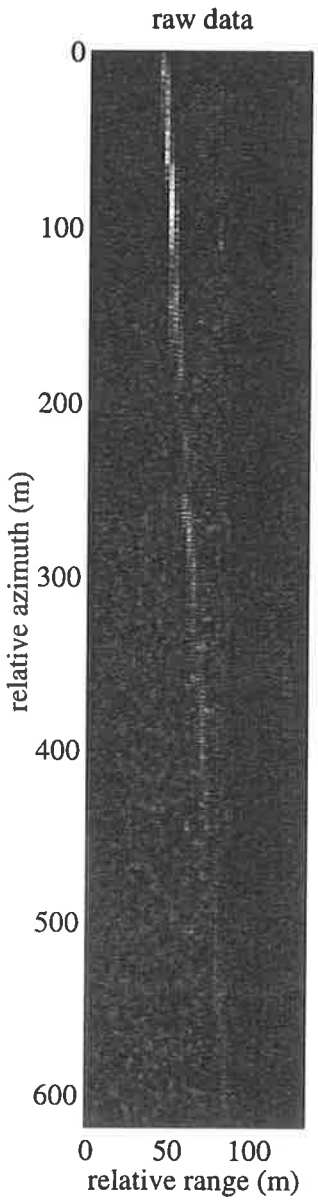

Figure 7.2: Range compressed data corresponding to the highlighted area in Figure 7.1(a).

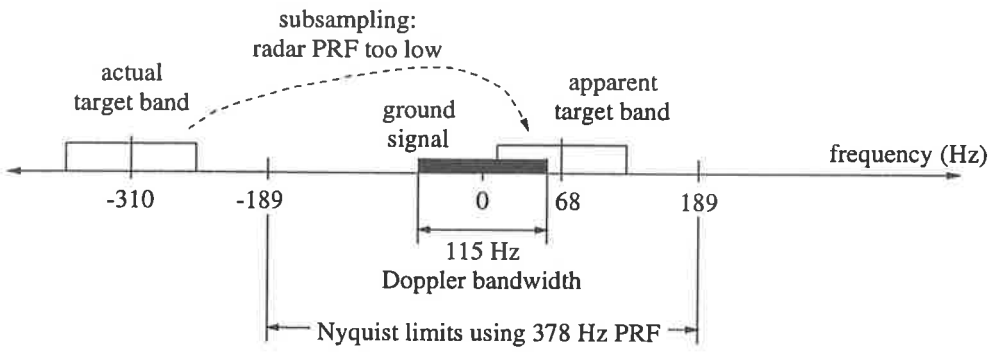

Figure 7.3: The spectrum of the signal and sampled data, showing the subsampling problem.

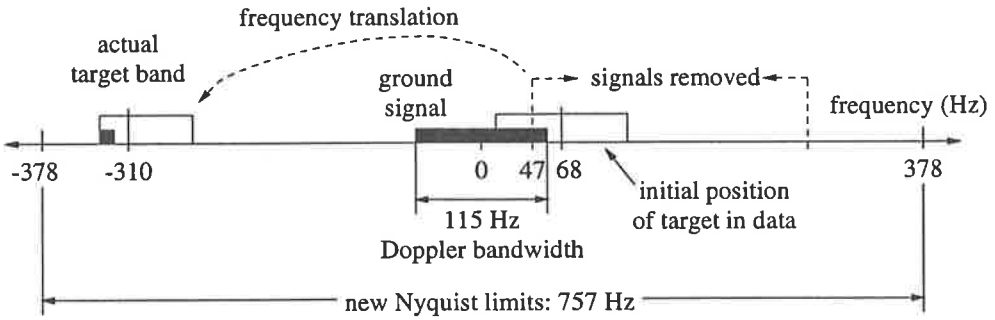

Figure 7.4: The spectrum of the upsampled data, showing the frequency translation of most of the moving target signal and some of the ground signal.

The steps were:

1. The azimuthal data in the highlighted area were first corrected for the Doppler centroid offset caused by a relative motion between the aircraft and ground in the range direction. This was done by multiplying by a complex exponential whose phase changed linearly as a function of position.

2. The data were then upsampled by a factor of two using MATLAB's[2] `resample` function.

3. Most of the moving target signal was separated from the ground clutter using a ninth order Butterworth bandpass filter implemented with the `filtfilt` function, which had zero phase distortion. The lower frequency of 47 Hz was chosen to best separate the moving and stationary targets, based on a visual inspection of the short time Fourier transform of the data.

4. The moving target (and part of the ground signal) was then subtracted from the upsampled data, translated by -378.47 Hz to its correct spectral position, and added to the data.

5. The data were then decimated by a factor of seven to give an effective PRF of 108.13 Hz.

Figure 7.5 shows the processed images, focussed with one dimensional filters. The integration time, used for both images, was much less than the optimum 11 s to allow for range migration. The moving target appears displaced from the road in the ground-focussed image, Figure 7.5(a). The ghosting of the tree line across the road is an artefact resulting from part of the ground data being shifted in frequency along with the moving target; it is analogous to azimuthal ambiguity, but appears at half the target–ambiguity separation.

[2]MATLAB version 4.2c, © 1984–94 The MathWorks, Inc.

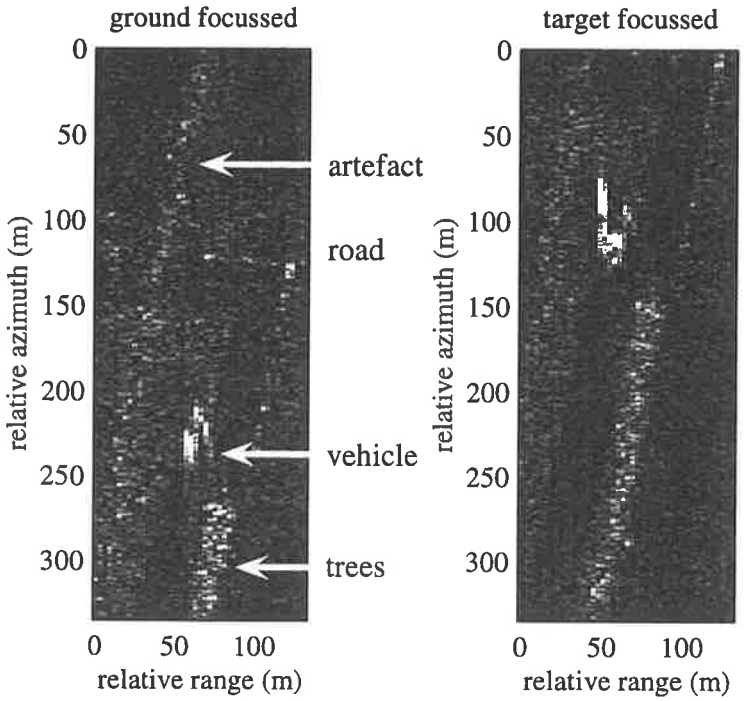

(a) Ground-focussed.

(b) Moving target focussed.

Figure 7.5: Conventional SAR images of the moving target area.

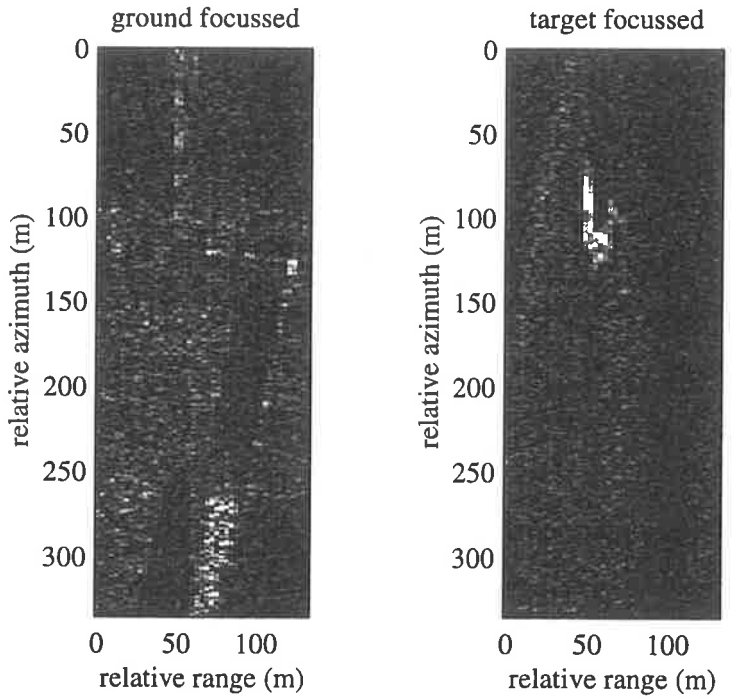

(a) Ground-focussed.

(b) Moving target focussed.

Figure 7.6: Non-uniform PRI SAR images of the moving target area.

Figure 7.5(b) was focussed with a filter tuned to the moving target parameters. (The azimuthal velocity was assumed to be zero and the range velocity was estimated using the knowledge that the target was travelling along the road). The target is in the correct position relative to the road in Figure 7.5(a), and is sharper than in that image. Its still blurry appearance in azimuth is due to the poor resolution (11 m), which results from the short integration time, and decorrelation, due to non-linear target motion. Both the short integration time and the range blurring were due to range migration.

The target in the moving target-focussed image has a higher amplitude than in the ground-focussed image. Its greater range extent results from an improved overlap between the target's phase history and the matched filter in the frequency domain. The filter's bandwidth is less than half that of the target, so much of its phase history was not compressed in the ground-focussed image.

In this example the target is clearly visible to a conventional SAR, albeit incorrectly positioned. Only in specialised cases would it be possible to infer the velocity of a moving target, knowing its position relative to the road on which it is travelling, due to subsampling ambiguities (which exist here) (Raney 1971). Targets with substantial azimuthal velocity components are far less visible, requiring filters at a variety of possible velocities.

7.2.1 *Non-Uniform PRI Simulation*

To simulate a radar with a non-uniform PRI, the data were upsampled and the moving target translated as before, and then upsampled further by a factor of 50. Samples of this were chosen using a non-uniform pattern where intervals were $\pm 20\%$ of the nominal PRI, which was the reciprocal of the 3 dB Doppler bandwidth. A summary of the data sampling rates is: 378.47 Hz (original PRF) $\rightarrow \times 2$ (for correct moving target positioning) $\rightarrow \times 50$ (interpolation) $\rightarrow \div 700$ (random decimation) $\rightarrow$ 108.13 Hz. (Of course, in practice the only data collected would correspond to the transmission times chosen, so no resampling would be necessary.) Resulting images are shown in Figure 7.6; as desired, the moving target is defocussed in Figure 7.6(a) and the ground is defocussed in Figure 7.6(b).

This is an important result. It demonstrates the potential of a SAR with non-uniform sampling to distinguish between stationary and moving scatterers, supporting the assertion discussed throughout this thesis.

Imaging sidelobes have caused a minor degradation of quality in the dark areas of Figure 7.6(a) compared with Figure 7.5(a) when they are at the same range as bright areas. The

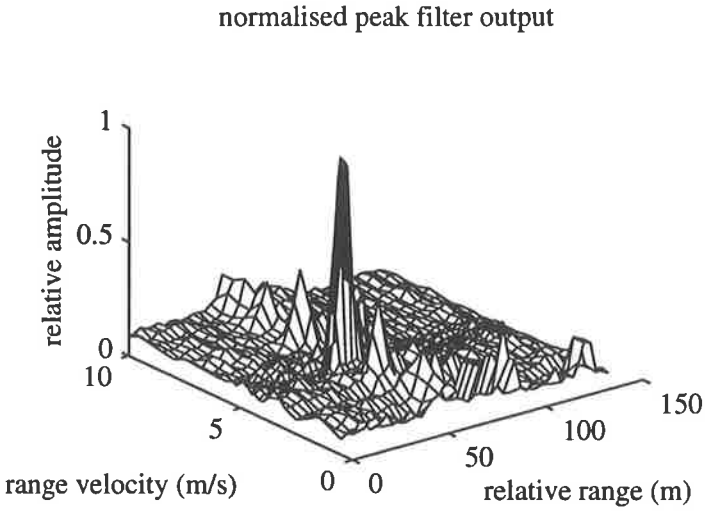

Figure 7.7: Peak filter outputs for different ranges and filter range velocity parameters; $\dot{y} = 0$ m/s.

significant features, such as the trees and the fence posts along the edge of the road, have been imaged similarly.

The diagonal artefact does not appear in Figure 7.6(a), having been defocussed as if it were a moving target. (Azimuthal ambiguity would be affected similarly, since it would occur at an equivalent speed of about 1.7 m/s. This suggests that non-uniform sampling can be used by a ground imaging radar to achieve the same azimuthal resolution as a conventional SAR, but with *fewer* samples. Equivalently, higher resolution could be obtained with the *same* number of samples[3]. This is analogous to a real, sparse array: higher resolution is achieved by the use of a larger aperture and the same number of antenna elements. An assumption is that the scene consists of relatively few, bright scatterers, which are the features of importance.)

7.3 Moving Target Parameter Estimation

In order to estimate the moving target's parameters from the data, the non-uniformly resampled azimuthal data were filtered repeatedly using various values for the range and azimuthal velocities. This is equivalent to an exhaustive search. Figure 7.7 shows the normalised magnitude of the peak filter outputs where the azimuthal velocity is zero and the range velocity is varied between 0 and 10 m/s. The position of the moving target in range can clearly be seen. The lower right hand edge of this plot, where $\dot{R} = 0$ m/s, corresponds to the peak output from the focussed *stationary* scatterers.

[3]This was suggested by Dr Alan Bolton, mid-1994.

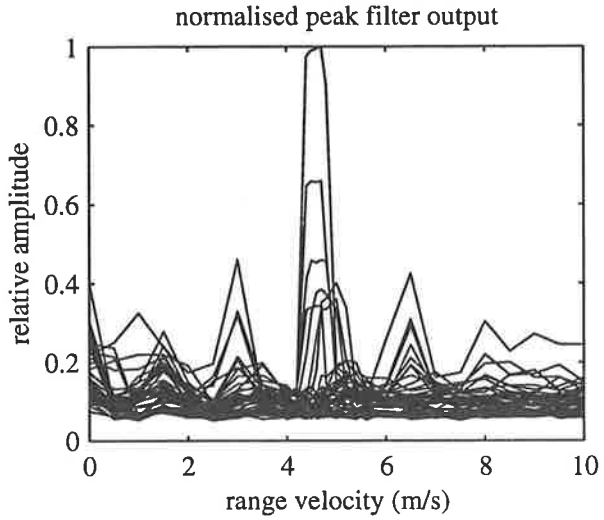

Figure 7.8: Peak filter outputs for different filter range velocity parameters; $\dot{y} = 0$ m/s. The curves correspond to data at different ranges.

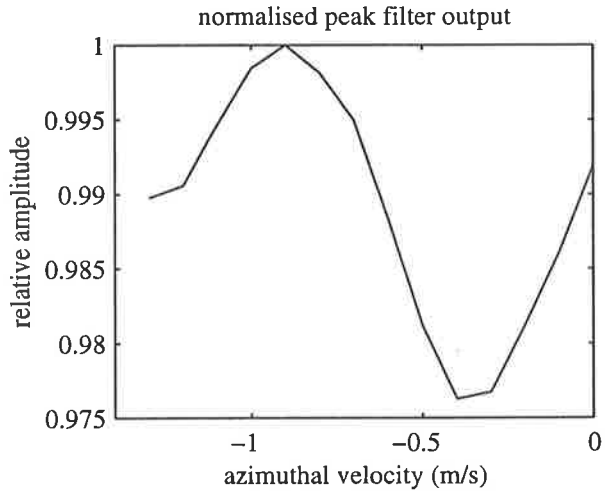

Figure 7.9: Peak filter outputs for different filter azimuthal velocity parameters; $\dot{R} = 4.7$ m/s.

These data are shown in two dimensions for clarity in Figure 7.8. The peak is at $\dot{R} = 4.7$ m/s. The discontinuities away from the central peak are due to the filter output being evaluated at large intervals.

Figure 7.9 shows the peak filter outputs when the data at the range giving the peak output in Figure 7.7 was processed with $\dot{R} = 4.7$ m/s and $\dot{y}$ varied. There is only a very slight change in this amplitude. The peak is at $\dot{y} = -0.9$ m/s, corresponding to the slightly diagonal path of the road in the image.

Figure 7.10 shows the moving target focussed using these estimated parameters: $\dot{R} = 4.7$ m/s and $\dot{y} = -0.9$ m/s. The target is clearly displaced from the road in this image, despite the parameter estimation. This is probably due to the vehicle-mounted corner reflector not

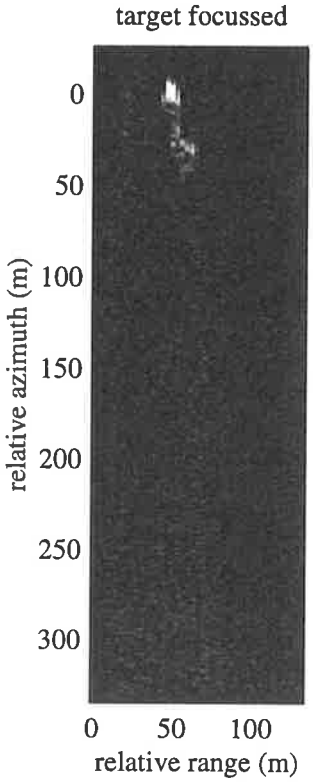

Figure 7.10: The moving target focussed image using the estimated parameters $\dot{R} = 4.7\,\text{m/s}$ and $\dot{y} = -0.9\,\text{m/s}$.

being aligned normally to the flight path of the radar, as noted earlier and shown in Figure 7.2. (It is interesting to note that this 100 m displacement from the road was due to only a 0.2 m/s (0.72 kph) error in range velocity.) This image is clearly better focussed than Figure 7.6(b), however. In addition, the background is clearly better suppressed than in that figure, which follows from the response shown in Figure 7.8: the filter has a much larger response for $\dot{R} = 4.7\,\text{m/s}$ than 4.9 m/s.

7.4 Clutter Cancellation

This section demonstrates clutter cancellation by implementing an approximation to the scheme discussed in Section 4.5. Figure 7.11 shows the incoherent difference between the ground-focussed images produced using conventional and non-uniformly sampled data.

The only visible features are the moving target and the diagonal artefact from the conventional image, and the defocussed moving target from the image generated from the non-uniformly sampled data. Stationary scatterers, including the trees, have very effectively been cancelled, permitting the target to be detected under conditions of severe clutter. This comes

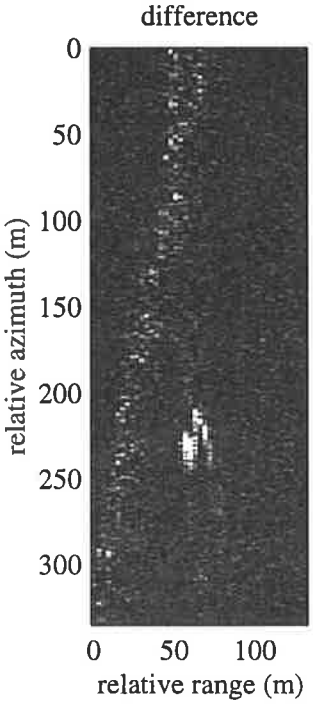

Figure 7.11: Clutter cancellation example: the difference between the ground-focussed images, Figure 7.5(a) and Figure 7.6(a).

at the expense of the volume of data being doubled, however.

Since the image's background shows little energy, it can be concluded that the image of the ground produced by the non-uniformly sampled data is very similar to the conventional SAR ground imagery.

7.5 Conclusions

This chapter's contribution was the demonstration of a SAR with a non-uniform PRI using real data. Processing included ground imaging, moving target imaging and parameter estimation, and clutter cancellation.

Although there is some degradation in the quality of the imagery produced by a radar using a non-uniform PRI in comparison with a conventional system, the former has successfully demonstrated the ability to unambiguously resolve moving targets and preserve the important features of the ground image *with real data,* whilst using the same quantity of data as the conventional SAR. It is to be noted, however, that the vehicle in this scene was a trials vehicle carrying a corner reflector; targets of opportunity may be more difficult to detect owing to their smaller radar cross sections.

CHAPTER 8

Summary

The major contribution of this thesis was the application of a non-uniform pulse repetition interval (PRI) to a synthetic aperture radar (SAR) to address the problem of simultaneous ground imaging and moving target detection (MTD).

In a wide area surveillance scenario, the detection of man made objects is of the highest priority. It was proposed for such a scenario that a SAR using the same average pulse repetition frequency as a conventional ground imaging radar could result in

- the minimum amount of data to be collected and processed,
- the multimode radar being able to perform other duties interleaved with these SAR MTD transmissions, such as searching for, tracking and identifying airborne targets,
- improved electronic warfare characteristics, including a lower probability of radar detection and increased difficulty of deception, and
- little or no range ambiguity penalty.

Section 8.1 summarises the technique by addressing the SAR MTD problems and considers advantages and disadvantages of non-uniform sampling, Section 8.2 lists areas of future research and Section 8.3 concludes this thesis.

8.1 Summary of the SAR MTD Technique

Addressing the issues of an imaging/MTD radar:

Ground imaging The ground is to be imaged faithfully at high resolution.

This is done accurately and efficiently by a conventional SAR.

Non-uniform samples lack the orthogonal properties of uniform samples, resulting in worse imaging sidelobes and a greater computational expense (Chapter 6).

Detection The existence of moving targets is to be determined.

This cannot easily be done by a conventional SAR due to the pulse repetition frequency being only sufficient to sample the ground—a moving target's aliased spectrum will always overlap that of the ground (Raney 1971) (Section 2.3).

A non-uniform PRI SAR is able to detect a moving target outside the unambiguous bandwidth of a conventional SAR (Chapter 4).

However, the target's Doppler centroid must be outside the bandwidth of the clutter (or its Doppler rate must be different from that of the clutter) in order for it to be detected, as discussed in Section 3.6. Since this bandwidth is proportional to the radar platform's velocity, it follows that slowly moving targets may only be detected when the platform travels slowly. This restriction results from using a single antenna; it is not specific to non-uniform sampling.

Since the target's motion may not be linear, or have random variations, the radar data will decorrelate if they are integrated over too long a period. This limits the radar's detection performance. (For a slow SAR platform operating at long range, as with the experimental data used in Chapter 7, the target is visible for several seconds.) Integration time can be minimised by:

- operating at shorter ranges,
- operating at broadside,
- using a larger antenna (to give a narrower beamwidth, since the integration time is proportional to this), and
- using a lower azimuthal resolution (*i.e.* multilook processing, which commonly performed for speckle reduction (Wehner 1995)).

Position and velocity estimation The target's position and velocity are important parameters to be estimated.

The estimation may be performed in two dimensions using non-uniform sampling. In contrast, conventional moving target indication systems have only coarse position information and determine only the range rate of the target (Shrader and Gregers-Hansen 1990).

The conventional ground imaging SAR has the problem of aliasing moving target signals, creating velocity ambiguities. These are resolved using non-uniform sampling (Chapter 5). Furthermore, the statistical variability of the estimates, as characterised by their Cramér-Rao lower bounds (Sections 5.4.2 and 5.5) is comparable to that of uniform sampling.

Target decorrelation is a problem for parameter estimation as well as detection, affecting the accuracy of the estimates. This is common to *all* SAR imaging with a single antenna, including those with unambiguous PRFs, since azimuthal resolution requires looks from different directions. If the target's specific motion or shape are of interest, inverse SAR imaging may be used (Section 2.5).

These issues have been discussed in detail in this thesis.

In addition, these advantages of non-uniform PRIs should be noted:

Efficient radar hardware use Simultaneous ground mapping and moving target detection can be performed with the same number of transmissions as conventional SAR. Additionally, a multimode radar with no strict requirements regarding transmission times may perform other functions between the transmissions to the ground.

Good electronic warfare characteristics A radar broadcasting few, non-uniformly spaced transmissions is relatively resistant to electronic warfare.

Range swath Since the minimum PRI is fairly long, MTD is achieved with little or no range swath penalty or ambiguity.

There is also the potential for a SAR to use non-uniform transmissions to defocus azimuthal ambiguities. (This was mentioned in Section 7.2.1). This technique would provide the radar with a very high azimuthal resolution in an environment with sparsely distributed scatterers.

Current problems with the technique include:

Scene complexity There may only be a few moving targets in the scene; otherwise, a higher mean PRF may be needed to capture the azimuthal signal (Section 2.7.7).

Computational cost Due to the non-uniform sampling, computationally efficient signal processing techniques cannot easily be used. This is an important consideration.

8.2 Future Research

There is much scope for future research on the topic of SAR with non-uniform sampling. Possible areas include

- determining the optimal transmission times for the radar to use, subject to the various criteria listed in Table 2.2 (see Appendix E),
- finding methods of processing non-uniformly sampled data to minimise the computational requirements,
- applying different techniques to estimate the parameters of moving targets and quantifying their performance relative to the Cramér-Rao lower bounds (Sections 5.4.2 and 5.5),
- applying different clutter cancellation methods to improve moving target detection performance (Section 4.5),
- determining the susceptibility of conventional and non-uniform PRI SARs to various electronic countermeasures (including jamming and deception),
- using non-uniform sampling to increase the radar's azimuthal resolution by permitting longer integration times, and
- the use of least squares (and other model-based techniques) to improve imaging performance over conventional methods (Section 6.3.1).

8.3 Conclusion

This thesis has investigated the novel application of non-uniform sampling to synthetic aperture radar moving target detection. The technique was analysed in detail from several viewpoints: the ambiguity function, optimal moving target detection, optimal parameter estimation and imaging. During this, several important results were found.

The non-uniform PRI SAR demonstrates the ability to unambiguously resolve moving target velocities and preserve the important features of the image while using the same average PRF as a conventional SAR. However, there is some degradation of image quality in areas which have low reflectivity compared with adjacent scatterers and there is a substantial computational penalty.

APPENDIX A

Extended Ambiguity Function Properties

The extended cross ambiguity function (AF), Equation (3.14), is duplicated here for reference:

$$\chi'_{s(t),r(t)}(\tau,\phi,\phi') \;=\; \int_{-\infty}^{\infty} s(t)\, r^*(t-\tau)\, e^{-j2\pi(\phi t+\phi' t^2)}\, dt.$$

Similarly to the conventional cross AF, Equation (2.16), this describes the radar receiver's response when it passes the signal returned from a distant, moving point target through a filter matched to the original signal. However, in addition to the radar's signals $s(t)$ and $r(t)$, the time delay τ and Doppler frequency ϕ, there is also a Doppler rate term ϕ' caused by the relative acceleration between the radar and the target.

If $r(t) = s(t)$, Equation (3.14) becomes

$$\begin{aligned}
\chi'_{s(t),s(t)}(\tau,\phi,\phi') &= \int_{-\infty}^{\infty} s(t)\, s^*(t-\tau)\, e^{-j2\pi(\phi t+\phi' t^2)}\, dt \\
&= e^{-j\pi(\phi\tau+\phi'\tau^2/2)} \int_{-\infty}^{\infty} s(t+\tau/2)\, s^*(t-\tau/2)\, e^{-j2\pi[(\phi+\phi'\tau)t+\phi' t^2]}\, dt \\
&= e^{-j\pi(\phi\tau+\phi'\tau^2/2)}\, \chi_s(\tau,x,\phi')
\end{aligned}$$

where $\chi_s(\tau,x,\phi')$ is referred to here as the *symmetric* extended ambiguity function. Note that $x = \phi + \phi'\tau$.

Properties of the symmetric extended AF follow. (Blahut (1991, page 16) and Cook and Bernfeld (1967, pages 68–76) list the properties of the conventional Woodward AF, Equation (2.15).) The conventional results are obtained from the following if $\phi' = 0$.

1. Let $\tau = 0$ and $\phi' = 0$: $\chi_s(0,x,0) = \int_{-\infty}^{\infty} |s(t)|^2\, e^{-j2\pi x t}\, dt$, which is the Fourier transform of the square of $s(t)$.

2. (**Origin**) Let $\tau = 0$, $x = 0$ and $\phi' = 0$: $\chi_s(0,0,0) = \int_{-\infty}^{\infty} |s(t)|^2\, dt = E_p$, the energy in $s(t)$.

3. (**Shift**) Let $s'(t) = s(t - \Delta)$. Then $\chi_{s'}(\tau, x, \phi') = e^{-j2\pi(x\Delta + \phi'\Delta^2)}\, \chi_s(\tau, x + 2\phi'\Delta, \phi')$.

4. (**Modulation**) Let $s'(t) = s(t)\, e^{j2\pi f t}$. Then $\chi_{s'}(\tau, x, \phi') = e^{j2\pi f \tau}\, \chi_s(\tau, x, \phi')$.

5. (**Symmetry**) $\chi_s(\tau, x, \phi') = \chi_s^*(-\tau, -x, -\phi')$.

6. (**Maximum**) The largest value of the AF always is at the origin.

$$|\chi_s(\tau, x, \phi')| \;\leq\; |\chi_s(0,0,0)| \;=\; E_p,$$

with strict inequality if $(\tau, x, \phi') \neq (0,0,0)$.

7. (**Scaling**) Let $s'(t) = s(at)$, with $a > 0$. Then

$$\chi_{s'}(\tau, x, \phi') \;=\; \frac{1}{a}\chi_s\left(a\tau, \frac{x}{a}, \frac{\phi'}{a^2}\right).$$

(Note that a does not need to be greater than zero with the normal AF, but instead requires $|a|$ in the denominator (Blahut 1991, page 16).)

8. (**Quadratic phase**) Let $s'(t) = s(t)\, e^{j\pi\alpha t^2}$. Then

$$\chi_{s'}(\tau, x, \phi') \;=\; \chi_s(\tau, x - \alpha\tau, \phi').$$

9. (**Volume property**) It is well known that

$$\int_{-\infty}^{\infty}\int_{-\infty}^{\infty} |\chi_s(\tau, x)|^2\, d\tau\, dx \;=\; |\chi_s(0,0)|^2 \;=\; E_p^2,$$

which implies that the shape of the envelope of the AF may be rearranged by altering $s(t)$, but not reduced overall.

However, I have not been able to show that

$$\int_{-\infty}^{\infty}\int_{-\infty}^{\infty}\int_{-\infty}^{\infty} |\chi_s(\tau, x, \phi')|^2\, d\tau\, dx\, d\phi' \;=\; \text{a constant.}$$

10. (**Product rule**) Let $z(t) = u(t)v(t)$. Then

$$\chi_z(\tau, x, \phi') \;=\; \int_{-\infty}^{\infty} \chi_u(\tau, \lambda, \phi'/2)\, \chi_v(\tau, x - \lambda, \phi'/2)\, d\lambda$$

is the convolution of the two individual functions in the Doppler domain, and a scaling in the Doppler rate domain.

APPENDIX B

SAR Clutter Modelling

This appendix derives a simple model for ground clutter in synthetic aperture radar (SAR) for the purpose of generating a covariance matrix as discussed in Section 4.2.4. This model is compared with those in the literature (Barbarossa 1992b, Ward 1994, Smith 1995).

The modelling of clutter is a significant field of radar (*e.g.*, (Skolnik 1990)). In order for a moving target detection radar to perform well, it is important that the model adopted by the signal processor accurately represent the scene visible to the radar.

The ground clutter model discussed in Section 4.2.4, developed by Barbarossa (1992b), is very simple; although it was derived from a Doppler viewpoint, it assumed no change in geometry during the integration period. It is shown here, however, that it is a very good approximation to the more accurate model derived in the next section.

B.1 Time Domain Clutter Modelling

The clutter vector $\boldsymbol{v}_c$ should be derived from the same model as the signal from a moving target, $\rho \boldsymbol{A}\boldsymbol{v}(\theta, \phi)$, as defined in Equation (4.4). The scenario is represented by Figure B.1, showing the clutter as a uniformly distributed collection of independent scatterers at similar ranges. (This is known as the 'sandpaper' clutter model (Smith 1995).) This is a changing geometry, rather than Doppler, viewpoint: it is the difference between the signals received by the radar in two different positions which are important, rather than the motion of the radar, as utilised by Barbarossa (1992b).

The covariance of the clutter $\boldsymbol{R}_c = \mathrm{E}\left[\boldsymbol{v}_c \boldsymbol{v}_c^H\right]$, so its entries

$$(\boldsymbol{R}_c)_{k,l} \;=\; \mathrm{E}[v_c(t_k; R)\, v_c^*(t_l; R)],$$

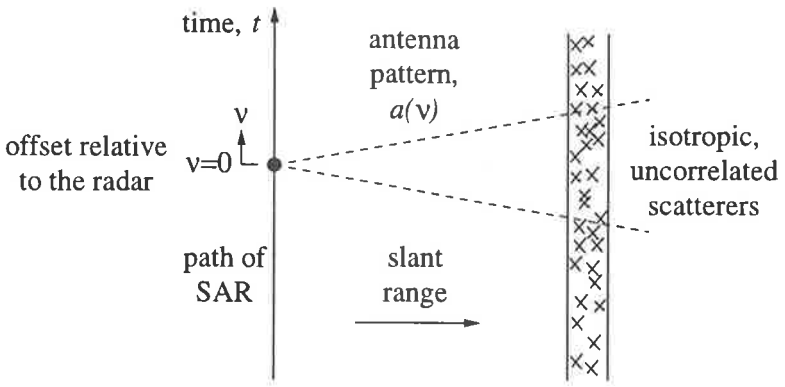

Figure B.1: A representation of the ground clutter model.

where $\{t_n\}$ are the sample times, ';' means 'parameterised by' and R is the minimum range of the many scatterers in the scene, assumed to be the same for the entire data set due to the prior range compression and narrow antenna beamwidth. The expectation is with respect to the random, complex amplitudes of the clutter returns, which are assumed to be statistically independent and identically distributed.

The clutter response at time t_k, $v_c(t_k; R)$, is modelled by integrating the range-compressed radar returns from all the scatterers:

$$v_c(t_k; R) \;=\; \int_{-\infty}^{\infty} \tilde{\rho}_{R,t_k+\nu}\; a(\nu; R)\, v_0(\nu; R)\; d\nu.$$

ν is the relative position of the radar and scatterer, expressed as a difference between the time the radar was in a particular position and the time it was adjacent to the scatterer. $\tilde{\rho}_{R,t_k+\nu}$ is the complex amplitude of the return from the scatterer adjacent to the radar at time $t_k + \nu$.

$$v_0(\nu; R) \;=\; \exp(j2\pi[F_{dc}\nu + F_{dr}(R)\nu^2/2]) \tag{B.1}$$

(Equation (2.10)) is the geometry-dependent phase term. F_{dc} is the Doppler centroid and F_{dr} is the Doppler rate. These are assumed to be the same for all scatterers due to the similar radar-scatterer geometries. (This formulation deliberately neglects constant gain terms, such as attenuation losses, being more concerned about the structure of the clutter.)

This model is similar to those used by Ward (1994) and Smith (1995), who formulate the clutter covariance for a space-time adaptive processing (STAP) application. Both use uncorrelated clutter (although Ward (1994) divides the scene into a finite number of uncorrelated clutter patches, rather than having infinitesimal patches). The coordinate systems are different from the one used here, with both references integrating around the azimuth angle rather

than incorporating the SAR-clutter geometry. That is more appropriate when the patterns of the receiving elements have large beamwidths; for a narrow beamwidth, as with SAR, it is reasonable to neglect range migration effects for small values of t_d.

Both references assume a linear phase dependent upon the scatterers' positions, rather than a quadratic phase. This is reasonable due to the very short length of a STAP antenna, but is inappropriate for a long, synthetic array. However, both models tend towards that of Barbarossa (1992b), Equation (4.8), when a narrow antenna beam and small radar position change are assumed.

Using Equation (B.1), the covariance

$$\begin{aligned}(\boldsymbol{R}_c)_{k,l} &= \mathrm{E}\Big[\iint \tilde{\rho}_{R,t_k+\nu_1}\,\tilde{\rho}^*_{R,t_l+\nu_2}\,a(\nu_1;R)\,a(\nu_2;R)\cdot \\ &\qquad \exp(j2\pi[F_{dc}(\nu_1-\nu_2)+F_{dr}(R)(\nu_1^2-\nu_2^2)/2])\,d\nu_1\,d\nu_2\Big] \\ &= \iint \mathrm{E}\Big[\tilde{\rho}_{R,t_k+\nu_1}\,\tilde{\rho}^*_{R,t_l+\nu_2}\Big]\;a(\nu_1;R)\,a(\nu_2;R)\;\cdot \\ &\qquad \exp(j2\pi[F_{dc}(\nu_1-\nu_2)+F_{dr}(R)(\nu_1^2-\nu_2^2)/2])\,d\nu_1\,d\nu_2.\end{aligned}$$

Since the scatterers' amplitudes are independent, they are uncorrelated:

$$\mathrm{E}\Big[\tilde{\rho}_{R,t_k+\nu_1}\tilde{\rho}^*_{R,t_l+\nu_2}\Big] \;=\; \rho^2\,\delta(t_k+\nu_1-t_l-\nu_2).$$

Then

$$\begin{aligned}(\boldsymbol{R}_c)_{k,l} &= \rho^2\int a(\nu_2+t_l-t_k;R)\,a(\nu_2;R)\;\cdot \\ &\qquad e^{j2\pi(F_{dc}(\nu_2+t_l-t_k-\nu_2)+F_{dr}[(\nu_2+t_l-t_k)^2-\nu_2^2]/2)}\,d\nu_2 \\ &= \rho^2\,e^{-j2\pi[F_{dc}t_d+F_{dr}t_d^2/2]}\;\cdot \\ &\qquad \int_{-\infty}^{\infty} a(\nu-t_d;R)\,a(\nu;R)\,e^{-j2\pi F_{dr}\nu t_d}\,d\nu \qquad \text{(B.2)} \\ &= r(t_d),\end{aligned}$$

where $t_d = t_k - t_l$ is the difference between the sample times of interest. Therefore, the covariance is a function of the timing differences. This reflects the stationarity of the clutter process.

For broadside stripmap operation, Equation (4.6) may be used with

$$\theta = v_p t/\sqrt{R^2+(v_p t)^2}, \qquad \text{(B.3)}$$

giving the antenna's normalised azimuthal power response

$$F(t) = \text{sinc}^4\left(\pi \frac{Dv_p t}{\lambda\sqrt{R^2 + (v_p t)^2}}\right). \tag{B.4}$$

Then

$$a(t) = \text{sinc}^2\left(\pi \frac{Dv_p t}{\lambda\sqrt{R^2 + (v_p t)^2}}\right).$$

This may be substituted into Equation (B.2). Now, either t_d is small (in the order of several seconds, say) in comparison with ν (which approaches $\pm\infty$) or t_d and ν have similar magnitudes, in which case $a(\nu - t_d; R)$ does not change much. (The limits of t_d were chosen to lie within the 3 dB beamwidth of the antenna.) It is therefore reasonable to allow $a(\nu - t_d; R) = a(\nu; R)$. Additionally, normalising and using the assumption that $F_{dc} = 0$ (since the scatterers are stationary) allows Equation (B.2) to be written

$$r(t_d) \approx e^{-j\pi F_{dr} t_d^2} \int_{-\infty}^{\infty} a^2(\nu; R)\, e^{-j2\pi F_{dr} \nu t_d}\, d\nu. \tag{B.5}$$

With a change of variables (Equation (B.3) for θ and Equation (4.7) for f, assuming that $R \gg v_p t$), this is similar to the model with the power spectral density given by Equation (4.8) (Barbarossa 1992b) except for the initial phase term. The next section shows a numerical comparison of the two.

B.2 Comparison between Doppler and Time Domain Models

Figure B.2(a) shows the power spectral density of the Doppler clutter model, Equation (4.8), with a range $R = 30\,\text{km}$, platform velocity $v_p = 70\,\text{m/s}$, wavelength $\lambda = 3.2\,\text{cm}$ and antenna length $D = 1.2\,\text{m}$.

Figure B.2(b) shows the incoherent difference between this and Equation (B.5). This difference is clearly very small, being in the order of -60 dB, justifying the use of Equation (4.8) for the numerical examples in this thesis.

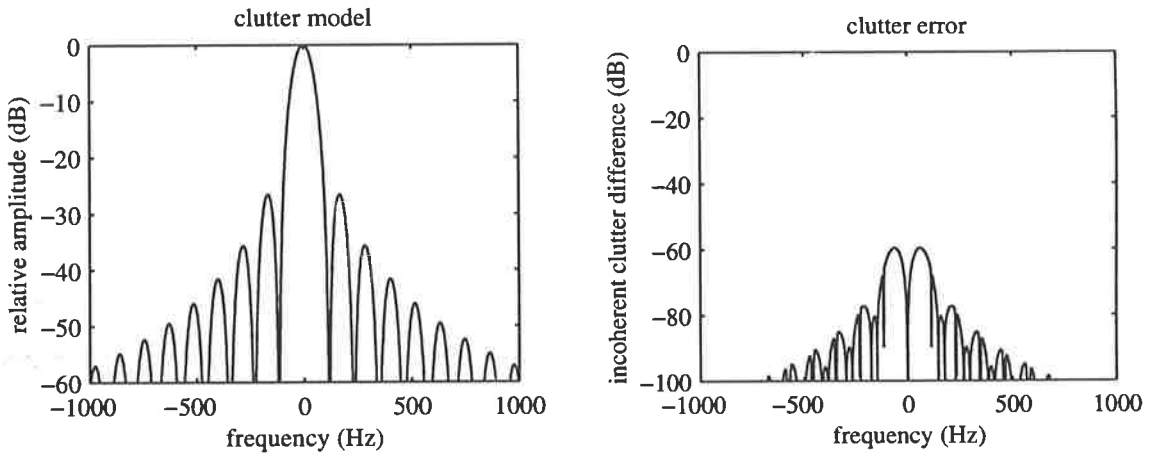

(a) Doppler clutter model.

(b) Incoherent difference between the Doppler and time domain models.

Figure B.2: A comparison between the Doppler and time domain SAR clutter models.

APPENDIX C

Biased Estimator Lower Variance Bounds

It is well known that the Cramér-Rao bound is the lower bound on the variance of an unbiased estimator. This appendix discusses the lower variance bound when a particular, biased estimator is used.

The Cramér-Rao bounds for the K unknown parameters stored in the vector $\boldsymbol{u}$ are given by

$$\mathrm{CRLB}\{(\hat{\boldsymbol{u}})_k\} \;=\; (\boldsymbol{J}^{-1})_{k,k}$$

where $\boldsymbol{J}$ is the Fisher information matrix, which has the entries

$$(\boldsymbol{J})_{k,l} \;\triangleq\; \mathrm{E}\left[\frac{\partial \ln p(\boldsymbol{y};\boldsymbol{u})}{\partial(\boldsymbol{u})_k}\frac{\partial \ln p(\boldsymbol{y};\boldsymbol{u})}{\partial(\boldsymbol{u})_l}\right]$$

(from Equation (5.6)). $p(\boldsymbol{y};\boldsymbol{u})$ is the probability density function of the measurement $\boldsymbol{y}$ parameterised by the unknowns. E[·] is the expectation operation.

Often we are interested in specific, possibly dimension reducing functions of the unknown parameters $\boldsymbol{u}$; let these be denoted by the $R \times 1$ vector $\boldsymbol{g} = \boldsymbol{g}(\boldsymbol{u})$. (An example of such a transformation is that of estimating the signal-to-noise ratio of a sinusoid when its amplitude and the variance of additive, white, Gaussian noise are unknown.)

It is shown by Kay (1993, page 45–46, 70–72) that the lower variance bounds for the estimation of a transformation of the unknown parameters satisfy

$$\boldsymbol{C}_{\boldsymbol{g}} - \frac{\partial \mathrm{E}[\hat{\boldsymbol{g}}]}{\partial \boldsymbol{u}}\boldsymbol{J}^{-1}\frac{\partial \mathrm{E}[\hat{\boldsymbol{g}}]^T}{\partial \boldsymbol{u}} \;\geq\; \boldsymbol{0} \qquad \text{(C.1)}$$

(meaning that the left hand side is non-negative definite). The Jacobian

$$\frac{\partial \mathrm{E}[\hat{\boldsymbol{g}}]}{\partial \boldsymbol{u}} = \begin{bmatrix} \frac{\partial \mathrm{E}[(\hat{\boldsymbol{g}})_1]}{\partial (\boldsymbol{u})_1} & \frac{\partial \mathrm{E}[(\hat{\boldsymbol{g}})_1]}{\partial (\boldsymbol{u})_2} & \cdots & \frac{\partial \mathrm{E}[(\hat{\boldsymbol{g}})_1]}{\partial (\boldsymbol{u})_K} \\ \frac{\partial \mathrm{E}[(\hat{\boldsymbol{g}})_2]}{\partial (\boldsymbol{u})_1} & \frac{\partial \mathrm{E}[(\hat{\boldsymbol{g}})_2]}{\partial (\boldsymbol{u})_2} & \cdots & \frac{\partial \mathrm{E}[(\hat{\boldsymbol{g}})_2]}{\partial (\boldsymbol{u})_K} \\ \vdots & \vdots & \ddots & \vdots \\ \frac{\partial \mathrm{E}[(\hat{\boldsymbol{g}})_R]}{\partial (\boldsymbol{u})_1} & \frac{\partial \mathrm{E}[(\hat{\boldsymbol{g}})_R]}{\partial (\boldsymbol{u})_2} & \cdots & \frac{\partial \mathrm{E}[(\hat{\boldsymbol{g}})_R]}{\partial (\boldsymbol{u})_K} \end{bmatrix}$$

and ^{T} is the matrix transpose operation. $\mathbf{0}$ is an $R \times R$ square matrix with all elements set to zero.

It follows that *the lower variance bound for a biased estimator may be found via Equation (C.1) by using the expected value of that estimator, expressed in terms of the actual parameters, as a variable transformation.* We then have $\boldsymbol{g}(\boldsymbol{u}) = \mathrm{E}[\hat{\boldsymbol{u}}]$. Then $\boldsymbol{g}$ is a $K \times 1$ vector. This gives

$$\boldsymbol{C}_{\hat{\boldsymbol{u}}} - \frac{\partial \mathrm{E}[\hat{\boldsymbol{u}}]}{\partial \boldsymbol{u}} \boldsymbol{J}^{-1} \frac{\partial \mathrm{E}[\hat{\boldsymbol{u}}]^T}{\partial \boldsymbol{u}} \geq \mathbf{0}, \tag{C.2}$$

so the lower bounds themselves are given by the diagonal of $\boldsymbol{C}_{\hat{\boldsymbol{u}}}$:

$$\mathrm{Var}[(\hat{\boldsymbol{u}})_k] \geq (\boldsymbol{C}_{\hat{\boldsymbol{u}}})_{k,k}.$$

This is the vector equivalent of the scalar result published in, *e.g.*, (Van Trees 1968, page 146).

In the limiting case, where an unbiased estimator is used, $\boldsymbol{g} = [(\boldsymbol{u})_1, (\boldsymbol{u})_2, \ldots, (\boldsymbol{u})_K]^T$, so that $\frac{\partial \mathrm{E}[\hat{\boldsymbol{g}}]}{\partial \boldsymbol{u}} = \boldsymbol{I}$, the identity matrix. Therefore, the lower variance bound

$$\mathrm{Var}[(\hat{\boldsymbol{u}})_k] \geq (\boldsymbol{C}_{\hat{\boldsymbol{u}}})_{k,k} = (\boldsymbol{J}^{-1})_{k,k} = \mathrm{CRLB}\{(\hat{\boldsymbol{u}})_k\},$$

the Cramér-Rao bound.

As a further example, for an additive bias, $\boldsymbol{g} = \boldsymbol{u} + \boldsymbol{b}$, where $\boldsymbol{b}$ is a vector of bias values. Then $\frac{\partial \mathrm{E}[\hat{\boldsymbol{g}}]}{\partial \boldsymbol{u}} = \boldsymbol{I}$ also, so from Equation (C.2) the lower variance bound is still the Cramér-Rao bound.

APPENDIX D

The Complex Gaussian Fisher Information Matrix

This appendix derives the Fisher information matrix for a random process $\boldsymbol{x} \sim \mathcal{CN}_N(\boldsymbol{m}(\boldsymbol{u}), \boldsymbol{R})$, where $\boldsymbol{m}(\boldsymbol{u})$ is an $N \times 1$ mean vector dependent upon the parameters $\boldsymbol{u} = [u_1, u_2, \ldots, u_M]^T$ and $\boldsymbol{R}$ is an $N \times N$ covariance matrix. This problem is similar to one solved by Kay (1993, page 73–76) for a real Gaussian distribution.

$\boldsymbol{x}$'s probability density function is

$$p(\boldsymbol{x}; \boldsymbol{u}) = \frac{1}{\pi^N} \left|\boldsymbol{R}^{-1}\right| \exp\left(-[\boldsymbol{x} - \boldsymbol{m}(\boldsymbol{u})]^H \boldsymbol{R}^{-1} [\boldsymbol{x} - \boldsymbol{m}(\boldsymbol{u})]\right)$$

(using Equation (4.12)), where ^{H} is the conjugate transpose operation.

The Fisher information matrix has the entries

$$(\boldsymbol{J})_{k,l} \triangleq \mathrm{E}\left[\frac{\partial \ln p(\boldsymbol{x}; \boldsymbol{u})}{\partial u_k} \frac{\partial \ln p(\boldsymbol{x}; \boldsymbol{u})}{\partial u_l}\right]$$

(from Equation (5.6)). The left term in the expectation is:

$$\frac{\partial \ln p(\boldsymbol{x}; \boldsymbol{u})}{\partial u_k} = \left[\frac{\partial \boldsymbol{m}(\boldsymbol{u})}{\partial u_k}\right]^H \boldsymbol{R}^{-1} [\boldsymbol{x} - \boldsymbol{m}(\boldsymbol{u})] + [\boldsymbol{x} - \boldsymbol{m}(\boldsymbol{u})]^H \boldsymbol{R}^{-1} \frac{\partial \boldsymbol{m}(\boldsymbol{u})}{\partial u_k}.$$

If we let $\boldsymbol{y} = \boldsymbol{x} - \boldsymbol{m}(\boldsymbol{u})$ be the random values centred on 0, then

$$
\begin{aligned}
&\frac{\partial \ln p(\boldsymbol{x};\boldsymbol{u})}{\partial u_k}\frac{\partial \ln p(\boldsymbol{x};\boldsymbol{u})}{\partial u_l} \\
&= \left(\frac{\partial \boldsymbol{m}(\boldsymbol{u})}{\partial u_k}^H \boldsymbol{R}^{-1}\boldsymbol{y} + \boldsymbol{y}^H\boldsymbol{R}^{-1}\frac{\partial \boldsymbol{m}(\boldsymbol{u})}{\partial u_k}\right)\frac{\partial \boldsymbol{m}(\boldsymbol{u})}{\partial u_l}^H \boldsymbol{R}^{-1}\boldsymbol{y} + \\
&\quad \left(\frac{\partial \boldsymbol{m}(\boldsymbol{u})}{\partial u_k}^H \boldsymbol{R}^{-1}\boldsymbol{y} + \boldsymbol{y}^H\boldsymbol{R}^{-1}\frac{\partial \boldsymbol{m}(\boldsymbol{u})}{\partial u_k}\right)\boldsymbol{y}^H\boldsymbol{R}^{-1}\frac{\partial \boldsymbol{m}(\boldsymbol{u})}{\partial u_l} \\
&= \underbrace{\frac{\partial \boldsymbol{m}(\boldsymbol{u})}{\partial u_k}^H \boldsymbol{R}^{-1}\boldsymbol{y}\frac{\partial \boldsymbol{m}(\boldsymbol{u})}{\partial u_l}^H \boldsymbol{R}^{-1}\boldsymbol{y}}_{(1)} + \underbrace{\boldsymbol{y}^H\boldsymbol{R}^{-1}\frac{\partial \boldsymbol{m}(\boldsymbol{u})}{\partial u_k}\frac{\partial \boldsymbol{m}(\boldsymbol{u})}{\partial u_l}^H \boldsymbol{R}^{-1}\boldsymbol{y}}_{(2)} + \\
&\quad \underbrace{\frac{\partial \boldsymbol{m}(\boldsymbol{u})}{\partial u_k}^H \boldsymbol{R}^{-1}\boldsymbol{y}\,\boldsymbol{y}^H\boldsymbol{R}^{-1}\frac{\partial \boldsymbol{m}(\boldsymbol{u})}{\partial u_l}}_{(3)} + \underbrace{\boldsymbol{y}^H\boldsymbol{R}^{-1}\frac{\partial \boldsymbol{m}(\boldsymbol{u})}{\partial u_k}\boldsymbol{y}^H\boldsymbol{R}^{-1}\frac{\partial \boldsymbol{m}(\boldsymbol{u})}{\partial u_l}}_{(4)}.
\end{aligned}
$$

The expected values of each of these terms will now be considered:

$$
\begin{aligned}
\mathrm{E}[(1)] &= \mathrm{E}\left[\frac{\partial \boldsymbol{m}(\boldsymbol{u})}{\partial u_k}^H \boldsymbol{R}^{-1}\boldsymbol{y}\,\boldsymbol{y}^T\boldsymbol{R}^{-1T}\frac{\partial \boldsymbol{m}(\boldsymbol{u})}{\partial u_l}^*\right] \\
&= \frac{\partial \boldsymbol{m}(\boldsymbol{u})}{\partial u_k}^H \boldsymbol{R}^{-1}\,\mathrm{E}\left[\boldsymbol{y}\boldsymbol{y}^T\right]\boldsymbol{R}^{-1T}\frac{\partial \boldsymbol{m}(\boldsymbol{u})}{\partial u_l}^*
\end{aligned}
$$

where ^{T} is the transpose operation and * indicates conjugation. (Note that $\boldsymbol{R}^{-1} = \boldsymbol{R}^{-1H}$.) Now,

$$
\begin{aligned}
\mathrm{E}\left[\boldsymbol{y}\boldsymbol{y}^T\right] &= \mathrm{E}\left[(\boldsymbol{a}+j\boldsymbol{b})(\boldsymbol{a}+j\boldsymbol{b})^T\right] \\
&= \mathrm{E}\left[\boldsymbol{a}\boldsymbol{a}^T\right] - \mathrm{E}\left[\boldsymbol{b}\boldsymbol{b}^T\right] - j\mathrm{E}\left[\boldsymbol{a}\boldsymbol{b}^T\right] - j\mathrm{E}\left[\boldsymbol{b}\boldsymbol{a}^T\right] \\
&= 0,
\end{aligned}
$$

so that $\mathrm{E}[(1)] = 0$ since the real and imaginary parts of $\boldsymbol{y}$ have equal autocovariances and are uncorrelated.

Next:

$$
\begin{aligned}
\mathrm{E}[(2)] &= \frac{\partial \boldsymbol{m}(\boldsymbol{u})}{\partial u_l}^H \boldsymbol{R}^{-1}\,\mathrm{E}\left[\boldsymbol{y}\boldsymbol{y}^H\right]\boldsymbol{R}^{-1}\frac{\partial \boldsymbol{m}(\boldsymbol{u})}{\partial u_k} \\
&= \frac{\partial \boldsymbol{m}(\boldsymbol{u})}{\partial u_l}^H \boldsymbol{R}^{-1}\frac{\partial \boldsymbol{m}(\boldsymbol{u})}{\partial u_k}
\end{aligned}
$$

since $\mathrm{E}\left[\boldsymbol{y}\boldsymbol{y}^H\right] = \boldsymbol{R}$.

It is easily seen that $\mathrm{E}[(3)] = \mathrm{E}[(2)]^*$, and that $\mathrm{E}[(4)] = 0$ using a similar argument to that used for $\mathrm{E}[(1)]$.

Therefore,

$$(\boldsymbol{J})_{k,l} = 2\Re\left\{ \frac{\partial \boldsymbol{m}(\boldsymbol{u})}{\partial u_k}^H \boldsymbol{R}^{-1} \frac{\partial \boldsymbol{m}(\boldsymbol{u})}{\partial u_l} \right\},$$

where $\Re\{\cdot\}$ returns the real part of its argument.

APPENDIX E

Notes Regarding the Optimal Transmission Times

This appendix discusses issues related to determining the transmission times to be used by a synthetic aperture radar (SAR) performing moving target detection and ground imaging with the minimum number of transmissions. An investigation into the relative performance of the multitude of possibilities is beyond the scope of this thesis.

E.1 Introduction

Although the randomly distributed sampling scheme may theoretically give the best performance with a large number of samples (Section 2.7), other non-uniform radar pulse repetition interval (PRI) schemes may be more appropriate for SAR. Note the specific SAR sampling requirements discussed in Section 2.7.7.

There are several SAR moving target performance requirements: ground imaging, moving target detection/indication (MTD) and moving target parameter estimation. The first should be representative of the scene, the second quick and reliable and the third accurate in both position and velocity. Estimating the target's radar cross section has a low priority.

Accordingly, each proposed sampling scheme should be rated according to its imaging performance, detection statistics, parameter estimation performance (bias and variance) and computational cost. (Its ambiguity function may also provide useful insights.) The performance requirements are listed in Table 2.2.

E.2 Possible Schemes

The author has divided sampling schemes into three classes: *deterministic: heuristic, deterministic: optimal* and *random.* These will now be discussed.

E.2.1 Deterministic: Heuristic

These sampling schemes usually consist of a fixed number of unique sampling intervals repeated continuously. They are chosen to satisfy a simple, common sense criterion, such as having only a few sampling intervals — under these conditions, fast Fourier transforms may be used and filter weights may be precalculated.

There are many possible schemes, some of which are:

High PRF bursts These may be separated by gaps, a low pulse repetition frequency (PRF) or random PRIs. They are intended to permit moving target indication (MTI) filtering by allowing processing over several equally spaced samples.

Different PRFs This is similar in concept to a Doppler centroid estimation technique discussed in Section 2.5 (Chang and Curlander 1992), where moving targets' Doppler centroids may be found unambiguously using MTI and the Chinese remainder theorem.

Minimum redundancy This scheme, based on sparse array theory, is discussed in detail in Section E.3.

E.2.2 Deterministic: Optimal

It may be possible to find schemes which optimise the different figures of merit derived in this thesis. Possibilities are

Imaging Transmission times may optimise the radar's azimuthal beam pattern, for example the integrated sidelobe ratio (as done in Section 6.4.3).

Moving target detection There are three MTD expressions from Chapter 4 which may be maximised with respect to the transmission times $\{t_i\}$: the signal-to-disturbance ratio improvement I_{sdr} (Equation (4.19)), the detection threshold γ (Equation (4.24)) and the α term in the Marcum-Q function used for the receiver operating characteristic. The optimal filter, Equation (4.16), is valid for any transmission times; substituting this into

each of these expressions gives the common result

$$\{t_i\}_{opt} = \underset{\{t_i\}}{\arg\max}\ \hat{\boldsymbol{v}}^H(\boldsymbol{\theta},\boldsymbol{t})\boldsymbol{R}_d(\boldsymbol{t})^{-1}\hat{\boldsymbol{v}}(\boldsymbol{\theta},\boldsymbol{t}) \tag{E.1}$$

where $\hat{\boldsymbol{v}}(\boldsymbol{\theta},\boldsymbol{t})$ is the signal weighted by the two-way antenna pattern, $\boldsymbol{\theta}$ contains the target's parameters, $(\boldsymbol{t})_i = t_i$ are the transmission times and $\boldsymbol{R}_d(\boldsymbol{t})$ is the disturbance correlation matrix.

A fourth alternative is to maximise the ratio of the signal-to-disturbance ratio improvement for non-uniform samples to the value for uniform samples, thereby minimising the impact of (or maximising the benefit from) the non-uniform transmission times[1]. However, since the denominator of this is independent of the non-uniform sampling times, the expression for the optimal times simplifies into Equation (E.1).

Due to the matrix inverse, Equation (E.1) is an extremely difficult equation to solve. Although this has been attempted by the author, no useful simplifications have been found, and the equation may have to be solved numerically.

Parameter estimation The estimation errors may be minimised by optimising the Fisher information matrix, Equation (5.7). This could be done by maximising its determinant, for example. This is another very difficult problem, since it cannot be assumed that the noise is white, and the covariance matrix depends upon the sampling times.

There may be little value in any of these results, since they may only be optimal when the parameters of the radar and target match those used during the optimisation process. For example, optimality may be achieved at a range of 30 km when a target in a certain azimuthal position has a ground velocity of 5 kph in range and 10 kph in azimuth. Suboptimal results may be achieved for a target in another position.

There is the possibility of adaptively changing the PRIs depending upon a suspected detection, however.

E.2.3 Random Sampling Schemes

It was shown in Section 3.7.1 that it is preferable from a spectral estimation point of view to use random sample times rather than repeated ones, as the sidelobes are spread out over a wide

[1] Conversation with D. Gray, 1996.

bandwidth. This is beneficial for SAR since

- with imaging they degrade the background, rather than cause azimuthal ambiguities,
- with parameter estimation they are less likely to affect the peak or cause ambiguities, and
- randomness gives improved electronic warfare characteristics due to its unpredictability.

However, randomness has the disadvantage of increased computational requirements: the filters required for processing the data have to be recomputed for every radar position and target velocity. Some possibilities are:

Good spectral estimation Equation (2.18), a relationship between the spectrum of the sampling process and the probability density function of the sampling intervals, may be used to design random sampling schemes which have good properties.

Work similar to this was done by Vergara-Dominguez (1993), who found the relationship between the sampling probability density function and the signal-to-disturbance ratio improvement and the velocity coverage percentage for both random intervals and random offsets. These could be applied to the SAR problem.

Random intervals Random intervals, correlated and uncorrelated, were discussed in detail in Section 2.7.6. They have good properties, tending towards those of uniformly distributed samples in the limit (but without the problem of infringing the minimum transmission interval). This means that the expected parameter estimation accuracy and imaging performance tend towards those of uniform sampling (Sections 5.5 and 6.6).

Random offsets Although the properties of random offsets may be inferior to those of random intervals, there is some potential for a computational saving: since small offsets do not affect a slowly changing phase very much, a conventional, position invariant matched filter may be applied to the central part of a target's azimuthal phase response, thereby partially focussing the scatterer. For high resolution focussing, far shorter, position-varying filters corresponding to the ends of the chirp may be applied and incorporated with the low resolution image[2].

Some sampling distributions may be mathematically interesting but unusable, such as the Poisson distribution, which gives alias free spectral estimates but violates the minimum PRI requirement.

---

[2]Dr Alan Bolton, 6th May, 1995.

Of course, it is possible to employ a sampling scheme which incorporates combinations of the schemes listed above.

E.3 Minimum Redundancy Sampling Scheme

This section describes a novel deterministic sampling scheme in detail.

The philosophy adopted here is to arrange the transmission times such that their *differences* span the range from half the reciprocal of the highest frequency of interest to the period of their total duration in equal increments. The smallest time difference is limited by the reduction in unambiguous range.

This is an original contribution. It is based on a technique used for sparse phased array antennas attempting to determine the direction of arrival of as many targets as possible, *e.g.* (Pearson et al. 1990). (Non-uniform arrays were mentioned briefly in Section 2.7.8.)

The covariance matrix corresponding to an arbitrary SAR scene is given by Equation (B.2), which is a function of the differences between the radar's N transmission times. Thus for the times $\boldsymbol{t} = [0, 1, 2, 3]^T$, there are four ways of finding $r(0)$, three ways of finding $r(1)$, two ways of finding $r(2)$ and one way of finding $r(3)$. However, if all the time differences were different, such as for $\boldsymbol{t} = [0, 0.5, 2, 3]^T$, many more values may be found for $r(\tau)$: in this case, $r(0)$, $r(0.5)$, $r(1)$, $r(1.5)$, $r(2)$, $r(2.5)$ and $r(3)$. Even though the latter sampling scheme has the same span as the former, it doubles the bandwidth of the unambiguous spectral estimate: the intervals between the $r(\cdot)$ estimates have been halved, and the estimated power spectrum is given by the Fourier transform of the covariance by the Wiener-Khinchine relation (eg, (Cooper and McGillem 1986, page 253)). Note that the covariance samples are uniformly spaced.

(For a phased array, the number of unique directions of arrival is given by the number of unique spacing separations between antenna elements. If the array had N uniformly spaced elements, this would be $N - 1$. With non-uniform arrays, the figure may be much larger — up to $N(N-1)/2$ (Pearson et al. 1990).)

Unfortunately, optimal spacings do not exist for more than four samples. Beyond this, the spacings with a minimum redundancy may be used. For a given N, these have a minimum number of repeated differences while guaranteeing that all differences are present. Pearson et al. (1990) present an algorithm for generating a close approximation to these optimal spacings.

This concept may be applied to SAR by first considering the highest unambiguous frequency desired. Suppose it were acceptable for the moving target to be detected unambiguously up to

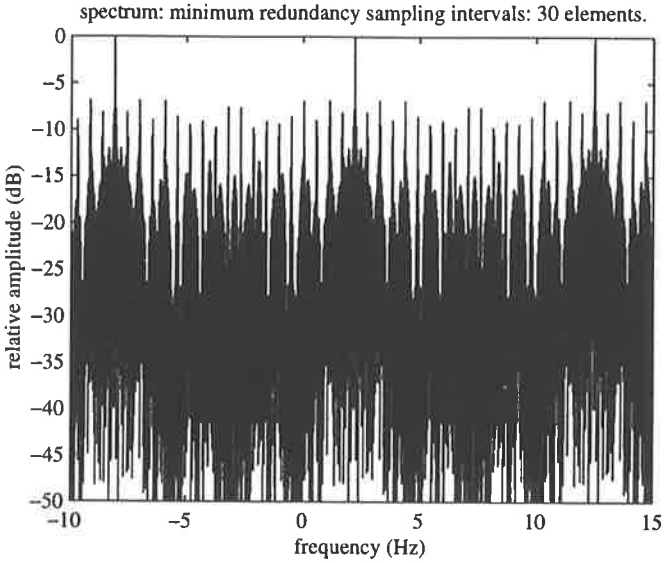

Figure E.1: Estimated spectrum; minimum redundancy intervals.

10 times the bandwidth of the ground clutter (which is realistic, due to range ambiguity effects and the increasingly non-linear moving target azimuthal response, Equation (3.11)). Using Pearson's algorithm, it was found that this requires $N = 30$; the time intervals, normalised to be in multiples of 1, are 1, 1, 1, 1, 10, 10, 10, 10, 10, 19, 19, 19, 19, 19, 19, 19, 19, 19, 19, 19, 9, 9, 9, 9, 5, 1, 1, 1, 1, giving a span of 308. Transmissions with these intervals could be generated repeatedly.

To detect targets, the returned signal is range compressed and dechirped at each Doppler rate of interest prior to finding a spectral estimate. (Dechirping is necessary since the technique relies on the signal being stationary.)

As an example of a spectral estimate, Figure E.1 shows the estimated spectrum of a 2.2 Hz cisoid sampled using four repeated sequences, each with a duration of thirty seconds. It can clearly be seen that the aliases occur at multiples of about 10 Hz. This figure should be compared with those of the random offsets and random intervals, Figures 2.10 and 2.12, respectively. The first sidelobe is at approximately -6 dB, as opposed to ≈ -13 dB for the latter two, and the noise floor is several decibels worse than either.

E.4 Conclusions

This appendix classified and discussed many potential SAR sampling schemes. Minimum redundancy sampling was described in detail. It is beyond the scope of this thesis to compare them quantitatively.

Bibliography

Barbarossa, S.: 1989, Doppler-rate filtering for detecting moving targets with synthetic aperture radar, *SPIE Millimeter Wave and Synthetic Aperture Radar* **1101**, 140–147.

Barbarossa, S.: 1992a, Detection and imaging of moving objects with synthetic aperture radar, Part 2: Joint time-frequency analysis by Wigner-Ville distribution, *IEE Proceedings-F* **139**(1), 89–97.

Barbarossa, S.: 1992b, Detection and imaging of moving objects with synthetic aperture radar, Part 1: Optimal detection and parameter estimation theory, *IEE Proceedings-F* **139**(1), 79–88.

Barbarossa, S. and Farina, A.: 1990, A novel procedure for detecting and focusing moving objects with SAR based on the Wigner-Ville distribution, *Proceedings of the IEEE International Radar Conference*, pp. 44–50.

Barbarossa, S. and Farina, A.: 1994, Space-time-frequency processing of synthetic aperture radar signals, *IEEE Transactions on Aerospace and Electronic Systems* **30**(2), 341–358.

Barbarossa, S. and Mascolo, G.: 1994, Autofocusing techniques for imaging moving targets by SAR based on multilinear time-frequency representations, *Proceedings of the International Conference on Radar*, SEE, pp. 284–289.

Barbarossa, S., Marsili, L. and Mungari, G.: 1996, SAR super-resolution imaging by signal subspace projection techniques, *Proceedings of EUSAR'96*, VDE-VERLAG GMBH, pp. 267–270.

Barbarossa, S., Porchia, A. and Scaglione, A.: 1996, Multiplicative multi-lag high order ambiguity function, *Proceedings of ICASSP'96*, IEEE, pp. 3022–3025.

Berkovitz, A. and Rusnak, I.: 1992, FFT processing of randomly sampled harmonic signals, *IEEE Transactions on Signal Processing* **40**(11), 2816–2819.

Bilinskis, I. and Mikelsons, A.: 1992, *Randomized Signal Processing*, Acoustics, Speech and Signal Processing series, Prentice Hall, UK.

Blahut, R. E.: 1991, Theory of remote surveillance algorithms, *in* R. E. Blahut, W. Miller and C. H. Wilcox (eds), *Radar and Sonar Part I*, Springer-Verlag.

Boni, C., Richard, M. and Barbarossa, S.: 1994, Optimal configuration and weighting of nonuniform arrays according to a maximum ISLR criterion, *Proceedings of ICASSP'94*, IEEE, pp. V–157–160.

Brennan, L. and Reed, I.: 1968, Optimum processing of unequally spaced radar pulse trains for clutter rejection, *IEEE Transactions on Aerospace and Electronic Systems* **AES–4**(3), 474–477.

Bühring, W.: 1980, Coherent signal processing in a frequency agile jittered pulse radar, *Proceedings of the IEEE International Radar Conference*, pp. 188–193.

Burden, R. L. and Faires, J. D.: 1985, *Numerical Analysis*, third edn, Prindle, Weber and Schmidt, Boston, MA.

Cashman, J.: 1997, SAR beamforming, Private facsimile.

Chang, C. and Curlander, J.: 1992, Application of the multiple PRF technique to resolve Doppler centroid estimation ambiguity for spaceborne SAR, *IEEE Transactions on Geoscience and Remote Sensing* **30**(5), 941–949.

Chen, H. and McGillem, C.: 1991, Target motion compensation in synthetic aperture radar, *IEEE Aerospace and Electronic Systems Magazine* pp. 14–18.

Coe, D. and White, D. R.: 1995, Moving target detection in SAR imagery: Experimental results, *Proceedings of the IEEE International Radar Conference*, pp. 644–649.

Cook, C. E. and Bernfeld, M.: 1967, *Radar Signals: An Introduction to Theory and Application*, Academic Press, New York.

Cooper, G. R. and McGillem, C. D.: 1986, *Probabilistic Methods of Signal and System Analysis*, second edn, CBS College Publishing, 383 Madison Avenue, New York, NY 10017.

Costas, J.: 1984, A study of a class of detection waveforms having nearly ideal range-Doppler ambiguity properties, *Proceedings of the IEEE* **72**(8), 996–1009.

Curlander, J. and McDonough, R.: 1991, *Synthetic Aperture Radar: Systems and Signal Processing*, Wiley Series in Remote Sensing, John Wiley and Sons, Inc., New York.

Cutrona, L.: 1990, Synthetic aperture radar, *in* M. Skolnik (ed.), *Radar Handbook*, second edn, McGraw-Hill, New York, chapter 21.

D'Addio, E. and Galati, G.: 1985, Adaptivity and design criteria of a latest-generation MTD processor, *IEE Proceedings-F* **132**(1), 58–65.

D'Addio, E., Di Bisceglie, M. and Bottalico, S.: 1994, Detection of moving objects with airborne SAR, *Signal Processing* **36**(2), 149–162.

Damini, A. and Haslam, G.: 1996, SAR/ISAR ship imaging: Theoretical analysis and practical results, *Proceedings of EUSAR'96*, VDE-VERLAG GMBH, pp. 443–446.

D'Assumpcao, H.: 1980, Some new signal processors for arrays of sensors, *IEEE Transactions on Information Theory* **IT-26**(4), 441–453.

D'Assumpcao, H. and Gray, D.: 1995, Array signal processing, A course held at the Signal Processing Research Institute, the Levels, South Australia.

Dowski, E., Whitmore, C. and Avery, S.: 1988, Estimation of randomly sampled sinusoids in additive noise, *IEEE Transactions on Acoustics, Speech and Signal Processing* **36**(12), 1906–1908.

Elachi, C.: 1988, *Spaceborne Radar Remote Sensing: Applications and Techniques*, IEEE Press, 345 East 47th Street, New York, NY 10017-2394. IEEE order number PC 02295.

Ender, J. H.: 1996, Detection and estimation of moving target signals by multi-channel SAR, *Proceedings of EUSAR'96*, VDE-VERLAG GMBH, pp. 411–417.

Farina, A.: 1990, Electronic counter-countermeasures, *in* M. Skolnik (ed.), *Radar Handbook*, second edn, McGraw-Hill, Inc, New York, chapter 9.

Flynn, T. J.: 1992, Wavenumber-domain SAR focussing from a nonuniform synthetic aperture, *Proceedings of ICASSP'92*, IEEE, pp. III–1–4.

Fowler, B.: 1996, The standoff observation of enemy ground forces or From project PEEK to JSTARS, Presentation to the Defence Science and Technology Organisation, Salisbury, Australia.

Freedman, A., Bose, R. and Steinberg, B. D.: 1996, Thinned stepped frequency waveforms to furnish existing radars with imaging capability, *IEEE Aerospace and Electronic Systems Magazine* **11**(11), 39–43.

Freeman, A.: 1984, Simple MTI using synthetic aperture radar, *Proceedings of IGARSS'84 Symposium*, ESA SP-215, pp. 65–70.

Friedlander, B. and Francos, J. M.: 1995, Estimation of amplitude and phase parameters of multicomponent signals, *IEEE Transactions on Signal Processing* **43**(4), 917–926.

Galati, G. and Crescimbeni, R.: 1993, Basic concepts on detection, estimation and optimum filtering, *in* G. Galati (ed.), *Advanced Radar Techniques and Systems*, Peter Peregrinus Ltd, chapter 1, pp. 1–151.

Golestani, Y., Chandrasekar, V. and Keeler, R. J.: 1995, Dual polarized staggered PRT scheme for weather radars: Analysis and applications, *IEEE Transactions on Geoscience and Remote Sensing* **33**(2), 239–246.

Hagfors, T. and Kofman, W.: 1991, Mapping of overspread targets in radar astronomy, *Radio Science* **26**(2), 403–416.

Hammerle, K.: 1990, Cascaded MTI and coherent integration techniques with motion compensation, *Proceedings of the IEEE International Radar Conference*, pp. 164–169.

Harmon, J. and Slade, M.: 1992, Radar mapping of Mercury: Full-disk images and polar anomalies, *Science* **258**, 640–643.

Harris, F.: 1978, On the use of windows for harmonic analysis with the discrete Fourier transform, *Proceedings of the IEEE* **66**(1), 51–83.

harris, f.: 1984, Observer adaptive PRF for synthetic aperture radar imaging, *Proceedings of ICASSP'84*, IEEE, pp. 24.10.1–4. San Diego, CA.

Haykin, S.: 1991, *Adaptive Filter Theory*, second edn, Prentice-Hall, Inc, NJ.

Hovanessian, S.: 1984, *Radar System Design and Analysis*, Artech House, Inc., Norwood, MA.

Hsiao, J.: 1974, On the optimization of MTI clutter rejection, *IEEE Transactions on Aerospace and Electronic Systems* **AES-10**(5), 622–629.

Ikram, M. Z., Abed-Meraim, K. and Hua, Y.: 1996, Estimating Doppler parameters in SAR imaging for moving targets, *Proceedings of 1996 IEEE Nordic Signal Processing Symposium.*

Jansen, W. and Kirchner, C.: 1996, ONEST: Concept of a real time SAR/MTI processor, *Proceedings of EUSAR'96*, VDE-VERLAG GMBH, pp. 349–352.

Jingwen, L., Junxiang, H., Yinqing, Z. and Shizhang, F.: 1995, Imaging of moving targets with SAR based on space-time two dimensional signal processing, *Proceedings of the IEEE International Radar Conference*, pp. 396–398.

Johnson, D. H. and Dudgeon, D. E.: 1993, *Array Signal Processing: Concepts and Techniques*, Signal Processing series, Prentice Hall, Englewood Cliffs, NJ 07632.

Kay, S.: 1988, Statistically/computationally efficient frequency estimation, *Proceedings of the IEEE International Conference on ASSP*, pp. 2292–2295.

Kay, S. M.: 1993, *Fundamentals of Statistical Signal Processing: Estimation Theory*, Prentice Hall signal processing series, PTR Prentice Hall, New Jersey.

Kent, S. and Paker, S.: 1996, Rejection of motion irregularities in SAR images, *Proceedings of EUSAR'96*, VDE-VERLAG GMBH, pp. 147–150.

Kesteven, M.: 1997, Imaging with a synthesis radiotelescope array, Presentation at the Cooperative Research Centre for Sensor Signal and Information Processing.

Kitchen, J.: 1992, Minimum variance estimation of polynomial phase signals, *Proceedings of ISSPA'92*, IEEE, pp. 360–363.

Klemm, R.: 1993, Adaptive air- and spaceborne MTI under jamming conditions, *Proceedings of the IEEE National Radar Conference*, pp. 167–172.

Klemm, R.: 1996a, Forward looking radar/SAR: Clutter and jammer rejection with STAP, *Proceedings of EUSAR'96*, VDE-VERLAG GMBH, pp. 485–488.

Klemm, R.: 1996b, Real-time adaptive airborne MTI, part I: Space-time processing, *Proceedings of the 1996 CIE International Conference of Radar*, pp. 755–760.

Klemm, R.: 1996c, Real-time adaptive airborne MTI, part II: Space-frequency processing, *Proceedings of the 1996 CIE International Conference of Radar*, pp. 430–433.

Li, F., Held, D., Curlander, J. and Wu, C.: 1985, Doppler parameter estimation for spaceborne synthetic-aperture radars, *IEEE Transactions on Geoscience and Remote Sensing* **GE-23**(1), 47–56.

Lomb, N.: 1976, Least-squares frequency analysis of unequally spaced data, *Astrophysics and Space Science* **39**, 447–462.

Lush, D. C.: 1990, Airborne radar analysis using the ambiguity function, *Proceedings of the IEEE International Radar Conference*, pp. 600–605.

Lush, D. C. and Hudson, D. A.: 1992, Resolution analysis of large time-bandwidth radars for non-uniform target motion, *Proceedings of Radar'92*, IEE, pp. 407–410.

Mao, Y. H.: 1993, MTI, MTD and adaptive clutter cancellation, *in* G. Galati (ed.), *Advanced Radar Techniques and Systems*, Peter Peregrinus Ltd, chapter 6, pp. 285–442.

Martin, N., Jain, L. and Bolton, A.: 1994, A technique for enhanced range resolution in SAR systems in knowledge-based environment, *IEEE Aerospace and Electronic Systems Magazine*.

Martin, R.: 1997, Nonuniformly sampled signals: Theory and techniques for analysis, Seminar at the University of South Australia's Institute for Telecommunications Research. GEC Hirst, UK.

Marvasti, F. A.: 1987, *A Unified Approach to Zero-Crossings and Nonuniform Sampling of Single and Multidimensional Signals and Systems*, Farokh A. Marvasti, Department of Electrical Engineering, Illinois Institute of Technology, Chicago, Illinois 60616, U.S.A.

McDonough, R. N. and Whalen, A. D.: 1995, *Detection of Signals in Noise*, second edn, Academic Press, Inc, San Diego.

Mobley, S.: 1995, Synthetic aperture radar system processing with a nonuniform pulse repetition interval, *Technical report*, Missile Guidance Directorate, Research, Development and Engineering Center, U.S. Army Missile Command.

Mobley, S. and Maier, M.: 1996, Synthetic aperture radar-systems processing with a non-uniform pulse repetition interval, *Proceedings of EUSAR'96*, VDE-VERLAG GMBH, pp. 407–410.

Novak, L.: 1996, SAR MTI with millimetre-wave radar, Discussion at EUSAR'96, Königswinter, Germany.

O'Shea, P.: 1996, An iterative algorithm for estimating the parameters of polynomial phase signals, *Proceedings of ISSPA'96*, IEEE, pp. 730–731.

Ouchi, K.: 1985, On the multilook images of moving targets by synthetic aperture radar, *IEEE Transactions on Antennas and Propagation* **AP-33**(8), 823–827.

Pearson, D., Pillai, S. U. and Lee, Y.: 1990, An algorithm for near-optimal placement of sensor elements, *IEEE Transactions on Information Theory* **36**(6), 1280–1284.

Peleg, S. and Porat, B.: 1991a, The Cramer-Rao lower bound for signals with constant amplitude and polynomial phase, *IEEE Transactions on Signal Processing* **39**(3), 749–752.

Peleg, S. and Porat, B.: 1991b, Estimation and classification of polynomial-phase signals, *IEEE Transactions on Information Theory* **37**(2), 422–430.

Peyregne, R.: 1996, SAR and MTI: A new synthesis for airborne SAR without using navigation system, *Proceedings of EUSAR'96*, VDE-VERLAG GMBH, pp. 489–492.

Ping, B. and Zongzhi, C.: 1996, A new synthetic aperture radar autofocusing approach, *Proceedings of the 1996 CIE International Conference of Radar*, pp. 326–329.

Porchia, A., Barbarossa, S., Scaglione, A. and Giannakis, G. B.: 1996, Autofocussing techniques for SAR imaging based on the multilag high order ambiguity function, *Proceedings of ICASSP'96*, IEEE, pp. 2086–2089.

Porter, N., Tough, R. and Ward, K.: 1993, SAR, ISAR and hybrid SAR/ISAR—a unified treatment of radar imaging, *Proceedings of the IEEE National Radar Conference*, pp. 134–139.

Raney, R.: 1971, Synthetic aperture imaging radar and moving targets, *IEEE Transactions on Aerospace and Electronic Systems* **AES-7**(3), 499–505.

Raney, R.: 1992, Special SAR techniques and applications, *Fundamentals and Special Problems of Synthetic Aperture Radar (SAR) (AGARD-LS-182)*, AGARD, pp. 10/1–15.

Rieck, W.: 1996, SAR imaging of moving targets: Application of time-frequency distribution for single- and multichannel data, *Proceedings of EUSAR'96*, VDE-VERLAG GMBH, pp. 431–434.

Rife, D. and Boorsteyn, R.: 1976, Multiple tone parameter estimation from discrete-time observations, *The Bell System Technical Journal* **55**(9), 1389–1410.

Rife, D. C. and Boorsteyn, R. R.: 1974, Single-tone parameter estimation from discrete-time observations, *IEEE Transactions on Information Theory* **IT-20**(5), 591–598.

Roberts, R. A. and Mullis, C. T.: 1987, *Digital Signal Processing*, Addison-Wesley Series in Electrical Engineering: Digital Signal Processing, Addison-Wesley, Reading, Massachusetts.

Runge, H. and Bamler, R.: 1989, PRF ambiguity resolving for SAR, *Proceedings of IGARSS 1989*, pp. 2572–2575.

Sakai, H.: 1986, Estimation of frequencies of sinusoids in colored noise, *Proceedings of ICASSP'86*, IEEE, pp. 177–180.

Scargle, J. D.: 1982, Studies in astronomical time series analysis. II. statistical aspects of spectral analysis of unevenly spaced data, *The Astrophysical Journal* **263**(2), 835–853.

Shrader, W. W. and Gregers-Hansen, V.: 1990, MTI radar, *in* M. Skolnik (ed.), *Radar Handbook*, second edn, McGraw-Hill, chapter 15.

Skolnik, M. I.: 1990, *Radar Handbook*, second edn, McGraw-Hill, Inc, New York.

Slocumb, B. and Kitchen, J.: 1994, A polynomial phase parameter estimation-phase unwrapping algorithm, *Proceedings of ICASSP'94*, IEEE.

Smith, R. and Clarkson, J.: 1992, Integrated adaptive nulling/DPCA processing for a moving look-down radar, *Proceedings of Radar'92*, IEE, pp. 300–303.

Smith, S. T.: 1995, Space-time clutter covariance matrix computation and interference subspace tracking, *Proceedings of the 29th Annual Asilomar Conference on Signals and Systems*.

Soumekh, M.: 1995, Reconnaissance with ultra wideband UHF synthetic aperture radar, *IEEE Signal Processing Magazine* **12**(4), 21–40.

Soumekh, M.: 1996, Super-resolution array processing in SAR, *IEEE Signal Processing Magazine* **13**(6), 14, 16, 18.

Stacy, N. and Burgess, M.: 1996, INGARA: The Australian airborne imaging radar land surveillance system, *Proceedings of EUSAR'96*, VDE-VERLAG GMBH, pp. 333–334.

Stankwitz, H., Dallaire, R. and Fienup, J.: 1995, Nonlinear apodization for sidelobe control in SAR imagery, *IEEE Transactions on Aerospace and Electronic Systems* **31**(1), 267–279.

Stark, H. and Woods, J. W.: 1986, *Probability, Random Processes, and Estimation Theory for Engineers*, Prentice-Hall, NJ.

Staudaher, F. M.: 1990, Airborne MTI, *in* M. Skolnik (ed.), *Radar Handbook*, second edn, McGraw-Hill.

Stimson, G.: 1983, *Introduction to Airborne Radar*, Hughes Aircraft Company, El Segundo, California.

Stone, M. and Ince, W.: 1980, Air-to-ground MTI radar using a displaced phase centre, phased array, *Proceedings of the IEEE International Radar Conference*, pp. 225–230.

Sulzer, M. P.: 1986, A radar technique for high range resolution incoherent scatter autocorrelation function measurements utilizing the full average power of klystron radars, *Radio Science* **21**(6), 1033–1040.

Swingler, D.: 1996, Approximations to the Cramer-Rao lower bound on frequency estimates for complex sinusoids in the presence of sampling jitter, *Signal Processing* **48**, 77–83.

Tobin, M.: 1996, Real time simultaneous SAR/GMTI in a tactical airborne environment, *Proceedings of EUSAR'96*, VDE-VERLAG GMBH, pp. 63–66.

Tomiyasu, K.: 1993, Synthetic aperture radar image processing of range ambiguous signals, *Proceedings of IGARSS'93 — IEEE International Geoscience and Remote Sensing Symposium*, pp. 1194–1195. Volume 3.

Vakman, D.: 1968, *Sophisticated Signals and the Uncertainty Principle in Radar*, Springer-Verlag, New York.

Van Trees, H. L.: 1968, *Detection, Estimation and Modulation Theory, Part I*, John Wiley & Sons, New York.

Vergara-Dominguez, L.: 1993, Analysis of the digital MTI filter with random PRI, *IEE Proceedings-F* **140**(2), 129–137.

Wang, Y., Wang, Z., Jing, L. and Liang, Y.: 1996, A new method for moving object detection in airborne SAR, *Proceedings of EUSAR'96*, VDE-VERLAG GMBH, pp. 533–536.

Ward, J.: 1994, Space-time adaptive processing for airborne radar, *Technical Report 1015*, MIT Lincoln Laboratory.

Wehner, D. R.: 1995, *High-Resolution Radar*, second edn, Artech House, Inc., MA.

White, R.: 1991, Change detection in SAR imagery, *International Journal of Remote Sensing* **12**(2), 339–360.

Wong, K., Luo, Z. and Jin, Q.: 1993, Design of optimum signals for the simultaneous estimation of time delay and Doppler shift, *IEEE Transactions on Signal Processing* **41**(6), 2141–2154.

Yang, H. and Soumekh, M.: 1992, Motion estimation and compensation in SAR/ISAR imaging, *Proceedings of ICASSP'92*, IEEE, pp. III–17–20.

Yang, H. and Soumekh, M.: 1993, Blind-velocity SAR/ISAR imaging of a moving target in a stationary background, *IEEE Transactions on Image Processing* **2**(1), 80–95.

Yinfang, M., Guoan, C. and Junfeng, W.: 1996, SAR/ISAR imaging of multiple moving targets based on combination of WVD and HT, *Proceedings of the 1996 CIE International Conference of Radar*, pp. 342–345.